
Doctoral Dissertations

Student Theses and Dissertations

Summer 2016

Bioactivity/cytotoxicity of micro-/nano-materials and novel development of fiber-optic probes for single cell monitoring

Qingbo Yang

Missouri University of Science and Technology, qyhb9@mst.edu

Follow this and additional works at: https://scholarsmine.mst.edu/doctoral_dissertations



Part of the [Biomedical Engineering and Bioengineering Commons](#), [Chemistry Commons](#), and the [Toxicology Commons](#)

Department: Chemistry

Recommended Citation

Yang, Qingbo, "Bioactivity/cytotoxicity of micro-/nano-materials and novel development of fiber-optic probes for single cell monitoring" (2016). *Doctoral Dissertations*. 2902.

https://scholarsmine.mst.edu/doctoral_dissertations/2902

This thesis is brought to you by Scholars' Mine, a service of the Missouri S&T Library and Learning Resources. This work is protected by U. S. Copyright Law. Unauthorized use including reproduction for redistribution requires the permission of the copyright holder. For more information, please contact scholarsmine@mst.edu.

BIOACTIVITY/CYTOTOXICITY OF MICRO-/NANO-MATERIALS AND NOVEL
DEVELOPMENT OF FIBER-OPTIC PROBES FOR SINGLE CELL MONITORING

by

QINGBO YANG

A DISSERTATION

Presented to the Faculty of the Graduate School of the
MISSOURI UNIVERSITY OF SCIENCE AND TECHNOLOGY

In Partial Fulfillment of the Requirements for the Degree

DOCTOR OF PHILOSOPHY

in

CHEMISTRY

2016

Approved

Yinfa Ma, Advisor

Hai Xiao

Honglan Shi

Jeffrey Winiarz

Paul Nam

© 2016

Qingbo Yang

All Rights Reserved

PUBLICATION DISSERTATION OPTION

This dissertation consists of the following six articles that have either been published (I - V) or prepared for submission (VI) as follows:

Paper I (Page 18-58) has been published on the INTERNATIONAL JOURNAL OF TOXICOLOGY (2014 Apr 3;1091581814529168).

Paper II (Page 59-88) has been published on the TOXICOLOGY RESEARCH (2016, 5, 482-491).

Paper III (Page 89-131) has been published on the MATERIAL SCIENCE AND ENGINEERING: C (2015 Oct 1;55:105-17).

Paper IV (Page 132-157) has been published on the SENSORS AND ACTUATORS B: CHEMICAL (2015 Feb 28;207:571-80).

Paper V (Page 158-186) has been published on the ANALYTICAL CHEMISTRY (2015 Jul 8;87(14):7171-9).

Paper VI (Page 187-207) has been prepared and is ready for submission to the NATURE COMMUNICATION.

ABSTRACT

Manufactured nano-/micro-materials (MNMs) have been widely used and their interactions with niche biological environment are highly concerned for both of their biohazardous and bioactive effects, whereas no available comprehensive evaluations or regulations have been provided yet. This dissertation thus focuses on three major aspects: 1) fundamental toxicity understandings of a typical MNMs (zinc oxide nanoparticles), 2) bioactivity evaluations of representative bioactive MNMs, and 3) development of novel micro-probes for high spatial resolution monitoring. Firstly, the NP's concentration, irradiation, hydrodynamic size, and the localized pH, ionic strength, NP zeta-potential as well as dissolved oxygen levels were found correlated with the production of hydroxyl radicals ($\bullet\text{OH}$). Thus a novel physicochemical mechanism was hypothesized on $\bullet\text{OH}$ generation from ZnO NPs to cast light on cytotoxic mechanisms of MNMs. Secondly, silicate-/borate-based nano-/micro-sized glass fibers showed good rehabilitation capability and the underlying mechanisms were revealed as that quicker ion releasing and glass conversion (into hydroxyapatite (HA)) are the key to promote cell proliferation and migration, thus the wound-healing effect. Thirdly, several types of fiber-optic-based probes were developed to better cope with high spatial resolution, niche biological environmental detection. Up to date the best probe is able to acquire a pH resolution of up to ~ 0.02 pH unit within biologically relevant pH range of 6.17 – 8.11 with fast sensing time of ~ 5 seconds. Real-time monitoring of single live human cells were also demonstrated and validated in cytotoxic studies to detect early-onset of cell deterioration on different stages, indicating its powerful potent on studies that focusing on MNMs and single cells.

ACKNOWLEDGMENTS

It has been my great honor to be able to work with many people on and out of MS&T campus throughout all these years. This is a moment I'd like to express my deepest appreciation to all these wonderful supports.

First of all, I want to sincerely thank my PhD advisor Dr. Yinfa Ma as well as one of my key co-advisor Dr. Honglan Shi, I thank them for their continual support and helpful discussions on many of my projects, providing numerous chances and opportunities for me not only to develop my scientific research ability but also to train my capabilities of handling high-risk multi-tasks, to better prepare myself for future academia career. I thank them to expose me with various interesting research fields and their constant encouragement to get in touch with frontier scientific topics.

I also want to thank my committee member Dr. Hai Xiao, in Clemson University, for his delicate support and master-level scientific guidance during our long-term collaborations. Together I want to thank Dr. Jeffrey Winiarz and Dr. Paul Nam for their being such wonderful models in both teaching and research, and their great advices and suggestions throughout these years.

I want to express my special appreciation to all my collaborators, lab mates and supportive technicians that I have been worked with. I appreciate funding agency and supportive on-campus research centers, especially CS³M, and our Chemistry Department for their tremendous support and help.

Finally, I gratefully thank all my family members and friends, especially, my wife Chenlan Qian, for her devotion and sacrifice, and her wonderful dedication in taking care of our family and our lovely daughter Caroline.

TABLE OF CONTENTS

	Page
PUBLICATION DISSERTATION OPTION.....	iii
ABSTRACT.....	iv
ACKNOWLEDGMENTS	v
LIST OF ILLUSTRATIONS.....	xii
LIST OF TABLES.....	xvi
 SECTION	
1. INTRODUCTION.....	1
1.1 NANOMATERIALS AND THEIR APPLICATIONS.....	1
1.2 NANOTOXICITY CONCERNS.....	2
1.3 CURRENT UNDERSTANDING OF NANOTOXICITY MECHANISM.....	3
1.4 CELL HETEROGENEITY AND THE EMPHASIS ON SINGLE CELL ANALYSIS	5
1.5 SINGLE CELL PH	7
1.6 TRENDS IN THE DEVELOPMENT OF SINGLE CELL RESEARCH TOOL KIT.....	8
1.7 UP-TO-DATE ACHIEVEMENTS AND FUTURE EXPECTATION.....	9
BIBLIOGRAPHY	11
 PAPER	
I. Irradiation-Enhanced Cytotoxicity of Zinc Oxide Nanoparticles.....	18
Abstract	19
Introduction.....	20
Materials and Methods.....	23
Reagents and Chemicals.....	23
Characterization of ZnO NPs	23
Lamp Information.....	24

Cell Culture and Treatment With ZnO NPs Under Various Irradiation Conditions	24
Cytotoxicity Assessment of ZnO NPs and Irradiation	26
Intracellular ROS Measurement	26
LDH Measurement	27
Cellular Staining With Fluorescent Probes	27
Tunneling Electron Microscopy Imaging	27
Statistical Analysis	28
Results	28
Characterization of ZnO NPs	28
Effects of Visible Light Exposure on Cytotoxicity of ZnO NPs	30
Effects of ZnO NP Dosages, Exposure Time and Irradiation Wavelengths on the Cytotoxicity of ZnO NPs	31
Cellular ROS Generation Induced by Exposure to ZnO Nanoparticles and Different Wavelengths of Irradiations	33
Cellular LDH Release after exposure to ZnO NPs at different irradiation conditions	35
Intracellular Damages Induced by ZnO NP Exposure and Irradiation	36
Remediation of Cytotoxicity Induced by ZnO NPs and Varied Irradiations Using NAC	40
Tunneling Electron Microscopy Images of Intracellular ZnO NPs	41
Discussion	44
Declaration of Conflicting Interests	55
Funding	55
References	55
II. Physicochemical insights of irradiation-enhanced hydroxyl radical generation from ZnO nanoparticles	59
Graphical Abstract	60
Abstract	61
Introduction	62

Experimental.....	64
Chemicals and reagents.....	64
ZnO particles characterization and suspension preparation.....	64
Electron spin resonance (ESR) experiments.....	65
Inductively-Coupled Plasma-Mass Spectrometry (ICP-MS) measurements....	66
Cell culture and treatment with ZnO NPs.....	67
Calcium imaging and three-dimensional (3-D) images plot.....	67
Results and discussion.....	68
The effect of irradiation on •OH generation.....	68
The effect of nanoparticle concentration on •OH generation.....	69
The effect of hydrodynamic size on •OH generation.....	71
The effect of pH on •OH generation.....	73
Effect of ionic strength and oxygen content on •OH generation.....	75
The effects of organic solvent and NP composition on •OH generation.....	78
Proposed cytotoxic mechanism.....	78
Extracellular calcium influx imaging.....	80
Conclusions.....	82
Associated content.....	83
Supporting Information.....	83
Author information.....	83
Conflict of interest.....	83
Acknowledgements.....	83
References.....	84
III. In vitro study of improved wound-healing effect of bioactive borate-based glass nano-/micro-fibers.....	89
ABSTRACT.....	90
Highlights.....	91
Table of Content Graphic (TOC).....	92

1. Introduction.....	93
2. Experimental section.....	96
2.1. Starting materials.....	96
2.2. In vitro fiber immersion, degradation, and conversion	96
2.3. Elemental analysis of ion releasing.....	98
2.4. Cell culture conditions and fiber dosing.....	99
2.5. In vitro cell proliferation and migration assay and confocal microscopic cell imaging.....	99
2.6. Statistical analysis	102
3. Results.....	102
3.1. Changes of fiber morphology under static mode	102
3.2. Changes of fiber morphology under dynamic-flow mode	106
3.3. Chemical characterization under static and dynamic modes.....	108
3.4. Elemental release pattern.....	109
3.5. Cell viability variation as function of fiber dosages and dosing time	112
3.6. Impact of pre-soaking of fibers on cell proliferation	113
3.7. Impact of dynamic mode on fiber-cell interaction	116
3.8. Impact of borate-based 1605 fibers on cell morphology and migration ..	117
4. Discussion.....	120
5. Conclusion	126
Author information	127
Acknowledgements.....	127
References.....	127
IV. Reflection-mode micro-spherical fiber-optic probes for in vitro real-time and single-cell level pH sensing.....	132
ABSTRACT.....	132
Highlights.....	133
Abbreviations.....	133
1. Introduction.....	135

2. Experiments	137
3. Results and discussions.....	141
4. Conclusions.....	152
Conflicting Interests.....	153
Acknowledgement	153
References.....	153
V. Fiber-Optic-Based Micro-Probe Using Hexagonal 1-in-6 Fiber Configuration for Intracellular Single-Cell pH Measurement	158
ABSTRACT.....	159
Table of Content Graphic:	160
INTRODUCTION	161
EXPERIMENTAL SECTION.....	164
Fabrication of Tapered Hexagonal Fiber Probe.	164
pH Sensing Layer Creation.	167
pH Sensing Principles and Optical Setups.	169
Characterization and Calibration of Sensor Probes.....	170
Cell Culture and Proof-of-Concept Single Cell pH Measurements.	171
RESULTS AND DISCUSSION.....	172
Probe Fabrication.	172
Probe Characterization.	173
System Setup and Laser Adjustment.....	175
Calibration and Linear Detection Range of the pH μ -Probe.	177
Intracellular pH Measurement in Single A549 Cells.	180
CONCLUSIONS	181
ASSOCIATED CONTENT	182
AUTHOR INFORMATION.....	182
ACKNOWLEDGMENTS	182
REFERENCES	183

VI. High spatiotemporal in situ pH monitoring in a single live cell using a micro-fiber-optic probe	187
Abstract	188
Introduction.....	188
Results.....	190
Design of the micro-fiber-optic based pH sensing system.....	190
μ -pH probe characterization and validation.	194
Intracellular pH measurement in a single live cell.	198
Monitoring of cell deterioration process by using this novel probe.....	199
Discussion.....	200
Acknowledgements.....	203
References.....	203
SECTION	
2. CONCLUSIONS.....	208
VITA	211

LIST OF ILLUSTRATIONS

	Page
PAPER I	
Figure 1. SEM images of 50-70 nm ZnO NP aggregations with or without ultrasonication.....	29
Figure 2. Cytotoxic effects of 50-70 nm ZnO NPs under visible light illumination on A549 cells..	31
Figure 3. Cytotoxicity effects of ZnO NP dosages, exposure time, and differed irradiation conditions on A549 cells.....	33
Figure 4. Effect of ZnO NPs on intracellular ROS generation under varied irradiation conditions.	34
Figure 5. LDH levels in cell culture medium after 6 hours of exposure to ZnO NPs under various irradiation conditions.....	36
Figure 6. Fluorescent and phase contrast microscopic images of A549 cells that were treated with 15 µg/mL and 25 µg/mL of ZnO nanoparticles under different irradiation conditions for 6 hours.....	38
Figure 7. Three-dimensional surface plots of FITC and DAPI merged images of A549 cells that were treated with ZnO NPs under varied irradiation conditions.....	40
Figure 8. Remediation effect of anti-oxidant NAC on A549 cells against cytotoxicity induced by ZnO NPs and varied irradiations.	41
Figure 9. TEM images of cellular destructions by ZnO NPs and irradiation treatment.	43
PAPER II	
Figure 1. ESR recording of •OH radical generation by 50-70 nm ZnO NPs in aqueous solution..	69
Figure 2. Continuous ESR recording of •OH by 50-70 nm ZnO NPs.....	71
Figure 3. Correlation of •OH generation and ZnO NPs hydrodynamic sizes.....	73
Figure 4. Physicochemical properties of ZnO NPs as functions of pH environment that presented through: a) ζ-potential, b) released zinc ions, and c) •OH generation.	75

Figure 5. Influences of radical production from (a) variable ionic strengths (IS) of ultra-pure water, tap water and a phosphate buffer solution (PBS), (b) varied oxygen abundances of non-aerated control (normal), N ₂ de-oxygenation, and O ₂ oxygenation treatments, and (c) non-centrifuged, centrifuged supernatant clear solution and re-suspended centrifugation-precipitation.	76
Scheme 1 Proposed mechanism of •OH generation by ZnO NPs mainly with assistance of irradiation and basic pH environment.	80
Figure 6 The correlation between ZnO NP uptake and intracellular calcium homeostasis.....	82
PAPER III	
Fig. 1. SEM images of silicate-based 45S5 glass fibers before (a, b) and after (c, d, e) 5 days soaking in cell culture medium under static mode.	103
Fig. 2. SEM images of borate-based 13-93B3 glass fibers before (a, b) and after (c, d) 5 days soaking in cell culture medium under static mode.....	104
Fig. 3. SEM images of borate-based 1605 glass fibers before (a, b) and after (c, d) 5 days soaking in cell culture medium under static mode.....	105
Fig. 4. SEM images of bioactive fiber end-faces before and after static-mode soaking in cell culture medium.....	106
Fig. 5. SEM images of bioactive fiber surface and end-face after dynamic-mode soaking in cell culture medium for 5 days.	107
Fig. 6. EDS scanning of elemental composition pattern of the as-received and post-soaking (5 days) bioactive glass micro-/nano-fibers (scanned areas are shown as red-squares that labelled in Fig. 1).	109
Fig. 7. Plot interpretation of ICP-OES data in comparison between fiber-released ion concentration and the soaking time, under either static (a - c) or dynamic (d - f) modes	110
Fig. 8. Forty-eight hours recording of viability when cells co-cultured with varied fiber dosages under static mode.....	113
Fig. 9. Viability assay using WST-1 when cells co-cultured with 100 µg/mL fresh fibers for 10 days under static mode.....	114
Fig. 10. WST-1 cell viability assay when co-cultured with (a) pre-soaked bioactive fibers for 72 hours, and (b) fiber-pre-soaked supernatants for 10 days, both under static mode.....	115

Fig. 11. WST-1 cell viability assay when cells co-cultured with 500 $\mu\text{g}/\text{mL}$ fresh fibers for 72 hours under dynamic mode.....	117
Fig. 12. Bioactive fiber influenced cell migration statistics under static/dynamic (inset) modes.	118
Fig. 13. Confocal microscopic images (a) and statistical analysis (b - d) of nucleus and mitochondrial staining of control and 1605 fiber co-cultured cells after a 72-hour dynamic mode treatment..	120

PAPER IV

Fig. 1 SEM images and EDS characterization of fabricated spherical head fiber-optic pH probe.....	140
Fig. 2 Configuration and microscopic images of BCECF dye covalent-bonded aerogel thin-layer on probing head with schematic diagram of whole system setup.....	142
Fig. 3 Reflection spectrum (fluorescent emission) from a pH sensitive thin film covered by BCECF dye doped ORMOSILs ultrathin layer.....	143
Fig. 4 Chemical characterization of optimized fabrication procedure of the ultrathin BCECF dye doped ORMOSILs layer by (a) TGA and (b) FT-IR.....	145
Fig. 5 Evaluation of environmental interference to the fabricated pH sensor by (a) ionic strength and (b) ambient temperature, respectively from 0.01 to 1 M and from 10 to 50°C.....	148
Fig. 6 Reflection mode detected fluorescent ratio (560/640 nm) spectra from fabricated fiber-optic pH sensor.....	150
Fig. 7 Repeatability and signal stability of the fabricated pH probe in a cycling measurement of pH6 (bottom), pH7 (middle) and pH8 (upper) buffer solutions for 35 minutes.	151

PAPER V

Figure 1. Detail coaxial-twisting/gravitational-stretching process in fabricating hexagonal pH μ -probe tip.....	166
Scheme 1. Major procedures that applied OrMoSils sol-gel dip-coating and HMDS vacuum priming for pH sensing layer fabrication.....	169

Figure 2. Finished hexagonal fiber taper probe configuration (a) and different imaging of twisting patterned area (b - d) under inverted microscope. A fully fabricated probe with fluorescent sensing layer coated and cured is shown under either white light (e) or fluorescein isothiocyanate (FITC) channel excitation light (f).....	173
Figure 3. Electron microscopic imaging and characterization of the newly developed pH probe.....	175
Figure 4. (A) Schematic diagram of the optical arrangement of the pH μ -probe; (B – C) Spectroscopic suppression of multiple laser peaks with power adjustment	176
Figure 5. (A) Fluorescence spectra of pH measurements under three different laser coupling powers (8.2 mW, 22 mW, and 39.8 mW); (B) Linear correlation curves between standard pHs and different laser powers. (C) pH detection resolution as functions of power laser as well as pH values.....	179
Figure 6. Preliminary measurement of intracellular pHs in single A549 cells using fabricated hexagonal pH μ -probe.	181
PAPER VI	
Scheme 1. Schematics of system setup and single cell μ -pH probe design.....	191
Figure 1. Fabrication and validation of the μ -pH probe.	197
Figure 2. Early-stage cell deterioration illustrations by in situ single cell pH sensing.	201

LIST OF TABLES

	Page
PAPER III	
Table 1	Original weight-percentage compositions of the bioactive glass nano-/micro-fiber that used in this study. 96
Table 2	Elemental releasing peak as percentage of theoretical total amount that would occur under ideal static condition. 112
PAPER V	
Table 1	Variation ranges of several key factors of a fully fabricated hexagonal 1-in-6 pH probe..... 167

SECTION

1. INTRODUCTION

1.1 NANOMATERIALS AND THEIR APPLICATIONS

Many physicochemical properties of materials when comes down to the nanometer scale become extremely unique, which have greatly improved or created fundamental researches as well as industrial applications that ranging from structural/strength enhancement, fluorescent dye/probe development, nanoscale device fabrication and manipulation, to energy collection and conservation, micro-laser construction as well as antimicrobial/sterilization products. These manufactured nanomaterials (MNMs) have also been widely used in infrastructure construction and agriculture related products. Thus, a variety of research and industrial fields that related to MNMs need to be reviewed to screen out possible environmental leakage and releasing circumstances, so that better conclusions could be drawn on how to rationally evaluate adverse effect of MNMs on a toxicology point of view, and to support the idea of developing regulatory guidelines for the fabrication, transportation, application, disposal and even recycling, in order to better protect our society and environment health.[1]

The fabricated MNMs embrace unique properties that their bulk counterpart do not have, such as high volume/surface ratio, surface tailorability, improved solubility, and multi-functionality, which in all opened numerous new possibilities for biomedicine research and application. Further, the intrinsic properties of nanomaterials, such like optical, magnetic and biological related properties provide splendid opportunities for future studying and regulating complicated biological process in an unprecedented

manner. After all, even life itself is fundamentally a handful of processes down to a nanoscale level with each cells.[2]

MNMs have been used for medical/clinical purposes, semiconductor manufacturing, as well as food processing, which are successful and yet, have no apparent safety issue appeared. However, recent applications in personal products and agriculture, especially when used for skin-contacting or crop protection and production, draw significant amount of public concerns, and intensive research efforts have already been conducted within these fields. For example, substantially large groups of studies have shown that some nanomaterials that composed of semiconductor metal oxides or non-metal oxides, such as SiO_2 , CeO_2 , ZnO , Al_2O_3 , etc., can pose high amount of cytotoxic risks on different *in vitro* cultured cell lines.[3-7] Recent studies found that irradiation (from UV to visible spectral wavelength) can greatly enhance the cytotoxic effect caused by ZnO nanoparticles.[8] Another example showing that the nanomaterials can potentially improve seed germination and whole plant growth through providing multiple protections for plant in detecting pathogens, as well as pesticide and herbicide residues.[9] Intrinsic abilities of these MNMs to interact with biological systems triggered synthesis of more nanowires, nanofibers, nanotubes, etc., and a variety of biological applications.

1.2 NANOTOXICITY CONCERNS

The bio-compatibility, cellular/sub-cellular distribution/localization and functional interferences are some key factors of these MNMs that determine their toxicities and, therefore, the extent to which they could be used. Recent studies indicated that engineered nanostructures may get in active contact with living organisms at realistic

doses; however, we may ignore their prolonged interaction with the niche tissues or cells that may ultimately disrupt normal activities and lead to malfunction or diseases, especially those nanomaterials that could be used for healing damaged organs. In this case, a possible long-term environmental and human health hazards need to be strictly supervised, and how those nanostructures entering and distributing inside the cell and body is critical.[10]

The interactions between nanoparticles and the cells have certain principles as those between colloidal particles and cells. The Van Der Waals forces (VDW), electrostatic, solvation as well as depletion forces are still applicable, but they need special requirements when considering events that occurred at nanoscale.[11-13] For instance, since nanoparticles contain relatively much less atoms, their VDW forces are highly dependent on the positioning of their surface atoms and their standard bulk permittivity functions. This sophisticated phenomenon may greatly influence the interactions between nanomaterials and biological systems. A simple example would be: the interaction between two silica particles, while compared with that between a SiO₂ particle and a fibroblast cell.[14]

1.3 CURRENT UNDERSTANDING OF NANOTOXICITY MECHANISM

Engineered nanomaterials mostly have structures with at least one dimension of 100 nanometers or less. Material size ranges may approach the scale at which some specific physical or chemical interactions can occur. Substantial property changes will discriminate them from their bulk materials, and this would allow them to perform exceptional feats of conductivity, reactivity, and optical sensitivity. MNMs with these extra capabilities can negatively interact with biological systems and the environment,

with the potential to generate toxicity. Possible nanotoxicity mechanisms may be related with physicochemical properties of the materials, Fenton chemistry, dissolution as well as irradiation induced radical formation, which will induce a series of toxic bio-effects such as: reactive oxygen species (ROS) production, proinflammatory effects, granulomatous inflammation, interstitial pulmonary fibrosis, membrane disruption/damage/thinning/leakage, damage to the acidifying endosomal compartment, DNA damage and broader oxidative stress, etc.[14] However, there are currently no conclusive data or scenarios that convincingly indicate these effects. Thus, complete and comprehensive safety evaluations on MNMs should be established immediately. Moreover, fundamental research and comprehensive understanding of such nanotoxicity as well as their possible correlation with any existing pathophysiological or carcinogenesis pathways should also be fully addressed.

The major problem in assessing the hazardous effects of MNMs is currently limited by the lack of empirical data as well as feasible devices. In addition, questionable data also exist from previous studies that did not use realistic evaluation condition or protocols in determining the dose/time/environmental-response parameters, which will greatly affect estimation accuracy of health risks associated with the MNMs. A number of open questions have been suggested and here we quote: (i) developing a combination of different analytical methods for determining MNMs concentration, size, shape, surface properties, and morphology in different environmental media, (ii) conducting toxicity studies using environmentally relevant exposure conditions and obtaining data relevant to developing quantitative nanostructure-toxicity relationships (QNTR), and (iii) developing guidelines for regulating exposure of engineered nanomaterials in the environment.[15]

Besides, a considerable effort is also needed to study the physiological effects of acute and chronic MNMs exposures. A profound illustration and full understanding of the biological interactions between NPs and proteins, cells and tissues, is vital for the future design of safe nanotechnologies. Prior to their wider adoption in everyday products and their clinical use, NP-products must be shown to have a high degree of biocompatibility, with minimal negative effects on blood components, genetic material, and cell viability.

In this regard, this dissertation tries to cover three major aspects that correlated with MNMs biofunctionality through providing: 1) phenomenon to mechanism illustration of nanotoxicity, 2) a case study of bioactive nano-/micro-glass fibers on wound-healing effects and 3) systematic developments of novel series of high resolution sensors, together to render a handful of knowledge and feasible new tools to pioneeringly pave the way to the fundamental research on the biofunctionality of MNMs.

1.4 CELL HETEROGENEITY AND THE EMPHASIS ON SINGLE CELL ANALYSIS

Although many efforts have been conducted in dealing with the MNMs toxicity as well as bioactivity on both phenomenon and mechanism levels, there is another important factor that greatly attenuates previously achieved knowledge and principles: cellular heterogeneity. Actually, cellular heterogeneity has been acknowledged as the major obstacle in understanding many real mechanisms of biological system functioning.[16-20] This is because that either cells or tissues are complex dynamic systems and the components change with time and depending on environment. For example, even under seemingly identical culturing conditions, cells often display certain types of heterogeneous behaviors due to the lack of synchronization among cells, which cannot be

easily detected using conventional techniques. Unfortunately, most of our current biological database and knowledge were acquired based on obscure, population-averaged experiments and measurements, and this becomes specifically questionable when we are trying to answer fundamental questions that related to individual cell heterogeneity. Thus, the lack of true mechanistic interpretation at the single-cell level has considerably hindered the progress of many key research areas, such as cell fate determination, cytotoxicity, drug discovery, stem cell differentiation, and carcinogenesis etc.

Therefore, it is crucial to firstly be able to monitor individual cell functioning under specific niche environmental condition by measuring particular extra-/intra-cellular parameters. Among all intracellular parameters, cytosolic proton concentration (or pH) (as well as temperature), serves as a universal indicator for fundamental cellular events, such as serving as a heterogeneity biomarker for early-stage cellular dynamics. However, the *in situ* intracellular pH (and temperature) measurement in a single cell with high spatiotemporal resolution, while the cell is fully functioning, is extremely challenging. Accurate measurements of intracellular pH (and temperature) are crucial because many biological processes are temperature and pH sensitive.[21-28] For instance, living cells change their temperature during cell activities such as division, gene expression, enzyme reaction, and metabolism.[24] The ratios between the extracellular temperature (T_e) and intracellular temperature (T_i) were different in disease or cancer cells when compared to normal healthy cells [29, 30]. In a similar study, cancerous cells have shown extraordinary heat generation.[31] Under external stimuli such as drug or toxic materials, cells may quickly change their metabolic activities, leading to acute variations in intracellular temperature, pH, and even structures from their normal states. Therefore,

reliable instrument to measure these parameters in a single cell is of utmost importance. Besides, cell signaling events such as pH changes, temperature oscillations, and signaling molecules, can trigger substantial responses including cell division, differentiation and death.[32]

1.5 SINGLE CELL PH

It has been noticed that cellular pH imbalance in carcinogenesis may represent novel therapeutic target and potentially has wide applicability. However, it requires better understandings of how individual cells respond to altered pHs. The intracellular pH (pH_i) of healthy adult cell is normally maintained near 7.2, which is lower than the extracellular environment. However, cancer cells maintain a higher pH_i (>7.4) but have characteristically lower extracellular pH (pH_e) (6.7 – 7.1) [33-35]. On one hand, increased pH_i has been shown to assist cell proliferation and evasion of apoptosis, to facilitate metabolic adaptation, as well as to improve cancer cell motility. Decreased pH_e , on the other hand, can stimulate acid-activated proteases to help tumor cells invasion and dissemination [36]. Moreover, a Na^+/H^+ exchanger, named NHE1, similar to those that exist in human melanoma cells (MV3), can generate a well-defined cell surface pH gradient at the outer leaflet of the plasma membrane to assist cell body polarity and migration [37]. In addition, the temporal pH change and spatial pH difference of individual cells may also play important roles during many cellular processes and disease development [36, 38-42]. Thus, accurate and *in situ*, real-time pH measurement in a individual living cell are important for understanding the cell biology and related processes.

1.6 TRENDS IN THE DEVELOPMENT OF SINGLE CELL RESEARCH TOOL KIT

While increasing evidences show that pH_i and pH_e playing critical roles for many biological processes (cell migration, proliferation, differentiation, carcinogenesis, etc.) [43-50], relevant techniques capable of monitoring microenvironment pH remain underdeveloped. ^1H based magnetic resonance spectroscopic (MRS) imaging has been used for pH_e mapping in rat brain gliomas [51] and on solid tumors of human breast cancer xenografts [52]. The low spatial resolution of MRS at the mm^3 scale makes it almost impossible to dynamically monitor a single cell. Dye-based pH sensing is not suitable for long-term pH_e measurement due to the potential carcinogenic risks [53, 54]. The recently reported approaches of near-IR fluorescent graphene oxide nano-sheet can response reversibly to extracellular pH and ionic strength [55]. A novel electrochemical probe for real-time detecting of extracellular pH with high spatial sensitivity has also been used to investigate fiber cells [56]. However, these matrix-based techniques need to be pre-planted in a confined area of cell growth and thus do not have the desired ability to measure a specific single cell target. As such, the major challenges tackle the cellular heterogeneity is the real time *in situ* measurement of the behavioral parameters of a single cell, which requires dedicated micro/nano size sensors that can be inserted into the cell for *in situ* measurement, yet without introducing significant damages or influences to the living cell. In this case, single cell analysis tools, especially the instrument for simultaneous multi-parametric measurement, are still in urgent need for both basic biomedical research and clinical applications.

A number of techniques have recently been explored for monitoring real single cell behaviors [57-64]. However, most of the reported techniques have been targeting one specific parameter. Comprehensive physical, chemical and biological analyses of a single cell, still present great challenges to the research community due to the small scale targets as well as the complicated processes of a single cell responding to its local environment and stimuli. Tremendous efforts on single cell pH have been attempted, [42, 65-68] including the mainstream labelling method, using artificially-modified fluorophores to stain subcellular compartments.[69-80] However, the applications of these methods are still limited because the chemicals used may alter the intercellular conditions and cell behaviors. The inevitably long and reinforced maintenance of the reagents within cytosol ruins the representativeness of derived signals. Potential cytotoxicity of excessive dye-usage, fluorescence attenuation, as well as non-continuous reagent passage to the offspring cells, can further deteriorate the accountability of staining-based assays. Last but not the least, another major weakness of cell staining/labelling methodology is that it cannot be used for continuous single-cell pH measurements when the cellular exposure environment changes.

1.7 UP-TO-DATE ACHIEVEMENTS AND FUTURE EXPECTATION

Optical fiber based sensors such as fiber gratings [81-83], optical interferometers [84, 85] and optical micro resonators [86, 87] are emerging for micro-/nano-meter scale measurements, and supposed to be a promising methodology for accurate, remote measurements with a real-time manner. The only problem is that most of the developed fiber sensors are still too large when compared with the size of a single cell. To overcome these limitation and challenges, we developed a μ -pH sensing probe [88, 89] in

combination with a homebuilt cell manipulation system. The experimental results demonstrated that these μ -probes are capable to measure real-time response in a single live cell with high sensitivity and spatial resolution.

Finally, our future plan include the development of an integrated μ -pH and μ -temperature dual functional probe to enable simultaneous measurements of pH_i/pH_e and T_i/T_e with minimum invasiveness to single living cell. This further development will ultimately result in an innovative single cell analyzer with enhanced functions, stability, robustness, resolution, and flexibility to fulfill the urgent needs for *in situ* multi-parametric measurements at the single cell level. We are looking forward to greatly benefit a wide range of biomedical and clinical researches by using this device and contribute to the next generation precise biomedical practices.

BIBLIOGRAPHY

- [1] Lee J, Mahendra S, Alvarez PJ. Nanomaterials in the construction industry: a review of their applications and environmental health and safety considerations. *ACS nano*. 2010;4:3580-90.
- [2] Mann S. Life as a nanoscale phenomenon. *Angewandte Chemie International Edition*. 2008;47:5306-20.
- [3] Lin W, Stayton I, Huang Y-w, Zhou X-D, Ma Y. Cytotoxicity and cell membrane depolarization induced by aluminum oxide nanoparticles in human lung epithelial cells A549. *Toxicological and Environmental Chemistry*. 2008;90:983-96.
- [4] Lin W, Xu Y, Huang C-C, Ma Y, Shannon KB, Chen D-R, et al. Toxicity of nano- and micro-sized ZnO particles in human lung epithelial cells. *Journal of Nanoparticle Research*. 2009;11:25-39.
- [5] Lin W, Huang Y-w, Zhou X-D, Ma Y. In vitro toxicity of silica nanoparticles in human lung cancer cells. *Toxicology and applied pharmacology*. 2006;217:252-9.
- [6] Lin W, Huang Y-w, Zhou X-D, Ma Y. Toxicity of cerium oxide nanoparticles in human lung cancer cells. *International Journal of toxicology*. 2006;25:451-7.
- [7] Adams M, Lin W, Ma Y. Quantitative determination of ZnO nano-particles in human bronchoalveolar carcinoma-derived lung cancer cells. 2007.
- [8] Yang Q, Ma Y. Irradiation-Enhanced Cytotoxicity of Zinc Oxide Nanoparticles. *International Journal of toxicology*. 2014:1091581814529168.
- [9] Khot LR, Sankaran S, Maja JM, Ehsani R, Schuster EW. Applications of nanomaterials in agricultural production and crop protection: a review. *Crop Protection*. 2012;35:64-70.
- [10] Casals E, Vázquez-Campos S, Bastús NG, Puntès V. Distribution and potential toxicity of engineered inorganic nanoparticles and carbon nanostructures in biological systems. *TrAC Trends in Analytical Chemistry*. 2008;27:672-83.
- [11] Min Y, Akbulut M, Kristiansen K, Golan Y, Israelachvili J. The role of interparticle and external forces in nanoparticle assembly. *Nature materials*. 2008;7:527-38.
- [12] Dagastine RR, Manica R, Carnie SL, Chan D, Stevens GW, Grieser F. Dynamic forces between two deformable oil droplets in water. *Science*. 2006;313:210-3.
- [13] Kim H-Y, Sofo JO, Velegol D, Cole MW, Lucas AA. van der Waals dispersion forces between dielectric nanoclusters. *Langmuir : the ACS journal of surfaces and colloids*. 2007;23:1735-40.

- [14] Nel AE, Mädler L, Velegol D, Xia T, Hoek EM, Somasundaran P, et al. Understanding biophysicochemical interactions at the nano–bio interface. *Nature materials*. 2009;8:543-57.
- [15] Kumar A, Kumar P, Anandan A, Fernandes TF, Ayoko GA, Biskos G. Engineered Nanomaterials: Knowledge Gaps in Fate, Exposure, Toxicity, and Future Directions. *Journal of Nanomaterials*. 2014;2014.
- [16] Arriaga EA. Single cell heterogeneity. *Single Cell Analysis: Technologies and Applications*. 2009:223-34.
- [17] Schroeder T. Heterogeneity of sister cell fates. *Nature Reviews Molecular Cell Biology*. 2013;14:327-.
- [18] Meacham CE, Morrison SJ. Tumour heterogeneity and cancer cell plasticity. *Nature*. 2013;501:328-37.
- [19] Tang DG. Understanding cancer stem cell heterogeneity and plasticity. *Cell research*. 2012;22:457-72.
- [20] Aird WC. Endothelial cell heterogeneity. *Cold Spring Harbor perspectives in medicine*. 2012;2:a006429.
- [21] Busa WB, Nuccitelli R. Metabolic regulation via intracellular pH. *Am J Physiol*. 1984;246:R409-38.
- [22] Boron WF, McCormick WC, Roos A. pH regulation in barnacle muscle fibers: dependence on extracellular sodium and bicarbonate. *Am J Physiol*. 1981;240:C80-9.
- [23] Boron WF, Boulpaep EL. Intracellular pH regulation in the renal proximal tubule of the salamander. Basolateral HCO₃⁻ transport. *J Gen Physiol*. 1983;81:53-94.
- [24] Francis D, Barlow PW. Temperature and the cell cycle. *Symp Soc Exp Biol*. 1988;42:181-201.
- [25] Busa W, Nuccitelli R. Metabolic regulation via intracellular pH. *American Journal of Physiology-Regulatory, Integrative and Comparative Physiology*. 1984;246:R409-R38.
- [26] Boron WF, McCormick WC, Roos A. pH regulation in barnacle muscle fibers: dependence on extracellular sodium and bicarbonate. *American Journal of Physiology-Cell Physiology*. 1981;240:C80-C9.
- [27] Boron WF, Boulpaep EL. Intracellular pH regulation in the renal proximal tubule of the salamander. Basolateral HCO₃⁻ transport. *The Journal of General Physiology*. 1983;81:53-94.
- [28] Francis D, Barlow P. Temperature and the cell cycle. *Symposia of the Society for Experimental Biology* 1987. p. 181-201.

- [29] Okabe K, Inada N, Gota C, Harada Y, Funatsu T, Uchiyama S. Intracellular temperature mapping with a fluorescent polymeric thermometer and fluorescence lifetime imaging microscopy. *Nature communications*. 2012;3:705.
- [30] Donner JS, Thompson SA, Kreuzer MP, Baffou G, Quidant R. Mapping intracellular temperature using green fluorescent protein. *Nano letters*. 2012;12:2107-11.
- [31] Monti M, Brandt L, Ikomi-Kumm J, Olsson H. Microcalorimetric investigation of cell metabolism in tumour cells from patients with non-Hodgkin lymphoma (NHL). *Scandinavian journal of haematology*. 1986;36:353-7.
- [32] Spiller DG, Wood CD, Rand DA, White MR. Measurement of single-cell dynamics. *Nature*. 2010;465:736-45.
- [33] Gillies RJ, Raghunand N, Karczmar GS, Bhujwala ZM. MRI of the tumor microenvironment. *Journal of Magnetic Resonance Imaging*. 2002;16:430-50.
- [34] Busco G, Cardone RA, Greco MR, Bellizzi A, Colella M, Antelmi E, et al. NHE1 promotes invadopodial ECM proteolysis through acidification of the peri-invadopodial space. *The FASEB Journal*. 2010;24:3903-15.
- [35] Gallagher FA, Kettunen MI, Day SE, Hu D-E, Ardenkjær-Larsen JH, Jensen PR, et al. Magnetic resonance imaging of pH in vivo using hyperpolarized ¹³C-labelled bicarbonate. *Nature*. 2008;453:940-3.
- [36] Webb BA, Chimenti M, Jacobson MP, Barber DL. Dysregulated pH: a perfect storm for cancer progression. *Nature Reviews Cancer*. 2011;11:671-7.
- [37] Stüwe L, Müller M, Fabian A, Waning J, Mally S, Noël J, et al. pH dependence of melanoma cell migration: protons extruded by NHE1 dominate protons of the bulk solution. *The Journal of physiology*. 2007;585:351-60.
- [38] Valli M, Sauer M, Branduardi P, Borth N, Porro D, Mattanovich D. Intracellular pH distribution in *Saccharomyces cerevisiae* cell populations, analyzed by flow cytometry. *Applied and environmental microbiology*. 2005;71:1515-21.
- [39] Estrella V, Chen T, Lloyd M, Wojtkowiak J, Cornell HH, Ibrahim-Hashim A, et al. Acidity generated by the tumor microenvironment drives local invasion. *Cancer research*. 2013;73:1524-35.
- [40] Gerweck LE, Seetharaman K. Cellular pH gradient in tumor versus normal tissue: potential exploitation for the treatment of cancer. *Cancer research*. 1996;56:1194-8.
- [41] Liechty WB, Peppas NA. Expert opinion: responsive polymer nanoparticles in cancer therapy. *European Journal of Pharmaceutics and Biopharmaceutics*. 2012;80:241-6.

- [42] Modi S, Swetha M, Goswami D, Gupta GD, Mayor S, Krishnan Y. A DNA nanomachine that maps spatial and temporal pH changes inside living cells. *Nature Nanotechnology*. 2009;4:325-30.
- [43] Stock C, Gassner B, Hauck CR, Arnold H, Mally S, Eble JA, et al. Migration of human melanoma cells depends on extracellular pH and Na⁺/H⁺ exchange. *The Journal of physiology*. 2005;567:225-38.
- [44] Xu L, Fukumura D, Jain RK. Acidic Extracellular pH Induces Vascular Endothelial Growth Factor (VEGF) in Human Glioblastoma Cells via ERK1/2 MAPK Signaling Pathway MECHANISM OF LOW pH-INDUCED VEGF. *Journal of Biological Chemistry*. 2002;277:11368-74.
- [45] Rofstad EK, Mathiesen B, Kindem K, Galappathi K. Acidic extracellular pH promotes experimental metastasis of human melanoma cells in athymic nude mice. *Cancer research*. 2006;66:6699-707.
- [46] Takahashi T, Lord B, Schulze PC, Fryer RM, Sarang SS, Gullans SR, et al. Ascorbic acid enhances differentiation of embryonic stem cells into cardiac myocytes. *Circulation*. 2003;107:1912-6.
- [47] Roberts AW, Haigler CH. Cell expansion and tracheary element differentiation are regulated by extracellular pH in mesophyll cultures of *Zinnia elegans* L. *Plant physiology*. 1994;105:699-706.
- [48] Watt FM, Huck WT. Role of the extracellular matrix in regulating stem cell fate. *Nature Reviews Molecular Cell Biology*. 2013;14:467-73.
- [49] Pellegrini P, Strambi A, Zipoli C, Hägg-Olofsson M, Buoncervello M, Linder S, et al. Acidic extracellular pH neutralizes the autophagy-inhibiting activity of chloroquine: Implications for cancer therapies. *Autophagy*. 2014;10:562-71.
- [50] Lee S, Mele M, Vahl P, Christiansen PM, Jensen VE, Boedtkjer E. Na⁺, HCO₃⁻-cotransport is functionally upregulated during human breast carcinogenesis and required for the inverted pH gradient across the plasma membrane. *Pflügers Archiv-European Journal of Physiology*. 2014;467:367-77.
- [51] García-Martín M-L, Hérigault G, Rémy C, Farion R, Ballesteros P, Coles JA, et al. Mapping Extracellular pH in rat Brain Gliomas in vivo by H Magnetic Resonance Spectroscopic Imaging: Comparison with maps of metabolites. *Cancer research*. 2001;61:6524-31.
- [52] Bhujwala Z, Artemov D, Ballesteros P, Cerdan S, Gillies R, Solaiyappan M. Combined vascular and extracellular pH imaging of solid tumors. *NMR in Biomedicine*. 2002;15:114-9.

- [53] Rota C, Chignell CF, Mason RP. Evidence for free radical formation during the oxidation of 2'-7'-dichlorofluorescein to the fluorescent dye 2'-7'-dichlorofluorescein by horseradish peroxidase.: Possible implications for oxidative stress measurements. *Free Radical Biology and Medicine*. 1999;27:873-81.
- [54] O'Brien J, Wilson I, Orton T, Pognan F. Investigation of the Alamar Blue (resazurin) fluorescent dye for the assessment of mammalian cell cytotoxicity. *European Journal of Biochemistry*. 2000;267:5421-6.
- [55] Chen J-L, Yan X-P. Ionic strength and pH reversible response of visible and near-infrared fluorescence of graphene oxide nanosheets for monitoring the extracellular pH. *Chemical Communications*. 2011;47:3135-7.
- [56] Thakur B, Jayakumar S, Sawant SN. Probing extracellular acidity of live cells in real time for cancer detection and monitoring anti-cancer drug activity. *Chemical Communications*. 2015;51:7015-8.
- [57] Nash MS, Young KW, Willars GB, Challiss RAJ, Nahorski SR. Single-cell imaging of graded Ins(1,4,5)P₃ production following G-protein-coupled-receptor activation. *Biochem J*. 2001;356:137-42.
- [58] Arai F, Ng C, Maruyama H, Ichikawa A, El-Shimy H, Fukuda T. On chip single-cell separation and immobilization using optical tweezers and thermosensitive hydrogel. *Lab Chip*. 2005;5:1399-403.
- [59] Plitzko JM. Cellular cryo-electron tomography (CET): towards a voyage to the inner space of cells. Wiley-VCH Verlag GmbH & Co. KGaA; 2009. p. 39-68.
- [60] Ros R, Hansmeier N. Gene classification and quantitative analysis of gene regulation in bacteria using cell atomic force microscopy and single molecule force spectroscopy. Wiley-VCH Verlag GmbH & Co. KGaA; 2009. p. 19-37.
- [61] Knolhoff AM, Rubakhin SS, Sweedler JV. Single-cell mass spectrometry. Wiley-VCH Verlag GmbH & Co. KGaA; 2010. p. 197-218.
- [62] Rusciano G. Experimental analysis of Hb oxy-deoxy transition in single optically stretched red blood cells. *Phys Med*. 2010;26:233-9.
- [63] Salehi-Reyhani A, Kaplinsky J, Burgin E, Novakova M, de MAJ, Templer RH, et al. A first step towards practical single cell proteomics: a microfluidic antibody capture chip with TIRF detection. *Lab Chip*. 2011;11:1256-61.
- [64] Xu C-X, Yin X-F. Continuous cell introduction and rapid dynamic lysis for high-throughput single-cell analysis on microfluidic chips with hydrodynamic focusing. *J Chromatogr, A*. 2011;1218:726-32.
- [65] Bradley M, Alexander L, Duncan K, Chennaoui M, Jones AC, Sánchez-Martín RM. pH sensing in living cells using fluorescent microspheres. *Bioorganic & medicinal chemistry letters*. 2008;18:313-7.

- [66] Ogikubo S, Nakabayashi T, Adachi T, Islam MS, Yoshizawa T, Kinjo M, et al. Intracellular pH sensing using autofluorescence lifetime microscopy. *The Journal of Physical Chemistry B*. 2011;115:10385-90.
- [67] Ohmichi T, Kawamoto Y, Wu P, Miyoshi D, Karimata H, Sugimoto N. DNA-based biosensor for monitoring pH in vitro and in living cells. *Biochemistry*. 2005;44:7125-30.
- [68] Albertazzi L, Storti B, Marchetti L, Beltram F. Delivery and subcellular targeting of dendrimer-based fluorescent pH sensors in living cells. *Journal of the American Chemical Society*. 2010;132:18158-67.
- [69] Heim N, Garaschuk O, Friedrich MW, Mank M, Milos RI, Kovalchuk Y, et al. Improved calcium imaging in transgenic mice expressing a troponin C-based biosensor. *Nature methods*. 2007;4:127-9.
- [70] Cheng A, Gonçalves JT, Golshani P, Arisaka K, Portera-Cailliau C. Simultaneous two-photon calcium imaging at different depths with spatiotemporal multiplexing. *Nature methods*. 2011;8:139-42.
- [71] Welsher K, Liu Z, Daranciang D, Dai H. Selective probing and imaging of cells with single walled carbon nanotubes as near-infrared fluorescent molecules. *Nano letters*. 2008;8:586-90.
- [72] Wang C, Cheng L, Xu H, Liu Z. Towards whole-body imaging at the single cell level using ultra-sensitive stem cell labeling with oligo-arginine modified upconversion nanoparticles. *Biomaterials*. 2012;33:4872-81.
- [73] Hennig S, van de Linde S, Lummer M, Simonis M, Huser T, Sauer M. Instant live-cell super-resolution imaging of cellular structures by nano-injection of fluorescent probes. *Nano letters*. 2015;15:1374-81.
- [74] Walker CL, Lukyanov KA, Yampolsky IV, Mishin AS, Bommarius AS, Duraj-Thatte AM, et al. Fluorescence imaging using synthetic GFP chromophores. *Current opinion in chemical biology*. 2015;27:64-74.
- [75] Mickler FM, Möckl L, Ruthardt N, Ogris M, Wagner E, Bräuchle C. Tuning nanoparticle uptake: live-cell imaging reveals two distinct endocytosis mechanisms mediated by natural and artificial EGFR targeting ligand. *Nano letters*. 2012;12:3417-23.
- [76] Kang B, Afifi MM, Austin LA, El-Sayed MA. Exploiting the nanoparticle plasmon effect: Observing drug delivery dynamics in single cells via Raman/fluorescence imaging spectroscopy. *Acs Nano*. 2013;7:7420-7.
- [77] Zrazhevskiy P, Gao X. Quantum dot imaging platform for single-cell molecular profiling. *Nature communications*. 2013;4:1619.
- [78] Alford R, Simpson HM, Duberman J, Hill GC, Ogawa M, Regino C, et al. Toxicity of organic fluorophores used in molecular imaging: literature review. *Molecular imaging*. 2009;8:341.

- [79] Albanese A, Tang PS, Chan WC. The effect of nanoparticle size, shape, and surface chemistry on biological systems. *Annual review of biomedical engineering*. 2012;14:1-16.
- [80] Hoshino A, Hanada S, Yamamoto K. Toxicity of nanocrystal quantum dots: the relevance of surface modifications. *Archives of toxicology*. 2011;85:707-20.
- [81] Rao YJ. In-fibre Bragg grating sensors. *Measurement Science and Technology*. 1997;8:355-75.
- [82] Mandal J, Pal S, Tong S, Grattan KTV, Augousti AT, Wade SA. Bragg grating-based fiber-optic laser probe for temperature sensing. *Photonics Technology Letters, IEEE*. 2004;16:218-20.
- [83] Bhatia V. Applications of long-period gratings to single and multi-parameter sensing. *Optics Express*. 1999;4:457-66.
- [84] Tao W, Xinwei L, Hai X. Fiber Inline Core-Cladding-Mode Mach-Zehnder Interferometer Fabricated by Two-Point CO₂ Laser Irradiations. *Photonics Technology Letters, IEEE*. 2009;21:669-71.
- [85] Yuan L, Wei T, Han Q, Wang H, Huang J, Jiang L, et al. Fiber inline Michelson interferometer fabricated by a femtosecond laser. *Optics Letters*. 2012;37:4489-91.
- [86] Dong CH, He L, Xiao YF, Gaddam VR, Ozdemir SK, Han ZF, et al. Fabrication of high-Q polydimethylsiloxane optical microspheres for thermal sensing. *Applied Physics Letters*. 2009;94.
- [87] De Berardis B, Civitelli G, Condello M, Lista P, Pozzi R, Arancia G, et al. Exposure to ZnO nanoparticles induces oxidative stress and cytotoxicity in human colon carcinoma cells. *Toxicology and applied pharmacology*. 2010;246:116-27.
- [88] Yang Q, Wang H, Lan X, Cheng B, Chen S, Shi H, et al. Reflection-mode microspherical fiber-optic probes for in vitro real-time and single-cell level pH sensing. *Sensors and Actuators B: Chemical*. 2015;207:571-80.
- [89] Yang Q, Wang H, Chen S, Lan X, Xiao H, Shi H, et al. Fiber-Optic-Based Micro-Probe Using Hexagonal 1-in-6 Fiber Configuration for Intracellular Single-Cell pH Measurement. *Analytical chemistry*. 2015;87:7171-9.

PAPER**I. Irradiation-Enhanced Cytotoxicity of Zinc Oxide Nanoparticles**

Qingbo Yang, Yinfa Ma *

Department of Chemistry and Environmental Research Center, Missouri University of
Science and Technology, Rolla, MO 65409, USA

* Corresponding Author

Address: Department of Chemistry

Missouri University of Science and Technology

400 West 11th Street

Rolla, MO 65409

Phone: 573-341-6220

Fax: 573-341-6033

E-mail: yinfa@mst.edu

Abstract

Zinc oxide (ZnO) nanoparticles (NPs) have been widely utilized in industry due to their versatile properties; this has drawn considerable public health concerns on their acute and chronic toxicity to humans. Although recent studies have shown cytotoxic effects of these nanoparticles, including oxidative stress, apoptosis and necrosis induction, genotoxicity, and others, irradiation-induced cytotoxicity, however, has not been studied. The goal of this study was to determine whether irradiation in the forms of visible light (approximately 400 – 600 nm), UVA (366 nm), and UVC (254 nm) would affect the cytotoxicity caused by ZnO NPs. The results of this study demonstrated that the cytotoxicity of 50-70 nm ZnO NPs to A549 cells is dosage-, time-, and wavelength-dependent. Nuclear decomposition by ZnO NPs, prior to membrane deformation, was found to be enhanced when exposed to irradiation. This study suggests that this phenomenon may be attributed to the irradiation-induced formation of positively charged sites on the ZnO NPs which enhances nuclear affinity and generation of reactive oxygen species (ROS). Finally, the data demonstrated that while ZnO NPs act preferentially toward nuclear regions, destructions of cell membrane and the cytosol have also been observed. Indeed, the photocatalytic properties of ZnO NPs play a critical role during the early stages of cell death, and their effects were reduced through the use of an antioxidant, N-acetylcysteine (NAC). In conclusion, irradiation has been found to enhance the cytotoxic effects of ZnO NPs, prompting the need for more thorough safety evaluations in the application of these particles.

Keywords: ZnO NPs, oxidative stress, cytotoxicity, A549 cells, irradiation, nuclear decomposition

Introduction

As one of the most widely used nanoparticles, ZnO nanoparticles (NPs) can be found in many skin care products, such as sunscreen lotions, creams, and cosmetics, as well as in pigments, tire compounds, nano-sensors, nano-cantilevers, field effect transistors, nano-resonators, and other industrial and medical applications ¹. Despite the positive impacts of ZnO NPs in human society, the adverse effects of ZnO NPs have drawn considerable public concerns ² because of the various routes of administration into human body including inhalation (respiratory tract), ingestion (gastrointestinal tract) and injection (blood circulation) ^{3,4}. *In vitro* studies using various cell lines demonstrated that ZnO NPs can cause cyto- and geno-toxicities, including elevated reactive oxygen species (ROS) levels, intracellular oxidative stress, lipid peroxidation, cell membrane leakage, oxidative DNA damage, among others ^{5,6}. Moreover, cosmetic products containing ZnO NPs are supposed to provide protection against ultraviolet (UV) irradiation. In support of this, it has been reported that the TiO₂ and/or ZnO NPs in sunscreen lotions cannot penetrate the skin barrier, and have been therefore labeled non-toxic ⁷. Furthermore, prolonged exposure to these products has also been reported to slow the development of squamous or basal cell carcinoma ⁸. Despite this *in vivo* support of ZnO NP-containing products, a number of *in vitro* studies have demonstrated a strong cytotoxicity.

Preliminary data demonstrated that the cellular uptake of ZnO NPs by human epidermal keratinocytes (HEK) cells and the destructive effects were both time- (6-24 hours) and dose- (8-20 µg/mL) dependent, especially toward mitochondrial activity and DNA integrity ⁹. Investigation of ZnO uptake, using human liver cells (HepG2), revealed

significant cytotoxic and genotoxic effects caused by intracellular ROS generation¹⁰. Another study using primary human nasal mucosa cells indicated distinctive cyto- and genotoxicities, as well as the pro-inflammatory potential of ZnO-NPs¹¹. Indeed, an earlier study showed that inflammation was related to sensitivity toward cytotoxic NPs, while the oxidative status of cells and tissues may further accentuate this effect¹². This may explain the typical cascade decreasing pattern of cell viability observed under constant exposure to toxic NPs. A comprehensive study reported that both remarkable cellular toxicity and increased intracellular calcium levels ($[Ca^{2+}]_{in}$) were observed when cells were treated with 20 nm ZnO NPs. Four genes related to apoptosis and oxidative stress responses were also found to be correlated with the NP cytotoxicity and calcium level variations¹³, these results provided a potential genetic risk even when cells were exposed to a sub-lethal concentration of ZnO NPs. A further study on the photo-cytotoxic effects of ZnO NPs under UVA irradiation with human head and neck squamous carcinoma (HNSCC) cell line reported a sharp reduction in cell viability, even when NPs were applied at low dosages and with a short illumination time¹⁴. A phytotoxicity study on *Allium cepa* with ZnO NPs treatment also demonstrated clastogenic/genotoxic and cytotoxic effects, thus stressing an environmental concern about widely used ZnO nanomaterials¹⁵.

Mechanism studies of ZnO NPs cytotoxicity have drawn increasing attention in recent years; however, several controversial conclusions have been reached from these studies. Our previous study of ZnO NPs cytotoxicity in human lung epithelial cells concluded that the free Zn^{2+} ions in ZnO NPs suspension were not responsible for the observed cytotoxicity². Nevertheless, another report on ZnO NPs attributed the

cytotoxicity of ZnO NPs to particle dissolution and Zn^{2+} release¹⁶. Other studies suggested that ZnO NP cytotoxicity was explained by a combination of effects, including labile zinc complexes, physicochemical properties, metal composition, particle scale, as well as metal solubility^{1,17}. In light of the inconclusive nature of this problem, it becomes clear that further investigation is required to reach a solid conclusion on the basis of the irradiation-induced cytotoxicity of ZnO NPs.

The inconclusive nature of the problem has led to a call for increased study of the photocatalytic properties of ZnO NPs under various irradiation conditions (Rasmussen *et al.*, 2010). Therefore, this study sought to elucidate the cytotoxicity of 50-70 nm ZnO NPs under various illumination conditions in order to uncover the underlying cytotoxic mechanisms. Since several of the aforementioned studies, including ours², were carried out on human lung epithelial cancer cell line A549, this cell line was chosen as a model paradigm for the study. It should be stated, however, that the further investigation of more diverse cell lines, such as keratinocytes that offer a more realistic exposure scenario, is required in order to provide a more representative sampling of the irradiation-induced cytotoxic effects of ZnO NPs. Visible light, UVA, and UVC irradiation have been chosen to provide a variety of irradiation types; the prior investigation of UVB irradiation excluded it from this study. As a control, dark incubation conditions were also employed in the design of this study.

Materials and Methods

Reagents and Chemicals

Fetal bovine serum was purchased from American Type Culture Collection (ATCC) (Manassas, VA, USA). Ham's F-12K medium with L-glutamine, was purchased from Fisher Scientific (Pittsburgh, PA, USA). Trypsin-EDTA (1×) and Hank's balanced salt solution (HBSS) were purchased from Invitrogen Inc. (Carlsbad, CA, USA). Penicillin–streptomycin, 2', 7'-dichlorofluorescein diacetate, (DCFH-DA) and N-acetylcysteine (NAC) were obtained from Sigma–Aldrich (Saint Louis, MO, USA). Lactate dehydrogenase (LDH) assay kits were purchased from Pointe Scientific (Lincoln Park, MI, USA). Ultra-pure DI-water (MQ water) was prepared using a Milli-Q system (Millipore, Bedford, MA, USA).

Characterization of ZnO NPs

ZnO NPs (50-70 nm) were purchased from Sigma–Aldrich (Saint Louis, MO, USA) at 99.0% purity. Particle size distributions were determined using a Philips EM430 transmission electron microscope (TEM) (Philips Electron Optics, Eindhoven, Netherlands). Crystal structure was characterized using a Scintag XDS 2000 diffractometer (Scintag, Inc., Cupertino, CA, USA). Scanning electron microscopy (SEM) images of ZnO NPs were taken by a Hitachi S-4700 field emission scanning electron microscope at 5 kV.

Suspensions of ZnO NPs were prepared in the cell culture medium and dispersed using a Fisher ultra-sonicator FS-60H (Fisher Scientific, Pittsburg, PA, USA) for 5

minutes. The suspension was freshly prepared, diluted to desired concentrations in serum-containing medium, and then immediately applied to the human bronchoalveolar carcinoma-derived cells (A549).

Lamp Information

UVGL-58 (UVA, irradiation peak at 366 nm) and UVGL-25 (UVC, irradiation peak at 254 nm) (115 volts and 60 Hz AC power supply) lamps were used as UVA and UVC irradiation sources. Visible light was generated using a phosphor-converted LED white light with broad band emission distributed from 400 to 700 nm. Two fluorescent tubes in each UV lamps, and multiple (2 to 4, depend on tested cell volume and area) LED white light sources, were used to provide evenly distributed surface irradiation intensity. Lamps were positioned above the cell culture area such that a final illumination output of 5 watts was achieved at the culture surface.

Cell Culture and Treatment With ZnO NPs Under Various Irradiation Conditions

The human bronchoalveolar carcinoma-derived cell line (A549) was purchased from ATCC (Manassas, VA, USA). This cell line has been widely used in *in vitro* particulate matter-related pulmonary toxicity studies^{18,19}, so the same cell line was used in this study for data comparison and data correlation. Cells were maintained in phenol red-free Ham's F-12 nutrient mixture purchased from Caisson Laboratories, Inc. (North Logan, UT, USA) that supplemented with L-glutamine, 5% fetal bovine serum, 100 units/ml penicillin, 100 µg/mL streptomycin, and grown at 37°C in a 5% CO₂ humidified environment. Freshly dispersed ZnO NPs suspensions in Ham's F-12 medium after 15 minutes ultra-sonication were then diluted to desired concentrations and immediately

applied to the cells. After proper proliferation conditions were achieved, cells were trypsinized and seeded into 96 well plates or 12 well plates (Corning Inc., NY, USA) at densities of 5×10^4 or 3×10^5 cells per well, respectively. Cells were then permitted to grow as a monolayer, with 75% surface area coverage, for 16-18 hours prior to any ZnO NPs treatment and irradiation exposure. The study was designed with four irradiation modes: (1) No light; (2) Visible light; (3) UVA; (4) UVC. Intra-control groups, lacking exposure to ZnO NPs, were included at each mode. The control group lacking exposure to both ZnO NPs and an irradiation source was treated as the inter-control group. A stock suspension of 100 $\mu\text{g}/\text{mL}$ ZnO NPs in serum-free Ham's 12-K medium was prepared from which a series of working ZnO NPs suspensions (5, 10, 15, 20, and 25 $\mu\text{g}/\text{ml}$) were prepared. Upon removal of culture medium from the normal groups and a subsequent 12-hour waiting period, 150 or 2000 μl freshly prepared ZnO NPs suspension was added into each well (96- and 12-well plates, respectively). Time-dependent responses were measured at 6, 12, and 24 hours upon treatment with the NPs. Two concentrations of ZnO NPs (15 and 25 $\mu\text{g}/\text{mL}$), representing high doses, were then used to examine cytotoxic biomarkers, oxidative stress, and membrane damage. Upon 6 hour incubation under the various irradiation modes, the cells and cell culture medium then examined for the above indicators. In order to validate the induced generation of reactive oxygen species, a side study involving co-treatment with the antioxidant, NAC, was performed. NAC was loaded into the wells and allowed to incubate for 24 hours followed by a cell viability assay.

Cytotoxicity Assessment of ZnO NPs and Irradiation

To determine the cytotoxicity of 50-70 nm ZnO NPs under different irradiations sources, the WST-1 assay (Cell Titer 96 Aqueous One Solution Assay, Promega) and Calcein-AM assay (Life Technologies Inc., Carlsbad, CA, USA) were used according to the manufacturers' instructions. Absorbance at 450 nm using WST-1, and fluorescent emission at 425 nm were measured using a micro-plate reader (FLOURstar, BMG Labtechnonogies, Durham, NC, USA).

Intracellular ROS Measurement

ROS generation was measured by using oxidation of 2', 7'-dichlorofluorescein (DCFH) and its diacetate form (2', 7'-DCFH-DA)²⁰. DCFH-DA is hydrolyzed by esterase to DCFH, a compound unable to cross the cellular membrane. This initially non-fluorescent molecule is oxidized by cellular oxidants to a highly fluorescent product, DCF. A DCFH-DA stock solution (in methanol) of 10 mM was diluted 500-fold in Hank's Balanced Salt Solution (HBSS) (Life Technology Inc., Carlsbad, CA, USA) without serum or other additive to yield a 20 μ M working solution. Cells were washed twice with HBSS, and then incubated with DCFH-DA working solution for 1 hour under a dark environment (37 °C incubator) followed by treatment with ZnO NPs for 24 hrs. After exposure, fluorescence was determined at 485 nm excitation and 520 nm emission using a micro-plate reader (FLOUR star, BMG Lab technologies, Durham, NC, USA).

LDH Measurement

Lactate dehydrogenase (LDH) activity in the cell culture medium was determined by an LDH Kit (Pointe Scientific, Lincoln Park, MI, USA)^{21,22}. The analysis required 100 μ L of culture. LDH catalyzed the oxidation of lactate to pyruvate with simultaneous reduction of NAD^+ to NADH. The rate of NAD^+ reduction was directly proportional to LDH activity in the cell medium. Absorption was measured using a Beckman DU-640B UV/Vis Spectrophotometer at 340 nm.

Cellular Staining With Fluorescent Probes

A549 cells seeded for 24 hrs were treated with 50-70 nm ZnO NPs under dark, visible light, UVA, and UVC irradiation conditions for 6 hrs. Cells were then treated with DCFH-DA for 1 hr without light, followed by 4',6-diamidino-2-phenylindole (DAPI) staining for 10 min. Cells were then imaged using an epifluorescence Olympus IX 51 microscope (Olympus America, Center Valley, PA, USA) equipped with a fluorescein filter. Fluorescent images were captured and analyzed using SlideBook 4.1 software (Intelligent Imaging Innovations, Denver, CO, USA). The final 3-D fluorescent images of cells were acquired by ImageJ software.

Tunneling Electron Microscopy Imaging

A TEM-specific thin layer carbon/nickel grid was seeded with A549 cells and allowed to rest for 24 hours. Upon resting, the grid was treated with with 50-70 nm ZnO NPs (25 μ g/mL) with or without visible light exposure for 6 hours. Non-irradiated grids lacking ZnO NPs were used as a control. Following irradiation, treated cells were washed with

0.1 M phosphate buffer, fixed with 2.5% glutaraldehyde in serum-free F12-K cell culture medium at room temperature for 12 hours. Then the cells were washed again with 0.1 M phosphate buffer, dehydrated in ascending grades of ethanol solutions of 50%, 70%, 80%, 90% and 100%, each for 15 minutes, and subsequently soaked in hexamethyldisilazane (HMDS)/ethanol ascending solutions of 1:2, 2:1 and total HMDS. The cells were then imaged on a Tecnai F20 STEM platform.

Statistical Analysis

Each component of the study was run in triplicate for statistical validation purposes. Data has been expressed as the mean \pm standard deviation. Statistical analyses were performed using Prism 5 (Graph-pad software, San Diego, CA) including a one-way ANOVA test followed by a post-hoc Turkeys test to determine statistical significance.

Results

Characterization of ZnO NPs

The size distribution of ZnO NPs was found to be 60 ± 10 nm by tunneling electron microscopy (TEM). X-ray diffraction (XRD) analysis revealed the ZnO NPs assumed a hexagonal structure. The surface area of ZnO NPs, which was measured by the Brunauer, Emmett and Teller (BET) method, was determined to be $12.16 \text{ m}^2/\text{g}$. Scanning electron microscopy (SEM) was used to provide an overview of particle shape and diameter. Since sonication affects the hydrodynamic size of the particles, sonicated and non-sonicated ZnO NPs were characterized by field emission scanning electron microscope (FESEM) (Figure 1). Bulk aggregation was present in non-sonicated particles (Figure 1A

and 1D), with sizes ranging up to 10 μm (Figure 1B) in diameter. The diameters of sonicated ZnO NPs were appreciably smaller than non-sonicated particles; nevertheless, aggregation was still found in aqueous phase solutions (as shown in Figure 1C, 1E, and 1F).

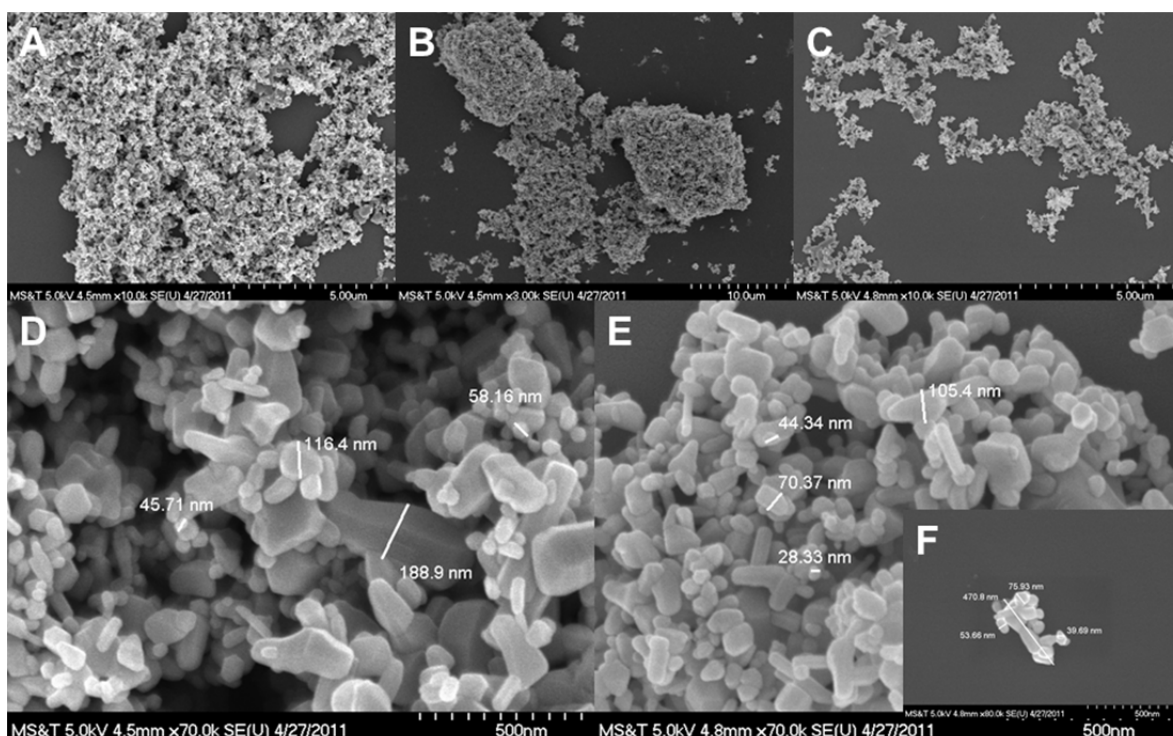


Figure 1. SEM images of 50-70 nm ZnO NP aggregations with or without ultrasonication. All NPs were prepared as described in the Materials and Methods section. Images C, E, and F were ZnO NPs that were sonicated. Images were taken with a Hitachi S-4700 field emission scanning electron microscope at 5 kV and varied scale bars of 10 μm (B), 5 μm (A, C) and 500 nm (D, E, F).

Effects of Visible Light Exposure on Cytotoxicity of ZnO NPs

Comparisons between cell viabilities under visible light and dark environments are shown in Figure 2. Earlier work by our group^{2,23} demonstrated that ZnO NPs are cytotoxic under dark conditions as a function of ZnO NPs concentrations. To revalidate this, the current study found that cell cultures under dark conditions treated with ZnO NP doses of 5 µg/mL, 10 µg/mL, 15 µg/mL, 20 µg/mL, and 25 µg/mL after 32 hours resulted in decreasing cell viabilities, specifically, 78.5%, 70.4%, 26.6%, 5.5% and 3.4%, respectively, (Figure 2A). The untreated control group failed to participate in this phenomenon ($p < 0.05$), thereby corroborates the previous study. Similarly, the cytotoxicity of equivalent ZnO NPs doses under visible light irradiation has been reported in Figure 2B. While both groups (with or without irradiation) have experienced marked decreases in cell viability within the first eight hours, the cell viabilities of the higher doses (with 15, 20 and 25 µg/mL ZnO NPs dosages) under visible light irradiation are substantially lower (Figure 2B). A cell viability reduction of roughly 10% was found overall for cells treated with ZnO NPs and visible light than those treated with ZnO NPs and dark conditions. Given the sharp reductions at the higher concentrations, doses of 15 µg/mL and 25 µg/mL were chosen for analysis in the time- and dose-dependent studies as well as the mechanistic studies.

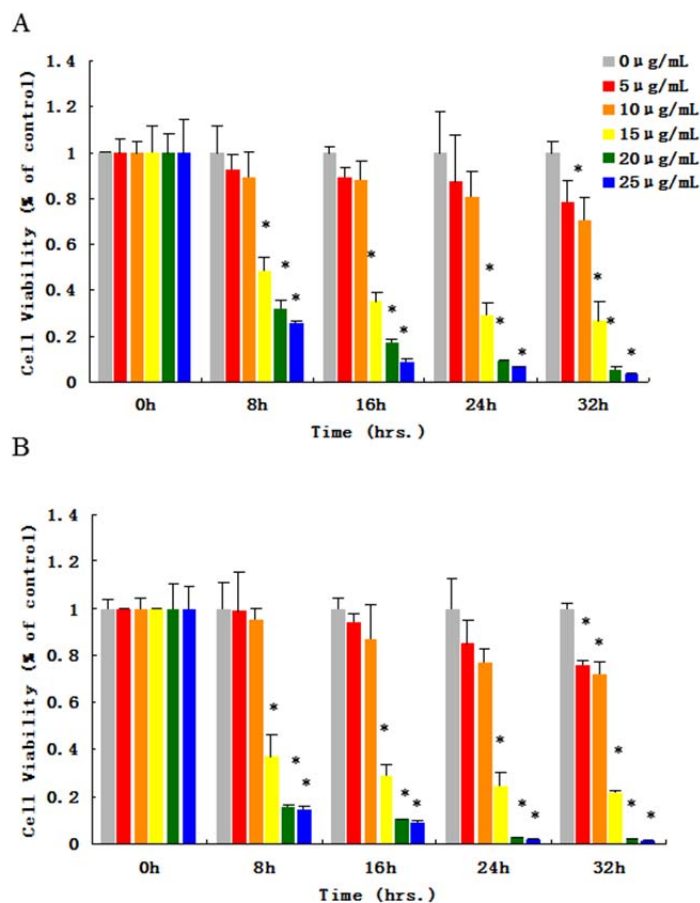


Figure 2. Cytotoxic effects of 50-70 nm ZnO NPs under visible light illumination on A549 cells. ZnO NP suspension was prepared in serum-free cell culture medium and ultrasonicated before dosing. (A) Cell viability after exposure to ZnO NPs under normal dark incubate condition; (B) Cell viability after exposure to both ZnO NPs and visible light at the same time. Each bar represents the mean \pm SD of three independent experiments. *Significantly different from the control at $P < 0.05$.

Effects of ZnO NP Dosages, Exposure Time and Irradiation Wavelengths on the Cytotoxicity of ZnO NPs

A549 cells were exposed to ZnO NPs at 15 $\mu\text{g/mL}$ and 25 $\mu\text{g/mL}$ dosage levels under various modes of irradiation, including dark, visible light, UVA, and UVC for 3, 6, 9, 12,

and 15 hours. All three variables of exposure time, dose level, and irradiation source have been implicated as cytotoxicity factors (Figure 3). Cells irradiated with visible light, UVA, and UVC sources experienced higher cytotoxicity under equivalent dose and time conditions when compared with the untreated, dark control group. Indeed, at the 15 $\mu\text{g}/\text{mL}$ and 25 $\mu\text{g}/\text{mL}$ levels after three hours exposure, cell viability decreased to 85.9% and 80.3%, respectively, under visible light, 77.7% and 53.5% under UVA light, and 45.9% and 49.1% under UVC light when compared with the control groups ($p < 0.05$). In contrast, non-irradiated cells only experienced a cell viability decrease to 85.6% and 85.9% compared with the control group ($p < 0.05$) under similar experimental conditions. This effect was even more accentuated after 12 hours of exposure. At the 15 $\mu\text{g}/\text{mL}$ and 25 $\mu\text{g}/\text{mL}$ ZnO NP levels, the non-irradiated cell viabilities dropped to 62.8% and 61.1%, respectively, 40.2% and 51.5% under visible light, 11.3% and 9.8% under UVA light, 15.2% and 17.7% under UVC light when compared with the control groups ($p < 0.05$). Control groups under different irradiation conditions while without ZnO NPs exposure only showed slightly differences (less than 12%) of cell viabilities, as a result of irradiation caused cytotoxicity. All controls were normalized as 100% cell viability in each group for clearer illustration.

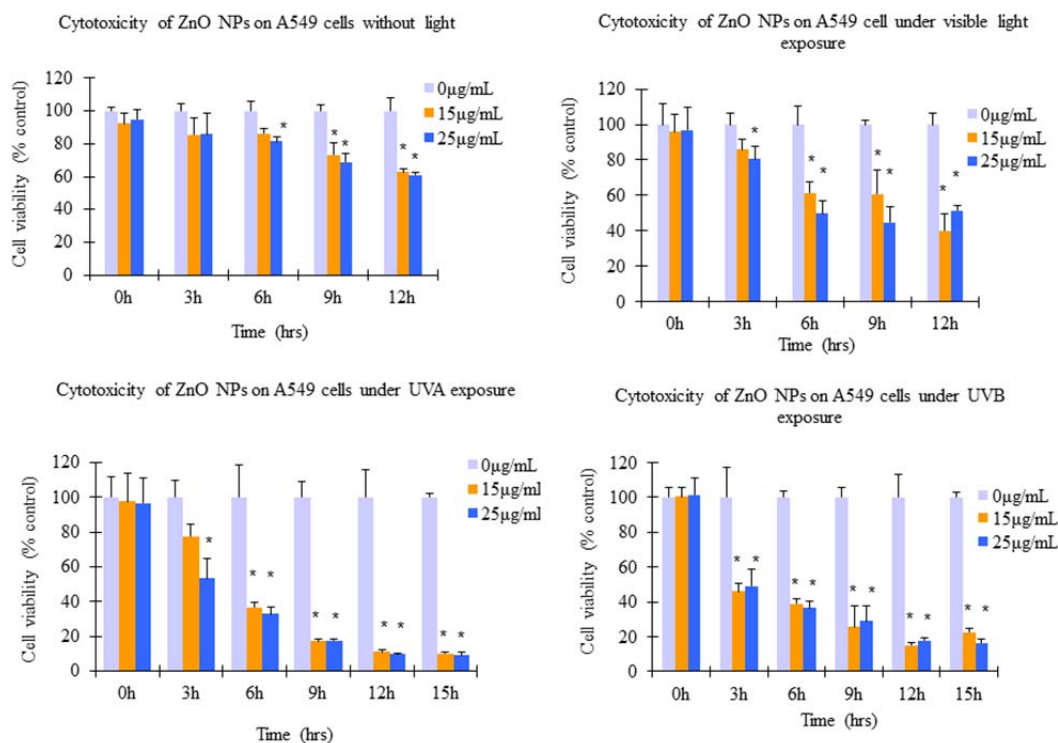


Figure 3. Cytotoxicity effects of ZnO NP dosages, exposure time, and differed irradiation conditions on A549 cells. Cells were seeded for 24 hours and then treated with ZnO NPs at dosages of 15 $\mu\text{g}/\text{mL}$ and 25 $\mu\text{g}/\text{mL}$ combined with: (A) normal dark culture, (B) visible light illumination for up to 12 hours; (C) UVA irradiation for up to 15 hours; (D) UVC irradiation for up to 15 hours. Calcein AM was used for cell viability evaluation. Each bar represents for the mean \pm SD of three independent experiments. *Significantly different from the control at $P < 0.05$.

Cellular ROS Generation Induced by Exposure to ZnO Nanoparticles and Different Wavelengths of Irradiations

DCFH-DA was used to assess the intracellular ROS generation after cells were exposed to ZnO NPs at concentrations of 15 $\mu\text{g}/\text{mL}$ and 25 $\mu\text{g}/\text{mL}$ and various irradiation conditions (Figure 4). Compared with the control group, DCF intensities of non-irradiation, visible light, UVA, and UVC treated groups increased by 12.8% and 74.5%,

33.9% and 78.9%, 148.1% and 172.3%, 155.8% and 162.9%, respectively, after four hours exposure. After six hours exposure, the DCF intensities has increased still, by 39.17% and 96.6%, 145.9% and 254.1%, 288.9% and 408.5%, 329.5% and 357.4%, respectively ($p < 0.05$).

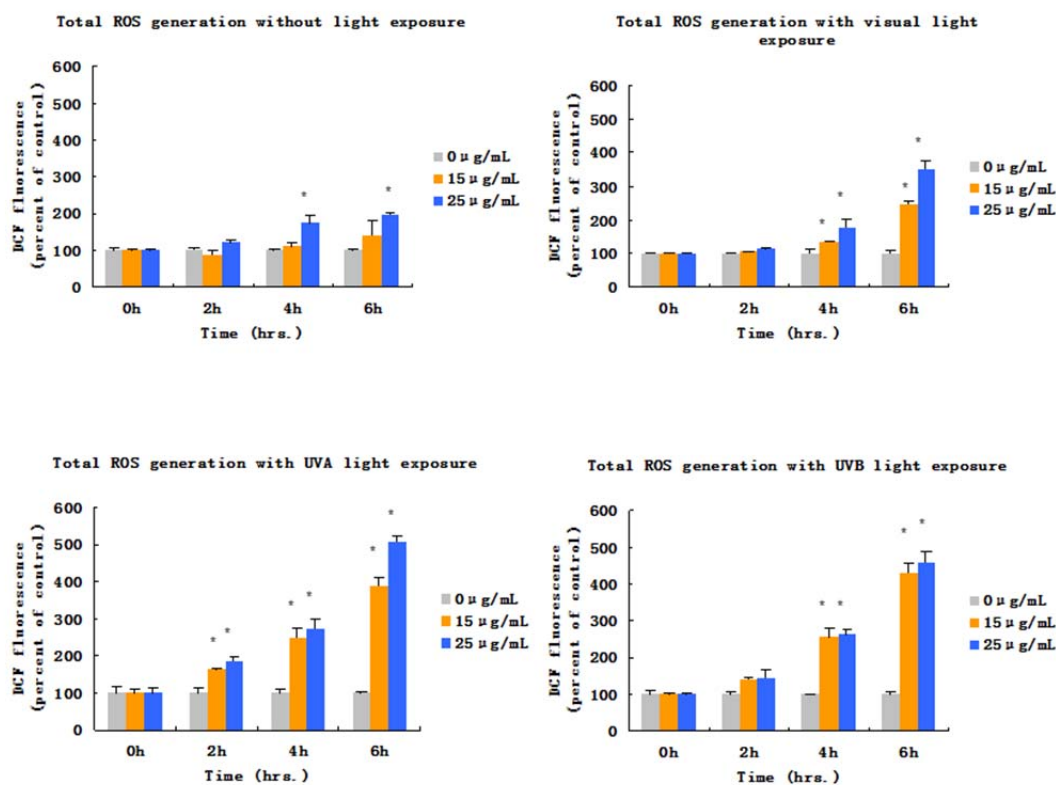


Figure 4. Effect of ZnO NPs on intracellular ROS generation under varied irradiation conditions. Seeded A549 cells were treated with ZnO NPs at dosages of 15 and 25 µg/mL for 6 hours under following differed conditions: (A) normal dark culture condition, (B) visible light illumination, (C) UVA irradiation, and (D) UVC irradiation. DCFH-DA for ROS generation assay was added immediately after all irradiation treatments and the fluorescent intensities were measured. Each bar represents the mean \pm SD of three independent experiments. *Significantly different from the control at $P < 0.05$.

Cellular LDH Release after exposure to ZnO NPs at different irradiation conditions

Release of lactate dehydrogenase (LDH) to the cell culture medium has been widely used as an indicator for cellular membrane damage. Cells were exposed to ZnO NPs at concentrations of 15 µg/mL and 25 µg/mL under various irradiation conditions (Figure 5). LDH levels from the non-irradiated groups at 15 µg/mL and 25 µg/mL ZnO NP doses gradually increased to 72.51 and 79.10 IU/L within six hours. In comparison, the control group acquired a six hour LDH level of only 13.18 IU/L. The LDH levels of all three irradiated cell groups initially increased, but ultimately decreased with prolonged exposure time. The highest levels of LDH in visible light and UVA irradiated groups reached 92.3 and 105.5 IU/L (visible light) and 118.7 and 125.2 IU/L (UVA) after four hours treatment. Meanwhile, LDH levels peaked at 125.2 and 118.7 IU/L under UVC exposure group after two hours treatment. The LDH levels of the control groups remained within the range of 6.59 to 13.18 IU/L ($p < 0.05$).

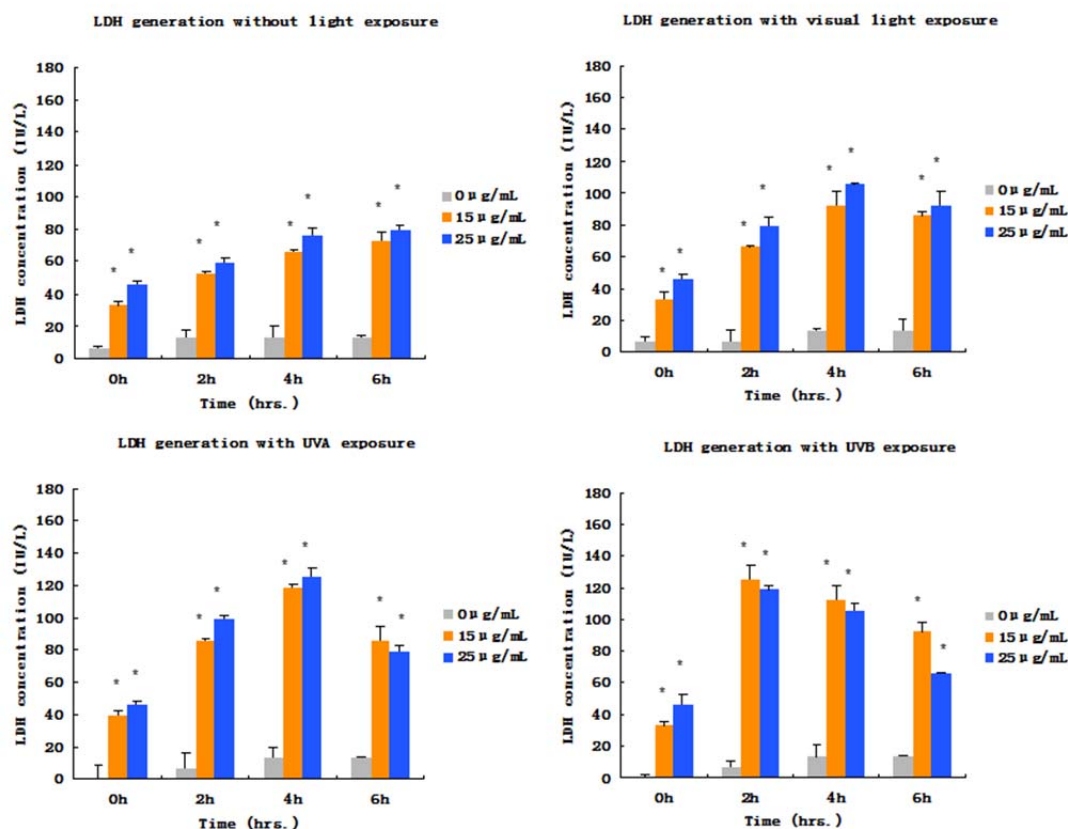


Figure 5. LDH levels in cell culture medium after 6 hours of exposure to ZnO NPs under various irradiation conditions. All A549 cells were treated with ZnO NPs at dosages of 15 $\mu\text{g/mL}$ and 25 $\mu\text{g/mL}$ combined with: (A) normal dark culture condition, (B) visible light illumination, (C) UVA irradiation, and (D) UVC irradiation, respectively. LDH correlated NAD^+ levels were measured by UV/Vis photometer at 340 nm. Each bar represents the mean \pm SD of three independent experiments. *Significantly different from the control at $P < 0.05$.

Intracellular Damages Induced by ZnO NP Exposure and Irradiation

To assess the levels of cell nucleus damage at different exposure conditions, fluorescent dyes and imaging technique were used to acquire semi-quantitative results. DCFH-DA combined with cell nuclei marker 4, 6-diamidino-2-phenylindole (DAPI) was used to conduct this portion of the study. A549 cells were exposed to 0 $\mu\text{g/mL}$, 15 $\mu\text{g/mL}$ and 25 $\mu\text{g/mL}$ ZnO NPs for six hours under varied irradiation conditions. Images of FITC,

DAPI, white (visible) light phase contrast, as well as fluorescent merging channels were taken and categorized for each irradiation condition (Figure 6). FITC channel intensities, which were analyzed using ImageJ software, indicated that intracellular DCF intensity was correlated with the generation of ROS. The data illustrates that signal intensity increases with increasing ZnO NP concentration under each irradiation condition (Figure 6, FITC channel). Control cells exposed to visible light, UVA, and UVC irradiations increased DCF intensity by 60.7%, 23.3%, and 30.7% compared with the non-irradiated cells. For the cells that were treated with a 15 $\mu\text{g}/\text{mL}$ dose of ZnO NPs, the DCF intensities under non-exposure, visible light, UVA, and UVC irradiation conditions increased by 58.8%, 108.9%, 94.4%, and 119.0%, respectively; for the cells that were treated with 25 $\mu\text{g}/\text{mL}$ dosage ZnO NPs, the DCF intensities increased by 88.5%, 114.8%, 127.9%, and 128.8%, respectively under the same conditions.

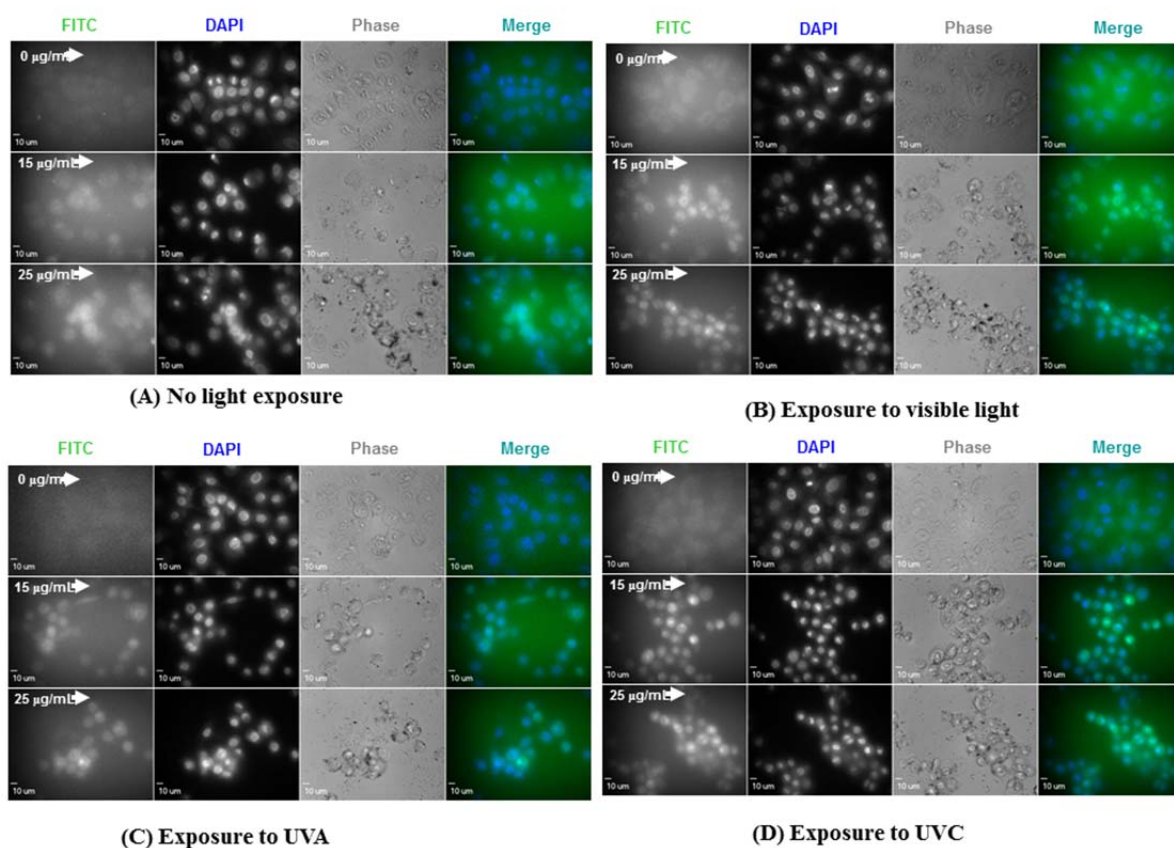


Figure 6. Fluorescent and phase contrast microscopic images of A549 cells that were treated with 15 µg/mL and 25 µg/mL of ZnO nanoparticles under different irradiation conditions for 6 hours. FITC, DAPI, phase contrast channels, as well as merged fluorescent images of were captured. DCF intensity in cell groups was quantified by ImageJ software.

A549 cell nuclei stained with DAPI exhibited a shrinking pattern with enhanced FL intensity, a typical phenomenon of cell damage. The images indicated that the DAPI fluorescence intensities increased with ZnO NP doses for all four groups. Greater damage occurred in irradiated groups compared with non-irradiated group (Figure 6, DAPI channel). The levels of cellular damage, represented by cell shape shrinkage and nuclear morphological transformation, became increasingly severe under the following order of

exposure conditions: dark < visible light < UVA < UVC, as is shown in the phase contrast channel (Figure 6, Phase channel). ZnO NP agglomerates can be seen in the 15 $\mu\text{g}/\text{mL}$ to 25 $\mu\text{g}/\text{mL}$ doses in each irradiation treatment; however, smaller sized agglomerates were observed in UVA and UVC irradiated groups.

An overlap of FITC and DAPI fluorescence signal in merged images was also arranged to show the status of nuclear damage and in this way, cell death. The overlapping percentage of these two fluorescent signals in 0, 15, and 25 $\mu\text{g}/\text{mL}$ ZnO NPs treated cells gradually increased in all four illumination groups (Figure 6, Merge channel). Steep peaks of FITC and DAPI merged fluorescent signals in the 3-Dimensional surface plot images indicate severe cell shrinkage as well as cellular damage (Figure 7). Moreover, higher and sharper peaks were observed in an increasing order from non-irradiated to UVC exposed groups (left to right) as well as from 0 $\mu\text{g}/\text{mL}$ to 25 $\mu\text{g}/\text{mL}$ dose levels (up to down) This indicated that cell shrinkage occurred as a function of both illumination and ZnO dosages (Figure 7).

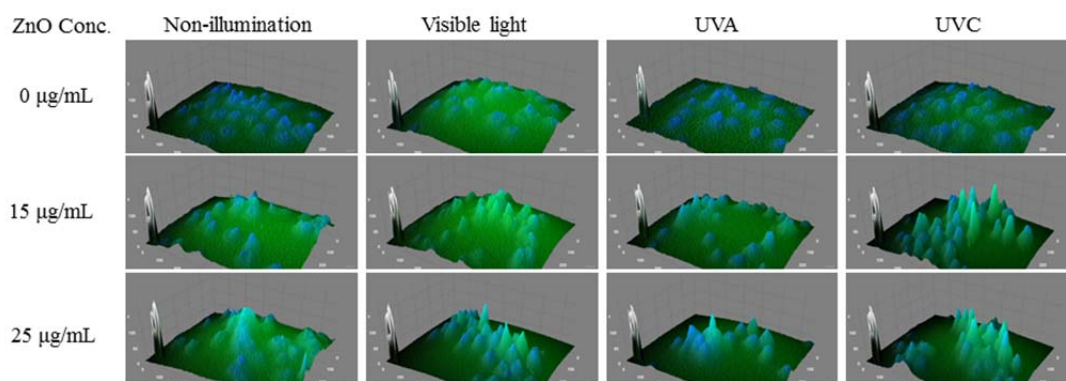


Figure 7. Three-dimensional surface plots of FITC and DAPI merged images of A549 cells that were treated with ZnO NPs under varied irradiation conditions. The merged images were processed and plotted using imageJ software.

Remediation of Cytotoxicity Induced by ZnO NPs and Varied Irradiations Using NAC

Remediation effects of an antioxidant NAC was further used as a cell viability recovery test. A549 cells that were exposed to ZnO NPs combined with different irradiation conditions and different dosages of NAC were used to examine changes in cell viabilities. The doses of NAC were 0, 0.1, 0.3, and 0.5 mM, and exposure time was 24 hours (Figure 8 Cell viability levels without addition of NAC were measured as 80%, 50%, 37% and 36% of control after 24 hour exposure to 25 µg/mL ZnO NPs under non-irradiation, visible light, UVA, and UVC exposure conditions, respectively. At 0.1, 0.3, and 0.5 mM NAC levels, cell viabilities increased to 83%, 87%, and 95% in the non-irradiation group, respectively, 62%, 81%, and 89% in the visible light exposure group, 43%, 57%, and 74% in the UVA exposure group, and 40%, 54% and 71% in the UVC exposure group.

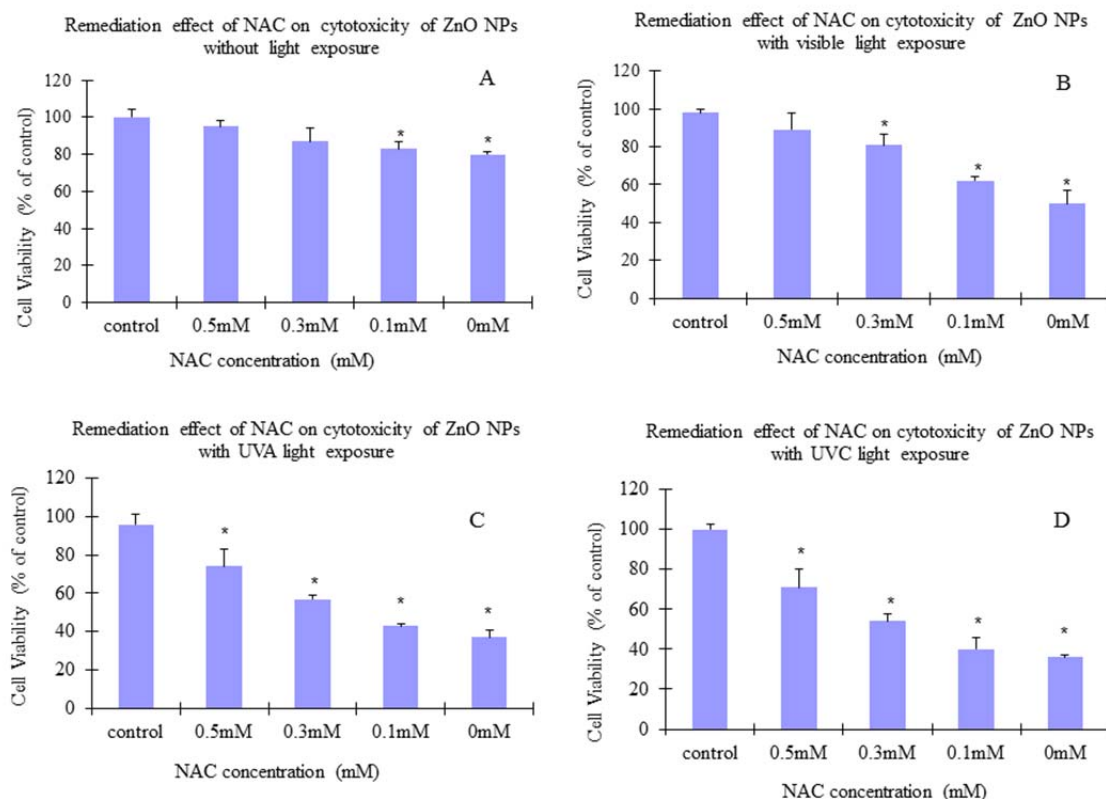


Figure 8. Remediation effect of anti-oxidant NAC on A549 cells against cytotoxicity induced by ZnO NPs and varied irradiations. ZnO NP concentration was 25 $\mu\text{g}/\text{mL}$ and the irradiation exposure time was 24 hours. NAC concentrations added: 0, 0.1, 0.3, and 0.5 mM. (A), normal dark culture condition; (B), visible light illumination; (C), UVA irradiation; (D) UVC irradiation. Calcein AM was used for cell viability measurement. Each bar represents the mean \pm SD of three independent experiments. *Significantly different from the control at $P < 0.05$.

Tunneling Electron Microscopy Images of Intracellular ZnO NPs

In order to evaluate the cytotoxic effects of ZnO NPs on the intracellular structure and cell organization, TEM images were taken of cells that were exposed to ZnO NPs. A549 cells were pre-seeded onto thin layer carbon membranes followed by treatments with ZnO NPs under dark culture conditions, ZnO NPs under visible light irradiation, and with

normal dark incubated cells serving as a control. After six hours of treatment, all samples were fixed with 2.5% glutaraldehyde solution in serum free F12-K cell culture medium overnight, and then dehydrated using ascending ethanol solutions of 50%, 70%, 80%, 90% and 100% concentrations. Samples were finally soaked in gradient HMDS/ethanol solutions and imaged by TECNAI F20 TEM. Intracellular structure damage was observed in the non-irradiated ZnO NP group and ZnO NP group exposed to visible light, while the intracellular structures of the control group cells remained well organized (Figure 9A). Gray or black randomly distributed intracellular agglomerates were observed in cell debris in both ZnO NP treated groups; however, more agglomerates with diverse shapes and sizes were observed in the irradiated cells than those of non-irradiated ones. The details of cellular destruction by ZnO NPs without irradiation are shown in Figure 9B. Aggregates were observed attached to or embedded in cellular cavity edges, indicating severe necrosis and cellular mass loss that the cells were undergone.

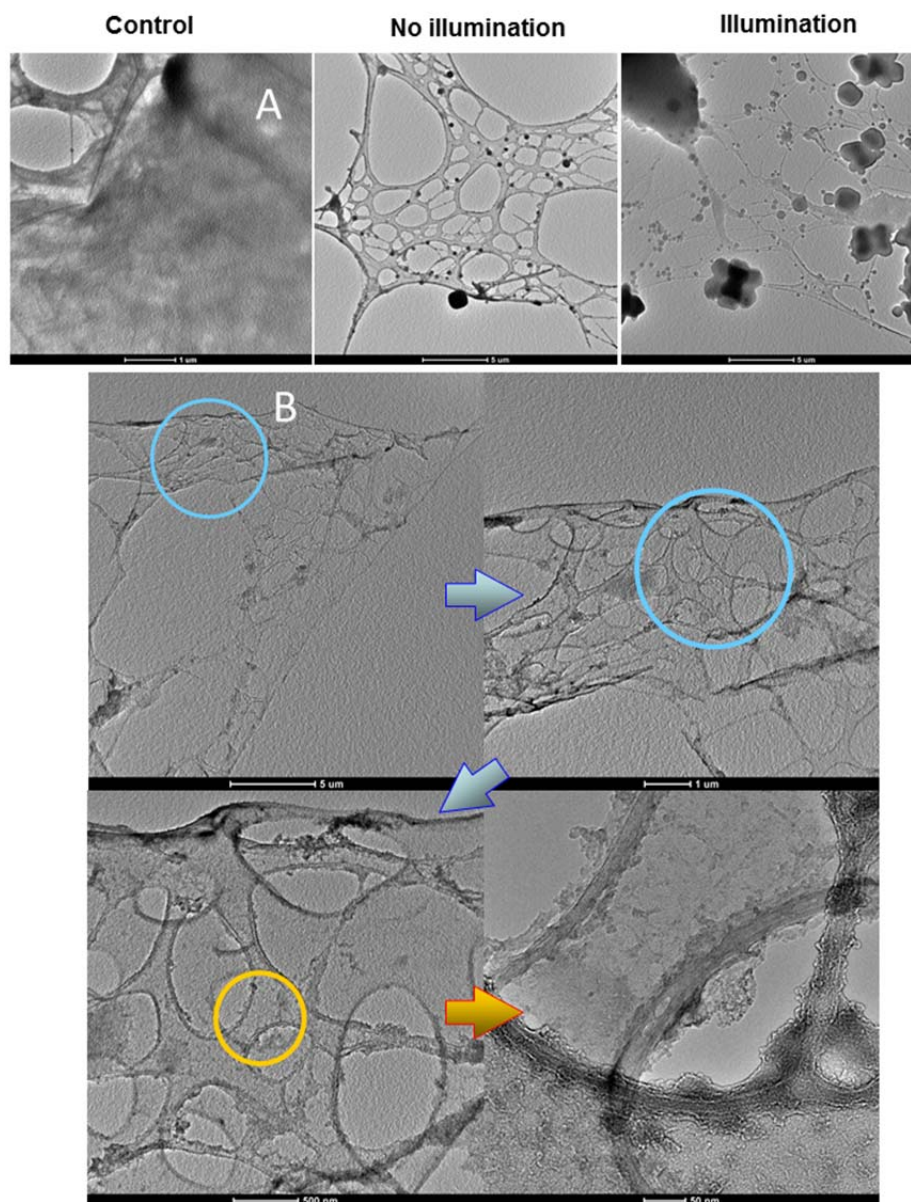


Figure 9. TEM images of cellular destructions by ZnO NPs and irradiation treatment. A549 cells were pre-seeded onto thin layer TEM carbon-nickel grid followed by treatments with 25 $\mu\text{g}/\text{mL}$ ZnO NPs only or 25 $\mu\text{g}/\text{mL}$ ZnO NPs plus visible light illumination. Normal dark incubated cells were set as control. After 6 hours treatment, cells were fixed overnight, followed by ethanol assisted dehydration and HMDS soaking. (A) Comparisons of cellular destruction in cells among control, ZnO NPs only, and ZnO NPs plus visible light illumination ; (B) Detailed structure destruction and NPs distribution. Pictures were taken with a Tecnai F20 STEM with varied scale bars of (A) 1 μm , 5 μm , and 5 μm (left to right), (B) 5 μm , 1 μm , 500 nm, and 50 nm (up left to bottom right).

Discussion

ZnO NPs have been widely implicated in both scientific research and industrial applications. Toxicity studies on micro- or nano-scaled ZnO materials, both *in vitro* and *in vivo*, have been conducted and have shown the potential toxic effects to humans. In our previous studies, we demonstrated a specific, dosage-dependent cytotoxicity of 50-70 nm and 420 nm ZnO on A549 cells^{2,23}. However, there is no published data regarding the cytotoxicity of ZnO NPs under different irradiation conditions. In this study, the cytotoxicity of 50-70 nm ZnO NPs under different irradiation conditions was investigated on the A549 cell line.

In summary, this study suggests that 50-70 nm ZnO NPs carry cytotoxicity effects at dose levels of 15 - 25 $\mu\text{g/mL}$, occurring in a dose-, time-, and irradiation-dependent manner. Investigations into cellular ROS generation demonstrated higher oxidative stress levels in irradiated groups as given by the following order: dark < visible light < UVA \approx UVC. LDH activities appeared attenuated under prolonged irradiation; however, cell membrane damage was observed, verifying worsening cellular conditions. A strong inverse relationship between decreasing cell viability and increasing ROS levels after 12 – 15 hours suggested that oxidative stress is the primary cause of cell death under the exposure conditions. These findings are partially in agreement with an *in vivo* study by Xiong²⁴ insofar as irradiation induced higher cytotoxicity caused by ZnO NPs. The authors showed acute toxicity, oxidative stress, and oxidative damage in zebrafish after treatment with ZnO NPs with more pronounced effects under visible light irradiation. Despite this, similar toxic effects of ZnO NPs, bulk ZnO suspension, and Zn^{2+} solution

were reported in their study, which at the time, was different from our prior conclusions. This discrepancy prompted the need for a more comprehensive mechanism study, as embodied by this study, to elucidate the toxic effects of nanoparticles under varied irradiation sources.

Throughout the study, the actual or effective size of the nanomaterial must be known and maintained. Failure for doing so may ruin subsequent particle size related data analysis, and hence, may render false conclusions. Indeed, it has been perceived that smaller particles have a greater toxicity²⁵⁻²⁷. Our previous study²⁸ suggested that hydrodynamic size, rather than manufactured particle size, dictated the physicochemical properties and thereby, the cytotoxic effects of the nanoparticles. Detailed SEM images (Figure 1) provide coincident evidences of this size discrepancy due to their hydrodynamic property. In preparation of this study's nanoparticles, ZnO NPs were initially mixed with ultra-pure water, followed by 15 minutes of either vortexing or ultra-sonication. Droplets of these freshly prepared ZnO NPs suspensions were immediately dehydrated in vacuum and analyzed with SEM. Particle aggregates with diverse diameters ranging from 10 μm to 100 nm were observed. Given this breadth of size, all subsequent data was based on the hydrodynamic aggregates. Furthermore, aggregate scales (diameter, thickness, etc.) seemed to vary significantly with and without ultra-sonication pretreatment (Figure 1 A-C). A closer view revealed more complicated surface structures with "deep" grooves in those samples lacking ultra-sonication (Figure 1 D-E), even though there were no significant size differences between groups. This study then suggests that aggregation occurred primarily due to two factors: particle surface charge and solvent surface tension. Ultra-sonication treatment removes fine air bubbles attached

to the surface of the nanoparticles, thereby weakening the surface tension induced hydrophobicity, and ultimately maintaining smaller aggregation size. Given the size range of the aggregates (Figure 1F), it was hypothesized that a dynamic nucleation and precipitation process may occur. Due to this, chronic cytotoxic or genotoxic effects on cells may be present, depending on the equilibrium of the dynamic process. Particularly, if the stability of the whole system is high enough, then a colloidal system should further be considered, as few cytotoxic studies have dealt with colloidal systems. Therefore, the interactions between cells and the NPs may not be significantly influenced by the manufactured particle size; rather, it will be highly affected by the NPs hydrodynamic size as well as the nucleation-precipitation dynamic equilibrium. This is a topic that requires further investigation.

ZnO NPs are widely used in daily care products such as cosmetics, sunscreen lotions, and facial creams. Even though the cytotoxic effects have been thoroughly studied under normal dark incubation conditions, the cytotoxic effects of ZnO NPs under different irradiation conditions have not been thoroughly addressed. In this study, our findings demonstrate that the cytotoxic effects of ZnO NPs are significantly enhanced under irradiation. Our previous studies showed that ZnO NPs were cytotoxic within the narrow dose range of 15 – 20 $\mu\text{g}/\text{mL}$. To revalidate this, A similar dose range (0 – 25 $\mu\text{g}/\text{mL}$) was used for 32 hours under visible light in comparison to the dark incubation control group (Figure 2). The cell viability results in Figure 2A are in agreement with the previous data, showing strong cytotoxic effects at concentrations equal to or higher than 15 $\mu\text{g}/\text{mL}$. The higher dosing levels (15, 20, and 25 $\mu\text{g}/\text{mL}$ ZnO NPs) however, exerted a 10% higher cytotoxicity than compared with the non-irradiated cell group. In this way,

visible light irradiation enhances the cytotoxic effects of ZnO NPs. It has been well acknowledged that ZnO has characteristic photocatalytic properties. A strong conjecture toward this phenomenon is that visible light irradiation can promote electrons from valence bands to conductive bands, which can enhance greater levels of free radical generation (Figure 4). It was noted that more drastic cell viability changes occurred within the first nine hours in both groups, suggesting quick destructive processes. Consequently, a more detailed viability study was conducted within the first 15 hours of treatment of ZnO NPs (Figure 3). In this study, two more irradiation sources were added, either with emission peaks at 375 nm (UVA) or 254 nm (UVC). Similar cell viability decreases were obtained in non-irradiated and visible light irradiated groups (Figure 3A, 3B) compared with the results in Figure 2, whereas those groups treated with UVA and UVC irradiation (Figure 3C, 3D) had higher death rates. Since UV irradiation itself is harmful to cells, cell viability would suffer even when there are no ZnO NPs being added. Therefore, all control groups in each irradiation test were treated with the same irradiation to eliminate the inherent cytotoxicity of UV light. A separate test (data not shown) conducted within the same time scale, with different irradiations but without ZnO NPs, revealed minor viability variations (<10%) when compared with the dark incubated cell group. This indicated that irradiation alone was negligible (Figure 3) in relation to the viability changes associated with the coupling of ZnO NP treatment and irradiation. This conclusion was found to be valid in a subsequent imaging trial with fluorescent dyes (Figure 6). The data in Figure 3 also shows that shorter wavelengths caused greater cell losses than the visible light. The possible reason for this phenomenon has been attributed to the chemico-physical properties of ZnO NPs. When the excitation photons have energy

higher than ZnO band gap (~ 3.6 eV, 375 nm), outer electrons will be promoted and thereby favor free radical generation, which is highly cytotoxic. The data quantitatively demonstrated that the cytotoxicity of ZnO NPs was dose-, time-, as well as irradiation wavelength-dependent. Furthermore, irradiation enhanced the cytotoxicity of ZnO NPs significantly, especially within the first 8 - 16 hours, further indicating that photocatalytic reactions were dominant during this early stage of cell destruction.

Two additional studies were conducted to examine ROS generation as well as cell membrane disturbances (Figure 4 and Figure 5). The first six hours were chosen for these two tests because cells can undergo severe destructive processes before a dominant cell death period occurred within 8 – 16 hours treatment. It was found that ROS generation occurred as the function of all three factors: NPs dose, duration time, and irradiation wavelengths (Figure 4). Addition of an ROS-specific fluorescent dye, DCFH-DA, prior to, or shortly after the irradiation exposure period was done to assess the amount of ROS present. Although only a slight difference was observed for these two methods when cells were incubated in the dark condition, totally different results were acquired when irradiation was included (data not shown). This was attributed to photo-bleaching and photo-degradation when the dye was added prior to irradiation. Therefore, dye was added after exposure, and a more representative result was acquired as shown in Figure 4. The authors acknowledge that this approach is not entirely representative, as the dye would not be able to capture transiently generated-and-consumed free radicals prior to the dye addition. Nevertheless, strong correlations were shown between the ROS generation and all three factors (Figure 4). Additional supplementary experiments were conducted to show the cell oxidative conditions through the release of lactate dehydrogenase (LDH)

from the cell membrane (Figure 5). Likewise, the results in the non-irradiated cell group corroborated our previous study (Figure 5A), while all three irradiation treated cell groups suffered signal loss after prolonged irradiation (Figure 5B-D). This study suspects that this phenomenon may be associated with inactivation of the enzymatic reactions caused by the accumulating free radicals.

By using two fluorescent dyes, more detailed examinations of the cytotoxic effects can be made (Figure 6). Specifically, cells uniformly stained with DCF and DAPI fluorescent dyes provide the following five conditions of the cells: 1) cellular ROS generation, through the increase of DCF fluorescence intensity at the FITC channel, 2) deterioration of cell health, through the morphological shrinkage of DCF-labeled cell body; 3) health of the cell nucleus, through the increase of DAPI fluorescence intensity at the DAPI channel, 4) cell viability decrease, through the morphological shrinkage of DAPI-labeled cell nucleus, and 5) deformation or decomposition of nuclear membrane, through overlapped fluorescence intensity of both DCF and DAPI dyes. Figure 6 shows increased cytotoxicity with increased ZnO NP doses and at short irradiation wavelengths. Both intensified fluorescence emissions and drastic morphological shrinkages were observed in the cell groups that were treated with high levels of ZnO NPs and irradiated with short wavelengths. It is important to mention that with the increase of ZnO NPs dose in each group, more cells stained with cyan colored fluorescence were observed in merged images, indicating a possible decomposition of the nucleus before the cell membrane was destructed. This phenomenon is also expressed in a 3-D diagram (Figure 7), which was based on merged images from Figure 6. The peak circumference represents the cell shape, and the peak height represents fluorescence intensity. Images from the up-

left to the down-right corner show the changes of following key parameters as higher doses of ZnO NPs and shorter wavelength irradiations were applied: 1) reduced circumference of each peak, 2) higher and steeper peak shapes, 3) brighter fluorescence signals, and 4) gradual change of color distribution pattern of each peak; in other words, more cyan colored peaks were seen in groups with higher doses of ZnO NPs and shorter wavelength irradiations. These signal changes are clear signs of cell shrinkage, cellular ROS generation, and nuclear decomposition. Despite the severe cytotoxic effects observed due to the exposure to ZnO NPs and irradiations with varied wavelengths, relatively higher cell viability, thus lower cytotoxicity, was achieved when NAC was applied in all cell groups (Figure 8). This is logical, as NAC is a strong antioxidant. The data indicates that the remediation effect of NAC is concentration-dependent and a greater viability recovery was achieved when a higher concentration of NAC was applied. Nevertheless, the antioxidant effects of NAC varied among irradiation sources, with lower remediation effects in the UVA and UVC irradiation cell groups. This suggests that an excessive amount of generated free radicals can surpass the antioxidant abilities of NAC.

A previous study on cytotoxicity of iron oxide NPs showed that the toxicity was generated through endocytosis via cytoplasm-bound vesicles in A549 cells ²⁹. A separate study on silver NP uptakes and intracellular distribution in human mesenchymal stem cells also showed a specific endo-lysosomal localization of silver NPs, and the primary uptake mechanisms were reported to be the clathrin-dependent endocytosis and macropinocytosis ³⁰. Although there were contrasting results showed that cell type and the mechanism of interactions play important roles in the cytotoxicity of NPs, the authors

suggested that a case-by-case basis would be favored on the investigation of NP aggregates behavior with cells³¹. Another study on the cytotoxicity of Monodisperse polypyrrole (PPy) NPs also showed endocytosis through transportation via endosomal networks to lysosomes³². Thus, it is reasonable to infer that most of the cellular uptake of nano-scale particles may go through a lysosomal-targeted endocytosis pathway. Our findings in this study are in agreement with these studies. Results reveal that ZnO NP agglomerates render small sizes and more amount of sub-cellular localization in irradiation cell groups (Figure 6-7) with worse cell viability compared with normal dark incubated cell group, suggesting that irradiation treatment can assist ZnO NPs to gain better dispersion conditions which may promote the uptake of ZnO NPs into cells, and thus elicit a higher cell death rate.

When considering the above results, it is worth mentioning that the appearance of cyan colored peaks shown in Figure 6 and Figure 7 indicate nuclear decomposition before the disintegration of the cell membrane. ZnO NPs that enter cells will generate intracellular ROS and induce nuclear decomposition prior to cell membrane disintegration. Such destructive effect depends on ZnO NPs dosages, duration time, as well as irradiation wavelengths. A separate experiment on intracellular calcium levels (data not shown) produced a similar result. When a lethal dose of ZnO NPs were applied to cells, increased intracellular calcium was observed. Moreover, fluorescent dye-labeled Ca^{2+} was observed transiently entering into cell nucleus and induced whole cell decomposition later on. This phenomenon, again, demonstrated a unique way of cell death induced by ZnO NPs, which has not been clearly reported yet. Nevertheless, few studies have showed correlations between nanotoxicity and priorities of destruction to

different cellular organelles, especially with respect to the cell nucleus. Since the super-active free radicals can react with many bioactive macromolecules swiftly and unselectively, we hypothesize that the unclear priority of destruction on cell nucleus can be attributed to specific chemico-physical properties of ZnO NPs. Moreover, considering the basic environment within the cell nucleus, due to the presence of a large amount of negatively-charged DNA molecules, we hypothesize that this basic environment in the nucleus would selectively attract positively charged “holes” generated on the ZnO NPs surface by irradiation, thus favoring the subsequent free radicals production specifically. Because both culture medium and cytoplasm were maintained at pH values close to 7.2 – 7.4, it follows that a basic environment would not be present elsewhere. Therefore, it may be the case that once ZnO NPs enter the A549 cells, these NPs preferentially destroys the cell nucleus rather than the cell membrane. For this reason, we attribute the observed decomposition of the nuclei prior to cellular membranes. Having said that, the detailed mechanisms are not clear yet and further studies are necessary to confirm this hypothesis.

Free radicals are very active species and can interact with many intracellular molecules. Reductive molecules (GSH, NADPH, etc.), sources (mitochondria) within cytoplasm, and other molecules distributed throughout the cytoplasm can all consume free radicals. Therefore, ZnO NPs will not only preferably destroy nuclei, but also contribute to whole cell degradation, unselectively. The TEM images (Figure 9) seem to support this. Cells treated with 25 μ g/mL 50-70 nm ZnO NPs in dark exhibited severe cytoplasmic destruction after six hours when compared with controls and an even more pronounced effect was observed when visible light irradiation was applied (Figure 9A). A partial view of a cell that was only treated with ZnO NPs provided closer details, showing

that membranes were being torn off while the cytosol was being depleted (Figure 9B). Since most cytoskeleton and microfilament structure can still be seen, we believe that this is due to their resilience and relatively lacking of reductive function groups.

The increased cytotoxic effects of ZnO nanoparticles under visible and UV irradiation may be attributed to their photo-catalytic reactivity. ZnO has been widely reported to have antibacterial activity, although the mechanism has not yet been clarified until only recently. UV-stimulated hydroxylation was observed at the surface reactive defective sites of ZnO crystals with atmospheric water molecules³³. Another electron paramagnetic resonance (EPR) study on visible light-induced ROS generation by ZnO NPs revealed that ZnO NPs in aqueous suspensions can produce increased levels hydroxyl radicals and singlet oxygen³⁴. Moreover, ZnO suspension can generate a greater amount of oxy radicals when irradiated with visible light at the range of 400-500 nm.

Even though the detailed mechanism of the cytotoxicity of ZnO NPs is not totally clear, there is evidence showing that ZnO NP-induced toxicity may be due to its dissolution in culture medium and endosomes. ZnO NPs were observed entering caveolae undissolved, or entering lysosomes in which smaller particle remnants dissolved in different cell types¹⁶. Muller et al.³⁵ indicated that ZnO NPs, which are comparatively stable at extracellular pH environment, can cause cell viability reduction through dissolution in lysosomes, intracellular release of ionic Zn^{2+} , and combined with severe structural changes of mitochondria. It was also found that intracellular Zn^{2+} toxicity was associated with mitochondrial dysfunction and mitochondria depolarization by Ca^{2+} and Zn^{2+} through considerably different mechanisms³⁶. Further, it has been reported that ZnO

NP exposure can increase the intracellular calcium levels in a concentration- and time-dependent manner¹³. Our calcium imaging tests are in agreement with this study, too. While in this case, the transient receptor potential melastatin 7 (TRPM7), a novel Ca^{2+} permeable non-selective cation channels, were found important in Zn^{2+} -mediated cellular injury³⁷. In conclusion, the studies above suggest the cytotoxic effects of ZnO NPs are attributed to ZnO dissolution. However, none of these studies can explain cell death through early-stage cell nucleus decomposition as shown in this study. Thus, more thorough studies are needed to elucidate a possible multi-pathway mechanism of ZnO NPs induced cytotoxicity.

In summary, we quantitatively demonstrated that the cytotoxicity of 50-70 nm ZnO NPs to A549 cells was dose-, time-, as well as irradiation wavelength-dependent, and these cytotoxic effects were due primarily to the presence of ZnO NPs, not irradiation. The NP-cell interactions were based on the hydrodynamic sizes of the ZnO NPs, not the manufactured size. It was found that the photo-catalytic properties of ZnO significantly enhanced the generation of ROS, which enhanced the cytotoxic effect of ZnO NPs. This cytotoxic effect, however, can be reduced through treatment with the antioxidant, NAC. Our detailed study also discovered a unique route of death: nuclear decomposition prior to cell membrane deformation. This phenomenon has not been previously reported. Based on this phenomenon, we suggest that the basic nuclear environment selectively attracts the positively charged “holes” on ZnO NP surfaces caused by irradiation. Finally, the study demonstrates that ZnO NPs unselectively contribute to whole cell degradation in addition to preferentially destroying cellular nuclei.

Declaration of Conflicting Interests

The author(s) declared no potential conflicts of interest with respect to the research, authorship, and/or publication of this article.

Funding

The author(s) disclosed receipt of the following financial support for the research, authorship, and/or publication of this article: This study was funded by Environmental Research Center and the Center for Biomedical Science & Engineering at Missouri University of Science and Technology.

References

1. Li M, Zhu L, Lin D. Toxicity of ZnO nanoparticles to *Escherichia coli*: mechanism and the influence of medium components. *Environ Sci Technol*. Mar 1 2011;45(5):1977-1983.
2. Lin W, Xu Y, Huang C-C, et al. Toxicity of nano- and micro-sized ZnO particles in human lung epithelial cells. *J. Nanopart. Res.* 2009;11(Copyright (C) 2011 American Chemical Society (ACS). All Rights Reserved.):25-39.
3. Nemmar A, Vanquickenborne B, Dinsdale D, et al. Passage of inhaled particles into the blood circulation in humans. *Circulation*. 2002;105(Copyright (C) 2011 American Chemical Society (ACS). All Rights Reserved.):411-414.
4. Koeneman BA, Zhang Y, Westerhoff P, Chen Y, Crittenden JC, Capco DG. Toxicity and cellular responses of intestinal cells exposed to titanium dioxide. *Cell Biol Toxicol*. Jun 2010;26(3):225-238.
5. Song W, Zhang J, Guo J, Ding F, Li L, Sun Z. Role of the dissolved zinc ion and reactive oxygen species in cytotoxicity of ZnO nanoparticles. *Toxicol Lett*. Dec 15 2010;199(3):389-397.
6. Sharma V, Singh P, Pandey AK, Dhawan A. Induction of oxidative stress, DNA damage and apoptosis in mouse liver after sub-acute oral exposure to zinc oxide nanoparticles. *Mutat Res*. Jun 14 2012;745(1-2):84-91.
7. Nohynek GJ, Dufour EK, Roberts MS. Nanotechnology, cosmetics and the skin: is there a health risk? *Skin Pharmacol Physiol*. 2008;21(3):136-149.

8. Murphy GM, Hawk JLM. Sunscreens and photocarcinogenesis. *Basic Clin. Dermatol.* 2009;43(Copyright (C) 2011 American Chemical Society (ACS). All Rights Reserved.):89-99.
9. Sharma V, Singh SK, Anderson D, Tobin DJ, Dhawan A. Zinc oxide nanoparticle induced genotoxicity in primary human epidermal keratinocytes. *J Nanosci Nanotechnol.* May 2011;11(5):3782-3788.
10. Sharma V, Anderson D, Dhawan A. Zinc oxide nanoparticles induce oxidative stress and genotoxicity in human liver cells (HepG2). *J Biomed Nanotechnol.* Feb 2011;7(1):98-99.
11. Hackenberg S, Scherzed A, Technau A, et al. Cytotoxic, genotoxic and pro-inflammatory effects of zinc oxide nanoparticles in human nasal mucosa cells in vitro. *Toxicol In Vitro.* Apr 2011;25(3):657-663.
12. Heng BC, Zhao X, Xiong S, Ng KW, Boey FY, Loo JS. Toxicity of zinc oxide (ZnO) nanoparticles on human bronchial epithelial cells (BEAS-2B) is accentuated by oxidative stress. *Food Chem Toxicol.* Jun 2010;48(6):1762-1766.
13. Huang CC, Aronstam RS, Chen DR, Huang YW. Oxidative stress, calcium homeostasis, and altered gene expression in human lung epithelial cells exposed to ZnO nanoparticles. *Toxicol In Vitro.* Feb 2010;24(1):45-55.
14. Hackenberg S, Scherzed A, Kessler M, et al. Zinc oxide nanoparticles induce photocatalytic cell death in human head and neck squamous cell carcinoma cell lines in vitro. *Int J Oncol.* Dec 2010;37(6):1583-1590.
15. Kumari M, Khan SS, Pakrashi S, Mukherjee A, Chandrasekaran N. Cytogenetic and genotoxic effects of zinc oxide nanoparticles on root cells of *Allium cepa*. *J Hazard Mater.* Jun 15 2011;190(1-3):613-621.
16. Xia T, Kovochich M, Liong M, et al. Comparison of the mechanism of toxicity of zinc oxide and cerium oxide nanoparticles based on dissolution and oxidative stress properties. *ACS Nano.* Oct 28 2008;2(10):2121-2134.
17. Pujalte I, Passagne I, Brouillaud B, et al. Cytotoxicity and oxidative stress induced by different metallic nanoparticles on human kidney cells. *Part Fibre Toxicol.* 2011;8:10.
18. Huang M, Khor E, Lim LY. Uptake and cytotoxicity of chitosan molecules and nanoparticles: effects of molecular weight and degree of deacetylation. *Pharm Res.* Feb 2004;21(2):344-353.
19. Bakand S, Winder C, Khalil C, Hayes A. A novel in vitro exposure technique for toxicity testing of selected volatile organic compounds. *J Environ Monit.* Jan 2006;8(1):100-105.

20. Wang H, Joseph JA. Quantifying cellular oxidative stress by dichlorofluorescein assay using microplate reader. *Free Radic Biol Med*. Sep 1999;27(5-6):612-616.
21. Ulmer DD, Vallee BL, Wacker WE. Metalloenzymes and myocardial infarction. II. Malic and lactic dehydrogenase activities and zinc concentrations in serum. *N Engl J Med*. Sep 6 1956;255(10):450-456.
22. Bagchi D, Bagchi M, Hassoun EA, Stohs SJ. In vitro and in vivo generation of reactive oxygen species, DNA damage and lactate dehydrogenase leakage by selected pesticides. *Toxicology*. Dec 15 1995;104(1-3):129-140.
23. Lin W. *In vitro toxicity and oxidative stress induced by silica, cerium oxide, and zinc oxide nanoparticles in human lung epithelial cells* 2007.
24. Xiong D-W, Fang T, Yu L-P, Sima X-F, Zhu W-T. Effects of nano-scale TiO₂, ZnO and their bulk counterparts on zebrafish: Acute toxicity, oxidative stress and oxidative damage. *Sci. Total Environ*. 2011;409(Copyright (C) 2011 American Chemical Society (ACS). All Rights Reserved.):1444-1452.
25. Kipen HM, Laskin DL. Smaller is not always better: nanotechnology yields nanotoxicology. *Am J Physiol Lung Cell Mol Physiol*. Nov 2005;289(5):L696-697.
26. Oberdorster G, Oberdorster E, Oberdorster J. Nanotoxicology: an emerging discipline evolving from studies of ultrafine particles. *Environ Health Perspect*. Jul 2005;113(7):823-839.
27. Nel A, Xia T, Madler L, Li N. Toxic potential of materials at the nanolevel. *Science*. Feb 3 2006;311(5761):622-627.
28. Lin W, Huang YW, Zhou XD, Ma Y. In vitro toxicity of silica nanoparticles in human lung cancer cells. *Toxicol Appl Pharmacol*. Dec 15 2006;217(3):252-259.
29. Konczol M, Ebeling S, Goldenberg E, et al. Cytotoxicity and genotoxicity of size-fractionated iron oxide (magnetite) in A549 human lung epithelial cells: role of ROS, JNK, and NF-kappaB. *Chem Res Toxicol*. Sep 19 2011;24(9):1460-1475.
30. Greulich C, Diendorf J, Simon T, Eggeler G, Epple M, Koller M. Uptake and intracellular distribution of silver nanoparticles in human mesenchymal stem cells. *Acta Biomater*. Jan 2011;7(1):347-354.
31. Albanese A, Chan WC. Effect of gold nanoparticle aggregation on cell uptake and toxicity. *ACS Nano*. Jul 26 2011;5(7):5478-5489.
32. Kim S, Oh WK, Jeong YS, et al. Cytotoxicity of, and innate immune response to, size-controlled polypyrrole nanoparticles in mammalian cells. *Biomaterials*. Mar 2011;32(9):2342-2350.

33. Asakuma N, Fukui T, Toki M, Awazu K, Imai H. Photoinduced hydroxylation at ZnO surface. *Thin Solid Films*. 2003;445(Copyright (C) 2011 American Chemical Society (ACS). All Rights Reserved.):284-287.
34. Lipovsky A, Tzitrinovich Z, Friedmann H, Applerot G, Gedanken A, Lubart R. EPR Study of Visible Light-Induced ROS Generation by Nanoparticles of ZnO. *J. Phys. Chem. C*. 2009;113(Copyright (C) 2011 American Chemical Society (ACS). All Rights Reserved.):15997-16001.
35. Muller KH, Kulkarni J, Motskin M, et al. pH-dependent toxicity of high aspect ratio ZnO nanowires in macrophages due to intracellular dissolution. *ACS Nano*. Nov 23 2010;4(11):6767-6779.
36. Devinney MJ, Malaiyandi LM, Vergun O, DeFranco DB, Hastings TG, Dineley KE. A comparison of Zn²⁺- and Ca²⁺-triggered depolarization of liver mitochondria reveals no evidence of Zn²⁺-induced permeability transition. *Cell Calcium*. May 2009;45(5):447-455.
37. Kim BJ. Transient receptor potential melastatin type 7 channels are involved in zinc-induced apoptosis in gastric cancer. *Anim. Cells Syst*. 2011;15(Copyright (C) 2011 American Chemical Society (ACS). All Rights Reserved.):123-130.

**II. Physicochemical insights of irradiation-enhanced hydroxyl radical generation
from ZnO nanoparticles**

Qingbo Yang,¹ Tien-Sung Lin,² Casey Burton,¹ Sung-Ho Park,² Yinfa Ma^{1*}

¹Department of Chemistry and Center for Single Nanoparticle, Single Cell, and Single Molecule Monitoring, Missouri University of Science and Technology, Rolla, MO 65409, United States

²Department of Chemistry, Washington University in St. Louis, St. Louis, MO 63130, United States

*Corresponding Author

Address: Department of Chemistry

Missouri University of Science and Technology

400 West 11th Street

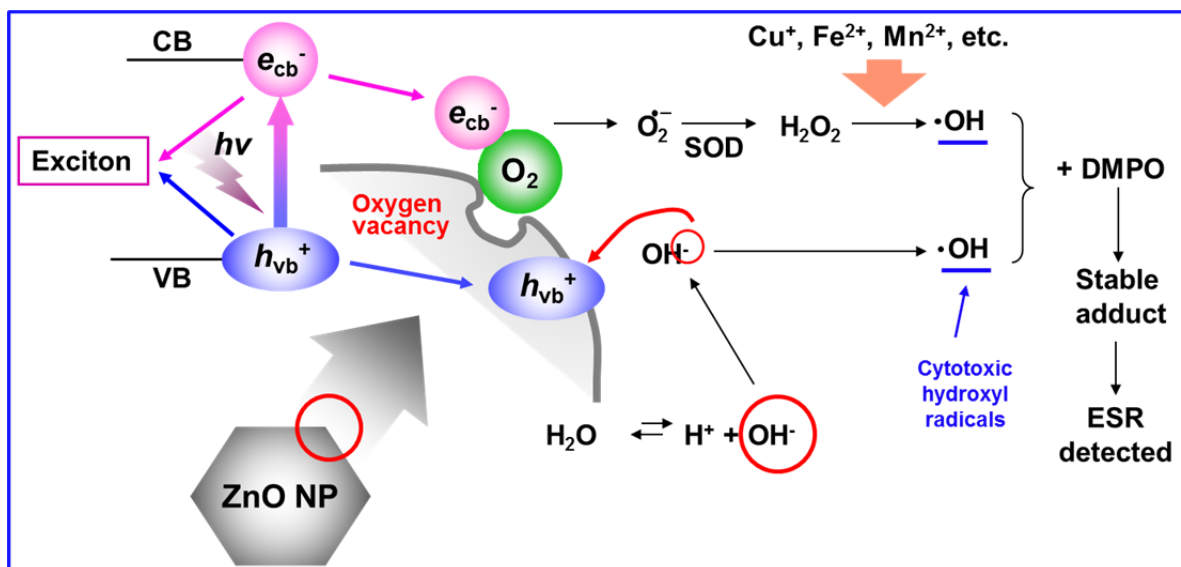
Rolla, MO65409

Phone: 573-341-6220

Fax: 573-341-6033

E-mail: yinfa@mst.edu

Graphical Abstract



Abstract

The widespread use of zinc oxide nanoparticles (ZnO NPs) has raised environmental and human health concerns owing to their significant cytotoxicity. Although their cytotoxic effects have been associated with reactive oxygen species (ROS), the physicochemical mechanism underlying this phenomenon remain poorly understood. In this study, the physicochemical properties of ZnO NPs were systematically investigated in relation to their effect on ROS generation. Factors that were found to affect hydroxyl radical ($\bullet\text{OH}$) generation included: NP concentration, irradiation, NP hydrodynamic size, localized pH, ionic strength, NP zeta-potential, and dissolved oxygen levels. The mechanism by which $\bullet\text{OH}$ was generated under alkaline conditions was found to obey first-order reaction kinetics that followed the conversion of OH^- anions and dissolved O_2 to $\bullet\text{OH}$. Based on these findings, we propose that ZnO NP cytotoxicity involves $\bullet\text{OH}$ adsorption to the nanoparticle surface, creating a highly localized source of ROS capable of potentiating oxidative damage to cellular structures. This hypothesis was evaluated with time-resolved intracellular calcium $[\text{Ca}]_i$ imaging that irradiated ZnO NPs triggered cytoplasmic calcium influxes and facilitated nuclear degradation. Together these findings present a novel physicochemical mechanism for $\bullet\text{OH}$ generation from ZnO NPs with significant implications for nanoparticle cytotoxicity and their relation to human health.

Keywords

ZnO NPs; irradiation-induced ROS generation; free hydroxyl radical ($\bullet\text{OH}$); electron spin resonance (ESR); physicochemical property; cytotoxicity.

Introduction

Zinc oxide nanoparticles (ZnO NPs) remain one of the most widely used nanomaterials with applications spanning research and industrial fields such as semiconductors, cosmetics, drug delivery agents, and more.¹ However, a growing body of literature has indicated ZnO NPs possess unique physicochemical properties that may lead to adverse biological effects.^{2, 3} For example, ZnO NPs adversely affect cells through membrane disruption,⁴ increased lipid peroxidation,⁵ reactive oxygen species (ROS) generation,⁶ and destruction of important organelles including mitochondria,⁶ lysosomes,⁶ and even nuclear degradation.⁷ Prior research has attributed ZnO NP cytotoxicity to the release of intracellular zinc ions^{8, 9} that contribute to oxidative stress, dysregulated calcium [Ca^{2+}],¹⁰ mitochondrial malfunction,¹¹ as well as interleukin (IL)-8 production.^{12, 13} Further efforts have attempted to correlate NP cytotoxicity with hydrodynamic size,¹⁴ dosage,⁵ and exposure conditions.^{5, 12} However, these factors alone overlook many of the unique physicochemical properties of ZnO. For example, ZnO is a semiconductor with remarkable photo-catalytic properties,¹⁵ especially at micro- and nano-sized levels. For this reason, ZnO NPs have been widely used for microorganism sterilization and wastewater treatment.¹⁶

Photocatalytic ROS generation from nanomaterials represents another potential mode of cytotoxicity.¹⁷ Jaeger and Bard demonstrated as early as the 1970s that irradiated TiO_2 generates hydroxyl radicals ($\bullet\text{OH}$) and perhydroxyl radicals ($\text{HO}_2\bullet$).¹⁸ Similarly, our group and others have successfully demonstrated the formation of reactive $\bullet\text{OH}$ from irradiated ZnO NPs.^{19, 20} To this end, electron spin resonance (ESR) spectroscopy has proved an invaluable technique for studying the formation of free hydroxyl radical

generation and irradiated ZnO NPs.^{12, 20, 21} The underlying mechanism is thought to arise from the transfer of absorbed photon energy through electron-hole pairs on the nanoparticle surface, although the extent to which this process generates ROS remains unclear. Current research in understanding this mechanism has not yet considered secondary interactions that arise from the surrounding environment.²² For example, ZnO NP suspensions behave as pseudo-colloidal system,²³ which has important biological ramifications including nanoparticle stability, dispersivity, surface charge, and aggregation and precipitation potentials in biological matrices. This potential for aggregation results in a net loss of reactive surface area and will consequently limit ROS generation by the nanoparticles.

We hypothesize that •OH generated from irradiated ZnO NPs is the causative agent for ZnO NP cytotoxicity. The lack of a comprehensive understanding of the effects of physicochemical properties on •OH formation inspired us to investigate these salient features in this study. This study was designed to monitor •OH formation using ESR spectroscopy combined with spin-trapping techniques, which have been recognized as powerful techniques for identifying and quantifying transient free radicals.²⁴ The ESR spin-trapping reagent 5, 5-dimethyl-1-pyrroline-N-oxide (DMPO) is particularly useful for sensitive and highly selective •OH quantification.²⁵ The systematic study of physicochemical factors including NP dosage, irradiation time, NP hydrodynamic size as well as buffer pH, ionic strength, and oxygen abundance by this technique enabled a comprehensive examination of the mechanisms underlying ROS generation from ZnO NPs. These new insights will lead to improved understanding of ZnO NP cytotoxicity and its relation to human health.

Experimental

Chemicals and reagents

ZnO NPs of 10 nm size were purchased from NanoScale Materials (Manhattan, Kansas, USA), while ZnO NPs of 50 - 70 nm size in addition to micro-sized ZnO powder (420 nm) and titanium (IV) oxide (TiO₂; 40 nm), cerium (IV) oxide (CeO₂; 20 nm) and silicon dioxide (SiO₂; 46 nm) nanoparticles were purchased from Sigma-Aldrich (Saint Louis, MO, USA) at 99.0% purity. The 5, 5-dimethyl-1-pyrroline-N-oxide (DMPO) spin-trapping agent and penicillin-streptomycin reagents were purchased from Sigma-Aldrich Chemical (St. Louis, MO, USA). Fetal bovine serum was purchased from American Type Culture Collection (ATCC) (Manassas, VA, USA). Ham's F-12K medium with added L-glutamine was purchased from Fisher Scientific (Pittsburgh, PA, USA). Fura-2 AM intracellular Calcium fluorescent dye, Trypsin-EDTA (0.25%), and 0.1 M phosphate buffered saline (PBS) were purchased from Life Technology Co. (Carlsbad, CA, USA). Ultra-pure water was generated with a Milli-Q system (Millipore, Bedford, MA, USA).

ZnO particles characterization and suspension preparation

The ZnO NPs used in this study have previously been characterized.^{5, 19} ZnO NP suspensions were freshly prepared in PBS buffer solution, ultra-pure (MQ) water, or serum-free culture medium based on experimental design. The selection of PBS buffer solution, despite its detrimental effects on photocatalytic oxidation by TiO₂, ZnO as well as FeO_x, was premised on its biological relevance.²⁶ Nanoparticles were dispersed using an ultrasonicator (FS-60H, Fisher Scientific, Pittsburg, PA, USA) for 15 minutes. Because ZnO NPs tend to aggregate or precipitate in suspensions, hydrodynamic sizes and zeta potentials of ZnO NPs in various dispersants (e.g. cell medium, ultra-pure water,

PBS buffer) at various concentrations were examined using dynamic light scattering (nano series Malvern Zetasizer ZEN 3690, Malvern Instruments Ltd., Worcestershire, UK). The UV–Vis spectra were recorded over the range of 350–900 nm with a Cary 50 UV–Vis spectrophotometer (Agilent Technologies, Santa Clara, CA). All pH measurements were conducted using an Accumet AB15 Plus pH meter (Thermo Fisher Scientific Inc., Waltham, MA, USA).

Electron spin resonance (ESR) experiments

DMPO spin adducts are stable nitroxides with unique ESR spectral patterns for each free radical (R•) added to the 2-position (β -carbon) of DMPO (Reaction 1) with particular sensitivity for •OH.^{20, 27, 28} Here, a 100 μ L addition of 100 mM DMPO was added to freshly prepared and ultrasonicated ZnO NPs in either ultra-pure water or PBS. The resulting mixture was introduced immediately into a tip-sealed disposal long tip pipette (OD = 1.2 mm, Pyrex, Fisher Scientific, Pittsburgh, PA, USA). The pipette was then inserted into the cavity of an X-band ESR spectrometer (Model JES-FA 100, JEOL Inc., Peabody, MA, USA). The JEOL rectangular resonator has a 0.5 inch hole in the front for light access. Spectrometer parameters included: microwave frequency: 8.8 - 9.0 GHz, power: 2 - 5 mW and modulation width: 0.01 - 0.05 mT. Single measurements were taken, as opposed to signal averaging, owing to the high sensitivity of the measurements. Moreover, daily standards were freshly prepared and examined as reference values with inter-daily precision less than 5% relative standard deviation (RSD). A combination of 100 W tungsten/halogen and 150 W Xenon/mercury lamps were used as irradiation sources. ESR signals were recorded before, during, and after irradiation to examine the effect of radiation on free radical generation, and all experiments were performed at room

temperature. The ESR experiments were confined to approximately 10 minutes in order to minimize heat generation caused by the irradiation. Control samples were additionally analyzed to consider the presence of interfering ESR artifacts such as oxaziranes that isomerized from spin trap nitrones.²⁵

Since dissolved oxygen in aqueous solutions may affect free radical generation, solutions purged at 50 mL gas/min with either nitrogen or oxygen were examined to study this effect. The sample tube was capped with a rubber septum with two hypodermic needles inserted (inlet and outlet) during the gas purging. Following purging, the needles were removed and the samples remained sealed with septa under a N₂ atmosphere during the ESR measurements.

Another interfering reaction involves the non-radical, nucleophilic reaction through the so-called Forrester-Hepburn mechanism²⁹. This reaction entails the formation of DMPO/[•]SO₃⁻ artifacts from bisulfite that is typically present under real biological conditions. In this study, cell extracts were not investigated with ESR spectroscopy, so this potential interference was not anticipated.

Inductively-Coupled Plasma-Mass Spectrometry (ICP-MS) measurements

An Elan DRCE ICP-MS (PerkinElmer, Waltham, MA, USA) was used to quantify zinc ions released from ZnO NPs. Zinc dissolution was measured in ZnO NP suspensions (500 µg/mL) prepared in 0.1 M PBS that were pH adjusted (1-14). Solutions were ultrasonicated for 15 minutes followed by vortex mixing for 3 minutes. Samples were then centrifuged at 12,000 g-force (5810 R Centrifuge, Eppendorf, Germany) and the supernatants were immediately filtered twice using disposable 0.22 µm nylon filters (Fisher Scientific, Pittsburgh, PA, USA). Samples were finally diluted using 1% nitric

acid (trace metal grade, Fisher Scientific, Pittsburgh, PA, USA) prior to HPLC-ICP-MS analysis.

Cell culture and treatment with ZnO NPs

The human alveolar carcinoma-derived cell line (A549) was purchased from ATCC (Manassas, VA, USA) and used as an *in vitro* cytotoxicity model in this study. This cell line has been widely used in particulate matter-related pulmonary toxicity studies,³⁰⁻³² and was used in our previous work to demonstrate irradiation-enhanced ZnO NP cytotoxicity.¹⁹ Cells were maintained in Ham's F-12K medium supplemented with 5% fetal bovine serum, 100 units/mL penicillin, 100 µg/mL streptomycin, and grown at 37 °C in a 5% CO₂ humidified environment. In each test, cells were seeded and allowed to attach for 48 hours prior to nanoparticle exposure. Cell densities between 5×10^4 to 1×10^5 cells per milliliter were used for analysis. Cells without ZnO NP exposure were used as the control group in each experiment.

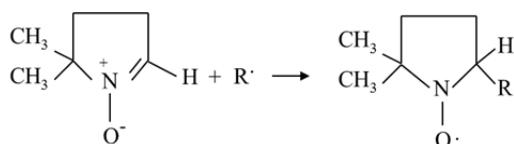
Calcium imaging and three-dimensional (3-D) images plot

Calcium imaging was performed using Fura-2 dye labels for intracellular calcium in A549 cells. Cells were pre-seeded onto confocal petri dishes in whole culture medium (with serum) 24 hours prior to ZnO NP exposure (serum free). A series of calcium images that displayed Fura-2 fluorescence intensity were continuously taken for up to 6 hours. Ratiometric data analysis was conducted to identify cells with intracellular calcium levels that exceeded a preselected threshold (100 nM $[Ca^{2+}]_i$). 3-D plots that represented dynamic changes in intracellular Ca^{2+} spatial distributions were drawn using ImageJ (National Institutes of Health, USA).

Results and discussion

The effect of irradiation on •OH generation

Free hydroxyl radicals have extremely short life spans and are therefore ill-suited for conventional quantitation techniques.³³ In this study, the highly sensitive and selective spin-trapping reagent, 5, 5-dimethyl-1-pyrroline-N-oxide (DMPO) was used to trap the transient •OH as stable DMPO-spin adducts (Reaction 1).



Reaction (1)

The spin-trapping spectrum of aqueous ZnO NPs using 150 W Xe/Hg lamp for irradiation has been shown in Fig. 1. Briefly, the 4-line spectrum characterized by its 1:2:2:1 pattern (Fig. 1a) is attributed to DMPO/•OH spin adducts with the following parameters: $g = 2.0046$, $a_N = a_{H\beta} = 1.49$ mT, which agrees with literature values for DMPO/•OH spin adducts.^{34, 35} A time profile of the third peak before and during irradiation was then recorded for eight minutes (Fig. 1b). The stabilization of the ESR signal during irradiation implied limited free radical formation that decreased linearly following cessation of irradiation. This gradual, linear decrease was attributed to the relative stability of the DMPO/•OH spin adducts which have a lifetime of several hours. A secondary explanation for this decrease is ZnO NP aggregation and precipitation,³⁶ which is a phenomenon that has been previously observed.¹⁹

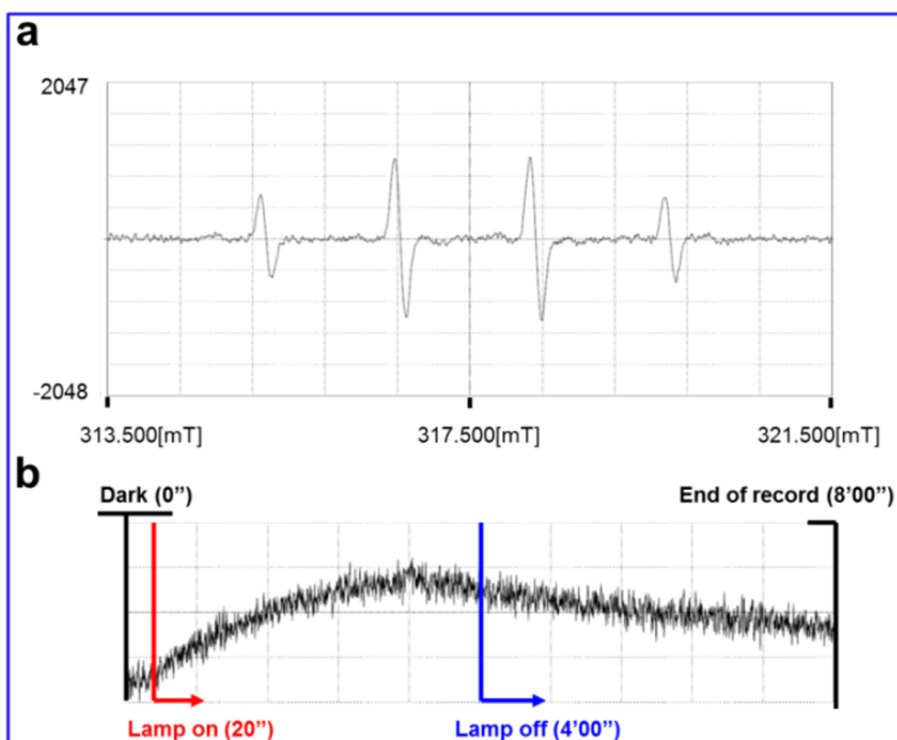


Figure 1. ESR recording of $\bullet\text{OH}$ radical generation by 50-70 nm ZnO NPs in aqueous solution. (a) Representative spectrum after 2 minutes irradiation, and (b) A time profile of ESR recording of the third peak for eight minutes. Instrumentation settings: frequency = 8905.758 MHz, field center = 317.500 mT, width (\pm) = 4.000 mT, MOD: $F_q = 100.00$ kHz, width = 0.1000 mT, power = 2 mW, sweep time = 2.0 min, mod amplitude: $\text{CH}_1 = 1000.0$, $\text{CH}_2 = 2.0$.

The effect of nanoparticle concentration on $\bullet\text{OH}$ generation

ESR measurements were performed on 50-70 nm ZnO NPs with doses ranging from 0.1 to 30 mg/mL (Fig. 2, Fig. S1). Our results demonstrated a non-linear relationship between $\bullet\text{OH}$ generation and ZnO NP concentration during the initial six minute irradiation period. Curiously, an inflection point was observed for 1 mg/mL ZnO NP doses (Fig. 2a, 1st irradiation), which suggested an equilibrium process between: 1) internal exciton formation and 2) interfacial electron transfer. The irradiation-induced electron-hole pairs will either combine together to form an exciton internally or are

charge transferred by interfacial reactions. Higher concentrations of nanoparticles will effectively shield inner nanoparticles, leading to decreased interfacial reactions and higher rates of internal exciton formation. This understanding has been attributed to the inflection point observed during this experiment.

ZnO NPs were then irradiated for six minutes followed by dark conditions (Fig. 2a, lamp off). Notably, the ESR signals under dark conditions failed to correlate with NP dosage. This could be readily explained by the nitroxide decomposition on the NP surface. A second irradiation period was then studied to determine whether NP aggregation would affect the result during the first dark cycle. Indeed, our hypothesis was supported by the observation in lower concentrated NPs (upper plot) in Fig. 2b, that the aggregation/precipitation did not significantly affect the $\bullet\text{OH}$ generation because a similar $\bullet\text{OH}$ generation was observed. However, this was not the case with higher NPs concentration (bottom plot in Fig. 2b). The observed inflecting effect (Fig. 2a) of NP dosage to the radical generation though, may also have an alternative explanation: higher NP concentration will induce stronger light scattering and weaker light absorption by DMPO. This will yield lower amount of the isomerized nitron, and thus lower adduct concentration.

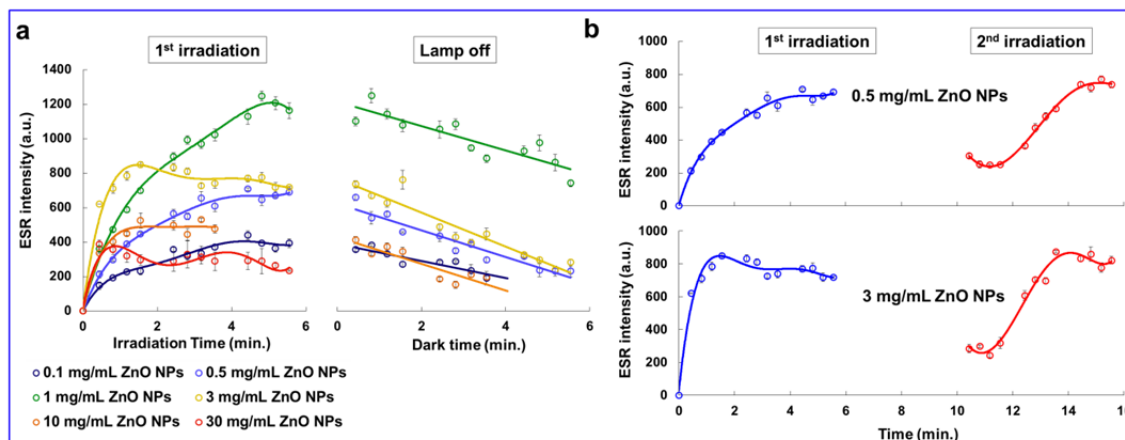


Figure 2. Continuous ESR recording of $\bullet\text{OH}$ by 50-70 nm ZnO NPs. (a) 1st irradiation and dark (lamp off) periods recording at NPs doses of 0.1, 0.5, 1, 3, 10 and 30 mg/mL; (b) 2nd irradiation at ZnO NPs doses of 0.5 and 3 mg/mL. Raw ESR data was normalized to (1) the temporal linear propagation rate for the first and fourth ESR peaks, (2) ESR instrumental parameters, and (3) a daily calibration standard using 1 mg/mL 50 – 70 nm ZnO NPs MQ water suspension, and the solid trend lines were drawn based on a 5th order of polynomial function.

The effect of hydrodynamic size on $\bullet\text{OH}$ generation

Previous NP toxicity studies have primarily focused on the relationship between nanoparticle size and cytotoxicity,^{37, 38} however, recent efforts have proposed that hydrodynamic size more accurately reflects nanoparticle cytotoxicity.³⁹ In this study, hydrodynamic size was measured using a real-time light scattering method coupled with ESR detection under irradiation (Fig. 3). Non-linear decreases in hydrodynamic size, as indicated by weight-averaged distribution peaks (1600 nm to 1200 nm) and relative peak intensities (7.5 to 4.7), suggested nanoparticle aggregation processes (Fig. 3 a, b) This trend continued until a critical size for precipitation was reached. Notably, this observation would imply that only small ZnO NPs were present at sufficiently long time periods (>80 min.) during the experiment described above. This aggregative process was characterized using UV/Vis spectrophotometry, wherein time-based decreases in

absorbance and band gap energy shift (from 3.36 to 3.29 eV) were observed (Fig. S2). This phenomenon, according to H. Weller, was a quantization effect, and the physicochemical properties are largely corresponding to the nature of the particle size and surface.⁴⁰ Together these results suggest that spontaneous aggregation of nanoparticles must be considered in the evaluation of their hydrodynamic size.

To determine the effect of hydrodynamic size on •OH generation, •OH generation was measured as a function of ZnO NP hydrodynamic size using bulk-form ZnO powder (420 nm) as a control (Fig. 3c) in which •OH generation from ZnO NPs greatly exceeded that of bulk ZnO. Ultrasonication of ZnO NPs similarly elicited greater •OH generation compared with NPs that were allowed to spontaneously aggregate (Fig. S3). Three groups of ZnO NPs prepared at 1 mg/mL (50-70 nm), 10 mg/mL (10 nm), and 10 mg/mL (50-70 nm) were then studied to determine the extent to which hydrodynamic size influenced •OH generation relative to ZnO NP concentration (Fig. 3d, S4). Hence, hydrodynamic size has a sizeable effect on •OH generation from ZnO NPs.

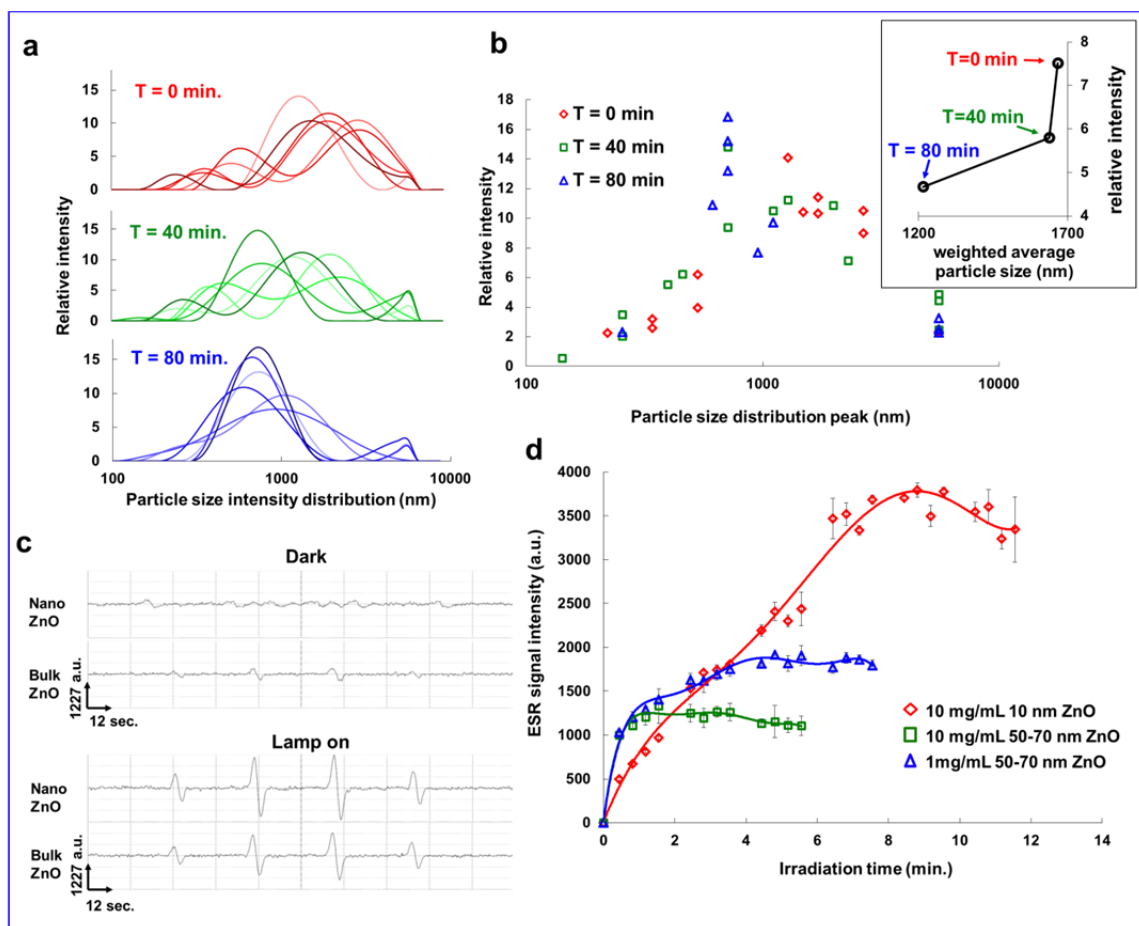


Figure 3. Correlation of $\bullet\text{OH}$ generation and ZnO NPs hydrodynamic sizes. First, time-lapsed measurement of 1 mg/mL 50-70 nm ZnO NPs hydrodynamic size were shown as (a) full spectrum distribution and (b) peak analysis. Inset plot in (b) indicates weighed-averaged particle size distribution. (c) Comparison of $\bullet\text{OH}$ generation by nano- (50 – 70 nm) and micro- (420 nm) sized ZnO NPs. (d) Comparison of $\bullet\text{OH}$ generation by 10 nm and 50-70 nm ZnO NPs at 1 mg/mL or 10 mg/mL dosage.

The effect of pH on $\bullet\text{OH}$ generation

We further evaluated the correlation between $\bullet\text{OH}$ formation and environmental physicochemical factors including radical quenching capacity, pH, matrix effect and ionic strength (IS).^{41, 42} The colloidal stability of ZnO NP suspension under a wide pH range was initially studied (Fig. 4). Fresh suspensions in PBS under varied pH conditions (from 1 to 14) were ultrasonicated followed by zeta (ζ)-potential measurements (Fig. 4a).

Ultrasonication minimally affected suspension pH, where only a 0.3 pH unit basic shift following ultrasonication was observed (Fig. S5). A typical colloidal ζ -potential stabilization range between pH 5 and 11 for both 10 nm and 50-70 nm ZnO NPs that was maintained between -15 and -25 mV was observed. These measurements also indicated that ZnO NPs dissolve beyond this pH range, which supported the ICP-MS analysis results (Fig. 4b). Orthogonal UV/Vis absorption analysis (Fig. S5-b) showed a strong positive correlation between pH and ZnO NP absorption. Note that a good linear correlation can be found under the basic pH conditions. Correspondingly, basic pH conditions resulted in increased hydroxyl radical generation as indicated by ESR analysis (Fig. 4c). A first-order reaction kinetics between hydroxide anions and free hydroxyl radical formation was similarly observed under alkaline conditions (Fig. 4d), which was plotted based on the first four-minute's irradiation generated ESR signal intensity. This finding indicates a direct pH-dependent process of hydroxyl radical generation by the ZnO NPs.

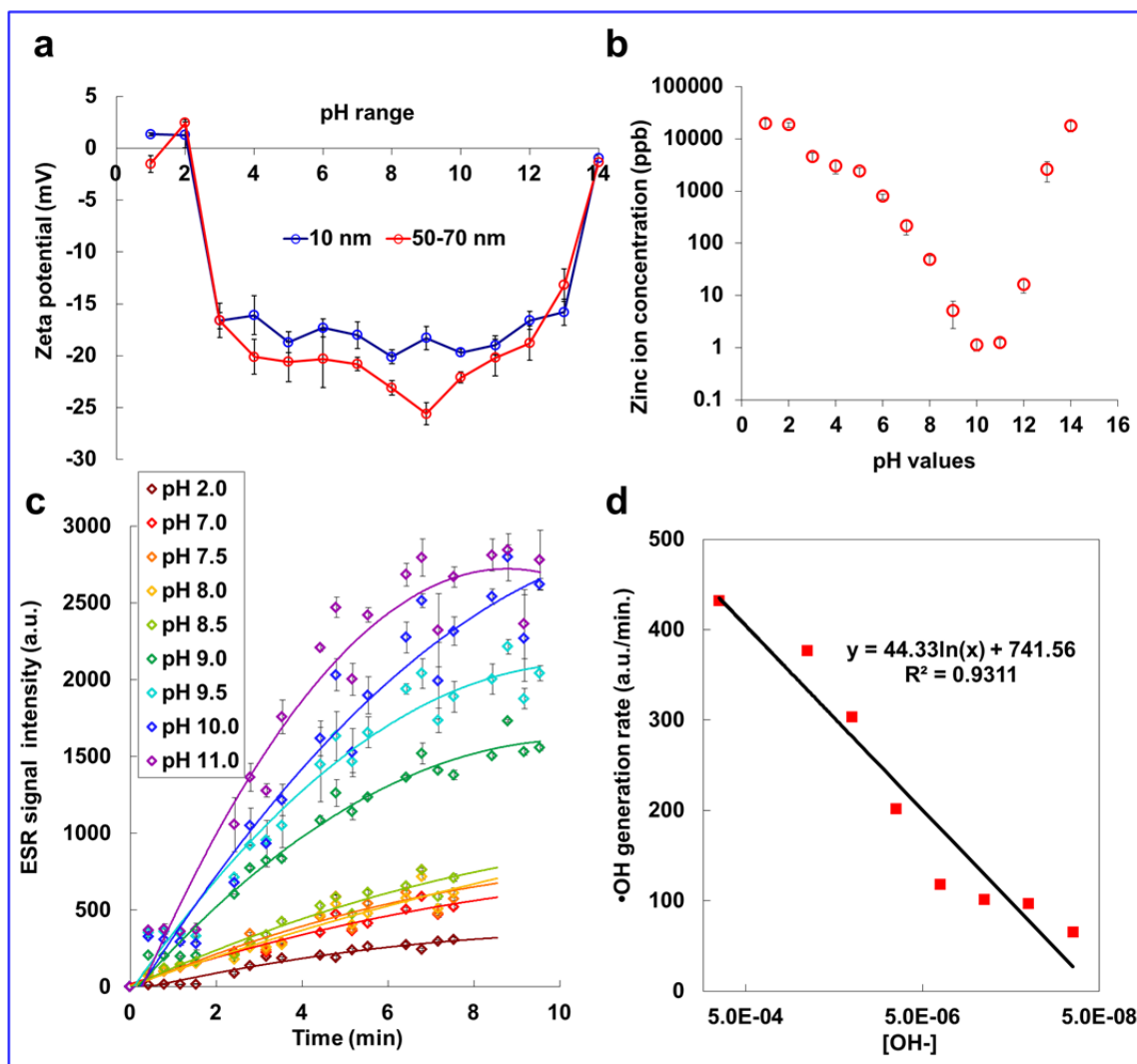


Figure 4. Physicochemical properties of ZnO NPs as functions of pH environment that presented through: a) ζ -potential, b) released zinc ions, and c) \bullet OH generation. d) Plot of initial four-minute irradiation hydroxyl radical production rate (as accumulated ESR signal intensity per minutes) vs. hydroxide anion concentration in varied pH buffers. A linear fitting was drawn to see if it falls into a first-order reaction kinetics. Data show in (a) to (c) are presented as mean \pm standard deviation after triplicate (or at least duplicate) measurements.

Effect of ionic strength and oxygen content on \bullet OH generation

Total ionic strength (IS)⁴² and the effective oxygen vacancy sites on ZnO NP surfaces⁴³ have also been reported to modulate ROS generation. This understanding was explored

using ultra-pure water (IS = 0.01 mM), tap water (IS = 2 mM), and PBS buffer (pH = 7, IS = 70 mM). Results shows that ionic strength generally exhibited an inverse relationship with $\bullet\text{OH}$ generation (Fig. 5a) that displayed non-linear complexities that were later attributed to radical quenching by inorganic anions.^{44, 45} Specifically, inorganic anions will compete for the photocatalytic oxidizing sites on the nanoparticle surface to form inorganic anion radicals that will not contribute to the ESR signal shown (Fig. 5a) per the Langmuir-Hinshelwood kinetic mode.²⁶

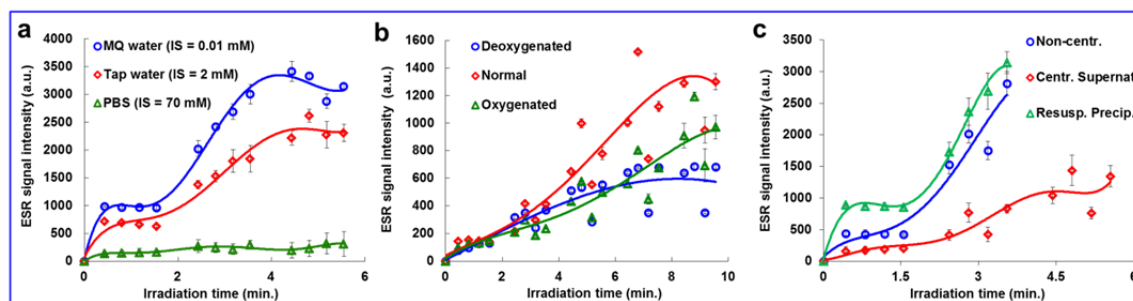


Figure 5. Influences of radical production from (a) variable ionic strengths (IS) of ultra-pure water, tap water and a phosphate buffer solution (PBS), (b) varied oxygen abundances of non-aerated control (normal), N_2 de-oxygenation, and O_2 oxygenation treatments, and (c) non-centrifuged, centrifuged supernatant clear solution and re-suspended centrifugation-precipitation.

Surface defects and oxygen vacancies on ZnO NP surfaces⁴⁶ further correlated with $\bullet\text{OH}$ formation.⁴⁷ In this study, ZnO NP suspensions underwent a five-minute pre-treatment of either 1) N_2 de-oxygenation, 2) O_2 oxygenation, or 3) no pre-treatment. Then DMPO was immediately added followed by ESR analysis for 10 minutes (Fig. 5b). Heightened $\bullet\text{OH}$ formation within the oxygenated group indicated dissolved oxygen facilitates $\bullet\text{OH}$ generation. This finding supported experimental evidence related to mitochondrial dysfunctions following ZnO NP exposure.⁴⁸ Finally, the non-aerated

control group contributed to the greatest $\bullet\text{OH}$ formation, although this occurrence is attributed to the poor stability of the NP suspension following aeration.

It was still unclear whether the newly formed $\bullet\text{OH}$ bind to ZnO NP active sites or are released into the surrounding environment, a distinction with substantial cytotoxic implications that merited additional study. To address this critical question, centrifuged, suspended, and control ZnO NP suspensions were compared by using ESR to determine the localization of the radicals. One mg/mL 50-70 nm ZnO NPs in PBS (pH = 7) were freshly prepared and divided into three groups before ESR analysis: (1) the original suspension, (2) the supernatant after centrifugation at 5,000 rpm for 15 seconds, and (3) the re-suspended precipitate following centrifugation (Fig. 5c). Decreased $\bullet\text{OH}$ formation was observed in the centrifuged group which was attributed to ZnO NP precipitation from the centrifugation process. This observation would imply that DMPO/ $\bullet\text{OH}$ adducts form on the nanoparticle surface, which was supported by the resuspended group having higher initial DMPO/ $\bullet\text{OH}$ levels than the control group. Moreover, the trends in the resuspended group closely paralleled those in the control group following additional irradiation. These findings suggest that $\bullet\text{OH}$ preferentially binds to the nanoparticle surface rather than being released into the surrounding environment. We further evaluated this hypothesis by adding DMPO before and after centrifugation to locate the $\bullet\text{OH}$. Similar ESR results were acquired in both setups, strongly indicating surface localization of the newly formed $\bullet\text{OH}$. Similar conclusions were suggested in a recent study, where ROS generation was inversely proportional to nanoparticle diameter, which demonstrated surface-catalyzed ROS generation.⁴⁹ This new $\bullet\text{OH}$ formation mechanism poses serious concerns for ZnO NP nanotoxicity under biologically relevant conditions.⁵⁰

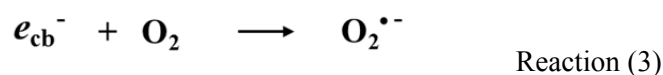
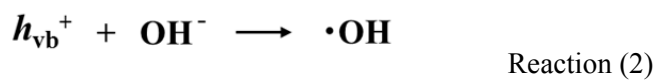
The effects of organic solvent and NP composition on •OH generation

In an extended ESR test, glycerol and ethanol were used to suspend ZnO NPs instead of water (Fig. S6). A six-peak signal was observed in both groups that were different from the typical four-peak signal of DMPO-trapped •OH adducts in water. We infer that it may correlate with carbon-centered radicals produced in organic environments.^{51, 52} Moreover, we found that the chemical composition of the ZnO NPs also play an important role in ESR spectra. Nanoparticles of differing composition, but similar concentration and size, namely TiO₂ (40 nm), SiO₂ (46 nm) and CeO₂ (20 nm) NPs produced remarkably different ESR spectra (Fig. S7). Weak or no •OH signals were observed with irradiated TiO₂ and SiO₂ NP while •OH formation occurred in irradiated CeO₂. Both four-peak (typical DMPO-trapped •OH) and six-peak signals were also shown in CeO₂ NP suspension (Fig. S7), suggesting •OH formation by CeO₂ proceeds via unique process.

Proposed cytotoxic mechanism

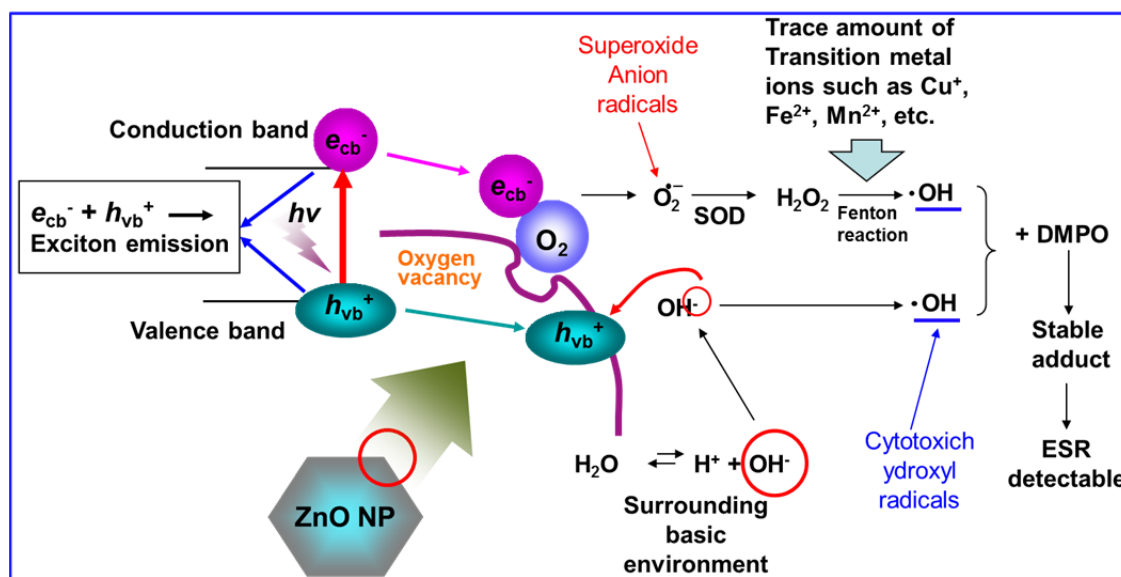
ZnO NPs can have several types of defects, such as interstitial atoms or vacancies, that are characterized as either anionic or cationic.⁵³ Singly ionized O vacancy site (V_O^\bullet), and (2) doubly ionized O vacancy site ($V_O^{\bullet\bullet}$) exist in ZnO NPs, which give rise to an overall positive charge on ZnO NP surfaces alongside excess amounts of Zn^{2+} , which have several key implications for •OH formation. First, V_O^\bullet is an ESR-active defect that has an effective monovalent positive charge with respect to regular O^{2-} sites. It lies approximately 2 eV below the ZnO conduction band and acts as a recombination center under irradiation. Second, $V_O^{\bullet\bullet}$ is a vacancy containing no electrons, having an effective divalent positive charge with respect to the normal O^{2-} sites, and can be formed when a

hole is trapped at a V_O^\bullet center. Emitted photons were mostly assigned to a shallowly trapped electron with a deeply trapped hole in a $V_O^{\bullet\bullet}$ center. The V_O^\bullet and $V_O^{\bullet\bullet}$ vacancy sites can chemo-adsorb negatively charged, polar molecules like OH^- , H_2O , and O_2 . Photon absorption (>3.6 eV) promotes an electron (e_{cb}^-)/hole (h_{vb}^+) pair, which may further react with adsorbed species, such as OH^- ions to form $\bullet\text{OH}$ free radicals (Reaction 2). The observed four-fold increase in $\bullet\text{OH}$ ESR signal intensity as solution pH was increased from 8.0 to 10.0 supported this understanding. Hence, locally adsorbed OH^- ions at vacancy sites have important roles in $\bullet\text{OH}$ photogeneration.



Furthermore, the e_{cb}^- can also react with locally adsorbed O_2 molecules to form superoxide anions (Reaction 3), which was observed by the weak set of ESR signals that were attributed to superoxide anions (Fig. 1a). These anions may be generated by nearby photo/Auger electron charge transfer.⁴⁹ Although superoxide anion radicals are cytotoxic, their highly transient nature limits their capacity to directly present cytotoxic effects. Biologically, $\text{O}_2^{\bullet-}$ is rapidly converted to H_2O_2 by superoxide dismutase (SOD) and further transformed to $\bullet\text{OH}$ via Fenton reaction assisted by trace amounts of transition metal ions (e.g. Cu^+ , Fe^{2+} , Mn^{2+}). Our ICP-MS analysis indicated the presence of these and other Fenton metals in both the 10 nm and 50 – 70 nm ZnO NPs (Fig. S8). Special attention is given here to trace metal contamination across different batches and vendors of nanoparticles that may lead to confounding results. These subtle variations in

nanoparticle compositions will not dramatically alter cytotoxic effects, but may lead to unique ROS generation properties. On the other hand, the trapping of “excited” electrons, e_{cb}^- , by O_2 at the vacancy sites, and their conversion to $O_2^{\cdot-}$ can further decelerate the recombination of e_{cb}^- with h_{vb}^+ , and thereby enhance $\bullet OH$ formation. These pathways can favorably proceed as long as the surface defects are localized to the irradiated sites that trap h_{vb}^+ and e_{cb}^- so as to prevent exciton emission. Hence, irradiated ZnO NPs may generate $\bullet OH$ from multiple, distinct pathways (Scheme 1), which leads us to posit that $\bullet OH$ formation by intact NPs is a more likely route for cytotoxicity than dissolved zinc ions which is minimally released under biologically relevant conditions.



Scheme 1 Proposed mechanism of $\bullet OH$ generation by ZnO NPs mainly with assistance of irradiation and basic pH environment. SOD: superoxide dismutase.

Extracellular calcium influx imaging

To support this hypothesis, we conducted an *in vitro* study to model ZnO NP cytotoxicity using extracellular calcium influx imaging. This approach is premised on the idea that divalent calcium (Ca^{2+}) is an important secondary messenger for cell signaling that can

be used to accurately monitor cytotoxic processes in a real-time manner.^{54, 55} Since calcium influxes can be activated by $\bullet\text{OH}$, its use in monitoring $\bullet\text{OH}$ cytotoxicity is particularly advantageous for studying ZnO NP cytotoxicity (Fig. 6).⁵⁶ Four ZnO NP concentrations (7.5, 15, 25 and 50 $\mu\text{g/mL}$) were used to induce extracellular ionic calcium ($[\text{Ca}^{2+}]_i$) influx in A549 epithelial lung cancer cells. A 100 nM intracellular Ca^{2+} level⁵⁴ was selected as the triggering threshold since $[\text{Ca}^{2+}]_i$ is physiologically maintained at or below this level. Extracellular Ca^{2+} influxes and subsequent cell nucleus decomposition were observed following exposure to ZnO NPs (Fig. 6a-c, three featured calcium imaging animations are also available in the electronic supplementary information (ESI)). Our findings indicated that ZnO NP exposure quickly induced Ca^{2+} influxes that were best modeled by a linear correlation between logarithmic NP concentration and the influx triggering time (Fig. 6d), indicating a first-order reaction kinetics as well. These findings also indicated that nuclear membrane damage occurred simultaneously with calcium influxes, which are tell-tale signs of cell apoptosis or autophagy.^{19, 57} This result revealed a unique way of ZnO NP cytotoxicity through nuclear deformation. This finding supports previously observed irradiation-enhanced nuclear decomposition by ZnO NPs.^{19, 57}

This is coincidentally supported by a recent study that high hydroxyl radical production was observed due to the formation of a structured water layer in the vicinity of the nanoparticle which possibly through the interaction between NP's charge and the water dipoles.²² Moreover, our results indicate ZnO NP $\bullet\text{OH}$ generation is accelerated under high oxygen and basic pH environments, which impart significant ZnO NP cytotoxicity implications as detailed visualized in Fig. S9. Together these findings will

likely impact toxicology research, chemical enhancement⁵⁸ and nanomedicine,²² such as by presenting novel therapeutic targets to limit ZnO NP cytotoxicity following exposure.

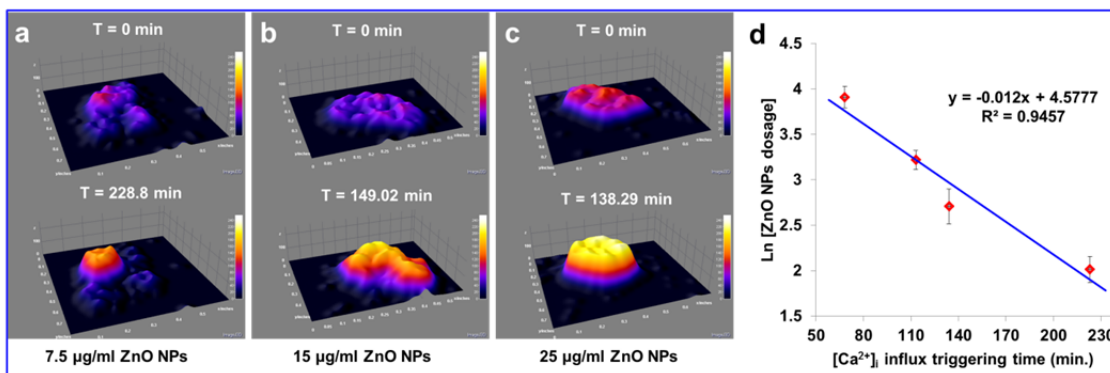


Figure 6 The correlation between ZnO NP uptake and intracellular calcium homeostasis; 3-D plot of intracellular calcium kinetics were established based on featured-cell's 2-D fluorescent intensity under three ZnO NP dosages of (a) 7.5, (b) 15, and (c) 25 µg/mL. (d) Linear correlation between the natural logarithmic concentration of ZnO NPs and the calcium influx triggering time. Pseudo-colored regions are selected cells that are stained with Fura-2 AM to show real-time variation of the intracellular calcium concentration. Blue-purple regions represent resting status with low $[Ca^{2+}]_i$, while red-yellow regions represent highly increased intracellular $[Ca^{2+}]_i$. Each point represents 20 averaged measurements and error bars represent standard deviations.

Conclusions

In summary, the physicochemical properties of ZnO NPs were systematically studied for their effects on ROS generation. ESR analysis demonstrated that $\bullet OH$ generation is influenced by irradiation time, hydrodynamic size, dosage, and local pH. Decreases in time-lapsed ESR measurements under dark conditions were attributed to nanoparticle aggregation and precipitation, which resulted in concentration-dependent inflection points in the ESR data. Preferential $\bullet OH$ generation was observed under the following conditions: irradiation, basic pH, high dissolved oxygen, and low ionic strength. Finally, the discovery of bound $\bullet OH$ to ZnO NP surfaces suggested highly concentrated, localized

ROS regions that may present a novel mechanism of cytotoxicity. Future work should aim to quantify NP surface vacancy sites and impurities to substantiate this proposed mechanism.

Associated content

Supporting Information

Additional data including raw ESR spectra, non-ultrasonicated ZnO NPs, time-lapse UV/Vis absorption spectra, ultrasonication influence on pH, trace elemental analysis of two different sizes of ZnO NPs, final proposed cellular cytotoxic pathways as well as three calcium imaging related animations are available in the electronic supplementary information (ESI) of this article.

Author information

Corresponding Author

Tel: 01-573-341-6220. Fax: 01-573-341-6033. E-mail: yinfa@mst.edu

Conflict of interest

The authors declare no competing financial interest.

Acknowledgements

The authors gratefully thank Dr. Robert S. Aronstam and Hsiu-Jen Wang for their technical assistance with the calcium imaging experiments as well as Yongbo Dan and

Kun Liu for their technical assistance with the ICP analysis. This project was supported by internal funding from the Center for Single Nanoparticle, Single Cell, and Single Molecule Monitoring (CS³M), and Department of Chemistry at Missouri University of Science and Technology. C. Burton received research funding through a National Science Foundation Graduate Research Fellowship (#DGE-1011744).

References

1. A. Nel, T. Xia, L. Madler and N. Li, *Science*, 2006, **311**, 622-627.
2. T. Xia, M. Kovichich, M. Liong, L. Mädler, B. Gilbert, H. Shi, J. I. Yeh, J. I. Zink and A. E. Nel, *Acs Nano*, 2008, **2**, 2121-2134.
3. P. Patra, S. Mitra, N. Debnath and A. Goswami, *Langmuir*, 2012, **28**, 16966-16978.
4. R. J. Vandebriel and W. H. De Jong, *Nanotechnology, science and applications*, 2012, **5**, 61.
5. W. Lin, Y. Xu, C.-C. Huang, Y. Ma, K. B. Shannon, D.-R. Chen and Y.-W. Huang, *Journal of Nanoparticle Research*, 2009, **11**, 25-39.
6. P. Kocbek, K. Teskač, M. E. Kreft and J. Kristl, *Small*, 2010, **6**, 1908-1917.
7. V. Sharma, R. K. Shukla, N. Saxena, D. Parmar, M. Das and A. Dhawan, *Toxicology letters*, 2009, **185**, 211-218.
8. S.-T. Yang, J.-H. Liu, J. Wang, Y. Yuan, A. Cao, H. Wang, Y. Liu and Y. Zhao, *Journal of nanoscience and nanotechnology*, 2010, **10**, 8638-8645.
9. I. Pujalté, I. Passagne, B. Brouillaud, M. Tréguer, E. Durand, C. Ohayon-Courtès and B. L'Azou, *Part. Fibre Toxicol.*, 2011, **8**, 1-16.
10. S. George, S. Pokhrel, T. Xia, B. Gilbert, Z. Ji, M. Schowalter, A. Rosenauer, R. Damoiseaux, K. A. Bradley and L. Mädler, *Acs Nano*, 2009, **4**, 15-29.
11. J.-h. Li, X.-r. Liu, Y. Zhang, F.-f. Tian, G.-y. Zhao, F.-l. Jiang and Y. Liu, *Toxicology Research*, 2012, **1**, 137-144.
12. B. De Berardis, G. Civitelli, M. Condello, P. Lista, R. Pozzi, G. Arancia and S. Meschini, *Toxicology and applied pharmacology*, 2010, **246**, 116-127.

13. S. Hackenberg, A. Scherzed, A. Technau, M. Kessler, K. Froelich, C. Ginzkey, C. Koehler, M. Burghartz, R. Hagen and N. Kleinsasser, *Toxicology in Vitro*, 2011, **25**, 657-663.
14. H. Kato, M. Suzuki, K. Fujita, M. Horie, S. Endoh, Y. Yoshida, H. Iwahashi, K. Takahashi, A. Nakamura and S. Kinugasa, *Toxicology in Vitro*, 2009, **23**, 927-934.
15. T. Xia, Y. Zhao, T. Sager, S. George, S. Pokhrel, N. Li, D. Schoenfeld, H. Meng, S. Lin and X. Wang, *Acs Nano*, 2011, **5**, 1223-1235.
16. J. H. Niazi and M. B. Gu, in *Atmospheric and Biological Environmental Monitoring*, Springer, 2009, pp. 193-206.
17. M. R. Hoffmann, S. T. Martin, W. Choi and D. W. Bahnemann, *Chemical reviews*, 1995, **95**, 69-96.
18. C. D. Jaeger and A. J. Bard, *Journal of Physical Chemistry*, 1979, **83**, 3146-3152.
19. Q. Yang and Y. Ma, *Int. J. Toxicol.*, 2014, 1091581814529168.
20. Z. A. Lewicka, W. Y. William, B. L. Oliva, E. Q. Contreras and V. L. Colvin, *Journal of Photochemistry and Photobiology A: Chemistry*, 2013, **263**, 24-33.
21. V. Kavitha and K. Palanivelu, *Journal of Photochemistry and Photobiology A: Chemistry*, 2005, **170**, 83-95.
22. C. Sicard-Roselli, E. Brun, M. Gilles, G. Baldacchino, C. Kelsey, H. McQuaid, C. Polin, N. Wardlow and F. Currell, *Small*, 2014, **10**, 3338-3346.
23. B. D. Johnston, T. M. Scown, J. Moger, S. A. Cumberland, M. Baalousha, K. Linge, R. van Aerle, K. Jarvis, J. R. Lead and C. R. Tyler, *Environmental science & technology*, 2010, **44**, 1144-1151.
24. W. He, H. Kim, W. Wamer, D. Melka, J. Callahan and J. Yin, *Journal of the American Chemical Society*, 2014, **136**, 750.
25. E. Finkelstein, G. M. Rosen and E. J. Rauckman, *Arch. Biochem. Biophys.*, 1980, **200**, 1-16.
26. M. Abdullah, G. K. Low and R. W. Matthews, *Journal of Physical Chemistry*, 1990, **94**, 6820-6825.
27. E. G. Janzen, *Acct. Chem. Res.*, 1971, **4**, 31
28. E. G. Janzen, *J. Mag. Res.*, 1973, **9**, 510.

29. K. Rangelova and R. P. Mason, *Magnetic Resonance in Chemistry*, 2011, **49**, 152-158.
30. R. Wottrich, S. Diabaté and H. F. Krug, *International journal of hygiene and environmental health*, 2004, **207**, 353-361.
31. D. Upadhyay, V. Panduri, A. Ghio and D. W. Kamp, *American journal of respiratory cell and molecular biology*, 2003, **29**, 180.
32. M. Huang, E. Khor and L.-Y. Lim, *Pharmaceutical research*, 2004, **21**, 344-353.
33. A. Lipovsky, Z. Tzitrinovich, H. Friedmann, G. Applerot, A. Gedanken and R. Lubart, *The Journal of Physical Chemistry C*, 2009, **113**, 15997-16001.
34. E. G. Janzen and J. I. Liu, *Journal of Magnetic Resonance (1969)*, 1973, **9**, 510-512.
35. E. Finkelstein, G. M. Rosen and E. J. Rauckman, *Journal of the American Chemical Society*, 1980, **102**, 4994-4999.
36. M. L. Fernández-Cruz, T. Lammel, M. Connolly, E. Conde, A. I. Barrado, S. Derick, Y. Perez, M. Fernandez, C. Furger and J. M. Navas, *Nanotoxicology*, 2013, **7**, 935-952.
37. C. Hanley, A. Thurber, C. Hanna, A. Punnoose, J. Zhang and D. G. Wingett, *Nanoscale research letters*, 2009, **4**, 1409-1420.
38. K. M. Reddy, K. Feris, J. Bell, D. G. Wingett, C. Hanley and A. Punnoose, *Applied physics letters*, 2007, **90**, 213902-213902-213903.
39. I.-L. Hsiao and Y.-J. Huang, *Science of the Total Environment*, 2011, **409**, 1219-1228.
40. H. Weller, *Angewandte Chemie International Edition in English*, 1993, **32**, 41-53.
41. E. Navarro, A. Baun, R. Behra, N. B. Hartmann, J. Filser, A.-J. Miao, A. Quigg, P. H. Santschi and L. Sigg, *Ecotoxicology*, 2008, **17**, 372-386.
42. H. Ma, P. L. Williams and S. A. Diamond, *Environmental Pollution*, 2013, **172**, 76-85.
43. K. Senthilkumar, M. Tokunaga, H. Okamoto, O. Senthilkumar and Y. Fujita, *Applied physics letters*, 2010, **97**, 091907.

44. M. Y. Guo, A. M. C. Ng, F. Liu, A. B. Djurišić, W. K. Chan, H. Su and K. S. Wong, *The Journal of Physical Chemistry C*, 2011, **115**, 11095-11101.
45. L. Li, Y. Abe, K. Kanagawa, N. Usui, K. Imai, T. Mashino, M. Mochizuki and N. Miyata, *Anal. Chim. Acta*, 2004, **512**, 121-124.
46. J.-Z. Kong, A.-D. Li, H.-F. Zhai, Y.-P. Gong, H. Li and D. Wu, *Journal of Solid State Chemistry*, 2009, **182**, 2061-2067.
47. G. Applerot, A. Lipovsky, R. Dror, N. Perkas, Y. Nitzan, R. Lubart and A. Gedanken, *Advanced Functional Materials*, 2009, **19**, 842-852.
48. K.-N. Yu, T.-J. Yoon, A. Minai-Tehrani, J.-E. Kim, S. J. Park, M. S. Jeong, S.-W. Ha, J.-K. Lee, J. S. Kim and M.-H. Cho, *Toxicology in Vitro*, 2013, **27**, 1187-1195.
49. M. Misawa and J. Takahashi, *Nanomedicine: Nanotechnology, Biology and Medicine*, 2011, **7**, 604-614.
50. R. Wahab, A. Mishra, S.-I. Yun, Y.-S. Kim and H.-S. Shin, *Applied microbiology and biotechnology*, 2010, **87**, 1917-1925.
51. A. MAZUMDAR, S. ADAK, R. CHATTERJEE and R. BANERJEE, *Biochem. J*, 1997, **324**, 713-719.
52. L. C. Wilms, J. Kleinjans, E. J. Moonen and J. J. Briedé, *Toxicology in Vitro*, 2008, **22**, 301-307.
53. M. McCluskey and S. Jokela, *Journal of applied physics*, 2009, **106**, 071101-071101-071113.
54. D. E. Clapham, *Cell*, 1995, **80**, 259-268.
55. M. Shi, T. Zhang, L. Sun, Y. Luo, D.-H. Liu, S.-T. Xie, X.-Y. Song, G.-F. Wang, X.-L. Chen and B.-C. Zhou, *Apoptosis*, 2013, **18**, 435-451.
56. M. Ishii, S. Shimizu, Y. Hara, T. Hagiwara, A. Miyazaki, Y. Mori and Y. Kiuchi, *Cell Calcium*, 2006, **39**, 487-494.

57. C.-C. Wang, S. Wang, Q. Xia, W. He, J.-J. Yin, P. P. Fu and J.-H. Li, *Journal of Nanoscience and Nanotechnology*, 2013, **13**, 3880-3888.
58. N. N. Cheng, Z. Starkewolf, R. A. Davidson, A. Sharmah, C. Lee, J. Lien and T. Guo, *Journal of the American Chemical Society*, 2012, **134**, 1950-1953.

III. In vitro study of improved wound-healing effect of bioactive borate-based glass nano-/micro-fibers

Qingbo Yang^{1,2,4}, Sisi Chen^{1,2}, Honglan Shi^{1,2,4}, Hai Xiao³, Yinfa Ma^{1,2,4*}

¹Department of Chemistry, Missouri University of Science and Technology, Rolla, MO 65409;

²Center for Biomedical Science and Engineering (CBSE), Missouri University of Science and Technology, Rolla, MO 65409;

³Department of Electrical and Computer Engineering, Clemson University, Clemson, SC 29634;

⁴Center for Single Nanoparticle, Single Cell and Single Molecule Monitoring (CS³M), Missouri University of Science and Technology, Rolla, MO 65409.

* Corresponding Author

Address: Department of Chemistry

Missouri University of Science and Technology

400 West 11th Street

Rolla, MO 65409

Phone: 573-341-6220

Fax: 573-341-6033

E-mail: yinfa@mst.edu

ABSTRACT

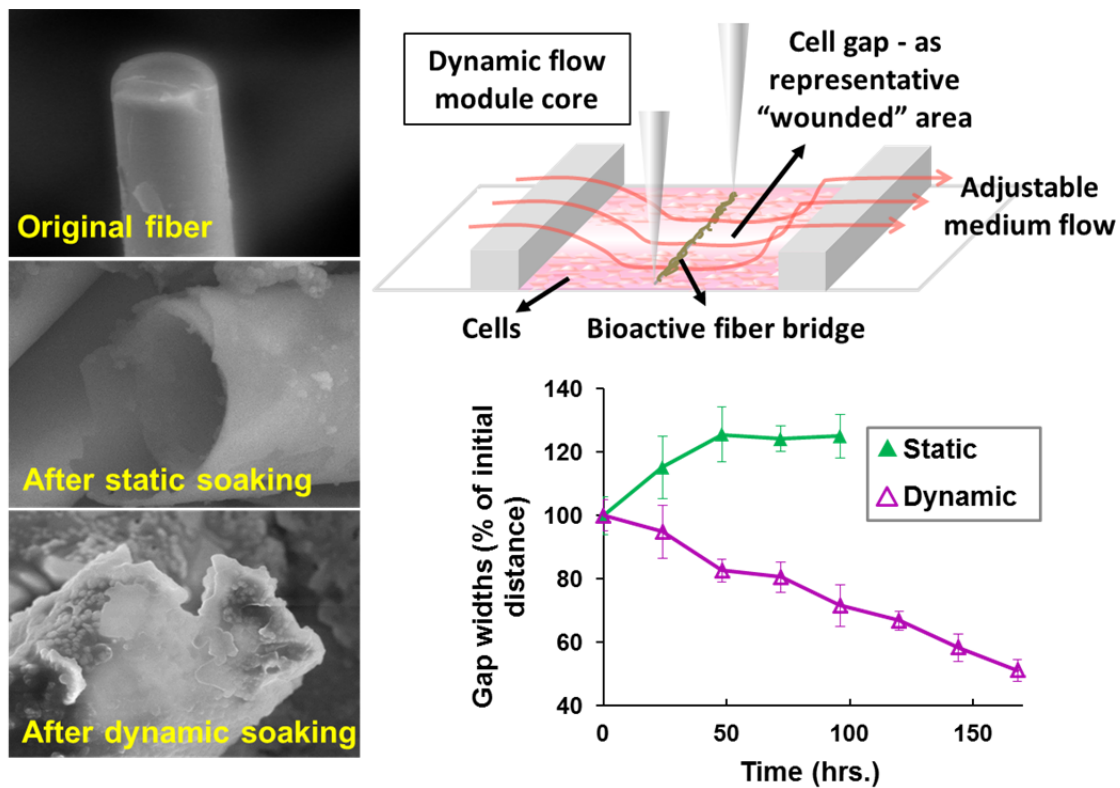
Because of the promising wound-healing capability, bioactive glasses have been considered as one of the next generation hard- and soft-tissue regeneration materials. The lack of understanding of the substantial mechanisms, however, indicates the need for further study on cell-glass interactions to better interpret the rehabilitation capability. In the present work, three bioactive glass nano-/micro-fibers, silicate-based 45S5, borate-based 13-93B3 and 1605 (additionally doped with copper and zinc), were firstly compared for their *in vitro* soaking/conversion rate. The results of elemental monitoring and electron microscopic characterization demonstrated that quicker ion releasing and glass conversion occurred in borate-based fibers than that of silicate-based one. This result was also reflected by the formation speed of hydroxyapatite (HA). This process was further correlated with original boron content and surrounding rheological condition. We showed that an optimal fiber pre-soaking time (or an ideal dynamic flow rate) should exist to stimulate the best cell proliferation and migration ability. Moreover, 13-93B3 and 1605 fibers showed different glass conversion and biocompatibility properties as well, indicating that trace amount variation in composition can also influence fiber's bioactivity. In sum, our *in vitro* rheological module closely simulated *in vivo* niche environment and proved a potentially improved wound-healing effect by borate-based glass fibers, and the results shall cast light on future improvement in bioactive glass fabrication.

Keywords: silicate-/borate-based bioactive glass fibers; glass conversion; hydroxyapatite formation; dynamic flow module; cell proliferation/migration; soft tissue wound-healing.

Highlights

- Bioactive glass nano-/micro-material was effectively used for tissue wound healing
- Silicate-based 45S5, borate-based 13-93B3 and 1605 fibers were firstly compared
- Glass conversion rate was compared under either static or dynamic-flow modes
- Glass composition and flow rate greatly influenced bioactivity and cell migration
- These results may cast light on future improvement of bioactive glass fabrication

Table of Content Graphic (TOC)



1. Introduction

Silicate-based bioactive glass has received considerable interest since the early 1970s¹⁻³ for its putative wound healing capabilities. Known mechanism involves the dissolution of the bioactive glass in body fluid and the subsequent conversion of the released ions to the important bone mineral, hydroxyapatite (HA).^{4,5} Clinical applications of silicate-based bioactive glasses, such as the well-established 45S5 formulation, have nevertheless been hindered by practical concerns including uncontrollable dissolution as well as slow, incomplete HA conversions, and thus insufficient bioactivity.⁶ Borate-⁷⁻⁹ and phosphate-¹⁰ based bioactive glasses have recently been reported to have improved bioactivity and more complete HA conversions.¹¹⁻¹³ These practical differences were highlighted in an *in vivo* study that demonstrated markedly improved bone growth in rat calvarias with borate-based bioactive glass scaffolds as opposed to silicate-based glasses.¹⁴

Further studies showed that HA conversion is not the only mechanism that responsible for bone tissue regeneration. Multiple studies showed inorganic ions that released from bioactive glasses, including silicon (Si),¹⁵⁻¹⁷ calcium (Ca),¹⁸⁻²¹ phosphorous (P),²² magnesium (Mg),²³⁻²⁸ and boron (B),^{29,30} were involved in many processes which include bone metabolism, growth, and mineralization. Many trace metal elements though, like strontium (Sr), copper (Cu), zinc (Zn), and cobalt (Co), etc., were also showed to participate in bone tissue regeneration and formation.³¹⁻³⁴ Besides, bioactive glasses have been reported to stimulate angiogenesis, the formation of new blood vessels,³⁵⁻³⁷ which is a crucial process for both hard and soft tissue regeneration.^{14,38} Actually, more attentions have been drawn within the area of soft tissue repair because recent study demonstrated

encouraging regeneration capabilities of skin tissues with promoted angiogenesis.³⁹ Although adequately reports and mechanisms have been proposed for the bone tissue healing effect of these glass materials, no convincing hypothesis is available yet to address the function mechanism of these materials on soft tissue healing effect. Moreover, the stimulating effect on fibroblast cells and granulation tissues has also been correlated with the induction of vascular endothelial growth factor (VEGF) and basic fibroblast growth factor (bFGF), which were evidently proved by increased numbers of rough endoplasmic reticula and newly formed micro-vessels.⁴⁰ These findings, nevertheless, greatly expanded the vision of both hard and soft tissue stimulating effect by bioactive glass materials.

However, two major aspects currently are hindering the way of further understanding the glass-cell interactions mechanisms, especially in the case of *in vitro* evaluation. On one hand, not well-simulated *in vivo* environment during *in vitro* study of cell-glass interactions. Most previous bioactivity studies were carried out with standard protocols for *in vitro* toxicity evaluation, like those that has been used for drug screening. A major problem in using the standard procedure is its requirement of static experimental condition which ignored the rheological influences within human body. Thus, a closer simulation to the in-body environment is the key issue when carrying on *in vitro* tests in order to better understand the actual functionality of these bioactive glass materials. Exceptional effort has been made by R. F. Brown et al., who designed his tests using a slowly-swaying platform, which successfully lower the *in-situ* boron dosage and had acquired meaningful results under a dynamic culturing condition.⁶ On the other hand, the cytotoxic effect that comes from released metal ions was mostly been simplified or

ignored. Studies showed that HA conversion in borosilicate and borate-based bioactive glasses was positively correlated with boron trioxide (B_2O_3),^{11,41} which was reported to have negative effect on cell proliferation and thus raising many concerns and doubts in their practical use. Besides, it has been shown that most of these bioactive glass materials will cause surrounding pH increasing onto a pretty harmful level (pH unit ranging from 8 to 11) in simulated body fluid (SBF),^{11,13,42,43} which again indicated a potential cytotoxic effect in long-term co-culturing with cell or tissues.

The objective of the present work is to therefore conduct a comprehensive evaluation of the HA conversion and glass-cell interactions under both static and dynamic-flow modes. Three nano- or micro- glass fibers, including silicate-based 45S5 (24.5% Na_2O , 24.5% CaO , 45% SiO_2 , 6% P_2O_5 (wt%)), borate-based 13-93B3 (5.5% Na_2O , 11.1% K_2O , 4.6% MgO , 18.5% CaO , 3.7% P_2O_5 , 56.6% B_2O_3 (wt%)), and borate-based 1605 (6% Na_2O , 12% K_2O , 5% MgO , 20% CaO , 4% P_2O_5 , 51.6% B_2O_3 , 0.4% CuO , 1% ZnO (wt%)) were used for comparison of their bioactive effect on a human fibroblast skin cell line (CCL-110). A dynamic-flow module with a continuous supply of fresh media was established for a close study of rheological evaluation. A combination of scanning electron microscopy/energy-dispersive X-ray spectroscopy (SEM/EDS) and inductively coupled plasma optical emission spectrometry (ICP-OES) were used to quantitatively measure the glass dissolution within the medium and ion deposition onto the entire fibers, respectively. Fiber bioactivity was assessed through cell viability, migration, and morphological assays. Finally, comprehensive evaluations of the employed three bioactive nano-/micro-glass fibers were thoroughly discussed for their bioactive effects.

2. Experimental section

2.1. Starting materials

The nano-/micro-fibrous bioactive glasses used in this study were provided by Mo-Sci (Rolla, Missouri). The overall appearance of these glass materials looked like cotton wool. Three formulations of glass were used (as shown in Table 1): two borate-based glass fibers designated as 13-93B3 and 1605, and one well-known silicate-based 45S5 glass fibers. The as-received glass microfibers have been thoroughly sterilized by γ -ray and vacuum sealed for shipment, thus all fibers were being freshly measured and used as-received for the following tests.

Table 1

Original weight-percentage compositions of the bioactive glass nano-/micro-fiber that used in this study.

Fiber name	Chemical composition (wt%)								
	Na ₂ O	K ₂ O	MgO	CaO	SiO ₂	P ₂ O ₅	B ₂ O ₃	CuO	ZnO
45S5	24.5	0	0	24.5	45	6	0	0	0
13-93B3	5.5	11.1	4.6	18.5	0	3.7	56.6	0	0
1605	6	12	5	20	0	4	51.6	0.4	1

2.2. *In vitro* fiber immersion, degradation, and conversion

Assessment of the *in vitro* degradation and conversion of the microfibrinous glasses was performed by immersing the materials in serum-free cell culture *Eagle's Minimum Essential Medium* (EMEM) (American type culture collection (ATCC), Manassas, Virginia), and characterizing the structural and compositional changes as a function of

immersion time. Briefly, each type of microfibrinous glass was accurately weighed and mixed with the EMEM medium, and the final mixture had a fiber dosage ranging from 5 to 2000 $\mu\text{g}/\text{mL}$ according to different experimental designs, with 0 $\mu\text{g}/\text{mL}$ dosage (no fiber, only medium) served as a control for each test. After being mixed, the fiber suspension was used for the experiment immediately in order to maintain a constant starting-point condition and to avoid compositional changes due to possible dissolving and reactions. Both static and dynamic-flow modes were used for fiber immersion in this study, and fiber degradation and conversion rate were then compared through microscopic imaging as well as chemical analyses. In detail, fibers were firstly analyzed for their interactions with cell culture medium. The 1 mg/mL starting fiber dosage was soaked in medium for the exposure time study ranged from 0 to 5 days. In both static and dynamic-flow treatments, all fibers were filtered out, heat dried, and imaged/examined by a field emission scanning electron microscopy (FESEM) (Hitachi 4700, Tokyo, Japan) with associated energy-dispersive X-ray spectroscopy (EDS) analyses (EDAX, Phoenix, Arizona) to analyze the morphological changes and reaction products that formed on both the outer and inner surfaces of the fiber. In addition, the media after fiber soaking were also collected through filtration by 0.22 μm filters, and were analyzed by using inductively coupled plasma - optical emission spectrometry (ICP-OES) (Perkin Elmer 2000D series, Waltham, Massachusetts) to quantify the released elements. In the fiber-cell interaction section, both fresh glass fibers and pre-soaked fibers were also used and compared for their stimulation effects on cell proliferation. The static and dynamic-flow conditions were not only tested and compared for their direct influences on fiber degradation and conversion, but also on their influences on fiber-cell interactions.

Finally, the specific borate fiber 1605 that was doped with copper and zinc were picked and studied for its influences on cell morphology and migration during its degradation and conversion process when it was co-cultured with cells. All experiments for each glass fibers at each time point were at least triplicated to acquire statistically meaningful data.

2.3. Elemental analysis of ion releasing

The concentration of ions that released from the fiber into culture medium was measured using ICP-OES. The initial fiber dosage of 1 mg/mL was applied in each testing group, and 120 hours or 72 hours total testing periods were used in static or dynamic-flow modes, respectively. The length of testing periods was decided when no further significant increasing/decreasing of signals was observed. For static mode, sterilized fibers of each composition were immersed in serum-free EMEM statically and incubated for up to 120 hours at constant 37 °C cell culturing environment. For dynamic-flow mode, a home-built dynamic-flow system was used to maintain a continuous flow of fresh serum-free culture medium through the fiber-containing chamber, and the flowing-by medium at the outlet vent was collected each time point and used for elemental analysis by using ICP-OES. Collected medium was filtered through 0.22 µm nylon filter membrane (Sigma-Aldrich, St. Louis, MO) and freshly diluted 10- to 20-fold with MQ water (EMD Millipore Corp., MA) (contains 1% HNO₃) in capped 10-mL conical tubes, and used for ICP-OES analysis. All data were normalized to the control and calculated back as the original concentrations.

2.4. Cell culture conditions and fiber dosing

The established human fibroblast cell line (CCL-110) was obtained from ATCC (Manassas, Virginia). The cells were grown in EMEM medium supplemented with 10% fetal bovine serum (FBS) (Life technology, Grand Island, New York), penicillin (100 I.U./mL) and streptomycin sulfate (100 $\mu\text{g}/\text{mL}$), plus 25 mM HEPES (pH 5 - 7.3). All incubations were performed at 37°C in a humidified atmosphere with 5% CO₂. In preparation for testing of cell responses to glass fibers, cells were pre-seeded with an initial confluence of 50,000 cells/cm² density and incubated for 48 hours to permit cell attachment and reach a good proliferation status. Glass fibers were then added, followed by either static or dynamic-flow incubation mode for varied durations. In addition to examine the cell-fiber interactions using freshly prepared fiber suspension, a setup of pre-immersed fibers was also tested for their stimulation effect on cell growth. After immersion in EMEM for different times, fibers and the soaked medium were collected separately. The soaked fibers were gently and briefly rinsed twice with fresh medium, heat dried, weighed, and immediately used for cell dosing. Separated soaking supernatants were further filtered through 0.22 μm filter, and also used for cell dosing.

2.5. In vitro cell proliferation and migration assay and confocal microscopic cell imaging

Human skin fibroblast cells CCL-110 were allowed to grow to 80% confluence in 48 hours prior to each cell test. Cells were then co-cultured either with (a) freshly weighed bioactive glass fibers, or (b) pre-soaked fibers, or (c) fiber pre-soaked supernatants, under static condition and for varied testing time periods, to induce differentiated proliferation and migration patterns. For cell viability assay, the WST-1

assay (Cell Titer 96 Aqueous One Solution Assay, Promega) was used according to the manufacturers' instructions. Absorbance at 450 nm using WST-1 was measured using a microplate reader (FLOURstar; BMG Labtechnologies, Durham, North Carolina). In cell viability test that used freshly prepared bioactive fiber suspension, the fiber dosages ranged from 0 to 2000 $\mu\text{g/mL}$, and were tested for 48 hours. A ten-day long cell viability assay was also carried out to evaluate the low fiber dosage influence on cell proliferation, where only 100 $\mu\text{g/mL}$ fiber concentrations were used. In addition, a pre-soaking process of the fibers was carried out to test the impact of after-soaking fibers and medium on cell proliferation, where a median fiber dosage of 250 $\mu\text{g/mL}$ was used before soaking. Pre-soaked fibers and after-soaking supernatant were separately collected and tested in cell viability assays for 72 hours and 10 days exposures, respectively. For the dynamic-flow mode experiments, considering the faster fiber-medium interaction efficiency, a higher fiber dosage of 500 $\mu\text{g/mL}$ was used and a 72 hours exposure was monitored for cell viability assay. Two control groups, one under static mode and another under dynamic-flow mode, were applied in this study to make statistical comparisons with the fiber-dosed cell groups under these two separate exposure modes. Because of the different flow rate of the dynamically controlled culture medium, the total medium replacement within the chamber was at different rate. In this study, we use the "total medium replacement time" (TMRT) to standardize all cell viability data, e.g. a 10-hour TMRT means it takes 10 hours to fully replace the medium within the chamber with the fresh medium. Thus the total medium flow rates (F_{total}) (assume the medium flow-in and flow-out at the same rate as designed) can be calculated and converted as TMRT since the total medium volume in the chamber (V_{chamber}) maintained the same ($F_{\text{total}} \times \text{TMRT} = V_{\text{chamber}}$). Here the concept

TMRT was used because it not only interprets and normalizes all actual flow rates, but also correlates flow rate with the whole chamber volume.

For the migration assay, scratching created “wounded” area of cell monolayers was performed using the tip of a 1,000 μ l pipette tip. A homemade bioactive glass fiber bridge composed of two stand posts and a thin straight line (single optical fiber with an outer diameter of 150 μ m) was applied to assist cells attachment and migration. Proper amount of bioactive glass fibers (total 100 μ g) were then uniformly and fully glued onto the thin optical fiber using PDMS. Once bioactive glass fibers were all attached onto the PDMS-rinsed optical fiber surface, a follow up 60 $^{\circ}$ C heating and curing process was used for 1 hour until all PDMS solidified. Cell migration rates within the distance of \pm 50 μ m to the fiber bridge were quantified and compared with those cultured without the bioactive fiber bridge influencing, through using software ImageJ (NIH, Bethesda, MD). The distance covered by cells in between the scratch-wound area was quantified as decreases of gap widths, and about 15 measurements were taken for each experimental condition. Three images were analyzed per condition, per time point, and averages and standard deviations were then calculated. Confocal cell images were also taken with a prior staining process with fluorescent dyes. Cell nucleus staining dye DAPI (Life technology, Grand Island, New York) and a mitochondria specific dye JC-1 (Life technology, Grand Island, NY) were used in this study; three fluorescent channels of DAPI, FITC and Cy5 were separately taken under the confocal inverted microscope (Eclipse Ti confocal microscope, Nikon, Japan).

2.6. Statistical analysis

Experimental data acquired from triplicated assays was normalized against each control group, and One-way ANOVA followed by Post Hoc test (if necessary) was taken for most statistical analysis. The results were expressed as mean \pm standard deviation (SD). The level of statistical significance for the comparison was set as p -value < 0.05 (*). Statistical analysis was also partially performed by MinitabTM software (State College, Pennsylvania).

3. Results

3.1. Changes of fiber morphology under static mode

Three formulations of bioactive glass fibers, silicate-based 45S5, borate-based 13-93B3, and borate-based 1605, were used in this study (Table 1). The portray field emission scanning electron microscopic (FESEM) images of original fibers and fibers immersed in the cell culture media for five days without any disturbance are shown in Fig. 1 - 3.

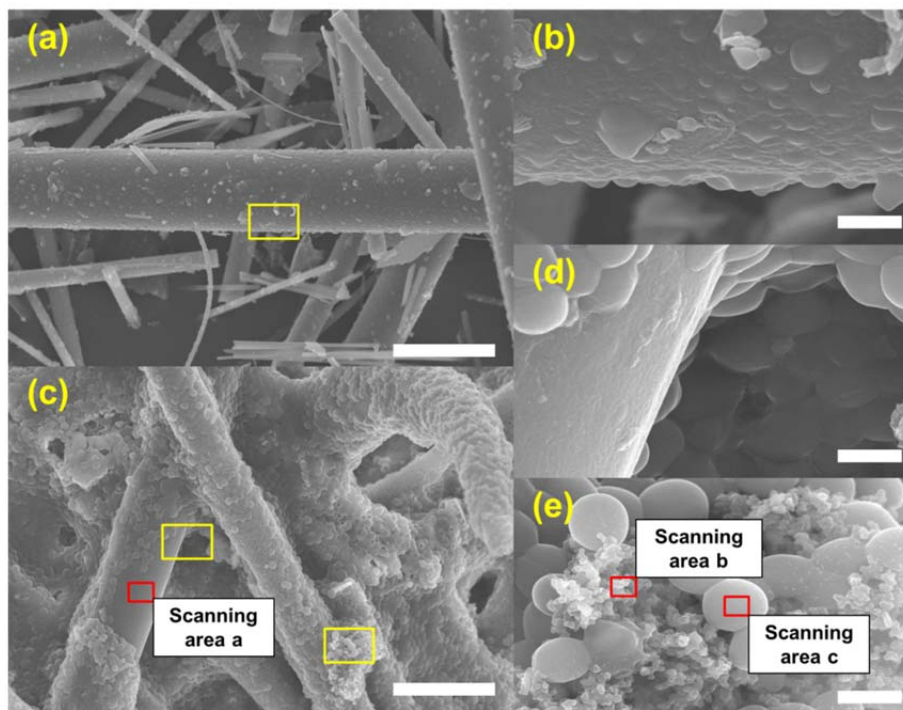


Fig. 1. SEM images of silicate-based 45S5 glass fibers before (a, b) and after (c, d, e) 5 days soaking in cell culture medium under static mode. Scale bar: 10 μm (a, c) and 1 μm (b, d, e).

High magnification (Fig. 1b) reveals uneven surfaces on the 45S5 fiber with papillary bulges resulting from trace crystals²¹, while the 13-93B3 and 1605 glass fibers are generally smooth (Fig. 2b, 3b). Notably, after five days immersion, all fibers are markedly roughed (Fig. 1c, 2c, 3c) and have umbilicated or hollowed fiber ends (Fig. 4). These physical changes suggest that ion release and chemical deposition occurred within and on the fibers. Ovate-shaped spherulites (400 – 600 nm diameters) and formation of small porous-network granules (50 – 200 nm diameters) were also observed on 45S5 fiber surfaces (Fig. 1d, 1e).

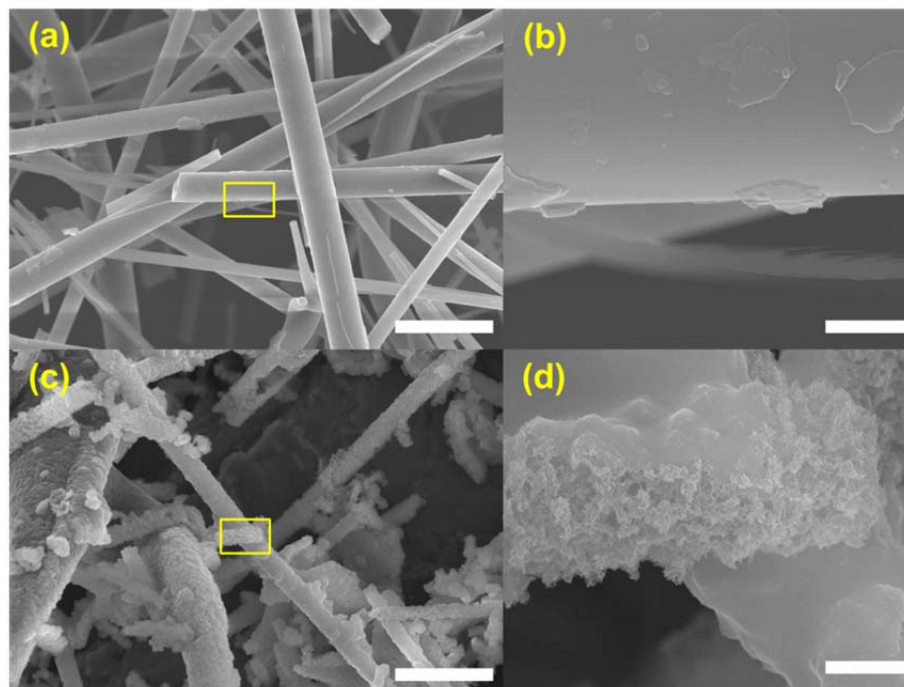


Fig. 2. SEM images of borate-based 13-93B3 glass fibers before (a, b) and after (c, d) 5 days soaking in cell culture medium under static mode. Scale bar: 10 μm (a, c) and 1 μm (b, d).

Similar spherulites (20 – 200 nm diameters) covered borate 13-93B3 fiber surface (Fig. 2c), while whisker- or flake-like fine structures were observed under high magnification (Fig. 2d). The borate 1605 glass fibers were highly fractured with lamellar surface structures (Fig. 3c, 3d) as well as partially dissolved fiber-fiber intersections (Fig. 3c).

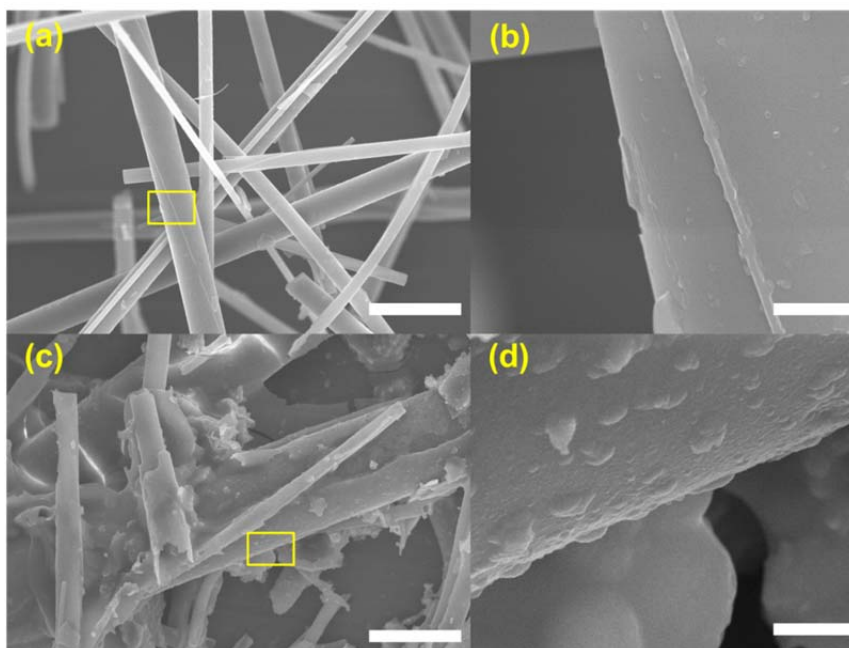


Fig. 3. SEM images of borate-based 1605 glass fibers before (a, b) and after (c, d) 5 days soaking in cell culture medium under static mode. Scale bar: 10 μm (a, c) and 1 μm (b, d).

Fig. 4 provides specific cross-section view of the three fibers before and after immersion. The original solid-and-smooth end faces (Fig. 4a - 4c) were roughened-and-eroded (Fig. 4d - 4f) after immersion. Silicate 45S5 fiber showed a core-shell fiber structure, where the core was still solid and less eroded (Fig. 4d). However, the borate 13-93B3 and 1605 fibers showed highly eroded fiber cores, and even became tubular shape in some cases (Fig. 4e, 4f).

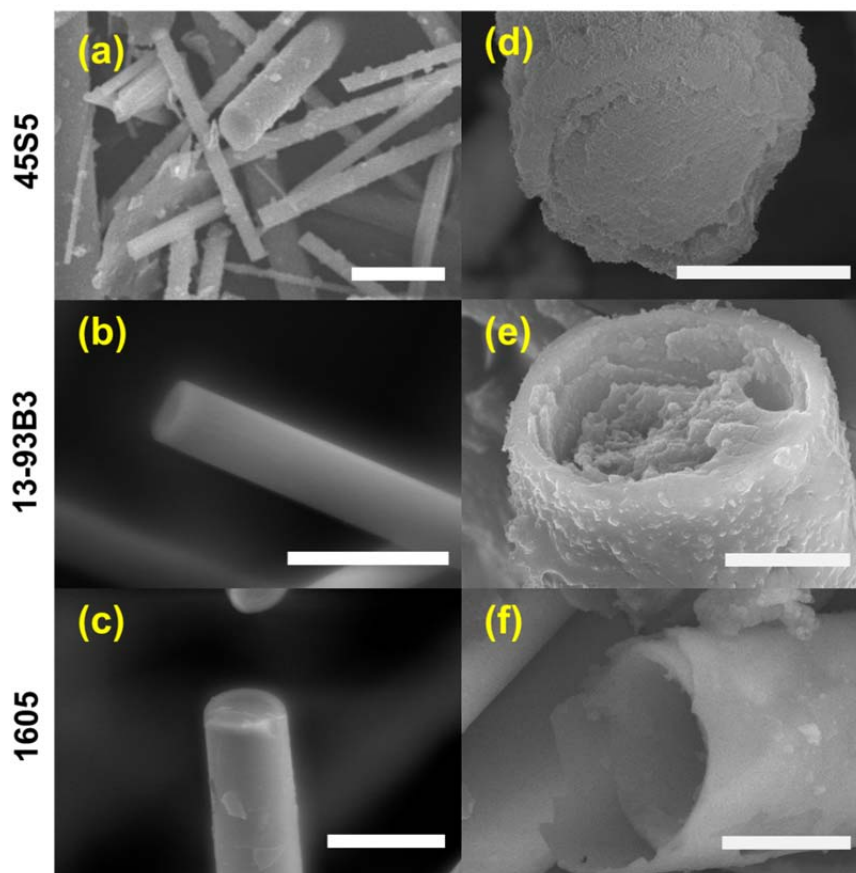


Fig. 4. SEM images of bioactive fiber end-faces before and after static-mode soaking in cell culture medium. Particularly, 45S5 fibers were shown in (a) (before soaking) and (d) (after soaking), 13-93B3 fibers were shown in (b) (before soaking) and (e) (after soaking), as well as 1605 fiber were shown in (c) (before soaking) and (f) (after soaking). Scale bar: 5 μm (a, b, c) and 3 μm (d, e, f).

3.2. Changes of fiber morphology under dynamic-flow mode

Morphological changes of three selected fibers were also studied under a dynamic-flow condition (or: dynamic mode) with a continuous supply of fresh media. The dynamic nature was expected to exert greater hydrodynamic forces on the fibers and therefore expected to considerably alter the morphological structure of the fibers. Indeed, as shown in Fig. 5, these fibers exhibited smooth surfaces with significantly fewer fine

structures (e.g. flakes and whiskers). High magnification images revealed eroded and porous inner structures under the lamellar surface in 45S5 fibers (Fig. 5a, 5b). A similar “polished” surface morphology (Fig. 5c) was observed in 13-93B3 fibers with a porous granule network underlying the surface layers (Fig. 5d). The borate-based 1605 fibers showed highly roughened surfaces and protruded spherical-shape structures (Fig. 5e). High magnification images revealed eroded fiber surfaces and hollowed cross sections (Fig. 5f).

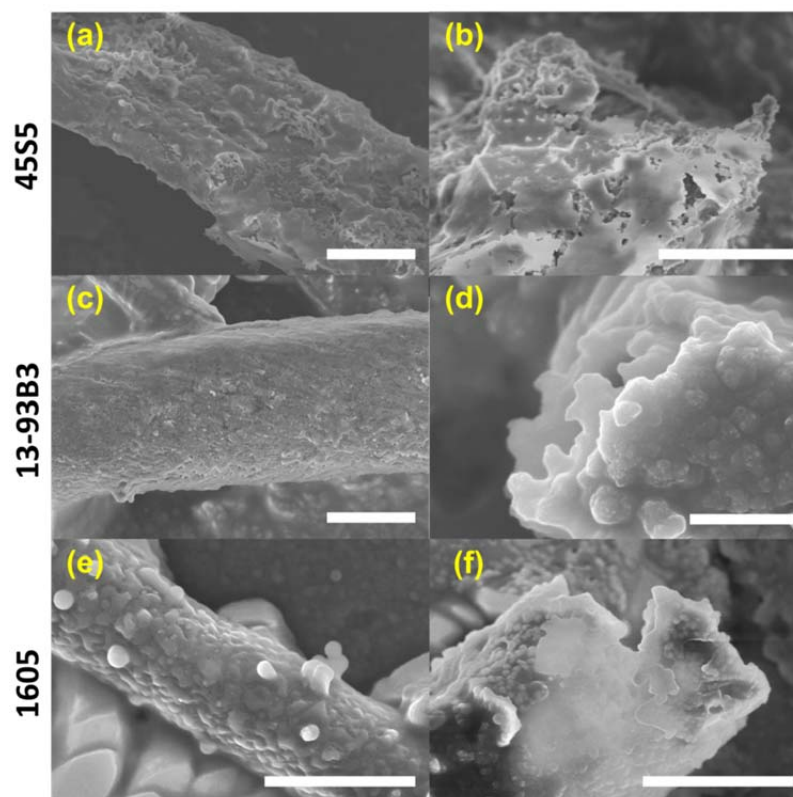


Fig. 5. SEM images of bioactive fiber surface and end-face after dynamic-mode soaking in cell culture medium for 5 days. The fibers shown are 45S5 (a, b), 13-93B3 (c, d), and 1605 (e, f), respectively. Scale bar: 5 μm (a, b, c), 500 nm (d) and 2 μm (e, f).

3.3. Chemical characterization under static and dynamic modes.

The energy-dispersive X-ray spectroscopy (EDS) scanning was used to characterize the fiber surface elemental compositions (as shown in Fig. 6). The intensities were normalized to calcium for clarity purpose. Fig. 6a showed the elemental surface changes in the silicate-based 45S5 fibers after five days immersion. Three specific surface morphologies were selected (see Fig. 1c, 1e) for analysis including: the “naked” fiber area (a), granule-shape area (b) and orbicular-shape area (c). The elemental compositions on the fiber surface of original and immersed fibers were also provided as atomic percentages (Fig. S1). Carbon content increased in all analyses, by approximately 50% in borate-based fibers and nearly 100% in silicate-based fibers (area a) under static modes, and by about 500%, 200%, and 800% in the 45S5, 13-93B3 and 1605 fibers, respectively, under dynamic mode. Oxygen content slightly decreased in all samples under static mode except at particular morphological sites (area b and c) in the silicate-based 45S5 fiber. Silicon and boron were released under both modes from respective fibers. Finally, phosphorous content increased under both modes, while calcium increased under static mode but not dynamic mode. The calcium contents in the plot were normalized as the same intensity (height) here, but calcium content in atomic ratio was actually increased under dynamic flow conditions as shown in Fig. S1.

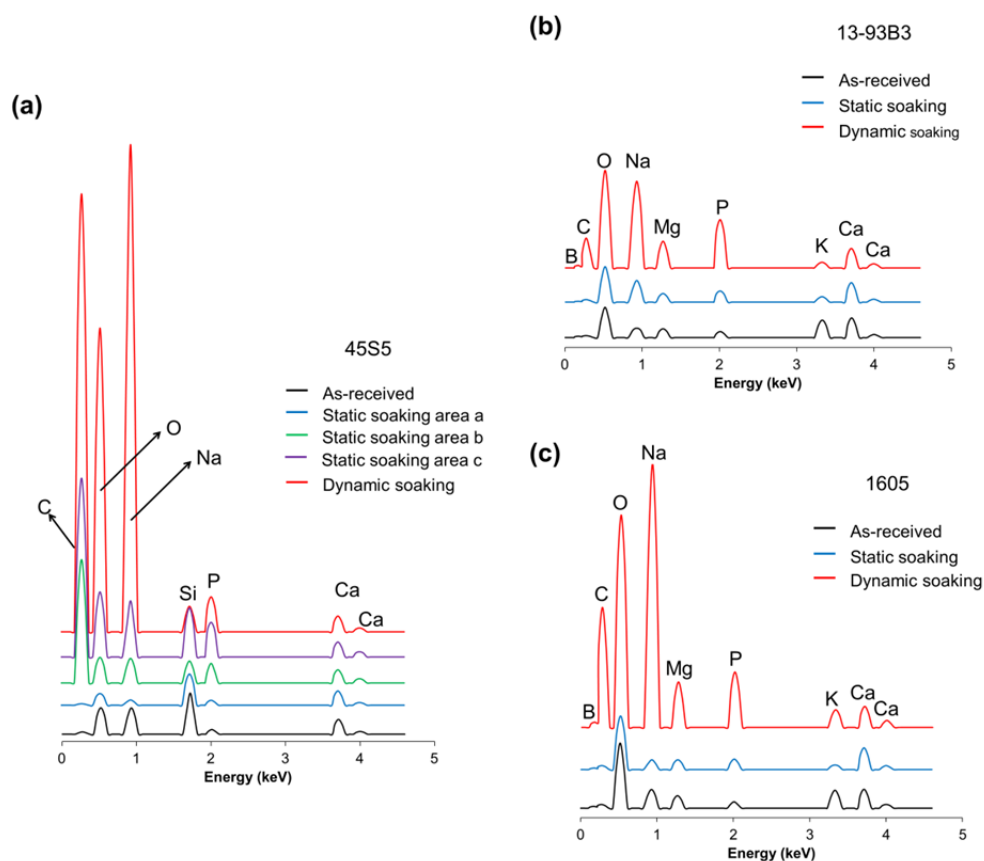


Fig. 6. EDS scanning of elemental composition pattern of the as-received and post-soaking (5 days) bioactive glass micro-/nano-fibers (scanned areas are shown as red-squares that labelled in Fig. 1).

3.4. Elemental release pattern

Inductively coupled plasma - optical emission spectrometry (ICP-OES) was used to quantitatively determine the elemental release from each fiber under each mode for a period of 72 hours (dynamic mode) and 120 hours (static mode) (as shown in Fig. 7). Data points were normalized to the elemental concentrations in control groups where no fibers were used.

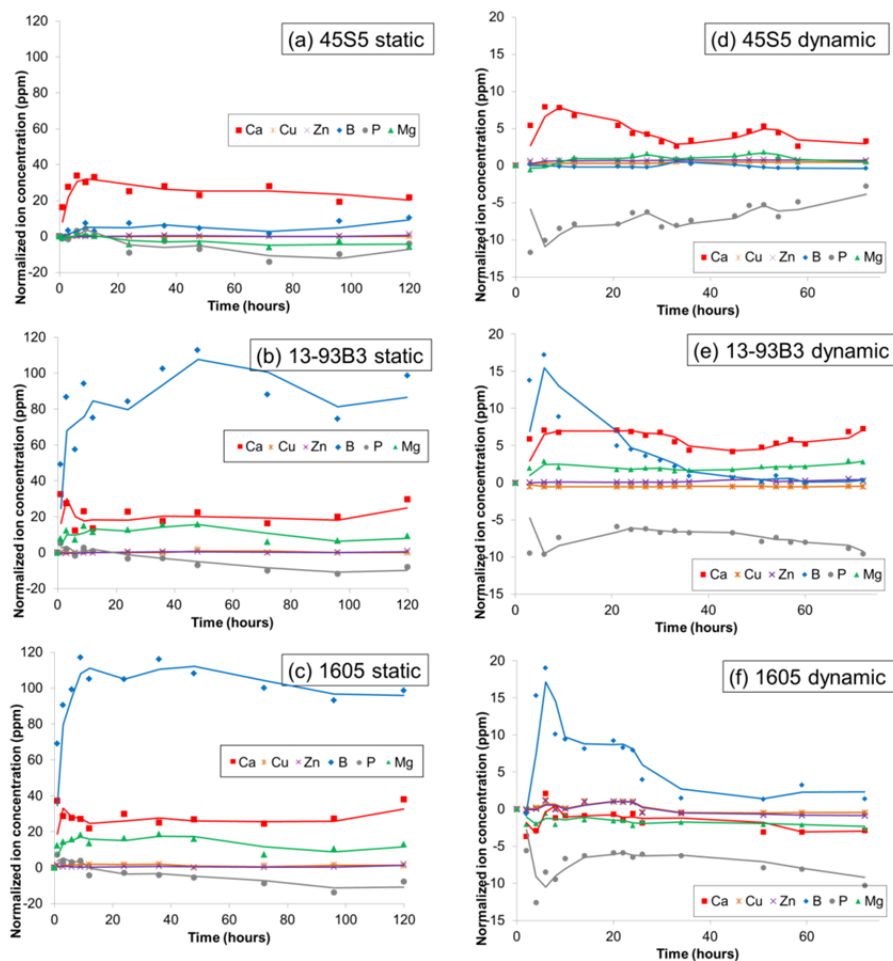


Fig. 7. Plot interpretation of ICP-OES data in comparison between fiber-released ion concentration and the soaking time, under either static (a - c) or dynamic (d - f) modes. Moving average trend lines were plotted to illustrate possible ion-releasing patterns.

The calcium content went through an increasing-decreasing process which occurred earlier (5 – 6 hours) in the fibers of borate-based than that of silicate-based. However, the total phosphorous content started to decrease readily after initial period of several hours in all three fibers, and negative values were shown after they were normalized to the control. Boron and magnesium that were only used in the formulation of borate-based fibers showed steep releasing patterns within 10 hours. Then copper and

zinc, though only slightly doped, were also detected. By comparing the measured and the theoretically calculated (result from complete fiber dissolution, see Table S1) ionic concentrations under static mode, a total percentage of elemental releasing has been provided in Table 2. The time needed for reaching each peak value was presented as consuming time in the bracket. Calcium and phosphorous contents in borate-based fibers reached to the positive peak values faster than those in the silicate-based fibers (statistically significant, $p < 0.05$). It was also noticed that slightly higher percentages of magnesium, calcium, phosphorous and boron were released from the copper/zinc containing fiber 1605 than fiber 13-93B3. A negatively labelled phosphorous shown in the table was representative of a final “withdrawing” effect by the chemical deposition process, which induced a slow but constant decreasing of phosphorous concentration in the solution. To some point a lower phosphorous concentration than control would be observed during the process. The longer consuming time, then the higher withdrawing percentage of phosphorous was observed in the borate-based fibers than the silicate-based fibers.

Under the dynamic mode, however, much lower elemental concentrations were detected mainly because of a faster diluting rate (Fig. 7d – 7f). The peak contents of calcium and boron appeared within 6 hours; meanwhile a negative peak of phosphorous was also shown for the same reason discussed above. According to the plotted trend, a further withdrawal of phosphorous might still be taken place in the borate fibers.

Table 2

Elemental releasing peak as percentage of theoretical total amount that would occur under ideal static condition.

Elemental releasing peak ^a (bracket: time in hrs.)							
	Mg	Ca	P	- P	B	Cu	Zn
45S5	–	19.29% (6)	16.40% (9)	-54.52% (72)	–	–	–
13-93B3	56.82% (48)	24.64% (1)	32.77% (1)	-72.71% (96)	63.38% (48)	–	–
1605	62.26% (48)	26.15% (1)	42.32% (1)	-78.93% (96)	72.16% (9)	64.93% (36)	25.02% (120)

^aElemental releasing peaks are presented as percentage of theoretical total amount.

3.5. Cell viability variation as function of fiber dosages and dosing time

Cell viability assays were firstly carried out using as-received (original) bioactive fibers at different dosages and varied testing times. Varied fiber dosages, from 5 to 2000 µg/mL, were used to evaluate their effects on cell viability at a 48-hour exposure time (Fig. S2). Since fibers showed a negative effect on the cell viability at high dosages, the x-axis was plotted in logarithmic scale to illustrate the impact of low fiber dosages on the cell proliferation (Fig. 8). Positive effects have been demonstrated to stimulate 20 – 40% higher cell proliferation than control with lower dosages of both 45S5 (≤ 750 µg/mL) and 1605 (≤ 250 µg/mL) fibers. Out of which, the 45S5 fibers showed a wider dosage range (up until 750 µg/mL) that was able to stimulate higher cell viability than the control. However, the borate-based 13-93B3 fibers did not show any significant stimulating effect on cell proliferation.

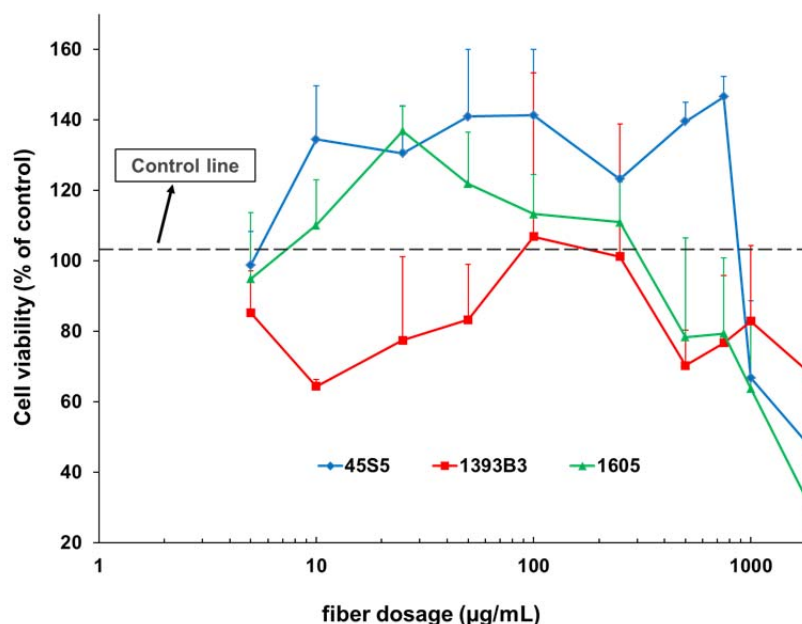


Fig. 8. Forty-eight hours recording of viability when cells co-cultured with varied fiber dosages under static mode. X-axis was plotted in logarithmic scale for clearer demonstration of cell performance within low fiber dosage range. Each data points represent mean + SD, $n \geq 3$.

A ten-day cell viability assay was also carried out to evaluate the influence of low-dosage fibers (100 µg/mL) on cell proliferation (Fig. 9). No significant decrease in cell viabilities was observed compared to the control until the fifth day, but further co-treatment with fibers under static mode greatly decreased cell viabilities.

3.6. Impact of pre-soaking of fibers on cell proliferation

In order to differentiate the influence on cell proliferation from fibers with their released ions, a separate mode cell viability assay has also been taken place with both pre-soaked fibers and fiber pre-soaked supernatants (Fig. 10). Fibers and serum-free cell culture medium were pre-soaked together (at initial dosage 250 µg/mL), filtered,

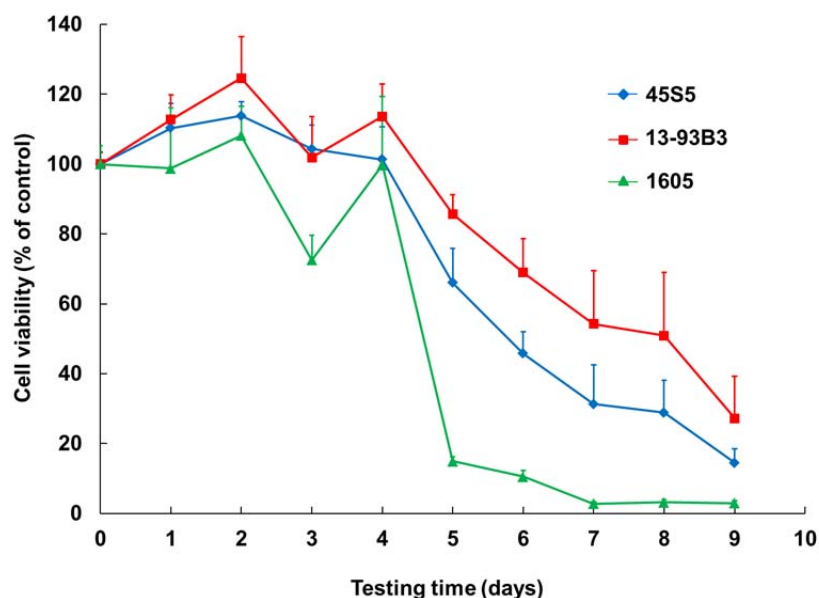


Fig. 9. Viability assay using WST-1 when cells co-cultured with 100 $\mu\text{g/mL}$ fresh fibers for 10 days under static mode. Each data points represent mean + SD, $n \geq 3$.

separated, and employed in cell culture. Viability of cells was tested and showed as percentage of control (fiber-free medium cultured cells). Fig. 10(a) showed the pre-soaked fibers influence on cell viability, where both 45S5 and 13-93B3 fibers stimulated cell proliferation by 35 – 40% more than control after one hour soaking. After a peak increase with all three fibers that were pre-soaked for 12 hours, cell viabilities were either kept increasing (with 1605), maintained (with 13-93B3) or substantially decreased (with 45S5) with fibers that were pre-soaked for longer time, among which, statistically higher ($p < 0.05$) cell viability was stimulated by 13-93B3 at 36 hours, and by 13-93B3 and 1605 at 72 hours, over 45S5 fibers. Finally, all fibers that pre-soaked for more than 48 hours showed much less stimulating effect on cell proliferation. In addition, cell viability was also tested with supernatants that derived from fiber pre-soaking (Fig. 10b).

Experimentally, supernatants were collected one aliquot per day for ten days since fibers were soaked, and were used for a 48-hour cell culture. Sharp decreasing of cell viability was observed with day-one borate-based fiber pre-soaked supernatants, while no further decreases were shown with the longer pre-soaked supernatants.

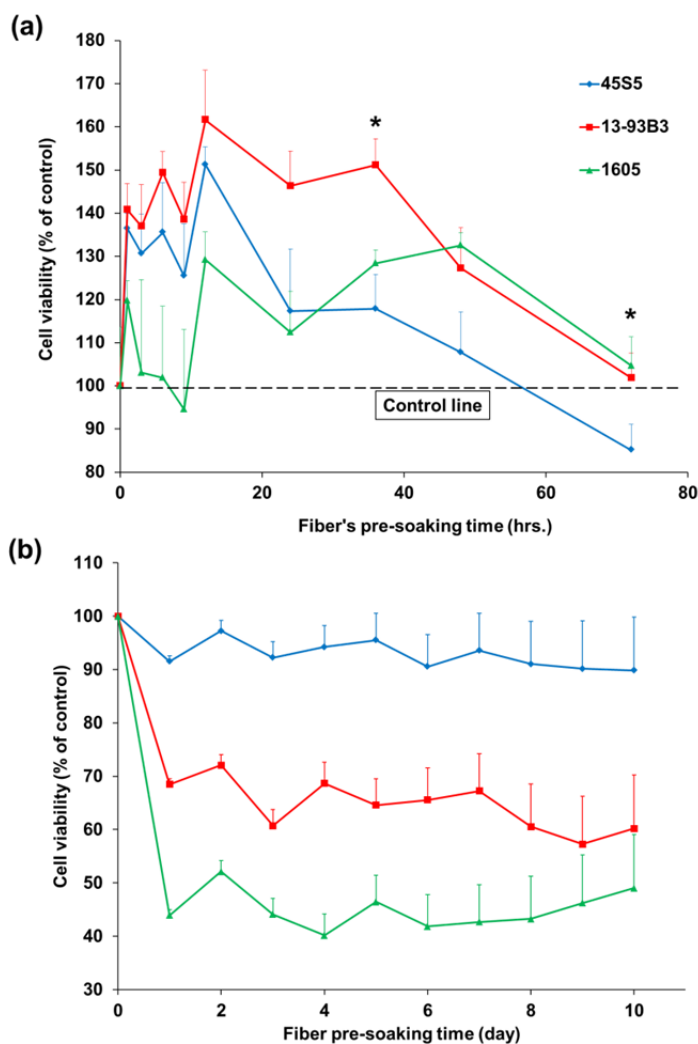


Fig. 10. WST-1 cell viability assay when co-cultured with (a) pre-soaked bioactive fibers for 72 hours, and (b) fiber-pre-soaked supernatants for 10 days, both under static mode. Each data points represent mean + SD, $n \geq 3$. * $p < 0.05$ vs. control glass 45S5.

3.7. Impact of dynamic mode on fiber-cell interaction

A simulated refreshing system (dynamic mode) was developed with capability of continually refreshing the medium without changing the total volume nor heavily disturbing the environment (Fig. 11). Original fibers at a dosage of 500 $\mu\text{g}/\text{mL}$ were used and various refreshing rate were tested and designated as total medium replacement time (TMRT). The concept TMRT was used because it not only interprets and normalizes all actual flow rates, but also correlates flow rate with the whole chamber volume. Cells without fiber co-culturing were used as controls under either static or dynamic modes for data normalization. Results showed steep increases of cell viability in all four groups when compared with static control, and peak values ($\sim 200\%$ higher than static control) were shown within a range of 24 to 36 hours of TMRT. It was notice that both borate-based fibers stimulated higher cell viability than the other two, while 1605 fiber exerted a cell viability enhancement earlier (24 hrs.) than the other three (36 hrs.). The inset plot specifically showed the comparison of three fibers with dynamic control, where significant increases of cell viability (25 – 30%) were observed with both borate-based fibers.

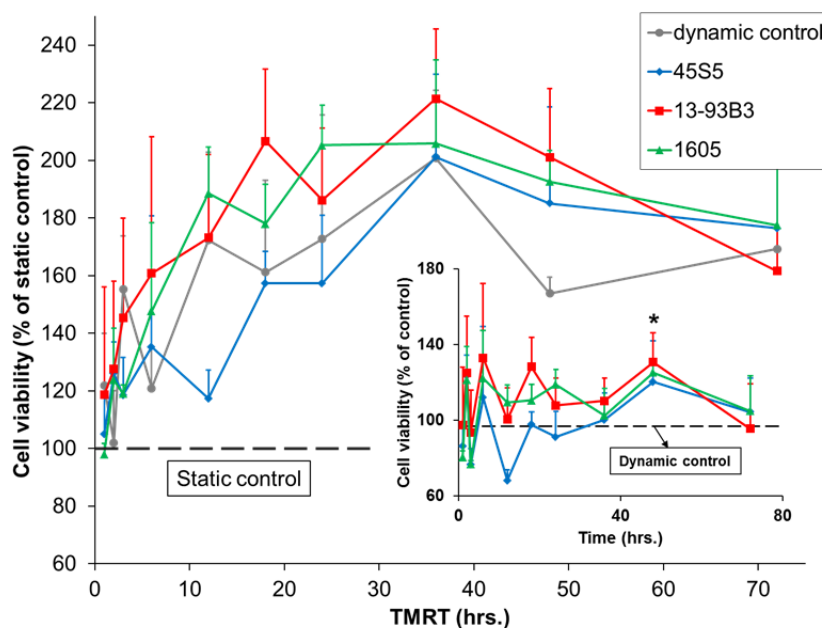


Fig. 11. WST-1 cell viability assay when cells co-cultured with 500 $\mu\text{g/mL}$ fresh fibers for 72 hours under dynamic mode. The x-axis in unit of hours is designated as the total medium replacement time (TMRT) of the chamber during dynamic flow. Data was firstly normalized to the static control data, and secondly to the dynamic control data (inset plot). Each data points represent mean + SD, $n \geq 3$. * $p < 0.05$ vs. dynamic control.

3.8. Impact of borate-based 1605 fibers on cell morphology and migration

The impact of bioactive fibers on cell migration ability was further evaluated on a well-defined cell-culture based “wound” model, where a “wound” gap was created through scraping across the diameter of a cell monolayer. Cell migration rate was recorded for at most 96 hours within an effective distance ($\pm 50 \mu\text{m}$) along a fiber-containing bridge under static mode, and the results are shown in Fig 12. Impaired wound closure ability was observed in cell groups that treated by each type of fibers and compared with control. Cells between the “wound” gap are then expected to proliferate to fill in the “wound” area with assistance of the fiber-attached bridge. Cell proliferation distance (migration rate) was measured to calculate influence to cell migration due to the

bioactive fiber bridge. However, cells that close to the bridge ($\pm 5 \mu\text{m}$) were not counted in to avoid false conclusion due to cell-fiber direct contact. Substantially lower recovery rates were observed with borate-based fibers, and even enlarged “wound” gaps were observed with fiber 1605. For comparison purpose, we further specifically evaluated the stimulating effect of fiber 1605 on cell migration under dynamic mode (24 hours medium replacing time) as shown in the inset plot of Fig. 12. Healthier cellular mobility was observed and thus indicating an improved stimulating effect from fiber 1605 under dynamic mode.

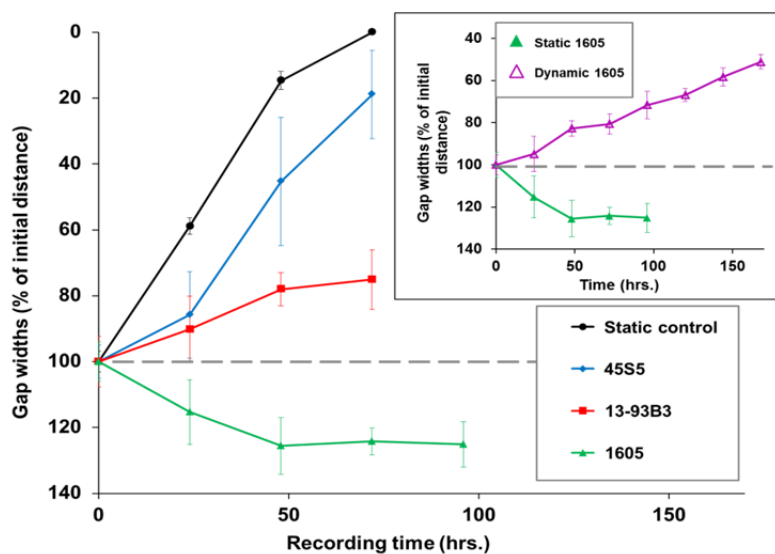


Fig. 12. Bioactive fiber influenced cell migration statistics under static/dynamic (inset) modes. Each data points represent mean \pm SD, $n \geq 10$ measurements.

Finally, a brief investigation has also been done focusing on the impact of such changed environment onto sub-cellular level infrastructure and behavior. Cell nucleus were pre-stained with DAPI followed by staining with a mitochondrial specific

fluorescent dye 5,5',6,6'-tetrachloro-1,1',3,3'-tetraethylbenzimidazolylcarbocyanine iodide (JC-1) and a 72-hour co-culturing with 200 $\mu\text{g}/\text{mL}$ borate-based 1605 fibers under dynamic mode. High resolution cell images were taken by using Nikon Eclipse Ti confocal microscope (Fig. 13a). Three channels (DAPI, FITC and Cy5) of fluorescent images were captured, and subcellular structures were compared between 1605 fiber treated or non-treated cells. 10% higher cell number was confirmed in 1605 fiber treated group than control, while no statistical differences were shown in terms of morphological changes and chromosome condensation. An averaged ratio of fluorescence intensity of Cy5/FITC channels in the cytoplasmic region of both control (Fig. 13b) and 1605 (Fig. 13c) fiber treated cells showed slightly, while not significantly, higher percentage (Fig. 13d) of mitochondrial membrane depolarization in borate 1605 fiber treated (0.533) than the control cells (0.701), indicating a moderately decreased mitochondrial activity level when the borate-based fiber 1605 was used.

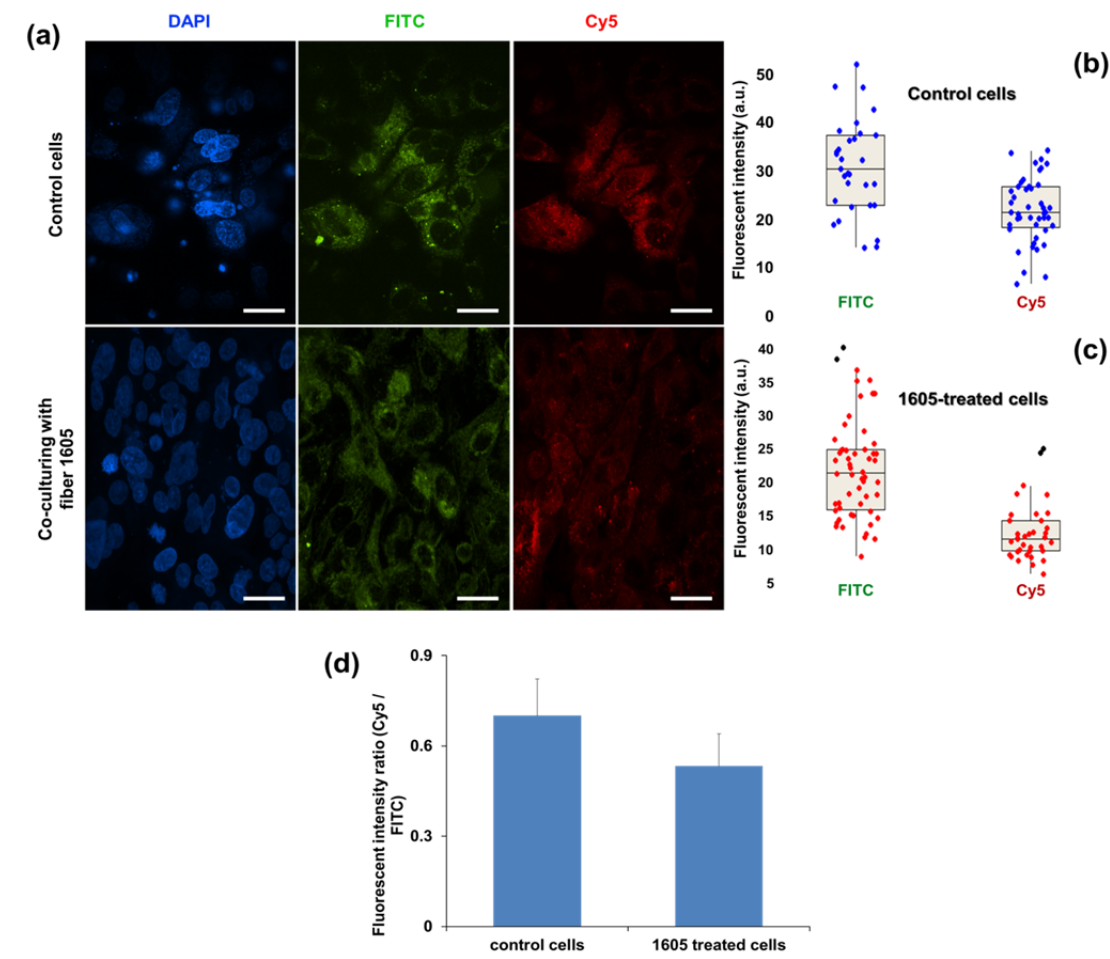


Fig. 13. Confocal microscopic images (a) and statistical analysis (b - d) of nucleus and mitochondrial staining of control and 1605 fiber co-cultured cells after a 72-hour dynamic mode treatment. Scale bar: 10 μm .

4. Discussion

A systematic degradation assay of three bioactive glass fibers was investigated *in vitro*. Scanning Electronic Microscopic imaging showed changed surface morphology in all fibers after five days immersion in serum free cell culture medium. Drastic changes occurred both outside and inside these fibers during the immersion (Fig. 1 - 5). Under the dynamic mode, smoother and porous fiber surface was mostly observed and less delicate

nano-structures appeared on the outmost layer, indicating the role played by hydro-mechanical forces during the conversion process. Unprecedented view (Fig. 4) indicated how ion-exchange influences the fiber interior region even when no significant outer-surface variation was observed. Further, highly carbonized surface was particularly seen under dynamic mode (Fig. 6, S1), indicating a highly increased conversion rate of carbonate-substituted hydroxyapatite (c-HA).

Bioactive glass conversion is attributed to multiple reactions,^{4,5} including rapid ion exchange, condensation and polymerization of previously resulted silanol groups, and formation of silica-rich layer on surface. Further dissolution and reaction with calcium and phosphorous would lead to a type of amorphous calcium phosphate (ACP) layer and would be finalized as crystallized HA.^{44,45} Borate-based glasses go through a similar process while without the formation of silica-rich layer which would slow down the crystallization of ACP layer on borate-based fibers.⁴⁶ ACP is prone to be substituted by cations and anions such as CO_3^{2-} , Mg^{2+} and $(\text{P}_2\text{O}_7)^{4-}$ even in small concentrations.⁴⁷ The presence of magnesium ions has also been reported to reduce the crystallization rate of HA product on 45S5 glass⁴⁸ and high content of magnesium ion concentration could even prevent formation of HA. EDS analysis results showed that a higher percentage of localized magnesium (normalized to the calcium concentration) was determined on fiber surface, and even higher percentages were determined under the dynamic conditions (Fig. 6, S1), thus a less concentrated Mg^{2+} could be contained in the medium so that a more efficient HA formation process would be expected.

Degradation of bioactive glass fibers and their conversion to HA is a rapid process that the major process will only take about 3 – 7 days.⁴⁶ Similar phenomenon was

observed in this study when under static condition. Particularly, the degradation of bioactive silicate or borosilicate glass materials would be slower than borate-based ones. However, the silicate 45S5 fiber showed much quicker releasing rate of calcium under dynamic conditions which even close to the rate of borate-based ones. This could attribute to faster ion exchange reactions between the network-modifying ions in the fiber (such as calcium and sodium ions) with hydrogen ions within the medium, thus supported the formation of a silica-rich layer on fiber surface in early stage.⁴⁹ The ICP-OES results indicated that a rapid elemental releasing process occurred during early stage of immersion, which turned out to be even faster under dynamic mode that mostly occurred within the first 10 hours. Phosphorous showed slow or rapid depletion patterns, under static and dynamic conditions, respectively. This phenomenon also indicate that a faster HA layer formation rate would be expected under dynamic mode. Such rapid releasing pattern may happen *in vivo* as well under a constant body fluid circulating system, thus future bioactive evaluation of these materials need more representative model for both *in vitro* and *in vivo* trials. The pH variation of the fiber-immersed medium is another practical concern during the HA formation process, because dissolution and consumption of sodium, boron, silica and phosphorous will highly influence the pH of the medium. A pH increase would be expected under static mode for the formation of weak acids (B(OH)₃, Si(OH)₄, etc.) as well as consumption of PO₄³⁻ ions.⁶ Accordingly, due to the increased boron content in borate-based fibers and faster ion releasing and elemental conversion (Fig. 7), steeper increase of pH would be expected within shorter period. While under the dynamic mode, despite of a faster ion releasing rate, relatively lower

boron (about 9 folds lower) and calcium (about 3-6 folds lower) concentrations were seen. In this case, system pH will not be influenced significantly.

Wound healing is a dynamic interaction process which includes soluble mediators, blood cells, extracellular matrix and parenchymal cells, etc..⁴⁰ The proliferative phase, that marked by fibroblasts proliferation, accumulation and granulation tissue formation,⁵⁰ is the key procedure for tissue formation and wound closure. Our results showed that the cell viability is function of both fiber dosage and treatment time (Fig. 8, S2, 9). Overall, fiber dosage that less than 200 $\mu\text{g}/\text{mL}$ provided moderately better cell viability than the control or equivalent as control. Among which the silicate-based 45S5 fiber has a wider dosage range to positively stimulate cell proliferation (below 1000 $\mu\text{g}/\text{mL}$, Fig. 8), while the borate-based fibers can potentially stimulate higher cell viability (Fig. 10a) with appropriate pre-soaking procedures. Quantitative measurement showed that an optimized pre-soaking period could be acquired for higher cell proliferations. Meanwhile, it has also been found that a prerequisite partial conversion of the fibers would highly reduce the cytotoxicity, mainly due to the rapid refreshing rate of dissolved boron and calcium, as well as improved surface elemental deposition. On the contrary, cells that have been co-cultured with fiber-pre-soaked medium showed mostly impaired viability (Fig. 10b), which indicated complicated roles of converted fiber surface and released ions in supporting cell proliferation. We thus highly recommend that the chemical, mechanical, and physical properties of bioactive fibers should all be taken into consideration for better bio-compatible evaluation. Under dynamic mode, higher cell viabilities were observed in all fiber groups and dynamic control group when compared with the static control (Fig. 11).

In addition, borate-based fiber can potentially stimulate higher cell viabilities than silicate-based glass fibers as well as the dynamic control (Fig. 11, inset).

Negative impact on the cell migration under static mode was observed in all fiber-treated groups, while borate-based fibers rendered higher impairment effects than the silicate ones (Fig. 12). However, cell migration performances was shown being inverted under dynamic mode as seen in the 1605 fiber (most toxic one under static condition) co-cultured group (Fig. 12, inset), indicating a high sensitivity of cell migration ability to fibers co-culturing. Such impairment can potentially be reversed through a moderate dynamic medium refreshing rate. New tissue formation during continuous wound healing processes is characterized by both cell migration and proliferation of the keratinocytes and fibroblast cells. Our results suggest a possible tissue repairing mechanism with fiber's stimulating effects on both cell proliferation and migration abilities. A confocal microscopic imaging assay (Fig. 13), showed a relatively higher percentage of mitochondrial membrane depolarization, indicating a slightly decreased mitochondrial activity level in fiber 1605 treated cells under dynamic mode, which is a representative sign for migration ability impairment and rescue.

A reliable strategy to carry out *in vitro* wound-healing studies should be conducted in a highly simulated niche-environment that would reach to similar results as the *in vivo* study. There hasn't been enough attention putting into this research field until Brown and his colleagues' work,⁶ where they indicated that a moderate dynamic condition may improve cell density when compared with that under static condition. Our results in this study comprehensively illustrate the fundamental impact of dynamically controlled environment (in terms of total medium replacing time, namely, TMRT) on

fiber surface morphology (Fig. 1 - 5), elemental deposition (Fig. 6, S1), ion concentration (Fig. 7), cell viability (Fig. 10, 11) and migration ability (Fig. 12). Thus, a combined procedure of well-controlled dynamic flow and appropriate fiber pre-soaking would thus provide an optimal cell proliferation as well as cell migration capability.

It is suggested that closer attention should also be paid to the original composition of the fiber. In particular, calcium can also activate Ca-sensing receptors in specific cell types and thus increase growth factor expression,^{20,21} which is crucial for cell proliferation. Calcium is also needed for epidermal cell migration and regeneration in late stage of wound healing,⁵¹ thus it is essential to finely adjust calcium concentration and doping ratio for optimizing wound healing effect of bioactive glasses.⁵² In addition, unforeseen complicated effect of trace metal ions may play a key role in bioactive glasses as well. Trivial difference of the original composition (Table 1) between two borate fibers showed either minor or major variations during tests. Copper ion, that appeared in human endothelial cells, was deemed as one of the key stimulation factors,⁵³ and it was considered as synergetic stimulator for angiogenesis⁵⁴ when combined with angiogenic growth factor FGF-2.⁵⁵ Zinc ions also need be further investigated on its cellular effects because of the multiple intra- and extra-cellular roles that it may play,⁵⁶ e.g., anti-inflammatory effect, bone tissue formation stimulation, protein synthesis activation⁵⁷ as well as transcriptional-level regulation of differentiation-related genes,⁵⁸ and so on.

Finally, vascular endothelial growth factor (VEGF), as a potential therapy reagent for improving wound-healing, is confronting some major problems in its application such as high diffusion ability and very short half-life during *in vivo* delivery.^{59,60} Thus the

potential capability of bioactive glass fibers in inducing angiogenesis could potentially provide robust alternative choices for the troublesome growth factors.

5. Conclusion

The present study showed a comprehensive material analysis and biocompatibility evaluation of a silicate-based (45S5) and two borate-based (13-93B3 and 1605) nano-/micro-scale bioactive glass fibers. Results showed substantial glass-conversion occurred during fiber immersion. An active ion-exchanging process exist between medium and fibers (both inside and outside), which will be highly influenced by original boron content as well as static/dynamic flow. In this case, HA formation efficiency would be determined mainly by the rate of glass decomposition and dynamic flow. Evaluation on human skin cell line demonstrated that borate-based fibers, though more toxic than silicate-based glass fiber under static condition, can significantly stimulate cell growth with higher cell proliferation rate and migration ability when appropriate pre-soaking time and dynamic flow rate were acquired. Moreover, the trace amount doping of metal species within the glass composition, such as copper and zinc, are also potentially important in glass conversion, biocompatibility as well as bioactivity. These results provided qualitative and quantitative basis not only for the biocompatible mechanism study but also for better guidance of bioactive glass materials fabrication in the future.

Notes

The authors declare no competing financial interest.

Associated content

Appendix A. Supplementary data

A supplementary file is available free of charge on line.

Author information

Corresponding Author

*E-mail: yinfa@mst.edu. Tel: (1) 573-341-6220, Fax: 573-341-6033.

Acknowledgements

This project was supported by the Center for Biomedical Science and Engineering (CBSE) and Center for Single Nanoparticle, Single cell, and Single Molecule Monitoring (CS³M), at Missouri University of Science and Technology. The authors gratefully acknowledge Yongbo Dan and Kun Liu, in chemistry department at Missouri University of science and technology (MS&T), for their assistance on ICP-OES testing. We also thank Clarissa A. Wisner and Casey F. Burton in MS&T for their great help on SEM/EDS scanning and providing language help, respectively.

References

- (1) Hench, L. L.; Splinter, R. J.; Allen, W.; Greenlee, T. *Journal of Biomedical Materials Research* **1971**, *5*, 117-141.
- (2) Hench, L. L.; Wilson, J. *Science* **1984**, *226*, 630-636.
- (3) Hench, L. L. *Journal of the American Ceramic Society* **1991**, *74*, 1487-1510.

- (4) Rahaman, M. N.; Day, D. E.; Sonny Bal, B.; Fu, Q.; Jung, S. B.; Bonewald, L. F.; Tomsia, A. P. *Acta biomaterialia* **2011**, *7*, 2355-2373.
- (5) Hench, L. L. *Journal of Materials Science: Materials in Medicine* **2006**, *17*, 967-978.
- (6) Brown, R. F.; Rahaman, M. N.; Dwilewicz, A. B.; Huang, W.; Day, D. E.; Li, Y.; Bal, B. S. *Journal of Biomedical Materials Research Part A* **2009**, *88*, 392-400.
- (7) Day, D.; White, J.; Brown, R.; McMenamin, K. *Glass Technology-European Journal of Glass Science and Technology Part A* **2003**, *44*, 75-81.
- (8) Han, X.; Day, D. E. *Journal of Materials Science: Materials in Medicine* **2007**, *18*, 1837-1847.
- (9) Day, D. E.; Erbe, E. M.; Richard, M.; Wojcik, J. A.; Google Patents, 2004.
- (10) Ahmed, I.; Collins, C.; Lewis, M.; Olsen, I.; Knowles, J. *Biomaterials* **2004**, *25*, 3223-3232.
- (11) Huang, W.; Day, D. E.; Kittiratanapiboon, K.; Rahaman, M. N. *Journal of Materials Science: Materials in Medicine* **2006**, *17*, 583-596.
- (12) Yao, A.; Wang, D.; Huang, W.; Fu, Q.; Rahaman, M. N.; Day, D. E. *Journal of the American Ceramic Society* **2007**, *90*, 303-306.
- (13) Fu, Q.; Rahaman, M. N.; Fu, H.; Liu, X. *Journal of Biomedical Materials Research Part A* **2010**, *95*, 164-171.
- (14) Jung, S. B. *Bio-Glasses: An Introduction* **2012**, 75-95.
- (15) Carlisle, E. M. *Calcified tissue international* **1981**, *33*, 27-34.
- (16) Carlisle, E. M. *Science* **1970**, *167*, 279-280.
- (17) Reffitt, D.; Ogston, N.; Jugdaohsingh, R.; Cheung, H.; Evans, B.; Thompson, R.; Powell, J.; Hampson, G. *Bone* **2003**, *32*, 127-135.
- (18) Hinoi, E.; Takarada, T.; Yoneda, Y. *Journal of pharmacological sciences* **2004**, *94*, 215-220.
- (19) Maeno, S.; Niki, Y.; Matsumoto, H.; Morioka, H.; Yatabe, T.; Funayama, A.; Toyama, Y.; Taguchi, T.; Tanaka, J. *Biomaterials* **2005**, *26*, 4847-4855.
- (20) Marie, P. J. *Bone* **2010**, *46*, 571-576.

- (21) Valerio, P.; Pereira, M.; Goes, A.; Leite, M. F. *Biomedical Materials* **2009**, *4*, 045011.
- (22) Julien, M.; Khoshniat, S.; Lacreusette, A.; Gatius, M.; Bozec, A.; Wagner, E. F.; Wittrant, Y.; Masson, M.; Weiss, P.; Beck, L. *Journal of Bone and Mineral Research* **2009**, *24*, 1856-1868.
- (23) Hartwig, A. *Mutation Research/Fundamental and Molecular Mechanisms of Mutagenesis* **2001**, *475*, 113-121.
- (24) Rude, R. K.; Gruber, H. E.; Norton, H. J.; Wei, L. Y.; Frausto, A.; Kilburn, J. *Bone* **2005**, *37*, 211-219.
- (25) Rude, R.; Gruber, H.; Wei, L.; Frausto, A.; Mills, B. *Calcified tissue international* **2003**, *72*, 32-41.
- (26) Staiger, M. P.; Pietak, A. M.; Huadmai, J.; Dias, G. *Biomaterials* **2006**, *27*, 1728-1734.
- (27) Tsuboi, S.; Nakagaki, H.; Ishiguro, K.; Kondo, K.; Mukai, M.; Robinson, C.; Weatherell, J. *Calcified tissue international* **1994**, *54*, 34-37.
- (28) Zreiqat, H.; Howlett, C.; Zannettino, A.; Evans, P.; Schulze-Tanzil, G.; Knabe, C.; Shakibaei, M. *Journal of Biomedical Materials Research* **2002**, *62*, 175-184.
- (29) Choi, M.; Kim, M.; Kang, M. *Food Science and Biotechnology* **2005**, *14*.
- (30) Uysal, T.; Ustdal, A.; Sonmez, M. F.; Ozturk, F. *The Angle Orthodontist* **2009**, *79*, 984-990.
- (31) Saltman, P. D.; Strause, L. G. *Journal of the American College of Nutrition* **1993**, *12*, 384-389.
- (32) Beattie, J. H.; Avenell, A. *Nutrition research reviews* **1992**, *5*, 167-188.
- (33) Nielsen, F. H. *Biological trace element research* **1990**, *26*, 599-611.
- (34) Sun, Z. L.; Wataha, J. C.; Hanks, C. T. **1997**.
- (35) Day, R. M. *Tissue engineering* **2005**, *11*, 768-777.
- (36) Day, R. M.; Boccaccini, A. R.; Shurey, S.; Roether, J. A.; Forbes, A.; Hench, L. L.; Gabe, S. M. *Biomaterials* **2004**, *25*, 5857-5866.
- (37) Keshaw, H.; Forbes, A.; Day, R. M. *Biomaterials* **2005**, *26*, 4171-4179.

- (38) Gorustovich, A. A.; Roether, J. A.; Boccaccini, A. R. *Tissue Engineering Part B: Reviews* **2009**, *16*, 199-207.
- (39) Liu, X.; Rahaman, M. N.; Day, D. E. *Journal of Materials Science: Materials in Medicine* **2013**, *24*, 583-595.
- (40) Lin, C.; Mao, C.; Zhang, J.; Li, Y.; Chen, X. *Biomedical Materials* **2012**, *7*, 045017.
- (41) Huang, W.; Rahaman, M. N.; Day, D. E.; Li, Y. *Physics and Chemistry of Glasses-European Journal of Glass Science and Technology Part B* **2006**, *47*, 647-658.
- (42) Liu, X.; Huang, W.; Fu, H.; Yao, A.; Wang, D.; Pan, H.; Lu, W. W.; Jiang, X.; Zhang, X. *Journal of Materials Science: Materials in Medicine* **2009**, *20*, 1237-1243.
- (43) Fu, H.; Fu, Q.; Zhou, N.; Huang, W.; Rahaman, M. N.; Wang, D.; Liu, X. *Materials Science and Engineering: C* **2009**, *29*, 2275-2281.
- (44) Pereira, M. M.; Clark, A. E.; Hench, L. L. *Journal of the American Ceramic Society* **1995**, *78*, 2463-2468.
- (45) Hayakawa, S.; Tsuru, K.; Ohtsuki, C.; Osaka, A. *Journal of the American Ceramic Society* **1999**, *82*, 2155-2160.
- (46) Liu, X.; Rahaman, M. N.; Day, D. E. *Journal of Materials Science: Materials in Medicine* **2013**, 1-13.
- (47) Dorozhkin, S. V. *Acta biomaterialia* **2010**, *6*, 4457-4475.
- (48) Filgueiras, M. R.; La Torre, G.; Hench, L. L. *Journal of biomedical materials research* **1993**, *27*, 445-453.
- (49) Bunker, B. *Journal of Non-Crystalline Solids* **1994**, *179*, 300-308.
- (50) Singer, A. J.; Clark, R. *N Engl J Med* **1999**, *341*, 738-746.
- (51) Lansdown, A. B. *Wound Repair and Regeneration* **2002**, *10*, 271-285.
- (52) Barnett, S.; Varley, S. *Annals of the Royal College of Surgeons of England* **1987**, *69*, 153.
- (53) Hu, G. f. *Journal of cellular biochemistry* **1998**, *69*, 326-335.
- (54) Finney, L.; Vogt, S.; Fukai, T.; Glesne, D. *Clinical and Experimental Pharmacology and Physiology* **2009**, *36*, 88-94.

- (55) Gérard, C.; Bordeleau, L.-J.; Barralet, J.; Doillon, C. J. *Biomaterials* **2010**, *31*, 824-831.
- (56) Courthéoux, L.; Lao, J.; Nedelec, J.-M.; Jallot, E. *The Journal of Physical Chemistry C* **2008**, *112*, 13663-13667.
- (57) Yamaguchi, M. *The Journal of Trace Elements in Experimental Medicine* **1998**, *11*, 119-135.
- (58) Kwun, I.-S.; Cho, Y.-E.; Lomeda, R.-A. R.; Shin, H.-I.; Choi, J.-Y.; Kang, Y.-H.; Beattie, J. H. *Bone* **2010**, *46*, 732-741.
- (59) Bennett, S.; Griffiths, G.; Schor, A.; Leese, G.; Schor, S. *British journal of surgery* **2003**, *90*, 133-146.
- (60) Goldman, R. *Advances in skin & wound care* **2004**, *17*, 24-35.

IV. Reflection-mode micro-spherical fiber-optic probes for *in vitro* real-time and single-cell level pH sensing

Qingbo Yang^{a,b}, Hanzheng Wang^c, Xinwei Lan^c, Baokai Cheng^c, Sisi Chen^{a,b}, Honglan Shi^{a,b}, Hai Xiao^c, Yinfa Ma^{a,b,*}

^aDepartment of Chemistry, Missouri University of Science and Technology, Rolla, MO 65409, USA

^bEnvironmental Research Center, Missouri University of Science and Technology, Rolla, MO 65409, USA

^cDepartment of Electrical and Computer Engineering, Clemson University, Clemson, SC 29634, USA

ABSTRACT

pH sensing at the single-cell level without negatively affecting living cells remains an important issue facing biomedical studies. A 70 μm reflection-mode fiber-optic micro-pH sensor is designed and fabricated by dip-coating thin layer of organically modified aerogel onto the tapered spherical probe head. A pH sensitive fluorescent dye 2', 7'-Bis(2-carbonylethyl)-5(6)-carboxyfluorescein (BCECF) was employed and covalently bonded within the aerogel networks. By tuning the alkoxides mixing ratio and adjusting hexamethyldisilazane (HMDS) priming procedure, the sensor can be optimized to have high stability and pH sensing ability. The *in vitro* real-time sensing capability was then demonstrated in a simple colorimetric way, and shows linear measurement responses with a pH resolution up to 0.049 pH unit within a narrow, but biological meaningful pH range of 6.12 – 7.81.

Keywords: pH sensing, tapered optical fiber spherical sensor, ORMOSILs ultra-thin layer coating, single-cell level detection.

Highlights

A 70 μm reflection mode fiber-optic micro-pH sensor was fabricated;

Spherical-headed probe shows high pH detecting spatial resolution;

ORMOSILs thin layer for covalent bonding with pH sensitive dye was employed;

This probe shows superior real-time pH sensing ability and repeatability;

A pH resolution up to 0.049 per pH unit was acquired within pH range of 6.12 – 7.81.

Abbreviations

BCECF: 2', 7'-Bis (2-carbonylethyl)-5(6)-carboxyfluorescein;

CTAB: hexadecyltrimethylammonium bromide;

DIAMO: n-(3-(trimethoxysilyl) propyl)-ethylenediamine;

DMSO: Dimethyl sulfoxide;

EDS: energy-dispersive X-ray spectroscopy;

FL: fluorescent;

FT-IR: fourier transform infrared spectroscopy;

FWHM: full width at half maximum;

HMDS: hexamethyldisilazane;

HMDS: hexamethyldisilazane;

HMDSO: hexamethyldisiloxane;

Hünigs base: *N*-ethyl-diisopropylamine;

MTES: methyltriethoxysilane;

ORMOSILs: ORganically MODified SILicates;

PBS: phosphate buffer solution;

S/N: signal-to-noise ratio;

SDS: Sodium dodecyl sulfate;

SEM/FIBs: scanning electronic microscope/focused ion beams;

TEOS: tetraethoxysilane;

TGA: thermal gravimetric analysis;

TMCS: trimethylchlorosilane;

TSTU: 2-succinimido-1, 1, 3, 3 tetramethyluronium tetrafluoroborate.

1. Introduction

Localized, real-time sensing of extra- or intra-cellular pH remains a pressing issue for the optical sensing research field [1-5]. Intracellular pH indicator has been greatly developed in recent years[6, 7] with higher signal-to-noise ratio (S/N), long term stability and specific capability of subcellular localization[8]. However, all these dye based pH sensing products can hardly get out of the cell or be properly degraded by cells once applied, which makes it almost impossible to maintain a long-term investigation of a representative cell condition without intervene, plus leaves a potentially carcinogenesis risk for either *in vitro* and/or *in vivo* application. Moreover, the necessity of equipment with high quality inverted microscopic device such as confocal system would further prevent such labelling techniques from being readily used for real-time and/or remote monitoring of the pH variation on a target system, and thus highly limited their application potentiality.

Sol-gel derived materials have been widely used in optical sensing areas [9-11]. The relatively fast and easy steps in either acidic or basic catalysis of alkoxides under room temperature, combined with multiple choices of lately introduced[12, 13] ORganically MOdified SILicates (ORMOSILs) in sol-gel formula provide very good optical transparency, stability, adjustable hydrophobicity and porosity[14-19], which made it easy to impart desired chemicals or properties in sensor fabrication. Thus, the introduction and entrapment of a specific sensing material into it would then be the key issue[20]. A vast majority of sol-gel based pH sensor are derived from tetraethoxysilane (TEOS) based aerogel but mostly suffer from long response time and limited long-term

stability [21-23]. Later development focused on covalent immobilization of the indicator molecules[24-26] and surface hydrophobicity modification with reagents with organic end-groups such as trimethylchlorosilane (TMCS), methyltriethoxysilane (MTES) or hexamethyldisiloxane (HMDSO), lead to appropriate replacement of $-OH$ with $-CH_3$ [27, 28], and thus a better performance was achieved with improved reproducibility, shorter response time and enhanced chemical stability. Surfactants such as Sodium dodecyl sulfate (SDS) and hexadecyltrimethylammonium bromide (CTAB) have also been introduced in recent years to form mesoporous structure of silica matrix to obtain efficient host of the sensing molecules[29, 30]. Together, initiation of these ORMOSILs-based sol-gel thin films appeared to be a promising structure in developing compact micro- or nano-scale sensing probes, which can well be integrated with many types of lab-on-chip-based devices[20, 31, 32].

The ORMOSILs based aerogel thin layer coating can be well fit fiber with fiber optic devices in small or remote sample sensing. Ultra-thin layer sol-gel could directly be dip-coated onto the end face of either as-synthesized or surface modified optical fiber probes. Sub-micron thickness pH sensing films have been developed on platforms like microfluidic device [33-35], and fiber-optics based pH sensor has appeared as well in recent years [36-38]. However, most of the reported devices were operated in relatively large scale (hundred micrometers to centimeter level), and could not provide sufficient spatial resolution, pH detection sensitivity or real-time monitoring ability. Other problems, such as fabrication difficulties, high cost and relatively poor repeatability and reproducibility, etc., were also seen in previous fiber-optic based pH sensors.

In this study, a reflection mode tapered fiber-optic pH probe was fabricated by carbon dioxide (CO₂) laser stretching system combined with fusion splicer device, and was functionalized by amide covalently bonding of a pH specific dye BCECF within a sol-gel dip-coated ultra-thin layer on a specific spherical probing head. The surface hydrophobicity has been modified and evaluated. The newly fabricated probes have been investigated *in vitro* with high spatial and pH resolutions as a real-time detecting manner, the reflection mode operation of the probe combined with fiber-optic remote sensing capability, provide promising way of chemical/biological sensing in many research and application fields, especially in cases of both *in vitro* and *in vivo* single-cell level non-invasive remote detecting applications.

2. Experiments

The spherical-headed tapered fiber-optic pH probe was fabricated from a single mode optical fiber (Corning SMF-28, USA) by using a homemade CO₂ laser fiber-stretching system combined with optical fiber fusion splicer (Fujikura, Japan). A sol-gel dip-coating method was employed in this study to form an ultra-thin aerogel layer onto the probe head surface, covalently bond with molecules of a specific pH-sensitive fluorescent dye 2', 7'-Bis (2-carbonylethyl)-5(6)-carboxyfluorescein (BCECF) (Life technologies, New York) through amide bonds (Fig. 1, 2).

A homemade CO₂ laser fiber-stretching system was employed to programmably control the taper length and waist diameter. Normally a length of 1.3 ± 0.2 cm "V" shape tapered optical fiber tip was firstly acquired with a waist diameter of around 50 ± 8 μm and tip size around 2 – 5 μm . A spherical head was specifically designed for maximizing

the contacting surface as well as signal reflection. It was fabricated using a distance-melting method on a fusion splicer device with a final diameter of around $70 \pm 10 \mu\text{m}$.

For ultrathin aerogel coating and BCECF dye covalent bonding, the silanol groups on the surface of the spherical probing head were activated through treatments with a) concentrated nitric acid for 12 hours and b) copious amounts of distilled water and ethanol, followed by drying at 100°C for 3 hours. Fluorescent dye BCECF (1 mg/mL) in Dimethyl sulfoxide (DMSO) was added with excess molar amount of 2-succinimido-1, 1, 3, 3 tetramethyluronium tetrafluoroborate (TSTU) that pre-dissolved in ethanol and small amount of *N*-ethyl-diisopropylamine (Hünigs base), and stir for 10 minutes. Let the reaction proceed for one hour at room temperature. Then the amino-functionalized *n*-(3-(trimethoxysilyl) propyl)-ethylenediamine (DIAMO) in ethanol was added into the succinimidyl-ester activated dye solution (BCECF: DIAMO = 1:10). Stir it for 10 min to generate amide bonds between dye and DIAMO. Then a mixture of alkoxides, which include tetraethoxysilane (TEOS), DIAMO and methyltrimethoxysilane (MTES) dissolved in methanol (TEOS:DIAMO:MTES = 4:1:1, v/v) and hydrochloric acid (0.1M), were combined with the BCECF - DIAMO - ethanol solution at a v/v ratio of 5:3 and magnetically stirred for 30 minutes, followed by stewing at room temperature in closed vial for 12 hours. Pre-heated tapered probe head were then cooled and dip-coated with the sol-gel solution with a drawing rate of 1 mm/s. Curing process was divided into two steps for gradual heating. Dip-coated probes were set in 50°C for 6 hours and then in 80°C for 24 hours. A surface hydrophobicity modification was finally carried out with a homemade hexamethyldisilazane (HMDS) priming chamber. A 100°C priming temperature was acquired in vacuum and an optimized 3 hours priming time was

employed in this study. All BCECF dye related procedure was done in dark condition. Chemicals were purchased from Sigma-Aldrich (St. Louis, Missouri) unless otherwise specified.

The whole probe head area that coated with dye doped aerogel was observed under inverted fluorescent microscope (Fig. 1). Both in-general and zoom-in view of the aerogel coated surface were shown in Fig. 1(a, b), characterized a uniform mesoporous network with protrude nano-scale sensing tails. Correspondingly, the energy-dispersive X-ray spectroscopy (EDS) scanning shows typical peaks of carbon, oxygen and silica within the aerogel surface, which represented successful fabrication of the dye-doped ORMOSILs thin layer onto the probe endface with uniform distribution (Fig. 1(c, d)). Further investigation of the aerogel layer thickness was also done through cross-section cutting by using a focused ion beam system (SEM/FIBs) (FEI, Hillsboro, Oregon) of the coated probe head as shown in Fig. 1(e) acquired an averaged coating layer thickness of ~400 nm.

A sol-gel thin layer coating as well as BCECF dye covalent bonding principle is shown in Figure 2(a). Together a brief schematic diagram of the optical setup combined with probe head image is also shown in Figure 2(b - d). The pH probe was excited using a solid-state 488 nm laser source to obtain the best excitation wavelength of the BCECF dye molecules. Laser intensity has been adjusted to acquire an optimized fluorescent signal while eliminating dye molecule photo bleaching. A colorimetric method was employed to acquire a normalized fluorescent signal ratio between the peak intensity (560 \pm 5 nm) and a constant irrelevant background at 640 nm. A USB2000 spectrometer (Ocean optics, Dunedin, Florida) was also used to collect sufficient reflected fluorescent

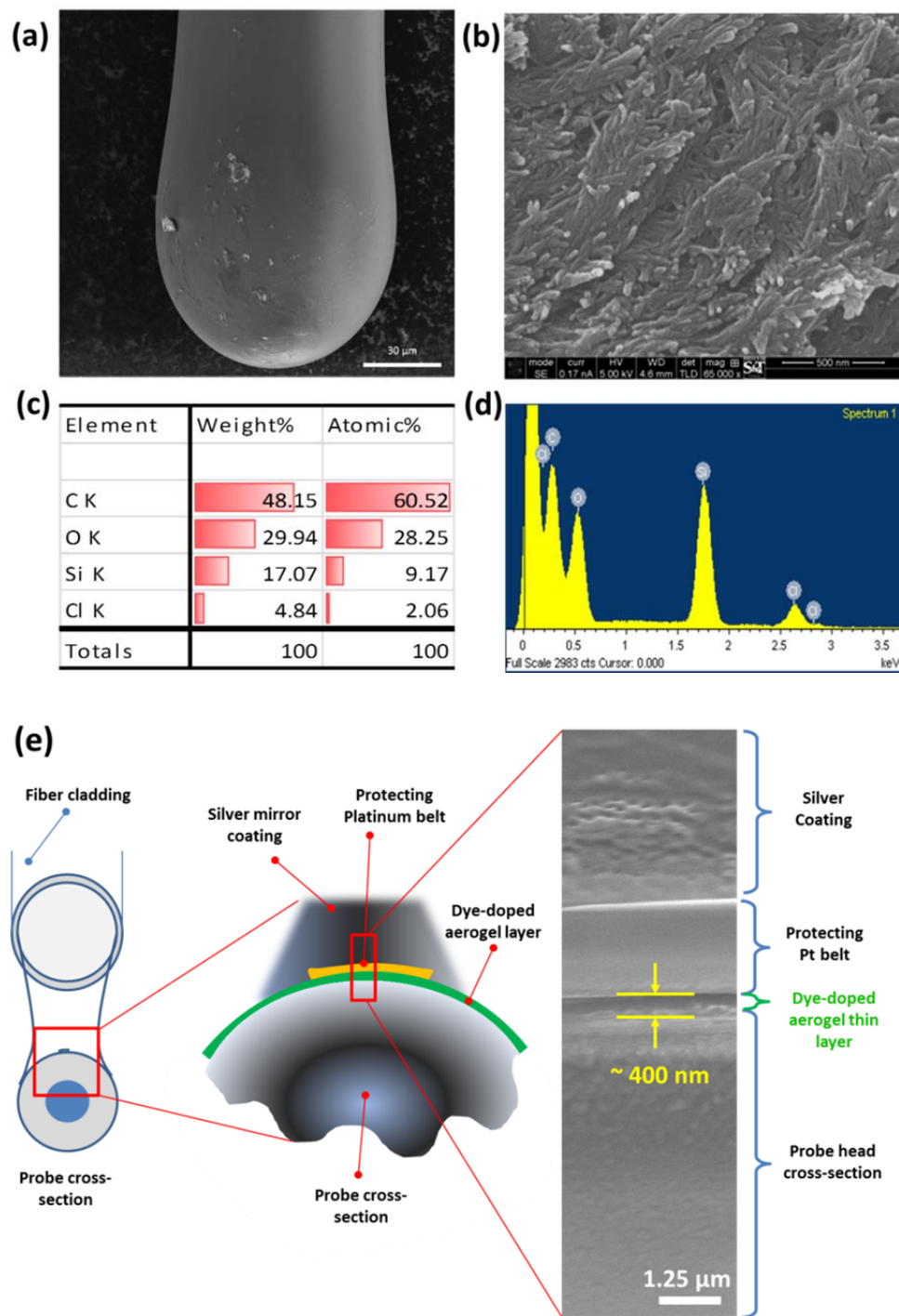


Fig. 1 SEM images and EDS characterization of fabricated spherical head fiber-optic pH probe. Overview of the pH sensor probe structure was shown in low (a) and high (b) magnification. Probe surface elemental characterization of carbon, oxygen, silica and chlorine was done by EDS scanning and showed both in chart (c) and energy distribution plot (d). Scale bar showed in SEM images are 30 μm (a) and 500 nm (b).

signals. In order to acquire a remote sensing capability as well as label free detection under real circumstance, a reflection based sensing method has been proposed and used in this study as the configuration shown in Fig. 2(d). During spectrum measurement, fabricated probe was backward fuse-connected with the sensor branch SMF optical fiber cleaved end, so that the using and changing of different probes did not influence the connector and detector interfaces during measurement.

3. Results and discussions

An aerogel based pH sensing ultra-thin film has been fabricated and its fluorescent spectrum is shown in Fig. 3. A bathochromic shift of the fluorescent peak up to 560 nm was observed when compared with the original 535 nm emission peak of BCECF dye in solution. This may due to an increased dielectric constant compared to a solution environment, and thus a changed polarity of the microenvironment of the dye molecules after covalent bonding with the aerogel macromolecule network[25]. A series of 0.1M PBS buffer solutions after pH calibration were freshly prepared probe calibration. Similar with original dye molecule, the probe responds to pH values as a function of peak intensity change, while maintained a relatively constant peak wavelength. This intensity change closely correlates with the probing sensitivity and resolution, and theoretically it can be influenced by testing time and surface property, due to a kinetic saturation rate of the aerogel thin film.

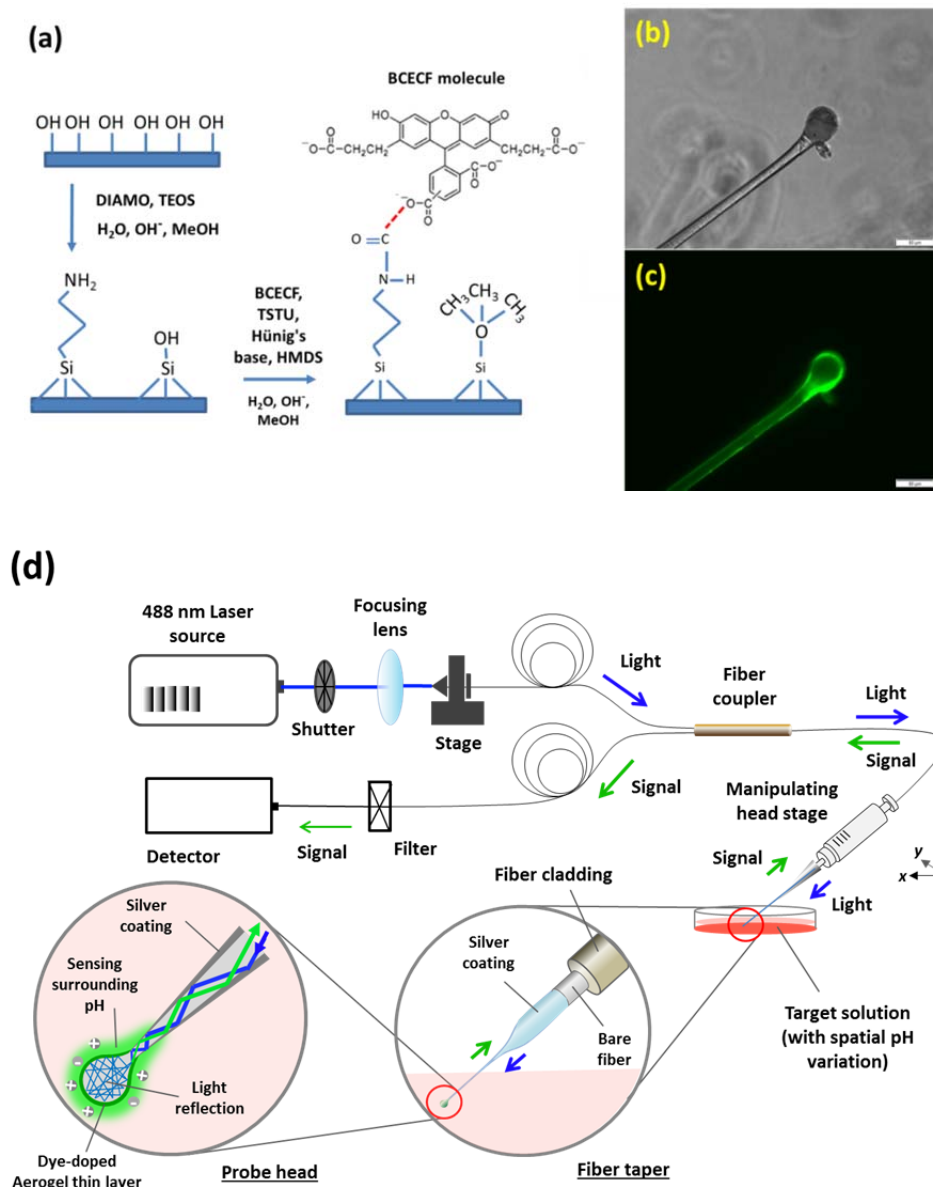


Fig. 2 Configuration and microscopic images of BCECF dye covalent-bonded aerogel thin-layer on probing head with schematic diagram of whole system setup. (a) Brief configuration of BCECF dye molecules covalently bond onto the ultrathin ORMOSILs network thin-layer, followed by HMDS priming for hydrophobicity modification; Tapered spherical head pH probe images under inverted fluorescent microscope with (b) white light and (c) 488 nm (FITC channel) illumination; and (d) Schematic diagram of the optical spectrum measurement setup.

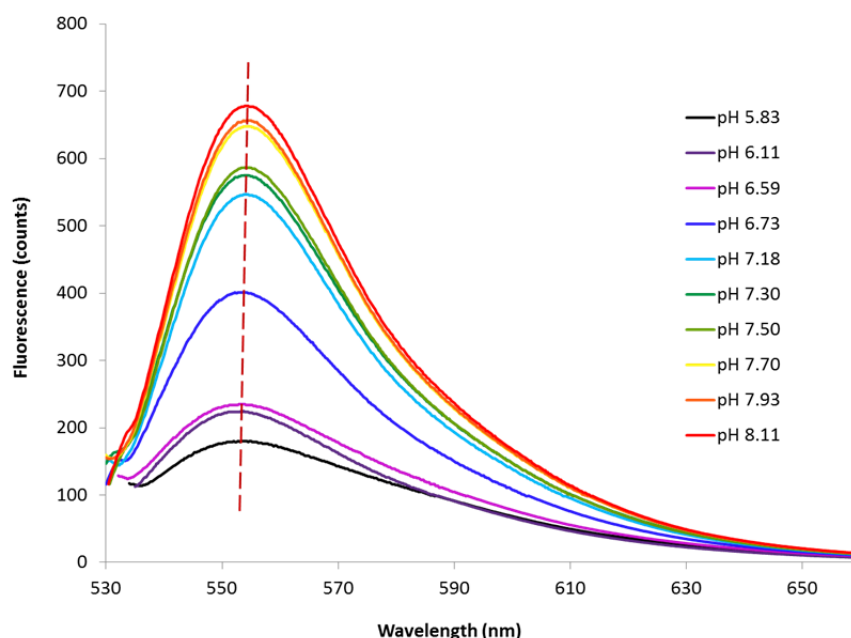


Fig. 3 Reflection spectrum (fluorescent emission) from a pH sensitive thin film covered by BCECF dye doped ORMOSILs ultrathin layer.

The pH sensing capability of the dye doped aerogel thin film is closely correlated with dye concentration and surface properties. Higher dye concentrations are assumed to boost increased signal intensity, however, a large excess of the dye would induce enhanced self-quenching as well as possible leaching of unbound dye molecules. Aerogel surface hydrophobicity is another key factor determining pH sensing capability of the probe. Because of abundant $-OH$ and $-NH_2$ groups stretching out, TEOS/DIAMO derived aerogel thin layer without further hydrophobic modification is vulnerable to water based solution, even when pH values were around neutral conditions. Whereas an appropriate mixing of MTES and an extra HMDS priming process would highly reduce the risk, due to the compensation of sufficient methylsilyl or trimethylsilyl groups.

A thermal gravimetric analysis (TGA) (Q50, TA instruments, New Castle, Delaware) was shown carried out then, for the ORMOSILs thin layer under nitrogen atmosphere with different surface modification (Fig. 4(a)). First main weight loss (0.2% in blue, 0.38% in red and 0.46% in green) around 70-160°C is attributed to evaporation of residual solvent and water molecules adsorbed by exposed OH groups. With BCECF dye doped in the sol-gel formula, about 0.25% more weight loss downfall was observed through comparison between the blue and green lines, indicating a successful immobilization of the dye molecules. It is notably that there was not a significant weight loss at temperature less than 200°C indicates a high degree of silanol poly-condensation in the sensor material[39, 40]. The second weight loss (1.62% in blue, 1.37% in red and 1.64%) at 300-600°C was believed to be attributed to the combustion of organic species, and the wide range of degradation line was due to the pore size distribution[41]. Further, these enhanced mesoporous silica networks is highly due to the introduction of SDS for its ability to host sensing molecules more efficiently[42].

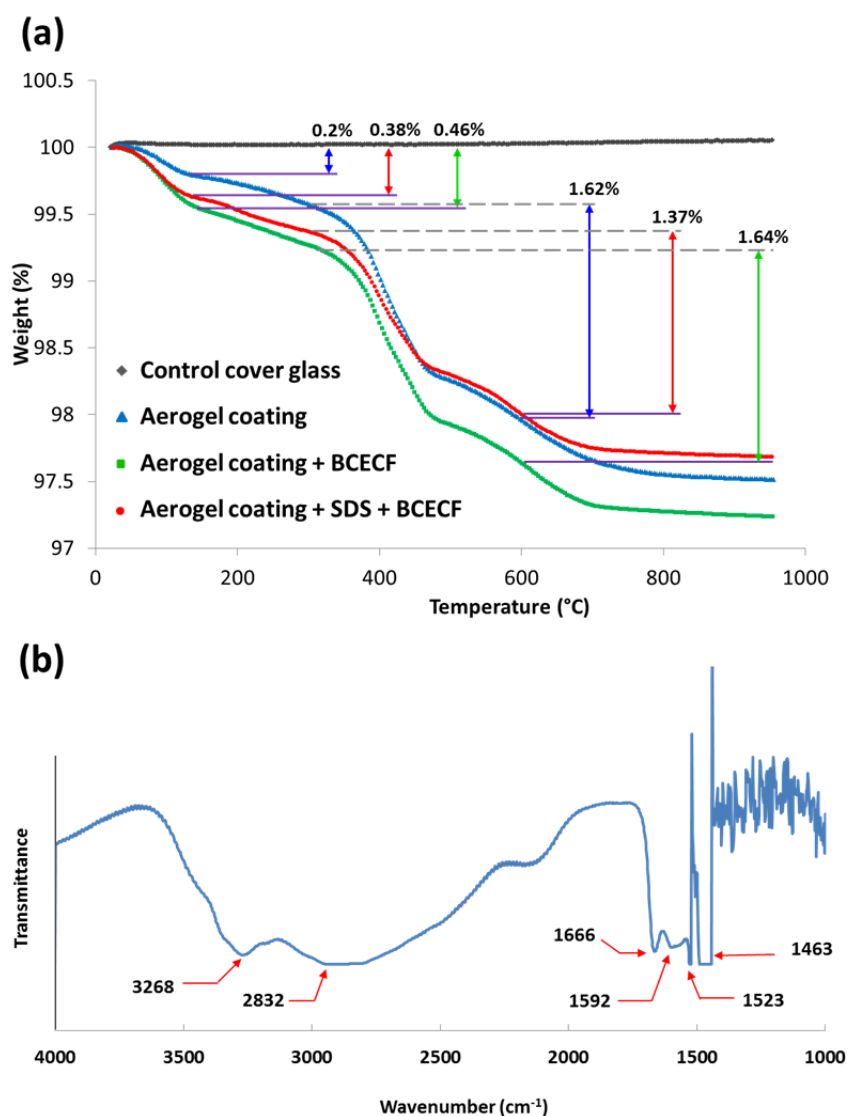


Fig. 4 Chemical characterization of optimized fabrication procedure of the ultrathin BCECF dye doped ORMOSILs layer by (a) TGA and (b) FT-IR.

The FT-IR spectrum of optimized representative sample is shown in Fig. 4(b). A characteristic feature of the spectrum is the presence of CH₂ related aliphatic chains of TEOS, MTES and DIAMO, indicated by a broad band in the region of 2882-2937 cm⁻¹, which is attributed to stretching modes of CH₂ and partially CH₃ groups. A wide band covers the region from 3100 to 3600 cm⁻¹ arises from the stretching OH mode of the

physically adsorbed water and/or residual silanol groups[43]. The representative primary amino groups that exist in DIAMO to form amide bond also showed characteristic peaks between $3500\text{-}3300\text{ cm}^{-1}$ as well as $1650\text{-}1550\text{ cm}^{-1}$ [25]. Despite peaks are mostly overlapped by other peaks, a peak at 1592 cm^{-1} explicitly shows the presence of primary amino groups[25]. Moreover, the containing of carboxylates or amino acid zwitterion was also proved as a C=O stretching at $1550\text{-}1610\text{ cm}^{-1}$ region.

In addition, ionic strength can influence the protonation/deprotonation processes of pH sensors. Excessive ionic strength can also impact the osmotic pressure applied on a porous sensing network[44, 45]. Negative effect of ionic strength in pH measuring has been reported with a sensing material shrunken accompanied by marginal sensitivity[46]. Biosensors for both *in vitro* and *in vivo* environment detections will be confronted to lots of variation of ionic strength change and thus the influences need to be evaluated carefully. Fig. 5(a) shows a drastic impact of pH variation in pH sensing capability. The appeared square box labels a normal extra- / intra-cellular ionic strength range which normally varies from 0.08 to 0.2 M[47]. Below or above this range, it is not recommended to measure pH with currently proposed probe, otherwise poor sensitivity and huge error would be highly expected. Also important is the proper storage of unused probe, prior immersion with solutions of high ionic strength can induce/form complexes that would hardly be dissolved and thus may irreversibly destroy the probe[46].

pH sensing capability would further be influenced by temperature. An actual temperature impact on pH sensing ability was observed within a relatively wider temperature range from 10 to 50°C . Fig. 5(b) shows the measured pH signal variations at

five different temperature conditions, each with a 10°C interval. Four pH buffer solutions with pH values of 6.07, 6.60, 6.96 and 7.82 were used. Temperature variation was found exponentially correlated with pH values, and an averaged 21.5% pH decreasing would be seen with every 10°C temperature increasing. This result is in accordance with previously claimed similar phenomenon[48]. However, since our ultimate goal was to monitor single cell level pH conditions where a drastic change of temperature would not be appeared, such thermal influence will not be a big issue in practical use, e.g., within the range of $37 \pm 0.5^\circ\text{C}$, which is the upper limitation of our incubating system, a pH measurement variation would be expected around 0.047 (with buffer pH of 7.82, green region) to 0.012 (with buffer pH of 6.07, blue region) in normalized fluorescent (FL) ratio of 560nm / 640nm. This variation is way smaller than the standard deviation of each pH measurement and thus would have much less impact on the final pH measurement resolution.

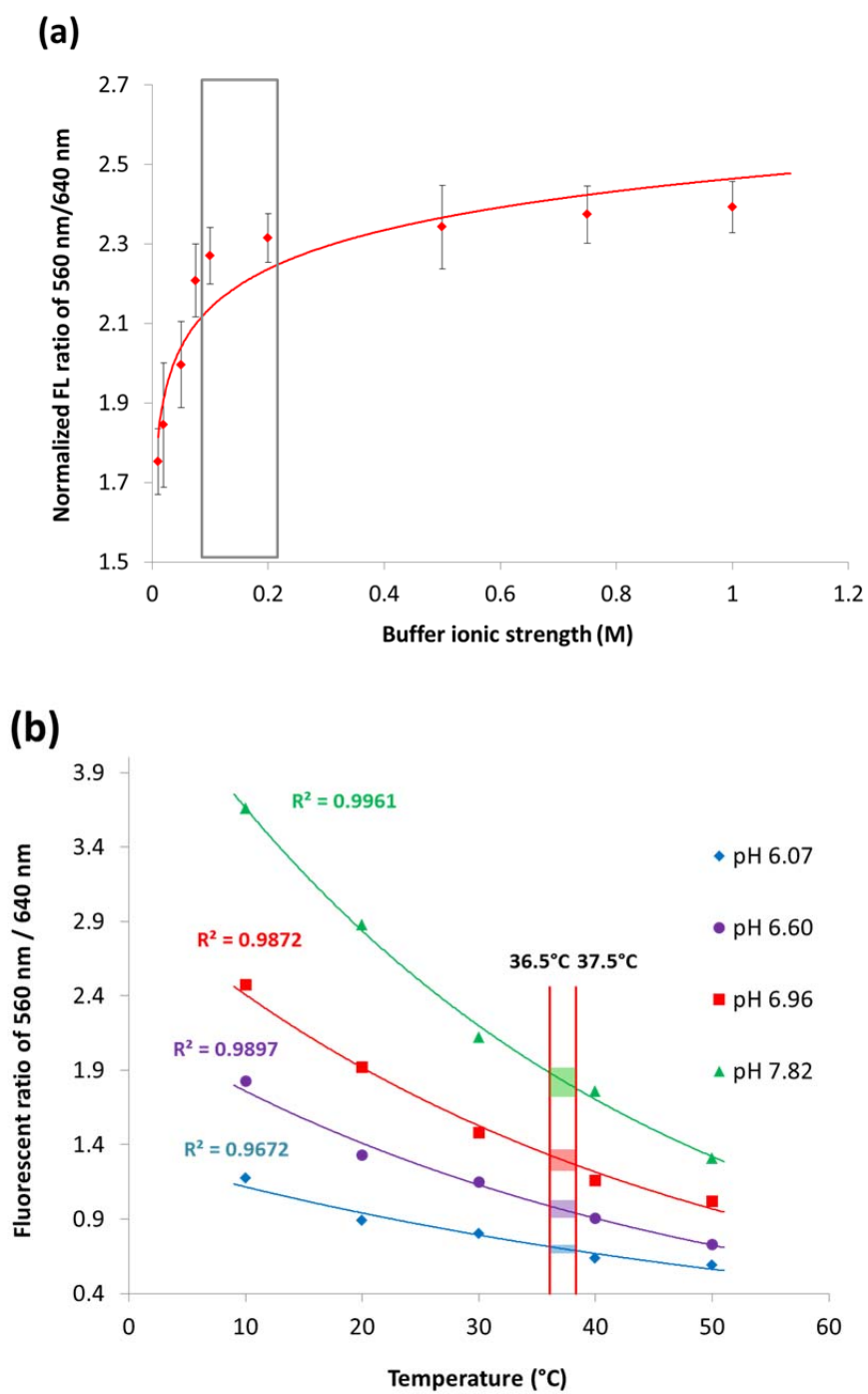


Fig. 5 Evaluation of environmental interference to the fabricated pH sensor by (a) ionic strength and (b) ambient temperature, respectively from 0.01 to 1 M and from 10 to 50°C.

A series of pH measurement with gradient buffer solutions are shown in Fig. 6(a). An average equilibrating time would be expected around 40 – 60 seconds. Measurement in each pH buffer solutions were kept still until a plateau of signal had been achieved. Normally, a period of 100 seconds is sufficient to acquire such plateau status and thus was used under all tested conditions.

Fig. 6(b) plots the fluorescent signal ratio of 560 nm / 640 nm as a function of buffer pH values, where a linear correlation within the pH ranges from 6.12 to 7.81 ($R^2 = 0.9874$). The linearity fitting of the experimental data indicates a pH sensing resolution of ~ 1.13 fluorescent ratio value (560 nm/640 nm) per pH unit. In addition, for each pH buffer solutions, the standard deviation based on triplicate measurements was distributed between 0.038 and 0.084 in FL ratio of 560 nm/640 nm, thus any two measured signals that have a higher intervals should be well differentiated. In this case, theoretically a pH resolution could come up with a range of 0.031 to 0.068 pH unit. This good linearity within such a focused pH working range can not only allow wide applications of a simple two-point calibration method[49], but also provide a sensitive and practical measurement capability of monitoring subtle pH change of ~ 0.049 (on average) pH units.

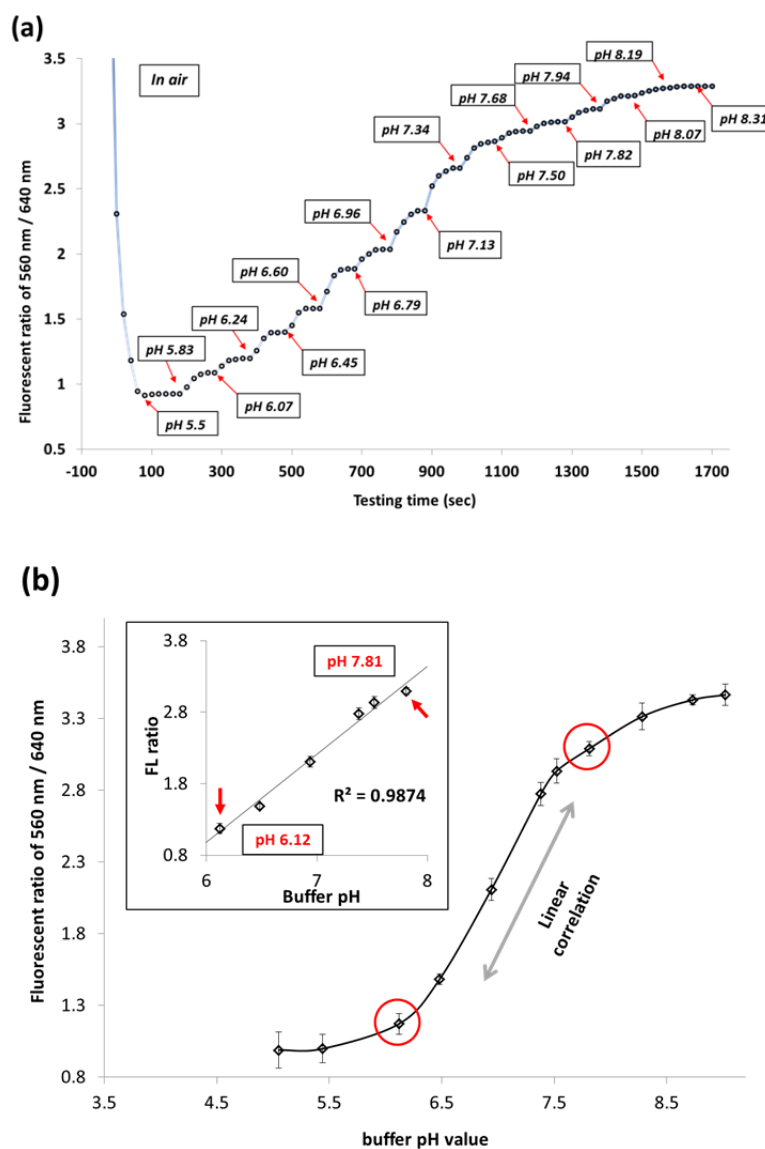


Fig. 6 Reflection mode detected fluorescent ratio (560/640 nm) spectra from fabricated fiber-optic pH sensor. A real-time manner measurement from ~pH 6 to ~pH 8 was show (a) combined with a pH sensitive region as well as linearity calculation of fluorescent ratio changes as a function of buffer pH values (b).

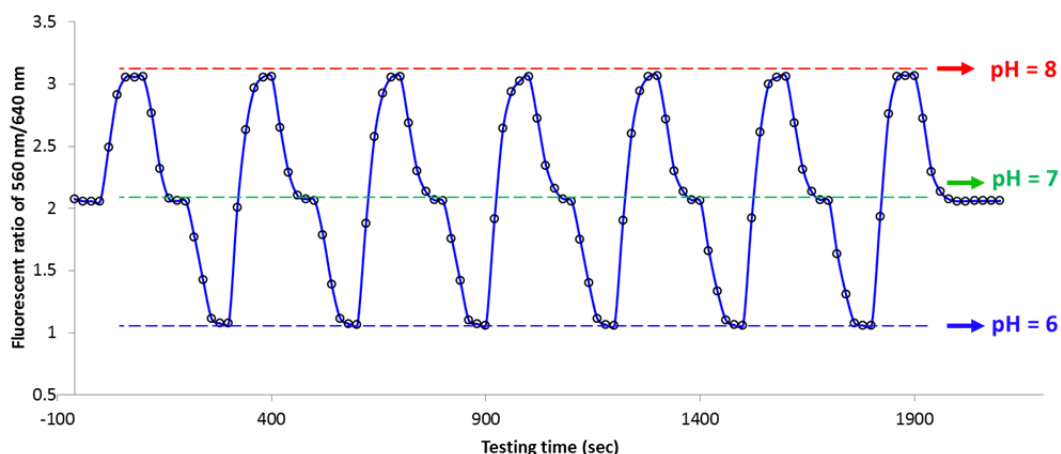


Fig. 7 Repeatability and signal stability of the fabricated pH probe in a cycling measurement of pH6 (bottom), pH7 (middle) and pH8 (upper) buffer solutions for 35 minutes.

The nominally 70 μm probe was then evaluated for its reproducibility in measurement under real circumstance. Cell culture grade 0.1 M PBS buffer solutions were prepared in three pH condition ranging from pH 6 to pH 8. The pH probes were continually inserted into three buffer solutions in the order of pH7 – pH8 – pH7 – pH6 – pH7 (and so force). 100 seconds interval between two pH buffers was set to acquire equilibration. Fig. 7 shows a partial record that lasts for about half an hour. An acceptable quality for repeating measurement (with signal intensity decreasing less than 2%) has been acquired. Besides, probes that were similarly fabricated showed satisfactory reproducibility as well (with less than 5 % variations). In addition, long term storage (three months) in sealed desiccator did not change the sensing capability of accordingly fabricated probes. However, after each measurement, the fiber probe need to be carefully rinsed in ethanol, followed by heat-drying right after rinsing. Fully removal of attached ions and vapor molecules from the surface aerogel networks is highly recommended to maintain its sensing ability and reusability.

In sum, with relatively low peak intensity and wide full width at half maximum (FWHM), the sensitivity of the proposed fiber optic based pH sensor is sufficient and comparable with other developed or commercialized pH sensors. The good point provided by this pH sensor is a smaller size ($\sim 70 \mu\text{m}$) and simplified sensing principle and procedure. Thus high spatial resolution (close to single cell level) could be easily equipped with considerably low cost. Its high sensitivity (~ 0.049 pH unit) that focused only on bio-sample related pH region (pH 6 to pH 8) paves its way to detect single-cell level extra-cellular pH variations. Together, the fast sensing rate (within 40 – 60 seconds) and continuous sensing ability, the reflection-based remote-sensing capability (several meters) combined with significantly simplified calibration process (due to the linear correlation of FL ratio and pH), provide promising application potentials of such probe in many fields.

4. Conclusions

We report a fiber-optic reflection-mode probe based on dye-doped ultra-thin aerogel dip-coating technique for pH sensing. The fabrication of tapered optical fiber with spherical head was assisted by carbon dioxide laser stretching system and optical fiber fusion splicer device. The aerogel ultra-thin layer coating was implemented by sol-gel dip-coating technique combined with pH sensitive dye covalent-bonding through introduction of ORMOSILs. The pH sensing capability could be modified through adjusting the sol-gel formula with different ratio of alkoxides as well as surface hydrophobicity through HMDS priming. In this study, an optimized fabricating procedure was developed, and the synthesized pH probe was evaluated and demonstrated to have *in*

in vitro pH sensing capability in a real-time manner. A colorimetric method was employed and showed a fine linear response to pH variations, with a resolution down to ~0.049 pH unit, within a biological meaningful pH range of 6.12 – 7.81. Such ability could be further influenced by extremely changed ionic strength and temperature, but no significant interference would be seen within a confined circumstance. In all, its micron-scale size with high spatial resolution, reflection mode operation, fast and repeatable recording, specific linear response within pH 6 to 8 region and a high pH resolution, make it a very cost-effective tool for chemical/biological sensing, especially within the single cell level research field.

Conflicting Interests

The author(s) declared no potential conflicts of interest.

Acknowledgement

The authors thank Clarissa A. Wisner for assistance with SEM and EDS scanning. This project was supported by a funded NIH Grant (Grant No.R21GM104696).

References

- [1] T. Paciorek, E. Zažímalová, N. Ruthardt, J. Petrášek, Y.-D. Stierhof, J. Kleine-Vehn, et al., Auxin inhibits endocytosis and promotes its own efflux from cells, *Nature*, 435(2005) 1251-6.
- [2] Z. Rosenzweig, R. Kopelman, Development of a submicrometer optical fiber oxygen sensor, *Analytical chemistry*, 67(1995) 2650-4.
- [3] W. Tan, Z.Y. Shi, R. Kopelman, Development of submicron chemical fiber optic sensors, *Analytical chemistry*, 64(1992) 2985-90.
- [4] T. Vo-Dinh, P. Kasili, Fiber-optic nanosensors for single-cell monitoring, *Analytical and bioanalytical chemistry*, 382(2005) 918-25.

- [5] Z. Rosenzweig, R. Kopelman, Analytical properties of miniaturized oxygen and glucose fiber optic sensors, *Sensors and Actuators B: Chemical*, 36(1996) 475-83.
- [6] M. Kneen, J. Farinas, Y. Li, A. Verkman, Green fluorescent protein as a noninvasive intracellular pH indicator, *Biophysical journal*, 74(1998) 1591-9.
- [7] O. Seksek, N. Henry-Toulmé, F. Sureau, J. Bolard, SNARF-1 as an intracellular pH indicator in laser microspectrofluorometry: a critical assessment, *Analytical biochemistry*, 193(1991) 49-54.
- [8] J. Han, K. Burgess, Fluorescent indicators for intracellular pH, *Chemical reviews*, 110(2009) 2709-28.
- [9] M.M. Collinson, Analytical applications of organically modified silicates, *Microchimica Acta*, 129(1998) 149-65.
- [10] B.D. MacCraith, C. McDonagh, Enhanced fluorescence sensing using sol-gel materials, *Journal of Fluorescence*, 12(2002) 333-42.
- [11] N. Chaudhury, R. Gupta, S. Gulia, Sol-gel Technology for Sensor Applications (Review Paper), *Defence Science Journal*, 57(2007) 241-53.
- [12] B. Lintner, N. Arfsten, H. Dislich, H. Schmidt, G. Philipp, B. Seiferling, A first look at the optical properties of ormosils, *Journal of Non-Crystalline Solids*, 100(1988) 378-82.
- [13] H. Schmidt, Organic modification of glass structure new glasses or new polymers?, *Journal of Non-Crystalline Solids*, 112(1989) 419-23.
- [14] C. Higgins, D. Wencel, C.S. Burke, B.D. MacCraith, C. McDonagh, Novel hybrid optical sensor materials for in-breath O₂ analysis, *Analyst*, 133(2008) 241-7.
- [15] C. Sanchez, B. Julián, P. Belleville, M. Popall, Applications of hybrid organic-inorganic nanocomposites, *Journal of Materials Chemistry*, 15(2005) 3559-92.
- [16] C. McDonagh, B. MacCraith, A. McEvoy, Tailoring of sol-gel films for optical sensing of oxygen in gas and aqueous phase, *Analytical chemistry*, 70(1998) 45-50.
- [17] R.M. Bukowski, M.D. Davenport, A.H. Titus, F.V. Bright, O₂-Responsive Chemical Sensors Based on Hybrid Xerogels that Contain Fluorinated Precursors, *Applied spectroscopy*, 60(2006) 951-7.
- [18] L. Guo, W. Zhang, Z. Xie, X. Lin, G. Chen, An organically modified sol-gel membrane for detection of mercury ions by using 5, 10, 15, 20-tetraphenylporphyrin as a fluorescence indicator, *Sensors and Actuators B: Chemical*, 119(2006) 209-14.

- [19] Š.M. Korent, A. Lobnik, G.J. Mohr, Sol-gel-based optical sensor for the detection of aqueous amines, *Analytical and bioanalytical chemistry*, 387(2007) 2863-70.
- [20] D. Wencel, M. Barczak, P. Borowski, C. McDonagh, The development and characterisation of novel hybrid sol-gel-derived films for optical pH sensing, *Journal of Materials Chemistry*, 22(2012) 11720-9.
- [21] S.A. Grant, R.S. Glass, A sol-gel based fiber optic sensor for local blood pH measurements, *Sensors and Actuators B: Chemical*, 45(1997) 35-42.
- [22] R. Makote, M. M Collinson, Organically modified silicate films for stable pH sensors, *Analytica chimica acta*, 394(1999) 195-200.
- [23] F. Ismail, C. Malins, N.J. Goddard, Alkali treatment of dye-doped sol-gel glass films for rapid optical pH sensing, *Analyst*, 127(2002) 253-7.
- [24] B.J. Scott, G. Wirnsberger, G.D. Stucky, Mesoporous and mesostructured materials for optical applications, *Chemistry of materials*, 13(2001) 3140-50.
- [25] A. Kriltz, C. Löser, G.J. Mohr, S. Trupp, Covalent immobilization of a fluorescent pH-sensitive naphthalimide dye in sol-gel films, *Journal of sol-gel science and technology*, 63(2012) 23-9.
- [26] D.A. Nivens, Y. Zhang, S.M. Angel, A fiber-optic pH sensor prepared using a base-catalyzed organo-silica sol-gel, *Analytica chimica acta*, 376(1998) 235-45.
- [27] N.D. Hegde, A. Venkateswara Rao, Organic modification of TEOS based silica aerogels using hexadecyltrimethoxysilane as a hydrophobic reagent, *Applied Surface Science*, 253(2006) 1566-72.
- [28] D.Y. Nadargi, A.V. Rao, Methyltriethoxysilane: New precursor for synthesizing silica aerogels, *Journal of alloys and compounds*, 467(2009) 397-404.
- [29] J.D. Wright, N. Sommerdijk, *Sol-Gel Materials: Chemistry and Applications*, 2001, Gordon and Breach Science Publishers, Amsterdam, The Netherlands.
- [30] I.M. El-Nahhal, S.M. Zourab, F.S. Kodeh, A. Al-Bawab, Behaviour of phenol red pH-sensors in the presence of different surfactants using the sol-gel process, *International Journal of Environmental Analytical Chemistry*, 90(2010) 644-56.
- [31] H. Budunoglu, A. Yildirim, M.O. Guler, M. Bayindir, Highly transparent, flexible, and thermally stable superhydrophobic ORMOSIL aerogel thin films, *ACS applied materials & interfaces*, 3(2011) 539-45.

- [32] S.S. Chauhan, R. Jasra, A. Sharma, Phenol Red Dye Functionalized Nanostructured Silica Films as Optical Filters and pH Sensors, *Industrial & Engineering Chemistry Research*, 51(2012) 10381-9.
- [33] D. Yan, J. Lu, J. Ma, M. Wei, D.G. Evans, X. Duan, Fabrication of an anionic polythiophene/layered double hydroxide ultrathin film showing red luminescence and reversible pH photoresponse, *AIChE Journal*, 57(2011) 1926-35.
- [34] P. Lin, F. Yan, Organic Thin-Film Transistors for Chemical and Biological Sensing, *Advanced Materials*, 24(2012) 34-51.
- [35] G. Ozaydin-Ince, A.M. Coclite, K.K. Gleason, CVD of polymeric thin films: applications in sensors, biotechnology, microelectronics/organic electronics, microfluidics, MEMS, composites and membranes, *Reports on Progress in Physics*, 75(2012) 016501.
- [36] S. Zhang, S. Tanaka, Y. Wickramasinghe, P. Rolfe, Fibre-optical sensor based on fluorescent indicator for monitoring physiological pH values, *Medical and Biological Engineering and Computing*, 33(1995) 152-6.
- [37] A.B. Ganesh, T. Radhakrishnan, Fiber-optic pH sensor, *Fiber and integrated optics*, 25(2006) 403-9.
- [38] B. Gu, M. Yin, A.P. Zhang, J. Qian, S. He, Biocompatible Fiber-Optic pH Sensor Based on Optical Fiber Modal Interferometer Self-Assembled With Sodium Alginate/Polyethylenimine Coating, *Sensors Journal, IEEE*, 12(2012) 1477-82.
- [39] Y.L. Liu, C.S. Wu, Y.S. Chiu, W.H. Ho, Preparation, thermal properties, and flame retardance of epoxy-silica hybrid resins, *Journal of Polymer Science Part A: Polymer Chemistry*, 41(2003) 2354-67.
- [40] B. Mena, M. Takahashi, P. Innocenzi, T. Yoko, Crystallization in hybrid organic-inorganic materials induced by self-organization in basic conditions, *Chemistry of materials*, 19(2007) 1946-53.
- [41] S.-A. Mirshafiei-Langari, H. Roghani-Mamaqani, M. Sobani, K. Khezri, In situ atom transfer radical polymerization of styrene in the presence of nanoporous silica aerogel: Kinetic study and investigation of thermal properties, *Journal of Polymer Research*, 20(2013) 1-11.
- [42] S.A. Taya, Sol-Gel Thin Films Immobilized with Bromocresol Purple pH-Sensitive Indicator in Presence of Surfactants, *ISRN Analytical Chemistry*, 2012(2012).
- [43] M. Takahashi, C. Figus, T. Kichob, S. Enzo, M. Casula, M. Valentini, et al., Self-Organized Nanocrystalline Organosilicates in Organic-Inorganic Hybrid Films, *Advanced Materials*, 21(2009) 1732-6.

- [44] A.E. English, T. Tanaka, E.R. Edelman, Equilibrium and non-equilibrium phase transitions in copolymer polyelectrolyte hydrogels, *The Journal of chemical physics*, 107(1997) 1645-54.
- [45] T. Tanaka, *Experimental methods in polymer science: modern methods in polymer research and technology*: Academic Press; 2000.
- [46] A. Richter, G. Paschew, S. Klatt, J. Lienig, K.-F. Arndt, H.-J.P. Adler, Review on hydrogel-based pH sensors and microsensors, *Sensors*, 8(2008) 561-81.
- [47] M. Mouat, K. Manchester, The intracellular ionic strength of red cells and the influence of complex formation, *Comparative Haematology International*, 8(1998) 58-60.
- [48] M. Herzog, *Thermophoresis and cooperative binding of nucleotides*: lmu; 2012.
- [49] N.F. Sheppard Jr, M.J. Lesho, P. McNally, A. Shaun Francomacaro, Microfabricated conductimetric pH sensor, *Sensors and Actuators B: Chemical*, 28(1995) 95-102.

**V. Fiber-Optic-Based Micro-Probe Using Hexagonal 1-in-6 Fiber Configuration for
Intracellular Single-Cell pH Measurement**

**Qingbo Yang,¹ Hanzheng Wang,² Sisi Chen,¹ Xinwei Lan,² Hai Xiao,² Honglan Shi,¹
Yinfa Ma^{1*}**

¹Department of Chemistry and Center for Single Nanoparticle, Single Cell, and Single
Molecular Monitoring, Missouri University of Science and Technology, Rolla, MO
65409, USA

²Department of Electrical and Computer Engineering, Clemson University, Clemson, SC
29634, USA

*Corresponding Author

Address: Department of Chemistry

Missouri University of Science and Technology

400 West 11th Street

Rolla, MO65409

Phone: 573-341-6220

Fax: 573-341-6033

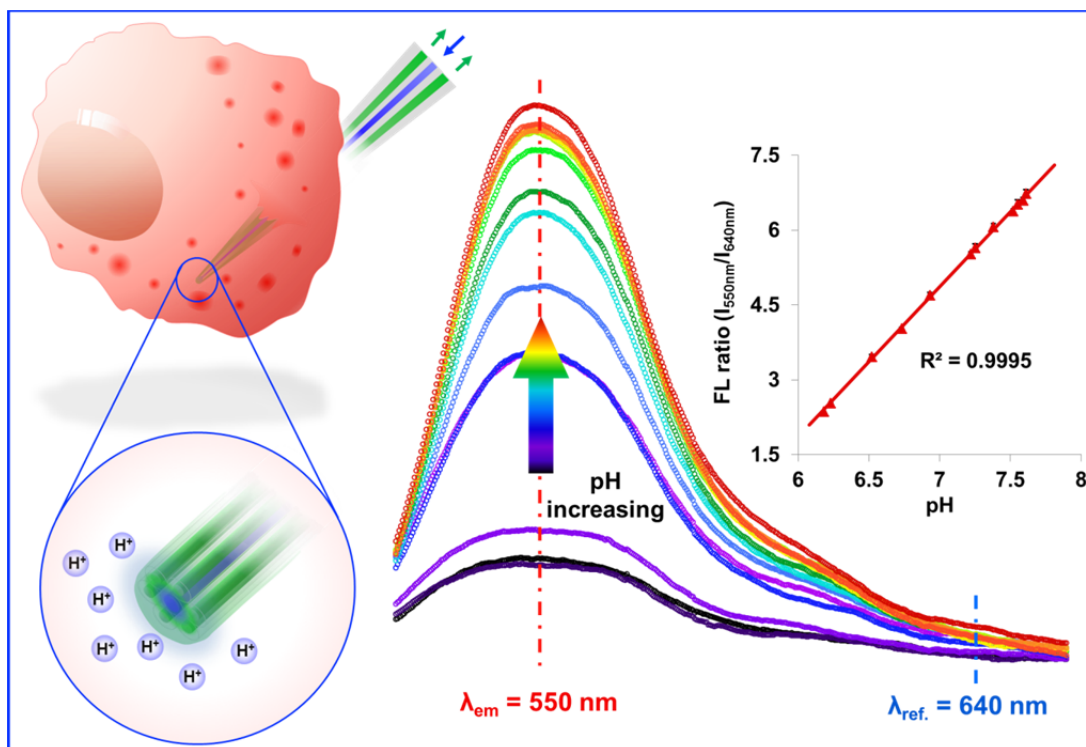
E-mail: yinfa@mst.edu

ABSTRACT

Single cell research is essential for understanding cell heterogeneity, cell differentiation, and carcinogenesis, among other important cellular processes. New techniques for intracellular pH monitoring are urgently needed to gain new insights into single cell responses to external stimuli. In this study, fiber-optic reflection-based pH micro (μ)-probes (tip diameter: 500 nm - 3,000 nm) were designed and fabricated using a novel hexagonal 1-in-6 fiber configuration. An organic-modified silicate (OrMoSils) sol-gel doped with a pH sensitive dye, 2',7'-bis-(2-carboxyethyl)-5-(and-6)-carboxyfluorescein (BCECF), were coated onto the probe sensing tip for pH detection. These probes enabled neutral pH monitoring and quasi-real-time data acquisition (response time: 20 ± 5 seconds). The fluorescence signals of the newly developed probes were found to correlate linearly with pH ($R^2 = 0.9869$ when coupling laser power was at 8.2 mW) within a biologically relevant pH range (6.18 – 7.80). The pH resolution was 0.038 pH unit. The miniaturized probes were validated in single human lung cancer A549 cells to demonstrate applicability in single cell experiments. In summary, novel pH μ -probes with excellent resolution and response times within a biologically relevant pH range were developed and they can be used for measuring pH changes in single cells.

Keywords: pH μ -probe; Hexagonal 1-in-6 fiber configuration; organically modified silicates (OrMoSils); Niche environment sensing; Single cell.

Table of Content Graphic:



INTRODUCTION

Cell heterogeneity plays an important role in determining cell plasticity and fate. For this reason, the ability to monitor subtle changes in a cell's microenvironment is highly desirable for understanding the individual responses of single cells to a niche environment. Cell signaling events such as pH changes, temperature oscillations, and signaling molecules, can trigger substantial responses including cell division, differentiation and death.¹ Unlike signaling molecules that are highly regulated, pH is a relatively macroscopic factor that can have broad impacts on cell fate. For example, low pH exposure can reprogram cells to induce pluripotency. A successful cell dedifferentiation was achieved by simply exposing to a low pH environment. The transformed cells were reported to acquire improved pluripotency to re-differentiate into somatic cells, germ cells, as well as extra-embryonic lineages.² Similarly, cellular pH imbalances in carcinogenesis may represent novel therapeutic targets that require a clearer understanding of how individual cells respond to altered pHs. The intracellular pH (pH_i) of healthy adult cell is normally maintained near 7.2, which is lower than the extracellular environment. However, cancer cells maintain a higher pH_i (>7.4) but have characteristically lower extracellular pH (pH_e) (6.7 – 7.1).³⁻⁵ Increased pH_i has been shown to assist cell proliferation and evasion of apoptosis, to facilitate metabolic adaptation, as well as to improve cancer cell motility; While decreased pH_e can stimulate acid-activated proteases to help tumor cells invasion and dissemination.⁶ Moreover, a Na^+/H^+ exchanger, named NHE1, similar to those that exist in human melanoma cells (MV3), can generate a well-defined cell surface pH gradient at the outer leaflet of the plasma membrane to assist cell body polarity and migration.⁷ These and more findings⁸⁻¹¹

highlight the importance of microenvironmental pH in understanding cell fate and disease. However, relevant techniques capable of monitoring microenvironment pH remain underdeveloped.

Intracellular pH labeling reagents have been broadly used to describe cellular pH and its spatiotemporal variations. Since their first introduction in the early 1980s by Roger Tsien et al.,¹² several types of pH-sensitive fluorescent dyes derived primarily from fluorescein have been developed, such as benzoxanthene, rhodol, cyanine, pyrene and miscellaneous small molecules. Some representative dyes, like 2',7'-bis(3-carboxypropyl)-5(6)-carboxyfluorescein (BCPCF),¹³ Benzenedicarboxylic acid formed 2-(4)-[10-(dimethylamino)-3-oxo-3H-benzo[c]xanthene-7-yl] (SNARFs),¹⁴ fluorescent norcarbocyanines indocyanine green (H-ICG),¹⁵ 8-hydroxypyrene-1,3,6-trisulfonic acid (HPTS),¹⁶ and others, were also introduced and widely used. Because of its neutral pK_a of 6.98 and linear correlation between fluorescence intensity and pH within the range of 6.1-7.8, 2',7'-bis-(2-carboxyethyl)-5-(and-6)-carboxyfluorescein (BCECF) and its derivatives have been used for intracellular pH measurements.^{16,17} However, due to the inherited drawbacks during endocytosis (hydrophobic modification) and long-term immobilization (leaking and degradation) within cells, many dye molecules have been considered as cytotoxic¹⁸ or carcinogenic¹⁹⁻²¹ and thus may not be able to represent the actual cellular pH status.

Other methods have also been developed to measure both extra- and intracellular pH. For example, quantum dots (QDs) have been used for intracellular sensing as an alternative approach based on superior quantum yield efficiencies and optical stability.^{22,23} When combined with fluorescence resonance energy transfer (FRET)^{24,25}

and specific modifications,²⁶⁻²⁸ QDs offer powerful sensing performance. However, the toxic concerns of heavy metals in many QD formulations limit their application to long-term monitoring. pH sensing probes have been developed in response to minimize the potentially harmful effects of free dyes and QDs. Principles and techniques employed to construct such pH sensing probes include field effect transistor,²⁹ microelectric probing,³⁰ fiber-optic pH sensing,³¹ and others.³²⁻³⁴ Among these proposed probes, optical fiber-based pH probes have shown the advantages of simple ratiometric working principle and easy-handling.^{35,36} In a basic fiber optic probe configuration, the excitation source is introduced into the optical fiber core and light is transmitted to the sensing tip. Sensing molecules bound to the tip of the probe emit signal back to the detector. The pH sensing capability of the probes varies greatly depending on the sensing materials being used. A porous molecular matrix and a pH sensitive reagent are typical strategies to maximize the interactions between the fluorescent reagent and external analyte. Malins et al. have successfully demonstrated a workable platform for pH sensing using such a strategy.³⁷ Recent attempts have also been made to extend the applicability of the ratiometric pH sensing approaches.^{38,39} We recently reported a micro-size (50 – 70 μm) reflection-based optical fiber pH sensor. With a pH resolution of 0.049 pH unit at neutral pH range (pH 6.2-8.0), the pH probe can potentially be used for real-time inter-cellular pH measurement at a quasi-single-cell level.⁴⁰

Some non-invasive sensing approaches for single cell pH measurement have also been reported, such as the Raman or magnetic resonance imaging (MRI) based sensing platforms.^{41,42} However, the limited selection of sensing molecules that are both pH sensitive and Raman active, the inevitable involvement of intracellular contrast agents in

MRI imaging, and cumbersome instrumentation, have limited development and application of non-invasive single-cell or quasi-single-cell level pH sensors.

In this study, a fiber optic reflection-based pH micro (μ)-probe was designed and fabricated with a hexagonal 1-in-6 fiber configuration. A coaxial-twisting and gravitational-stretching procedure was utilized for optimal signal collection and minimal interference. The pH sensing capability was enabled by sol-gel dip coating of an OrMoSils layer on the probe tip. The newly developed pH μ -probes were calibrated in the biologically relevant pH ranges (6 - 8), and were finally validated using human lung cancer A549 cells.

EXPERIMENTAL SECTION

Fabrication of Tapered Hexagonal Fiber Probe. The hexagonal-shaped 1-in-6 optical fiber tip was fabricated as the probe's sensing head, with 1 - 1.5 cm taper length, 500 - 3,000 nm tip diameter and 2° - 8° tapering angle. A bundle of seven multimode optical fibers with core and cladding diameters of 62.5 and 125 μm (Corning, USA), respectively, were aligned into a six-surrounding-one pattern to ensure a hexagonal cross-section. As shown in Figure 1, a homemade coaxial-twisting and gravitational-stretching system was employed to fabricate the probe, with assistance of a butane-fueled pencil torch (Blazer PT-4000). Four plates (from I to IV) with 7 through holes arranged in a hexagonal pattern were used in the fabrication system to align the 7 fibers. Plate I worked as a holding clamp to maintain all fibers position without relative displacement. Plate II and III both have hexagonal apertures to allow each fiber pass through freely, while plate IV clamped all fibers and worked as a plummet to enable gravitational stretching. Upon twisting of plate III and IV together, all six peripheral fibers converged around the central

fiber. After multiple twisting revolutions, a coaxial pattern fiber alignment was achieved. The use of coaxial-twisting procedure was aimed to provide extra tenacity during heat stretching and cell sensing.

To make the hexagonal 1-in-6 tapered fiber tip (Figure 1), a pencil flame torch was positioned perpendicularly to the fiber twisting area. Butane was used as fuel, and the torch temperature reached approximately 1,400 °C. Once the polymer jackets were removed by the torch, the exposed bare fiber twisting area was gradually melted by torch heating and tapered by gravitational pulling by plate IV. The tapered tip was found to be appreciably fragile and optimal strength performance was noted for tip lengths fewer than 2 cm. In order to make the probe tip straight, a vertical, gravitational stretching force was applied rather than a horizontal stretching configuration. The fabrication parameters such as twisting angle (4 to 6 revolutions), hexagonal fiber alignment, tapering length (1 – 1.5 cm), tip diameter (500 – 3,000 nm) and tapering angle (2° - 8°), etc., were finely optimized and controlled to assure the performance of the probe (Table 1).

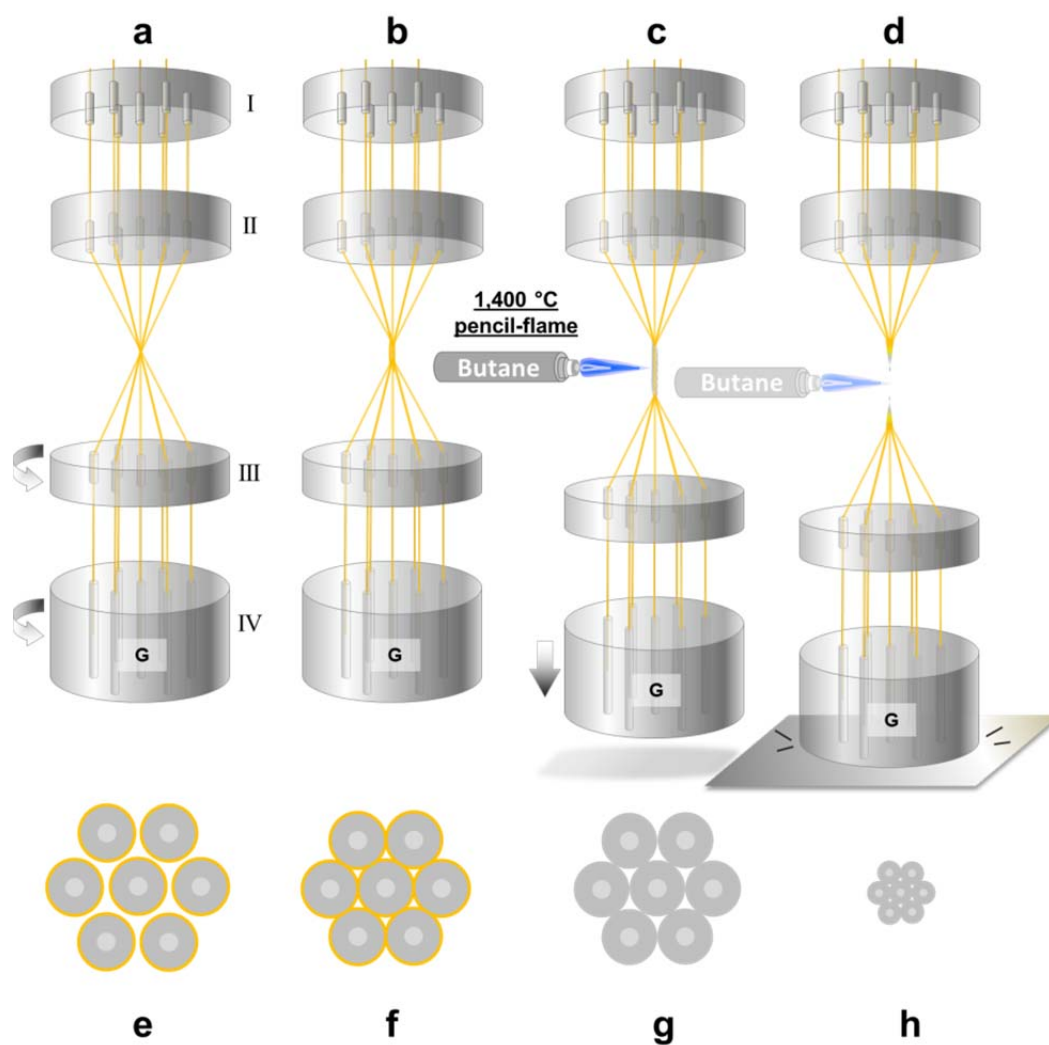


Figure 1. Detail coaxial-twisting/gravitational-stretching process in fabricating hexagonal pH μ -probe tip. Sub-figures a to d Show four-step procedures in coaxial twisting and gravitational stretching, and sub-figures e to h show the status quo of fiber cross-section twisting steps. Along with the process going, hexagonally, loosely aligned fibers were tightly twisted, burned by 1,400 °C to remove the fiber jacket layers, and finally melted/stretched as one intact tip. It is noted that the diameter of each intersection scheme (e - h) is not drawn according to actual size.

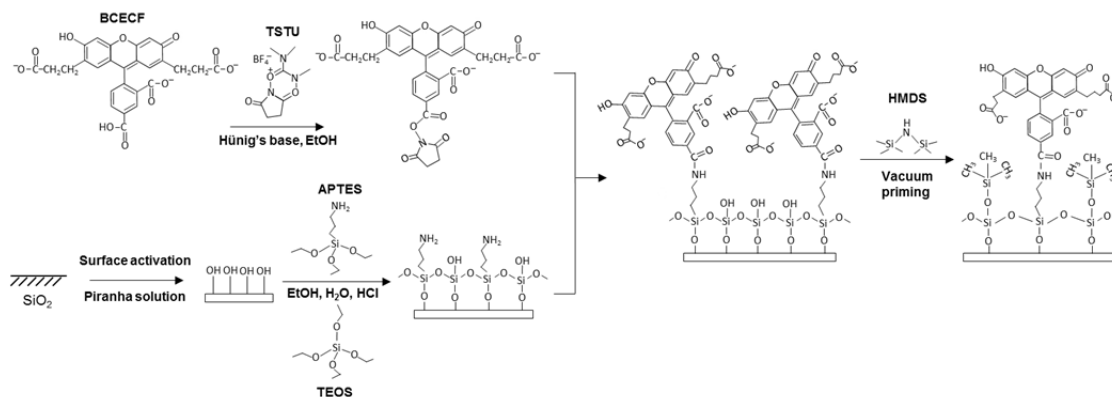
Table 1. Variation Ranges of Several Key Factors of a Fully Fabricated Hexagonal 1-in-6 pH Probe.

Key factors of a fabricated probe	Variation range
Taper length	1 - 1.5 cm
Tip diameter	500 - 3, 000 nm
Tapering angle	2° - 8°
peripheral fiber twisting angle	1440° - 2160° (4 - 6 revolutions*)
Fiber alignment configuration	One central fiber in hexagonally surrounded six fibers
Dye bonded aerogel sensing layer thickness	400 - 600 nm

* Revolution indicates the plate III and IV turn coaxially to the plate II and I. One revolution equals to 360°.

pH Sensing Layer Creation. A pH sensitive fluorescent dye BCECF was covalently embedded into an ultra-thin aerogel network layer created via amide bonding at the tip surface under dark conditions (Scheme 1). A modified sol-gel dip-coating procedure described elsewhere was used in this study.⁴⁰ Briefly, the surface silanol groups of the freshly tapered hexagonal optical fiber probe were activated through three steps: 1) acidic activation by concentrated nitric acid for 12 hours, 2) washing with copious amounts of ultra-pure water followed by pure ethanol, and 3) drying at 100 °C for 3 hours. An amino-functionalization procedure was then applied to the heated probe surface using previously aged (12 hours) alkoxides mixture (sol) in methanol, including tetraethoxysilane (TEOS), (3-aminopropyl) triethoxysilane (APTES) and methyltrimethoxysilane (MTES) at a mixing ratio of 4:1:1 (v/v) with catalytic amount (2% of total volume) of hydrochloric acid (0.1 M). A dip-coating process was used for the 100 °C dried tapers with a drawing rate of 1 mm/s. The dip-coating step was repeated for about 8 - 10 rounds, depending on the required thickness (400 – 600 nm) of final

aerogel networks after curing. BCECF sodium salt was prepared in MQ water (18.2 M Ω , EMD Millipore Corp., MA, USA) at concentration of 1 mg/mL and further mixed with excess 2-succinimido-1, 1, 3, 3 tetramethyluronium tetrafluoroborate (TSTU) prepared in ethanol (1 mg/mL). Small catalytic amount (1-2% of total volume) of N-ethyl-diisopropylamine (Hünig's base) was added to promote the activation of carboxyls to succinimidyl-ester groups. The reaction was allowed to proceed for at least one hour at room temperature. The cured tips were then dipped into this activated succinimidyl-ester dye solution (final BCECF concentration at ~10 – 20 μ g/mL) for 10 – 30 minutes with constant stirring for amide bond formation. The probe was then fully dehydrated and cured at 50 °C for 6 hours and then at 80 °C for 24 hours. Finally, a quick hydrophobic modification was introduced to the probe tip surface using a home-built hexamethyldisilazane (HMDS, purity > 99%) (Ted Pella Inc., Redding, CA, USA) priming chamber. Briefly, the treated probe was placed into a small (7.5 cm \times 7.5 cm \times 25 cm) chamber and heated to 100 °C. Upon heating, 5 mL HMDS was placed into the now evacuated chamber and allowed to sit for 3 hours at 100 °C. This final step enabled hydrophobic HMDS vapors to react with the exposed hydroxyl groups on the aerogel surface. Notice that all BCECF dye-related reactions were taken place under dark conditions. All chemicals were purchased from Sigma-Aldrich (St. Louis, MO, USA) unless otherwise specified.



Scheme 1. Major procedures that applied OrMoSils sol-gel dip-coating and HMDS vacuum priming for pH sensing layer fabrication.

pH Sensing Principles and Optical Setups. The BCECF dye has been used as a ratiometric pH indicator (either excitation/emission or dual excitation methods) since the emission peak intensity change significantly with pH.^{16,43} In this study, we adopted the ratiometric principle for pH detection using the excitation wavelength of $\lambda = 488$ nm and two fluorescent emissions of $\lambda = 550$ nm and $\lambda = 640$ nm and the ratio of these two wavelengths' fluorescence intensity was correlated to standard pH via *ex vivo* calibration using Thomas' method.⁴⁴ The optical fiber in the center of hexagonal probe's configuration was connected to the excitation laser, while the peripheral six optical fibers were combined together for collecting and transmitting emission light to a USB2000 spectrometer (Ocean optics, Dunedin, FL, USA). A continuous-wave (CW) Argon ion laser source (Spectra-Physics Lasers, Mountain view, California, USA) was used to excite BCECF dye molecules (Figure 4). The laser power was adjusted to achieve optimal fluorescence intensity. A laser beam shutter with a maximum switching speed of 1 millisecond was used to control the irradiation time. A 20 \times objective was used to focus the laser beam into the center fiber. A fiber-coupling syringe was immobilized onto a

three-dimensional (3-D) manipulation μ -stage with stepping accuracy of 0.05 μm . The probe's sensing head was protected using a stainless steel probe guide to ensure that the probe head is exposed only when it was applied. In an actual measurement, the probe tip was immersed into an analyte solution for a few seconds (20 ± 5 s) for equilibration purposes. The fluorescence signal was transmitted by the peripheral six fiber-cores around the central fiber to the spectrometer using a SMA type fiber connector. The ratio between the peak fluorescent intensity (I_{peak}) at 550 nm and the reference intensity ($I_{\text{reference}}$) at the wavelength of 640 nm ($I_{\text{peak}}/I_{\text{reference}}$) was calculated and correlated with the pH value. A 100 ms integration time was used for data collection and processing. A boxcar function with the factor of 20 was used for spectral smoothing.

Characterization and Calibration of Sensor Probes. Fabricated probes were imaged using an inverted fluorescent microscope (Olympus IX51, Olympus, Center Valley, PA, USA) as well as scanning electron microscopy (SEM) and experimentally characterized by energy-dispersive X-ray spectroscopy (EDS) (FEI, Hillsboro, OR, USA). Both white light field and fluorescein isothiocyanate (FITC) fluorescent channel (for examination of the BCECF dye embedded coating) images were taken under the inverted microscope. Six major elements were scanned using EDS including carbon (C), nitrogen (N), oxygen (O), silicon (Si), silver (Ag) and gold (Au). A focused ion beam system (FIBs) was used to cut the probe tip at its very end to expose the cross section. Calibration standards were prepared with 0.1M phosphate buffer solutions that were prepared using 1 M sodium hydroxide or 1 M hydrochloric acid. Buffer solutions ranged from pH 6 to pH 8 at 0.2 ± 0.1 increments and measured with an Accumet AB15+ pH meter (Fisher scientific, Pittsburgh, PA, USA). After dipping the sensing probe into the

standard pH buffer solutions, the acquired fluorescent intensity ratio of 550 nm and 640 nm was correlated with the calibrated pH values. Normally, the sensing period of each probe lasted for about 20 ± 5 seconds until a plateau was achieved, and all measurements were triplicated. Fabricated probes were also subjected to post-measurement testing using standard pH solution buffers through a simplified procedure that was similar to probe calibration, to assure the reproducibility of the measurements.

Cell Culture and Proof-of-Concept Single Cell pH Measurements. Human bronchoalveolar carcinoma-derived A549 cell line was used in this study and was purchased from the American Type Culture Collection (Manassas, VA, USA). Briefly, the A549 cell line has been widely used in *in vitro* culture and cytotoxicity evaluations and was deemed appropriate for evaluation of the newly developed pH probes in this study.^{45,46} Cells were cultured in a phenol red free Ham's F-12K nutrient mixture from Caisson Laboratories Inc. (North Logan, UT, USA), supplemented with L-glutamine. A complete culture medium was made using F-12K with 5% fetal bovine serum (FBS) (Gibco/Life technology, New York, USA), 100 units/mL penicillin and 100 mg/mL streptomycin (Life technology, New York, USA). The cells were seeded and proliferated at 37 °C in a home-built humidifying chamber at 5% CO₂. The chamber was mounted on the stage of an Olympus IX51 inverted fluorescent microscope to enable long-term cell observation, manipulation, and measurement. A single cell suspension was prepared using trypsin-EDTA (Life technology, New York, USA) followed by single cell measurements using a microscope to guide insertion of the probe. The probe was inserted 3 – 8 μm into the cytosol to measure intracellular pH. All measurements were triplicated for probe validation purposes.

RESULTS AND DISCUSSION

Probe Fabrication. The extra- or intra-cellular pH sensing for a single cell requires a miniaturized probe sensor with high stability, high sensitivity, and high pH resolution. This was achieved through a specially designed hexagonal 1-in-6 fiber-optic probe tip (Figure 1). Figure 2 shows different tip regions of a representative probe. All parameters can be optimized as listed in Table 1.. Figure 2a is a schematic configuration of the coaxially twisted tip, while the figures below (2b - 2d) show the actual microscopic images of a probe in different regions from upper stem to its tip. A finished probe tip was also imaged under either white light or FITC channel (Figure 2e, 2f). A series of SEM images of the tip configuration were also shown in Figure S-1. As expected, the seven highly twisted fibers were gradually stretched in parallel toward the tip. Thus all fiber diameters were decreased uniformly, and the tip diameter of all seven fibers was measured in the range of 500 to 3,000 nm. This probe configuration was optimized to reduce scattered excitation light and maximize emission signals. Briefly, this is different from our previous work, where a 2-in-1 fiber coupler was used and both excitation and emission light passed through the same sensing shaft.⁴⁰ The earlier approach suffered from considerable background noise, difficulty in controlling the transmission ratio, and substantial signal losses due to ~50% of the signal being lost at the coupler. In comparison, the new hexagonal configuration was designed to overcome the challenges by complete separation of the excitation and emission light. Specifically, the core fiber transmitted excitation light while the peripheral fiber optics transmitted the emission signal. This separation was necessary to enhance sensitivity and enable probe miniaturization for single cell analyses. While additional fiber configurations such as 1-

in-4 design or non-twisted probes were also evaluated, the hexagonal 1-in-6 configuration provided optimal probe durability and sensitivity.

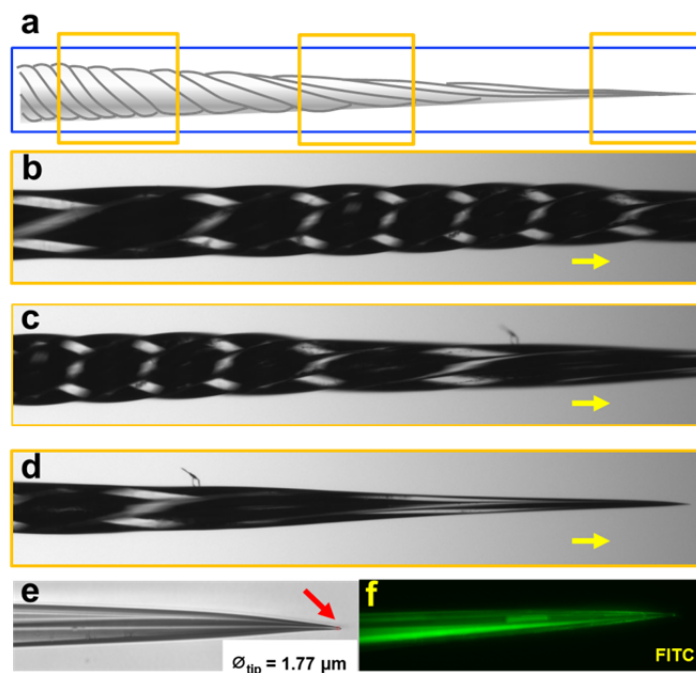


Figure 2. Finished hexagonal fiber taper probe configuration (a) and different imaging of twisting patterned area (b - d) under inverted microscope. A fully fabricated probe with fluorescent sensing layer coated and cured is shown under either white light (e) or fluorescein isothiocyanate (FITC) channel excitation light (f).

Probe Characterization. The pH sensing molecules were covalently bound to the aerogel via amide bonding for improved structural durability and minimization of dye leakage from the probe. A succinimidyl-ester activation reaction was used to enable the covalent amide bond formation between BCECF molecules and one of the aerogel backbone molecules (APTES) (Scheme 1). The hexagonal fiber alignment images at the probe tip were shown in Figure 3A and 3B before and after FIBs cutting. The hexagonal configuration was maintained throughout the probe including the tip. The sealed

triangular spaces between fibers (Figure 3B) indicated incomplete fusing during heating and stretching. These structural flaws may prevent light coupling due to their variable refractive indices.

The OrMoSils coated area yielded a roughened surface which indicated the area was successfully modified with a hydrophobic character (Figure 3C, D). A peeled off layer of the coating at the tip area was also imaged and the thickness of the coating was measured to be 441 nm (Figure 3C, E). A corresponding EDS scan was taken with peak intensities (in atomic percentage) of carbon (43.8%), nitrogen (20.0%), oxygen (18.1%) and silica (6.8%). High amounts of carbon indicated BCECF and HDMS bonding to the tip surface while the presence of nitrogen indicated success of the amide bonding procedure. Finally, trace surface silica indicated high coating efficiency of the original tip (Figure 3G).

Hydroxyl and amine groups prevalent on the aerogel surface were derivatized with MTES and HMDS priming processes, so the new methylsilyl and trimethylsilyl modalities provided a hydrophobic character to the sensor surface.⁴⁷⁻⁴⁹ This modification will limit adverse effects caused by water penetration into the sensor. The water penetration has deleterious impact of the response times and reproducibility.

In addition, thermal gravimetric analysis and Infrared spectral measurements of the same aerogel coating were acquired in our previous report.⁴⁰ Briefly, peaks from 2882 - 2937 cm^{-1} showed the $-\text{CH}_2$ stretching which is attributed to aliphatic chains in TEOS, APTES and MTES. Peaks between 3500 - 3300 cm^{-1} and 1650 - 1550 cm^{-1} were representative signs of amino groups in APTES and the formed amide bonds. The carbonyl ($\text{C}=\text{O}$) stretching peak between 1550 - 1610 cm^{-1} was also shown as proof of the existence of carboxylates or amino acid zwitterions.⁴⁰

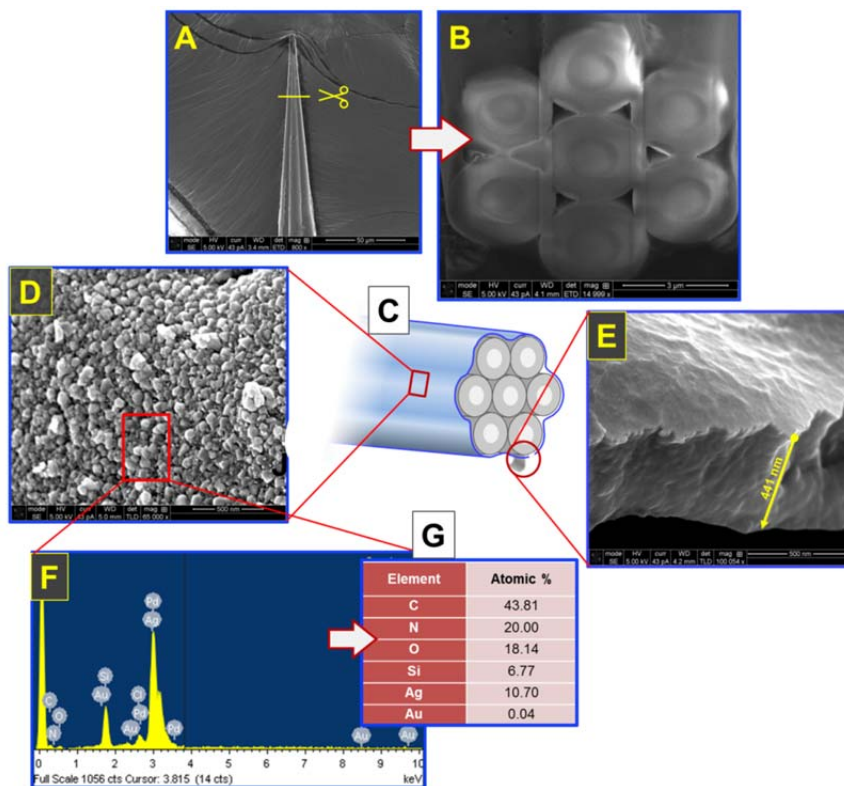


Figure 3. Electron microscopic imaging and characterization of the newly developed pH probe. (A) SEM image of the tip area; (B) SEM image of an intersection cut by using FIBs at the yellow line labelled area that showed in (A). (C) A schematic of the new hexagonal probe configuration detailing areas imaged with SEM in (D) and (E); (F) EDS scans on elemental intensity; (G) atomic abundance. Scale bars: (A) 50 μm , (B) 3 μm , (D, E) 500 nm.

System Setup and Laser Adjustment. The final system set up for the intracellular pH measurement is shown in Figure 4A. The excitation at 488 nm was achieved by splitting the laser with a prism module. A programmable beam shutter was used to control laser application time. The beam was focused onto the flat end of the central fiber and transmitted to the pH sensitive tip. The fluorescence signal was collected using the peripheral fibers and transmitted to the detector. This approach successfully complete separation of excitation and emission signals within a single, coherent probe. An additional silver mirror coating (by using the silver mirror reaction) on the bare,

unmodified probe surface was further minimized signal leakage and exterior light interferences. Although dichroic mirrors are commonly used to minimize Rayleigh scattering, it was not used in this approach due to the excellent spectral splitting observed by the triangular prism and split mode of fiber alignment.

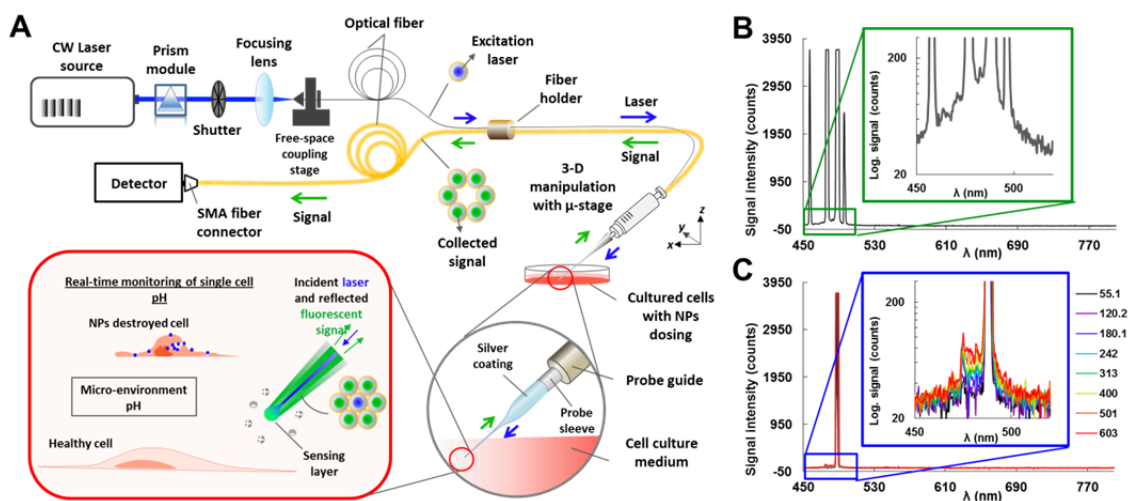


Figure 4. (A) Schematic diagram of the optical arrangement of the pH μ -probe; (B – C) Spectroscopic suppression of multiple laser peaks with power adjustment. Full spectra (450 nm to 800 nm) signals were monitored either (B) before or (C) after multi-peak suppression. Inset figures are enlarged portions of the laser peak area (450 – 520 nm, blue box). A wide range of laser power has been applied (from 55.1 mW to 603.0 mW) and was labeled in different color.

Sensitive pH measurements by using this μ -pH probe require optimization of peak signals and reduction of background noise. This was complicated by laser source defects that resulted in multiple, often broad laser lines that can excite fluorescent molecules. This was overcome in part by actively selecting 488 nm light by filtering the adverse peaks using a triangular prism module. Figure 4 displays unfiltered and filtered laser line spectra as observed without any probe coatings. The triangular prism afforded a single

peak centered at 488 ± 3 nm and effectively removed the adverse peaks centered at 457 nm, 476 nm, and 496 nm. Moreover, the spectral baseline was considerably improved using the prism module (41.6 counts vs 137.6 counts). Laser output power at 488 nm was linearly correlated with observed laser power at the fiber coupling site from 55.1 mW to 603 mW (Figure S-2A). Notably, the spectral baseline did not vary significantly as laser output power was modulated. Absorption spectra of the BCECF dye in phosphate buffer (0.1 M) at pH values between 4.63 (isosbestic point) and 9.20 appeared as an increasing trend (non-linear) with dual absorption peak at 450 nm and 500 nm,⁴³ thus a poor control in selecting single wavelength excitation source will compromise emission spectra accuracy in differentiating minor changes of pH values. Our result in wavelength selection and baseline suppression is thus of great importance when considering the tip size is at μ -scale, since a highly purified single-wavelength excitation source and suppressed background noise are necessary in order to obtain small changes of fluorescence signals.

Calibration and Linear Detection Range of the pH μ -Probe. Calibration of the pH μ -probe was conducted using a series of freshly standardized phosphate buffer solutions prepared at a pH range from 6 to 8 with 0.2 pH unit increments (Figure 5A). As the pH increased, higher fluorescent spectra peak intensities at 550 nm were observed. Tested buffer pH values and corresponding fluorescent intensity ratios of 550 nm/640 nm were found linearly correlated throughout this biologically relevant pH range (Figure 5B). In this study, three levels of laser coupling power (8.2, 22, and 39.8 mW) were used for pH measurements. The experimental results showed that improved linear correlation between fluorescent intensity ratio of 550 nm/640 nm and buffer pHs was observed as

laser power increased (from $R^2_{(8.2 \text{ mW})} = 0.9869$ to $R^2_{(39.8 \text{ mW})} = 0.9995$). Sensitivity in terms of fluorescent intensity ratio of $I_{550 \text{ nm}}/I_{640 \text{ nm}}$ per pH unit was also found increased (from 0.558 to 2.519). For each pH measurement, the standard deviation in triplicate measurements ranged between 0.0126 and 0.0836 pH units when 39.8 mW laser coupling power was used. Therefore, the pH resolution can theoretically be in the range of 0.010 - 0.066 pH units. Similarly, a theoretical pH resolution range of 0.0196 – 0.1236 pH units can be achieved when low coupling laser power of 5.8 mW was applied. Figure 5C provides a full interpretation of the pH detection resolution as functions of laser power used as well as the pH values of analytes. It shows that an optimal pH detection resolution can be obtained within the pH region of $\sim 6.9 - 7.2$, and increased laser power can further improve pH resolution below and above this region. This good linearity and sensitivity within the focused biological pH range not only provides a simple two-point calibration method, but also enables measurement for subtle environmental pH changes (0.038 ± 0.028 pH units). Besides, since the laser coupling power was linearly correlated with the original laser output power, and the laser power loss was also correlated with original output power as a natural logarithm function (Figure S-2A), then, higher pH detection sensitivity would be expected when a higher laser power is used (Figure S-2B). Strategic enhancement of the sensor's sensitivity may also be realized through incorporating a higher concentration of the pH sensitive dye to increase the total emitted photons. However, excessive dye molecules may compromise probe efficiency due to possible self-quenching and dye leaching. Thus, fine adjustment of laser power is potentially a convenient way to improve μ -probe performance, though over-heating and photo-bleaching effects should be considered accordingly.

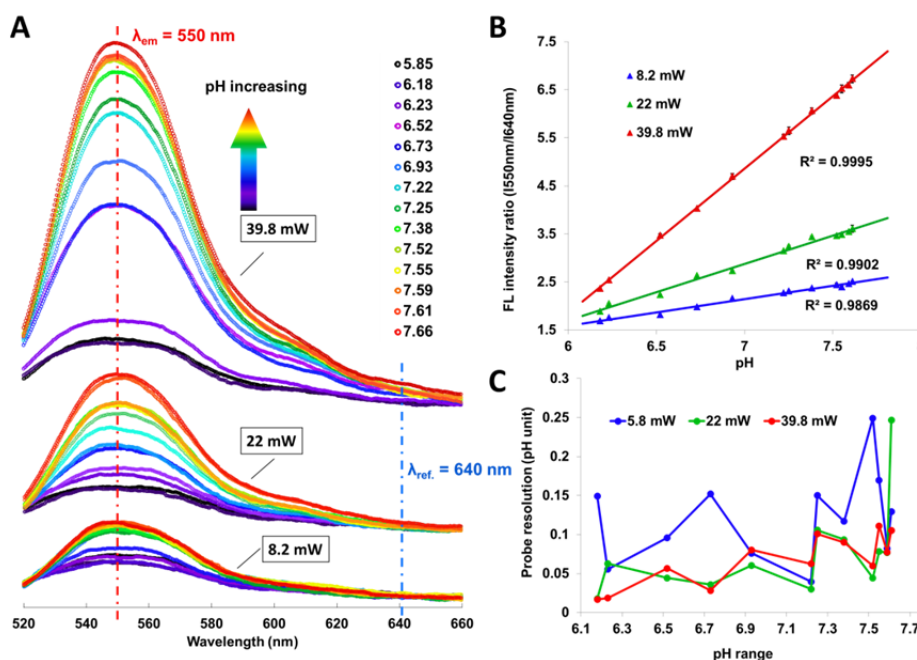


Figure 5. (A) Fluorescence spectra of pH measurements under three different laser coupling powers (8.2 mW, 22 mW, and 39.8 mW); (B) Linear correlation curves between standard pHs and different laser powers. (C) pH detection resolution as functions of power laser as well as pH values. The excitation wavelength applied was at 488 nm, the fluorescence wavelength at 550 nm, and the reference wavelength at 640 nm. The signal collecting integration time was 100 ms. “FL” is an abbreviation of fluorescence.

A bathochromic shift of the fluorescent peak near 550 nm was observed when comparing with the original 535 nm emission peak of BCECF dye in solution which was also observed in our prior work.⁴⁰ This phenomenon may be attributed to the increased dielectric constant of the bound dye molecules relative to aqueous, unbound conditions.⁵⁰ Similarly, localized ionic strength and temperature may influence pH measurements. Probe stability was measured to evaluate these influences by monitoring pH measurements over an extended time frame. The probes provided stable pH measurements for up to 30 minutes with minimal variance (2% relative standard deviation) and up to one month when stored in a sealed desiccator. The sol-gel

formulation was also highly stable under biologically important conditions with good performance under normal intracellular ionic strengths ranging from 0.08 – 0.20 M and cell culturing temperature range between 36.5 and 37.5 °C. These findings were in accordance with our prior work.⁴⁰

Intracellular pH Measurement in Single A549 Cells. The applicability of the newly developed pH μ -probes was preliminarily demonstrated in single A549 cell pH measurements (Figure 6). The probe was inserted 2-8 μm into the single cell cytosol by demobilizing the cell against a hollow capillary tube (Figure 6A). The pH probe was inserted into each cell three different times for statistical data acquisition. Probe excitation occurred for 20 ± 5 seconds using an automated beam shutter and the signal integration was 100 ms. Representative spectra from the single cells are shown in Figure 6B. Variance among the intracellular pH measurements was subjected to statistical group comparison analyses using a two-tailed Student's t-Test, although the limited sample size limits useful conclusions from being drawn (Figure 6C). Significant differences were observed among the three cells (P -value < 0.01) although no speculation about these differences and the underlying biological mechanisms responsible for these observations were made yet due to the small sampling number. After intracellular testing, all probes were subjected to immediate accuracy testing using standard pH buffers to confirmation probe's capability for repeatable measurements.

Hence, we have successfully demonstrated the newly developed probes which can measure intracellular or localized pH with minimal invasiveness and dye leakage. We anticipate these probes may be used in a range of fields for remote sensing or large-scale

matrix sensor integration, *in vivo* measurements, as well as ultra-small sample detection at nano-liter level.

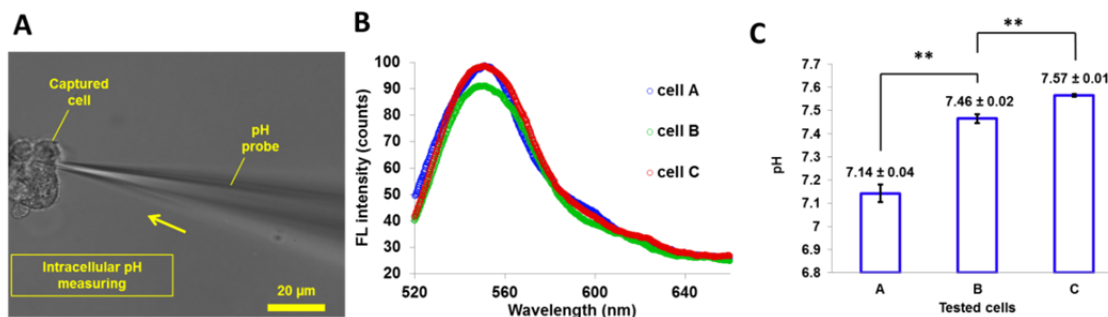


Figure 6. Preliminary measurement of intracellular pHs in single A549 cells using fabricated hexagonal pH μ -probe. (A) Randomly picked three single cells were separately manipulated and measured in a real-time manner. (B) Fluorescent spectra were acquired for each cell assay and (C) calculated pH values of each cell were established based on at least triplicate measurements and previously created calibration curve.

CONCLUSIONS

In the present study, a fiber-optic reflection-based pH μ -probe was developed for intracellular pH measurements. A coaxial-twisting and gravitational-stretching method was utilized to fabricate a unique hexagonal 1-in-6 fiber configuration. An OrMoSils-based dye-doping technique was used to covalently bind the dye molecules to the sensor tip. Additional surface modification using MTES and HDMS was used to provide a hydrophobic character to the surface to limit water penetration into the probe. The newly developed probed (tip diameter: 500 nm – 3 μ m) was evaluated in terms of resolution, stability, and sensitivity, all of which can be fine-tuned by the thickness of the surface coating, dye molecule concentration, and excitation light intensity. Under optimized conditions, the newly developed probe was found to correlate well with standardized pH under biologically relevant pH values (6.18-7.80) with excellent sensitivity ($0.038 \pm$

0.028 pH units). The newly developed probe was finally validated by application to single lung cancer A549 cells. Our results indicate that this novel pH probe may be applied to sensitive pH measurements at the single cell level and may have considerable impact for advancing understanding of important cellular processes such as cell differentiation and carcinogenesis.

ASSOCIATED CONTENT

Supporting Information Available:

These material is available free of charge via the Internet at <http://pubs.acs.org/>.

AUTHOR INFORMATION

Corresponding Author

***Tel.: (573) 341-6220, Fax: (573) 341-6033**

***E-mail: yinfa@mst.edu.**

NOTES

The authors declare no competing financial interest.

ACKNOWLEDGMENTS

The authors gratefully thank Qianyao Li for her assistance in SEM/FIBs imaging and characterization of the fabricated pH probes, and thank Casey Burton for his helpful language revisions and helpful discussions. This research was financially supported by National Institutes of Health grant (Award No. 1R21GM104696-01).

REFERENCES

- (1) Spiller, D. G.; Wood, C. D.; Rand, D. A.; White, M. R. *Nature* **2010**, *465*, 736-745.
- (2) Baumann, K. *Nature Reviews Molecular Cell Biology* **2014**.
- (3) Gillies, R. J.; Raghunand, N.; Karczmar, G. S.; Bhujwalla, Z. M. *Journal of Magnetic Resonance Imaging* **2002**, *16*, 430-450.
- (4) Busco, G.; Cardone, R. A.; Greco, M. R.; Bellizzi, A.; Colella, M.; Antelmi, E.; Mancini, M. T.; Dell'Aquila, M. E.; Casavola, V.; Paradiso, A. *The FASEB Journal* **2010**, *24*, 3903-3915.
- (5) Gallagher, F. A.; Kettunen, M. I.; Day, S. E.; Hu, D.-E.; Ardenkjær-Larsen, J. H. *Nature* **2008**, *453*, 940-943.
- (6) Webb, B. A.; Chimenti, M.; Jacobson, M. P.; Barber, D. L. *Nature Reviews Cancer* **2011**, *11*, 671-677.
- (7) Stüwe, L.; Müller, M.; Fabian, A.; Waning, J.; Mally, S.; Noël, J.; Schwab, A.; Stock, C. *The Journal of physiology* **2007**, *585*, 351-360.
- (8) Chattwood, A.; Thompson, C. R. *Development, growth & differentiation* **2011**, *53*, 558-566.
- (9) Riemann, A.; Ihling, A.; Schneider, B.; Gekle, M.; Thews, O. In *Oxygen Transport to Tissue XXXV*; Springer, 2013, pp 221-228.
- (10) Wojtkowiak, J. W.; Rothberg, J. M.; Kumar, V.; Schramm, K. J.; Haller, E.; Proemsey, J. B.; Lloyd, M. C.; Sloane, B. F.; Gillies, R. J. *Cancer research* **2012**, *72*, 3938-3947.
- (11) Gillies, R. J.; Verduzco, D.; Gatenby, R. A. *Nature Reviews Cancer* **2012**, *12*, 487-493.
- (12) Rink, T.; Tsien, R.; Pozzan, T. *The Journal of Cell Biology* **1982**, *95*, 189-196.
- (13) LIU, J.; DIWU, Z.; KLAUBERT, D. *ChemInform* **1998**, *29*.
- (14) Whitaker, J. E.; Haugland, R. P.; Prendergast, F. G. *Analytical biochemistry* **1991**, *194*, 330-344.
- (15) Zhang, Z.; Achilefu, S. *Chem. Commun.* **2005**, 5887-5889.
- (16) Han, J.; Burgess, K. *Chemical reviews* **2009**, *110*, 2709-2728.

- (17) SCHWIENING, C. J. In *SEMINAR SERIES-SOCIETY FOR EXPERIMENTAL BIOLOGY*, 1999, pp 1-18.
- (18) Resch-Genger, U.; Grabolle, M.; Cavaliere-Jaricot, S.; Nitschke, R.; Nann, T. *Nature methods* **2008**, *5*, 763-775.
- (19) Singer, V. L.; Lawlor, T. E.; Yue, S. *Mutation Research/Genetic Toxicology and Environmental Mutagenesis* **1999**, *439*, 37-47.
- (20) Alves de Lima, R. O.; Bazo, A. P.; Salvadori, D. M. F.; Rech, C. M.; de Palma Oliveira, D.; de Aragão Umbuzeiro, G. *Mutation Research/Genetic Toxicology and Environmental Mutagenesis* **2007**, *626*, 53-60.
- (21) Baird, G. S.; Zacharias, D. A.; Tsien, R. Y. *Proceedings of the National Academy of Sciences* **2000**, *97*, 11984-11989.
- (22) Ballou, B.; Lagerholm, B. C.; Ernst, L. A.; Bruchez, M. P.; Waggoner, A. S. *Bioconjugate chemistry* **2004**, *15*, 79-86.
- (23) Medintz, I. L.; Uyeda, H. T.; Goldman, E. R.; Mattoussi, H. *Nature materials* **2005**, *4*, 435-446.
- (24) Snee, P. T.; Somers, R. C.; Nair, G.; Zimmer, J. P.; Bawendi, M. G.; Nocera, D. G. *Journal of the American Chemical Society* **2006**, *128*, 13320-13321.
- (25) Dennis, A. M.; Rhee, W. J.; Sotto, D.; Dublin, S. N.; Bao, G. *Acs Nano* **2012**, *6*, 2917-2924.
- (26) Almutairi, A.; Guillaudeu, S. J.; Berezin, M. Y.; Achilefu, S.; Fréchet, J. M. *Journal of the American Chemical Society* **2008**, *130*, 444-445.
- (27) Medintz, I. L.; Stewart, M. H.; Trammell, S. A.; Susumu, K.; Delehanty, J. B.; Mei, B. C.; Melinger, J. S.; Blanco-Canosa, J. B.; Dawson, P. E.; Mattoussi, H. *Nature materials* **2010**, *9*, 676-684.
- (28) He, C.; Lu, K.; Lin, W. *Journal of the American Chemical Society* **2014**, *136*, 12253-12256.
- (29) Cheng, Y.; Xiong, P.; Yun, C. S.; Strouse, G.; Zheng, J.; Yang, R.; Wang, Z. *Nano Letters* **2008**, *8*, 4179-4184.
- (30) Huang, X.-r.; Ren, Q.-q.; Yuan, X.-j.; Wen, W.; Chen, W.; Zhan, D.-p. *Electrochemistry Communications* **2014**, *40*, 35-37.
- (31) Lin, J. *TrAC Trends in Analytical Chemistry* **2000**, *19*, 541-552.

- (32) Singh, S.; Gupta, B. D. *Sensors and Actuators B: Chemical* **2012**, *173*, 268-273.
- (33) Gu, B.; Yin, M.; Zhang, A. P.; Qian, J.; He, S. *Sensors Journal, IEEE* **2012**, *12*, 1477-1482.
- (34) Banshi, D. *Analyst* **2013**, *138*, 2640-2646.
- (35) Peterson, J. I.; Goldstein, S. R.; Fitzgerald, R. V.; Buckhold, D. K. *Analytical Chemistry* **1980**, *52*, 864-869.
- (36) Deboux, B.-C.; Lewis, E.; Scully, P.; Edwards, R. *Lightwave Technology, Journal of* **1995**, *13*, 1407-1414.
- (37) Malins, C.; Glever, H.; Keyes, T.; Vos, J.; Dressick, W.; MacCraith, B. *Sensors and Actuators B: Chemical* **2000**, *67*, 89-95.
- (38) Wencel, D.; MacCraith, B.; McDonagh, C. *Sensors and Actuators B: Chemical* **2009**, *139*, 208-213.
- (39) Maule, C.; Gonçalves, H.; Mendonça, C.; Sampaio, P.; Esteves da Silva, J. C.; Jorge, P. *Talanta* **2010**, *80*, 1932-1938.
- (40) Yang, Q.; Wang, H.; Lan, X.; Cheng, B.; Chen, S.; Shi, H.; Xiao, H.; Ma, Y. *Sensors and Actuators B: Chemical* **2015**, *207*, 571-580.
- (41) Scaffidi, J. P.; Gregas, M. K.; Seewaldt, V.; Vo-Dinh, T. *Analytical and bioanalytical chemistry* **2009**, *393*, 1135-1141.
- (42) Shapiro, E. M.; Sharer, K.; Skrtic, S.; Koretsky, A. P. *Magnetic Resonance in Medicine* **2006**, *55*, 242-249.
- (43) Boens, N.; Qin, W.; Basaric, N.; Orte, A.; Talavera, E. M.; Alvarez-Pez, J. M. *The Journal of Physical Chemistry A* **2006**, *110*, 9334-9343.
- (44) Thomas, J. A.; Buchsbaum, R. N.; Zimniak, A.; Racker, E. *Biochemistry* **1979**, *18*, 2210-2218.
- (45) Lin, W.; Huang, Y.-w.; Zhou, X.-D.; Ma, Y. *Toxicology and applied pharmacology* **2006**, *217*, 252-259.
- (46) Yang, Q.; Ma, Y. *International journal of toxicology* **2014**, 1091581814529168.
- (47) Nadargi, D. Y.; Latthe, S. S.; Hirashima, H.; Rao, A. V. *Microporous and Mesoporous Materials* **2009**, *117*, 617-626.

(48) Tasaltin, N.; Sanli, D.; Jonáš, A.; Kiraz, A.; Erkey, C. *Nanoscale research letters* **2011**, *6*, 1-8.

(49) Mirshafiei-Langari, S.-A.; Roghani-Mamaqani, H.; Sobani, M.; Khezri, K. *Journal of Polymer Research* **2013**, *20*, 1-11.

(50) Kriltz, A.; Löser, C.; Mohr, G. J.; Trupp, S. *Journal of sol-gel science and technology* **2012**, *63*, 23-29.

VI. High spatiotemporal in situ pH monitoring in a single live cell using a micro-fiber-optic probe

Qingbo Yang,¹ Xiaobei Zhang,² Yang Song,² Ke Li,¹ Honglan Shi,¹ Yinfu Ma,^{1*} Hai Xiao^{2*}

¹Department of Chemistry and Center for Single Nanoparticle, Single Cell, and Single Molecular Monitoring, Missouri University of Science and Technology, Rolla, MO 65409, USA

²Department of Electrical and Computer Engineering, Clemson University, Clemson, SC 29634, USA

*Corresponding Author

Address: Department of Electrical and Computer Engineering, Center for Optical Materials Science and Engineering Technologies (COMSET)

Clemson University

Clemson, SC29634, USA

E-mail: haix@clemson.edu

Abstract

Intracellular pH has long been recognized as an important indicator of dynamic cellular events as well as a universal marker of cell response and fate during its interaction with surrounding environments. To monitor the *in situ* pH in a single live cell, a micro-fiber-optic probe ($\sim 3\mu\text{m}$ in length) was developed and demonstrated for *in situ* intracellular pH monitoring with high spatiotemporal resolutions. The probe had a resolution of ~ 0.02 pH unit in the biologically relevant pH range of 6.17 to 8.11, with a fast response time of ~ 5 seconds. The probe examined by monitoring the pH changes in a single cell that caused by carbonyl cyanide *m*-chlorophenyl hydrazine (CCCP) and TiO_2 nanoparticles (NPs) exposure, showing an excellent capability in detecting early-stage cell deteriorations. Because of its high spatiotemporal resolution, this micro pH probe provides a powerful technique for researchers who are conduct single-cell-relevant researches.

Introduction

Cellular heterogeneity has been acknowledged as the major obstacle in understanding mechanisms of biological system functioning.¹ Therefore, it is crucial to monitor how each cell function individually under different environmental conditions by measuring the key intracellular parameters. Among all intracellular parameters, cytosolic proton concentration (or pH) serves as a universal indicator for fundamental cellular events, such as serving as a heterogeneity biomarker for early-stage cellular dynamics. However, the *in situ* intracellular pH measurement in a single cell with high spatiotemporal resolution, while the cell is fully functioning, is very challenge. The current intracellular pH detection mainly relies on artificially-modified fluorophores as cell staining/labelling

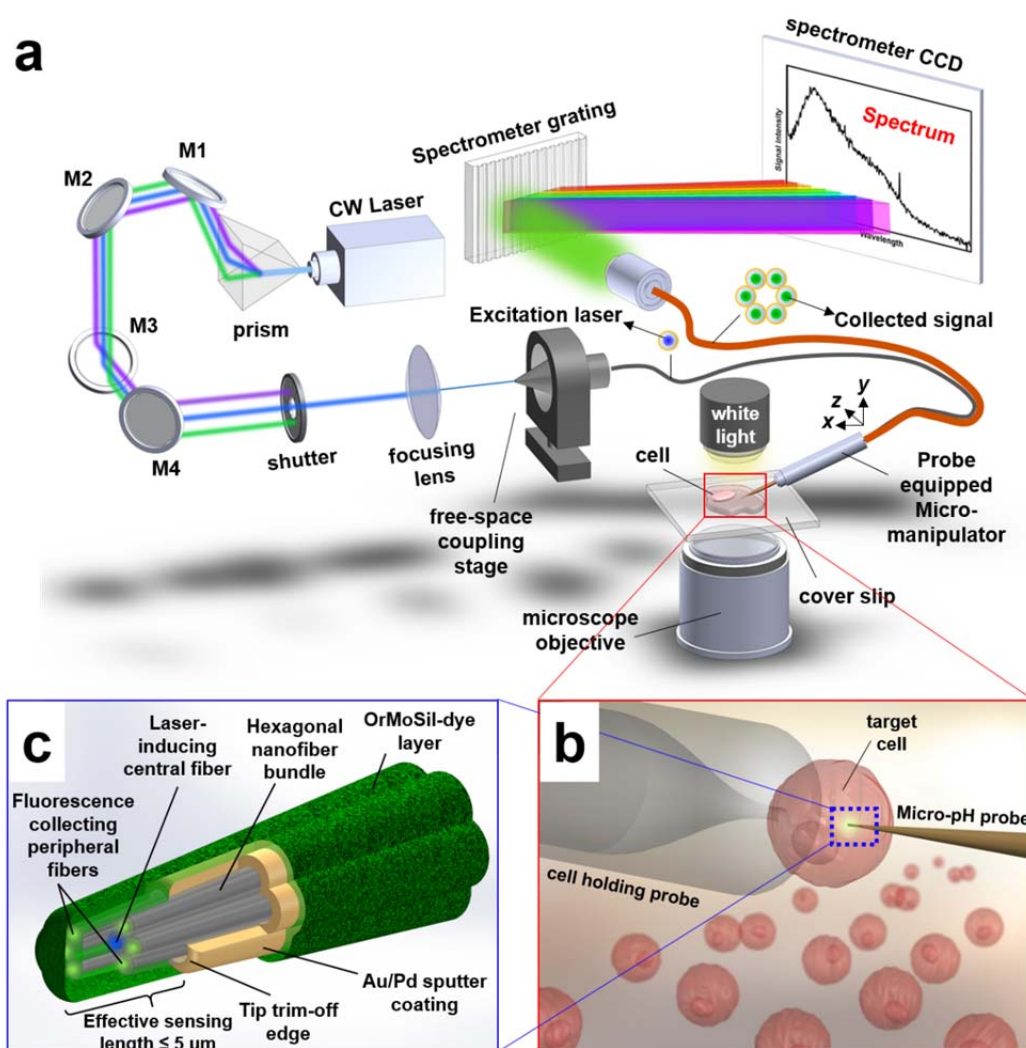
reagents.¹⁷⁻²⁸ The inevitably long and reinforced maintenance of the reagents within cytosol ruins the representativeness of derived signals. Potential cytotoxicity of excessive dye-usage, fluorescence attenuation, and non-continuous reagent passage to offspring cells, further deteriorate the accountability of staining-based assays. The major weakness of cell staining/labelling methodology is that it cannot be used for continuous single-cell pH measurements when the cellular exposure environment changes.

Recently, novel μ -probes with hexagonal 1-in-6 fiber configuration have been developed for fast intracellular pH measurement in a single cell. This novel single-cell pH probe has minimum invasiveness and negligible negative effect on the target cell.⁴⁶⁻⁵⁰ An organic modified silicates (OrMoSils) sensing layer was applied by embedding a pH sensitive dye, 2',7'-bis(2-carboxyethyl)-5-(and-6)-carboxyfluorescein (BCECF).⁴⁸ The pH sensing probe has a good linear response ($R^2 = 0.9869$) in the pH range of 6.18 – 7.80 and a pH resolution of ~ 0.038 pH unit. However, the major limitation of the existing single-cell pH probes is their relatively low spatial-resolution for smaller cells.

In this study, a novel *in situ* μ -pH-probe featured with a “tip-cut” high-spatial-resolution single-cell pH probe has been developed and a modified OrMoSil-dye coating using 8-hydroxypyrene-1, 3, 6-trisulfonate (HPTS) dye was used for pH sensing. . This probe was used to monitor the pH status of a single A549 cell under both normal-culturing and toxicant-exposure conditions. The probe was demonstrated to be able to differentiate heterogeneity from similar cells, and has the ability of sensing early-stage cell deteriorating process during toxicant-exposure, suggesting a great potentiality of this probe for broad applications in real-time single cell level researches.

Results

Design of the micro-fiber-optic based pH sensing system. A novel single-cell pH monitoring system was developed for high-spatiotemporal resolution pH measurement with minimal cellular invasiveness (Scheme 1a). A 488 nm laser beam was used for excitation⁴⁸ and free-space-coupled into the central fiber using a focusing lens and controlled by a programmable beam shutter. The fluorescent signal was collected and transmitted by the peripheral six fibers to a spectrometer. Due to the unique design of this novel probe, only the fluorescent signal at the tip (~3-microns) was collected so that the excitation and emission photons can be separated to minimize any signal leakage and avoid interferences from exterior light, which significantly enhance the sensitivity. A zoom-in schematic (Scheme 1b) illustrates how the probe was inserted into the cytoplasmic region of a single cell for pH sensing. An oil-pressure controlled hollow cell holding probe was used for cell micromanipulation and immobilization and to assist steady probe insertion. This probe can not only be used on trypsinized (detached) cells, but also for attaching-cultured cells. Scheme 1c shows a zoom-in view of the probe tip. The exposed inner structures clearly indicate a four-hierarchy configuration of the probe head, which composed of: 1) the central layer excitation beam introducing-fiber, 2) the peripheral six fluorescence signal-collection fibers, 3) the gold (Au)/palladium (Pd) sputtered shielding layer, and 4) the outmost OrMoSil-dye coating layer. The Au/Pd shielding layer was specifically designed to be trimmed off at the very tip region so that the exposed short length (less than 5 microns) of the probe tip can be the only effective shaft for signal production. In this case, although the upper part of the probe was also dip-coated with OrMoSil-dye layer and can be sensitive to pH changes, the fluorescence



Scheme 1. Schematics of system setup and single cell μ -pH probe design. (a) Schematic illustration of the single cell pH probing system assisted with an inverted epifluorescence microscope. A continuous wave Ar-ion laser was used as excitation source and was optically coupled into the central fiber for excitation, and the surrounding six fibers were fixed onto a portable spectrometer (USB2000, Ocean Optics). Accurate single cell insertion was achieved by an oil-pressured single cell capturing device and a 3-D micro-probe manipulation platform. (b) A schematic zoom-in view of a single cell probing device. A cell holding probe assists single cell capturing and probe insertion. (c) Schematic of The pH probe head structure and the sensing principle. The probe was consisted of a bundle of highly tapered, seven hexagonally configured optical multimode fibers using a coaxial-twisting and gravitational-stretching system. A gold (Au)/palladium (Pd) shielding layer is deposited onto the peripheral six fibers with a tip trimming-off region ($\leq 5 \mu\text{m}$), which was finally covered by the OrMoSil-dye sensing layer. The excitation laser was introduced through the central fiber and the peripheral six fibers collected fluorescent signals only at the non-shielded region.

generated from this part will not be collected due to the shielding effect of the coated Au/Pd underneath. Another advantage of the Au/Pd coating is that the background noise from the environment can be eliminated to enhance the sensitivity. Overall, this novel pH probe can provide higher sensing accuracy and selectivity up to several folds in decoding subcellular signals to help us better understand cellular heterogeneity between each single cells.

The μ -pH probe was fabricated by utilizing our home-built coaxial-twisting and gravitational-stretching method⁴⁸ (Supplementary Fig. 1, a - c) and a novel tapered hexagonal 1-in-6 fiber configuration was created to enhance the sensitivity significantly (Fig. 1 and Supplementary Fig. 1). The macroscopic (Supplementary Fig. 1d), schematic (Fig. 1a) and microscopic (Fig. 1b) view of the fabricated taper-shaft were demonstrated, respectively. The shaft was subjected to a Au/Pd sputter coating under a maximum 50 mA current for about 15 minutes (Fig. 1d, Supplementary 1i), followed by trimming off the very tip-region sputtered Au/Pd layer using focused ion beams (FIBs, Helios Nanolab 600, FEI) milling under scanning electron microscope (SEM)(Fig. 1e, Supplementary 1j). Approximately 250 – 300 nm Au/Pd was uniformly deposited onto the surface, of which only the tip part (less than 5 micron length) was milled. Dispersive X-ray spectroscopic (EDS) mapping (Fig. 1f and Supplementary Fig. 2) indicated a successful removing of the sputtered metal layer at the tip without damaging the underlying fibers. Immediate sol-gel dip-coating and aging, curing was conducted (Supplementary Fig. 1h), to form rigid bonds between exposed silica surface and the dye-doped hybrid sol-gel. The resulted probe was finally achieved with a typical “tip-cut” configuration that only the fluorescence emission at the tip (Fig. g, h, Supplementary Fig. k) was collected. The

novelty of this configuration is that it confines the fluorescent signal-collecting area at the 3 μm tip to avoid massive interfering lights from other areas of the sensor tip, which significantly enhanced the spatial resolution of the probe when only the proton concentrations inside the cell is interested. Technically, the fiber pre-alignment (Supplementary Fig. 1b) and tensile strength balancing should be properly conducted in order to produce rigid tapering. The twisted shaft stem is further demonstrated (Supplementary fig. 1e – g) and the detailed tip imaging showed that each single fiber diameter within the tip fiber bundle has gone down to ~ 100 nm width.

The pH-sensing ability of the probe was realized by utilizing a pH sensitive HPTS dye⁵¹⁻⁵³ and a hybrid sol gel method (Fig. 1, l). The pH sensitive HPTS dye was mixed (1:2 in molar ratio) with cetyl-trimethyl ammonium bromide (CTAB) to form the HPTS-CTAB ion pair complex, followed by mixing with the prepared ethyltriethoxysilane (ETEOS) and (3-glycidoxypropyl)trimethoxysilane (GPTMS) based sols, and the complete entrapment within the ultimate nano-structured aerogel networks was formed after curing. The microstructure of the thin OrMoSil film was tailored to ensure completely encapsulation of the dye-containing ion-pairs without leaching. The detailed procedures can be found in the method section.

The HPTS dye has superior photo-stability at the pK_a of ~ 7.30 , and its conjugation with CTAB through ion-pairing strengthened the dye immobilization to avoid unnecessary disorder of molecular resonance and bathochromic shift that may occur by covalent bond. The polar GPTMS precursor was used to provide a hydrophilic matrix to promote proton permeability and the ETEOS precursor was used to provide mechanical stability and inner hydrophobic backbone (Fig. 1l).⁵⁴ The molar ratio of

reactants and catalyst were adjusted to obtain optimized dye loading capability, sensing ability and film stability.⁵⁴ A 488 nm wavelength was used for excitation and the fluorescent signals were collected at ~510 nm in response to the varied pHs in a single cell, though other choices may also be applied.⁵⁴ With this novel design, no dye leaking was observed during the protonation and deprotonation process (Fig. 1m).

μ -pH probe characterization and validation. The fabricated probe was characterized through SEM/FIBs/EDS scanning and validated by pH measurements under physiologically-relevant conditions. Fig. 1i clearly shows the cross-section view of the probe tip (~15 μ m away from the tip end), where seven fibers were hexagonally aligned. All of the seven fiber cores are still well-separated, which can avoid direct light passing-through between central and peripheral fibers. Fig. 1j and 1k are zoom-in views of the porous nano-networks as well as the depth (~450 nm) of the OrMoSil-dye coating layer as yellow square boxes labelled in Fig. 1i. An enriched level of carbon (C) with lower levels of O and Si from EDS results clearly demonstrates a uniform deposition of the OrMoSil-dye layer.

Photonic simulation was conducted in parallel to better understand the photon behaviors at the probe tip, thus optimize the fabrication process and prove the sensing capability at such a small probe tip (Supplementary Fig. 3, a - d). The central fiber wave-guided 488 nm laser beam was found to start weakly oscillate between the central and peripheral fibers in the tapering tip at < 4 μ m (Supplementary Fig. 3e). This is mainly because of the changed permeability of the cladding after tapering. Once the diameter

becomes small, it allows the evanescent wave to pass through in-and-out of the central fiber substantially, which ultimately can be coupled out of the probe at the last 15 μm length region of the probe tip (Supplementary Fig. 3, f - i). The additional confinement of the “tip-cut” region by the sputtered Au/Pd shielding layer is thus necessary to prevent any lights from outside of the cell being collected by the probe and only so that the 510 nm fluorescence inside the cell can well be collected by the probe tip.

The $\mu\text{-pH}$ probe was calibrated using standardized pH buffers under constant conditions (Fig. 1n), and a good linear correlation ($R^2 = 0.9827$) between applied pHs and spectra peak area (Fig. 1o) was demonstrated. A higher coefficient can be obtained ($R^2 = 0.9895$) in a narrower pH range from 6.17 to 8.11. It was found that using peak area provided a better linearity than the double-wavelength ratiometric method (560nm/640nm) because the spectra fluctuation can be mostly eliminated⁴⁸ (Supplementary Fig. 4, a - i). Therefore, the entire data in this study were collected by using the peak area and the pH sensitivity was calculated in terms of change in fluorescent peak area per pH unit. An average of 14,867 unit change in peak area was found corresponding to one pH unit variation within the biologically-relevant pH range. The pH resolution was calculated with an average of 0.0657 pH unit. An iteration-based curve-fitting process (OriginLab) was used to smooth the curves (Supplementary fig. 4j) and the optimize pH resolution can reach to ~ 0.02 pH unit.

To evaluate the probe under realistic biological conditions and exclude cytoplasmic matrix influences, the $\mu\text{-pH}$ probe was further evaluated by using an intracellular pH calibration kit through measuring the same series of cells under a fixed pH buffer condition and clamped intracellular pH using valinomycin and nigericin (Fig.

1p).^{55,56} A 95% measuring accuracy was confirmed by comparing the measured pH results between using the kit and using the probe. Afterwards, four key parameters were examined on how each of the parameters affect the accuracy of pH measurement (Fig. 1, q - t). it was found that there was significant change of ionic strength with temperature within the physiologically-relevant pH range (Fig. 1, q and r),⁵⁷ and neither the glucose nor the bovine serum albumin (BSA) interferes the probe performances (Fig. 1, s and t). These evaluations demonstrated that the sensing feasibility of the probe under *in vitro* physiological circumstances. The potential photo-bleaching was also evaluated by irradiating a glass cover slip that coated with the same aerogel layer (Supplementary Fig. 5). Gradual fluorescence attenuation of ~10% and 20% intensity-drop between 900 and 1500 seconds were observed respectively, which is appreciably acceptable, since the laser beam was permitted to transmit to the probe tip for merely ~ 5 seconds in real pH measurement.

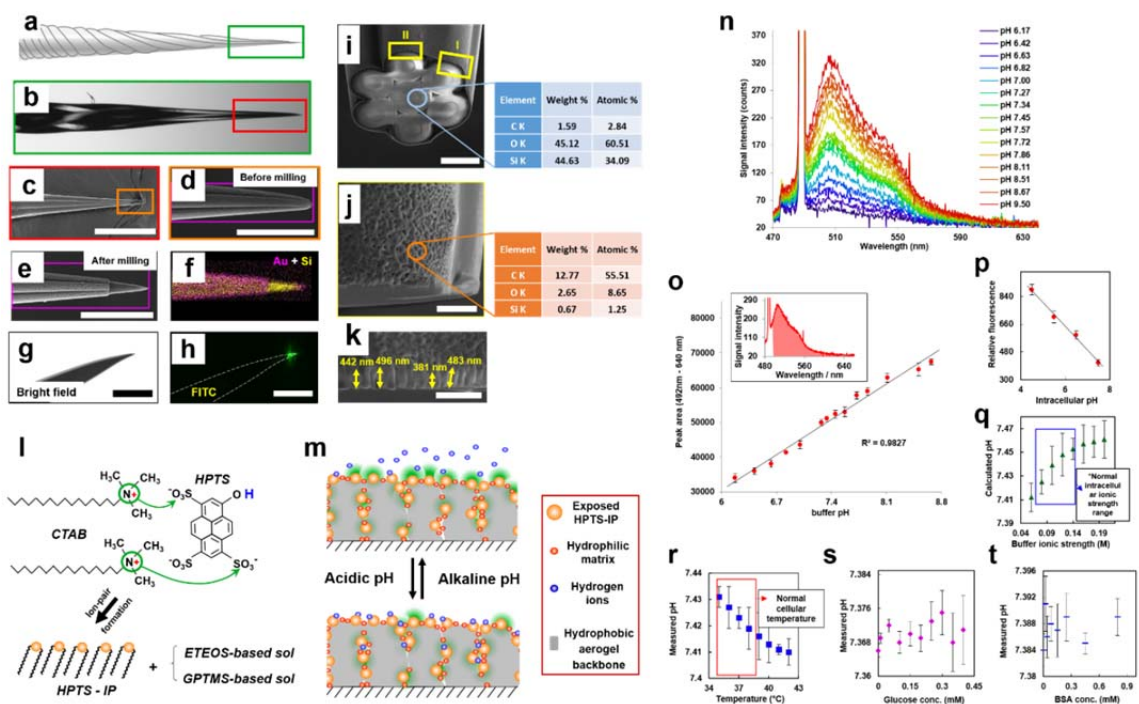


Figure 1 Fabrication and validation of the μ -pH probe. (a) Schematic representation of the coaxially twisted probe tip. The squared green box was shown in (b), indicating the actual tip configuration imaged in bright-field channel under inverted microscope. The red squared box was then shown in (c) under SEM, with a tip diameter around 500 nm – 1 μ m. (d) Enlarged area of the squared orange box in c, to show the tip after a thick sputter coating of Au and Pd. (e) An exemplary probe tip after FIBs milling (cutting) of the first 5 μ m sputter-coated Au/Pd layer to expose the underneath SiO₂ surface. (f) EDS mapping of the “tip-cut” area to show the exposed underneath Si after sputter-coated Au being milled off by FIBs. A fully fabricated probe with OrMoSil-dye coating is then shown under inverted microscope in (g) bright-field, and (h) FITC channels. (i) SEM image of the cross-section of the probe (positioned 15 μ m away from the tip-end) indicates a well-maintained hexagonal configuration until the very end of the probe. (j) A zoom-in view of the porous nanostructure of the OrMoSil-dye coated probe surface (the right yellow square box in i). The comparison of EDS elemental scanning between i and j illustrate a substantial distribution of carbon on the outer probe layer, demonstrating a successful aerogel deposition. (k) A zoom-in view of the left yellow square box in i shows an averaged \sim 450 nm thickness of the coated OrMoSil-dye sensing layer. (l) Sketch showing the ion pair (IP) formation of the HPTS-CTAB conjugates, as well as the basic formula of the hybrid OrMoSil sol-gel for probe dip-coating. (m) Schematic representation of the pH-sensing principle of the porous OrMoSil sensing layer with entrapped HPTS-IP complex. (n) Detected fluorescent spectra by the probe using standardized gradient pH buffer solutions. (o) Linear correlation between standardized pHs and signal peak-area covers a wavelength range from 492 nm to 640 nm. The measurement of the pH probe was further confirmed by using an intracellular pH calibration kit (p), and validated using varied (q) ionic strength (sodium chloride), (r)

temperature, (s) glucose concentration as well as (t) BSA concentration, under the same pH and physiological-relevant conditions. Objects are not drawn to scale. Scale bars: c, g, h, 50 μm ; d, 6 μm ; e, 10 μm ; I, 5 μm and j, k, 1 μm .

Intracellular pH measurement in a single live cell. The capability of the developed μ -probe to measure intracellular pH in a single cell was tested using freshly-trypsinized single A549 cells (Fig. 3). Three exemplary probe insertion and *in situ* pH measurements were demonstrated with randomly selected cells (Fig. 2, a-f). Bright-field channel images (Fig. 2, a, c, e) show a shallow cytoplasmic insertion of the probe in each measurement, while the merged fluorescent images (Fig. 2, b, d, f) show DAPI stained cell nucleus and the lightening spot (FITC channel) of the inserted probe tip. Inserts are zoom-in view of each lightening spots which only occupy an average of $\sim 500 \text{ nm}^3$ volume. The total insertion-equilibrating and signal-acquisition time was less than 5 seconds. Therefore, this novel probe can be used for *in situ* pH measurements with high spatiotemporal resolution. The whole process for cell capturing, inserting, and releasing process was shown in the supplementary figure and video (Supplementary Fig. 6, Supplementary video clip #1). The unique advantage of this probe is that the whole probe insertion process maintains a minimum invasiveness to the cell membrane, and the cell viability was not shown significant differences between probed and non-probed cells for at least 24 hours. Additional twelve individual cells were also captured and tested using this probe and the results were summarized in a bar graph (Fig. 2g). Even two possible outliers (green dots) were excluded, an overall larger than one pH unit differentiation was found between the cell with the highest pH (pH 7.78) and the cells with the lowest pH (pH 6.72) unprecedentedly exhibits a distinctive heterogeneity among the seemingly identical cells under the same culturing environment.

Monitoring of cell deterioration process by using this novel probe. The probe was applied for dynamic cell sensing under two different cytotoxicating conditions using carbonyl cyanide *m*-chlorophenyl hydrazine (CCCP) and a 40 nm titanium dioxide (TiO₂) nanoparticles (NPs). Mitochondria are known for their energy metabolism controlling and are crucial organelle involves in many cellular events and responses to surrounding environment.⁵⁸ Interrupted mitochondrial function will directly damage cellular energy consumption and even cause cell death.⁵⁹⁻⁶² We applied a mild dose (50 μM) of CCCP in cells to purposely cause negative effect on the mitochondrial inner membrane potential ($\Delta\psi_m$) through depolarization.⁶³ Then the cellular statuses were closely monitored by using the novel μ-pH probe and a $\Delta\psi_m$ sensitive dye J-aggregate-forming lipophilic cation (JC-1).^{64,65} JC-1-stained cell images (Fig. 2h) were quantified and plotted based on the fluorescent intensity ratio of Cy3/FITC (Fig. 2i), and compared with measured pHs with the developed μ-pH probe measured from 10 individual cells (Fig. 2j). Results show a quick pH decreasing within 40 minutes (Fig. 2j) from averaged pH level ~ 7.5 down to ~ 5.3, meanwhile no apparent cell deterioration trend was observed in the JC-1-stained group (Fig. 3i). A longer time of monitoring did not show apparent $\Delta\psi_m$ damaging by using JC-1 staining until 3 hours after CCCP-dosing, which demonstrated the sensitivity of the this novel probe that has great potential in detecting early-stage intracellular dynamic events.⁶⁶⁻⁶⁹ The result obtained from our study is consistent with the previously reported stringent connection between intracellular pH and mitochondria,⁶⁶⁻⁶⁹ and suggests that the intracellular pH change can potentially serve as an alternative indicator for mitochondria dysfunction and cell deterioration. We further conducted a twelve-hour single cell pH measurements with and without exposure to 100

$\mu\text{g/mL}$, 40 nm TiO_2 NPs. Fundamental heterogeneity was clearly observed through significantly varied single cell responses ($n_{\text{total}} = 23$) to the same NP-exposure condition (Fig. 2k), and a statistically significant difference ($p < 0.05$) between control and NP-exposed cells were observed after the first two hours NP-exposure.

Discussion

A novel ratiometric-free, fiber-optic $\mu\text{-pH}$ probe that can be feasibly applied in biophysiological niche environmental pH measurements was developed and demonstrated. The pH sensitive dye molecules are well-confined within the OrMoSils aerogel thin layer, and a featured “tip-cut” design enables its high spatial-resolution sensing ability. The linear pH sensing range of the probe perfectly fits the physiologically-relevant condition from $\sim 6.0 - 8.0$, and an optimized pH resolution up to ~ 0.02 pH unit significantly enhances its applicability in tracking subtle cellular pH variations. The effective sensing surface area can further be tailored by simply modifying the “tip-cut” region into desired tip length. The unique advantages of this novel probe are that its high-spatial-resolution was not compromised by sacrificing its extraordinary temporal resolution, and a real-time sensing can be achieved because of its fast equilibrating process. Moreover, the steady signal acquisition of the probe can be maintained for hours, thus it is very useful for intracellular macromolecular kinetics sensing (e.g. endoplasmic reticulum and mitochondria). The high-spatiotemporal resolution character of the probe provides biomedical researchers opportunity to study early-stage cell events in one single cell.

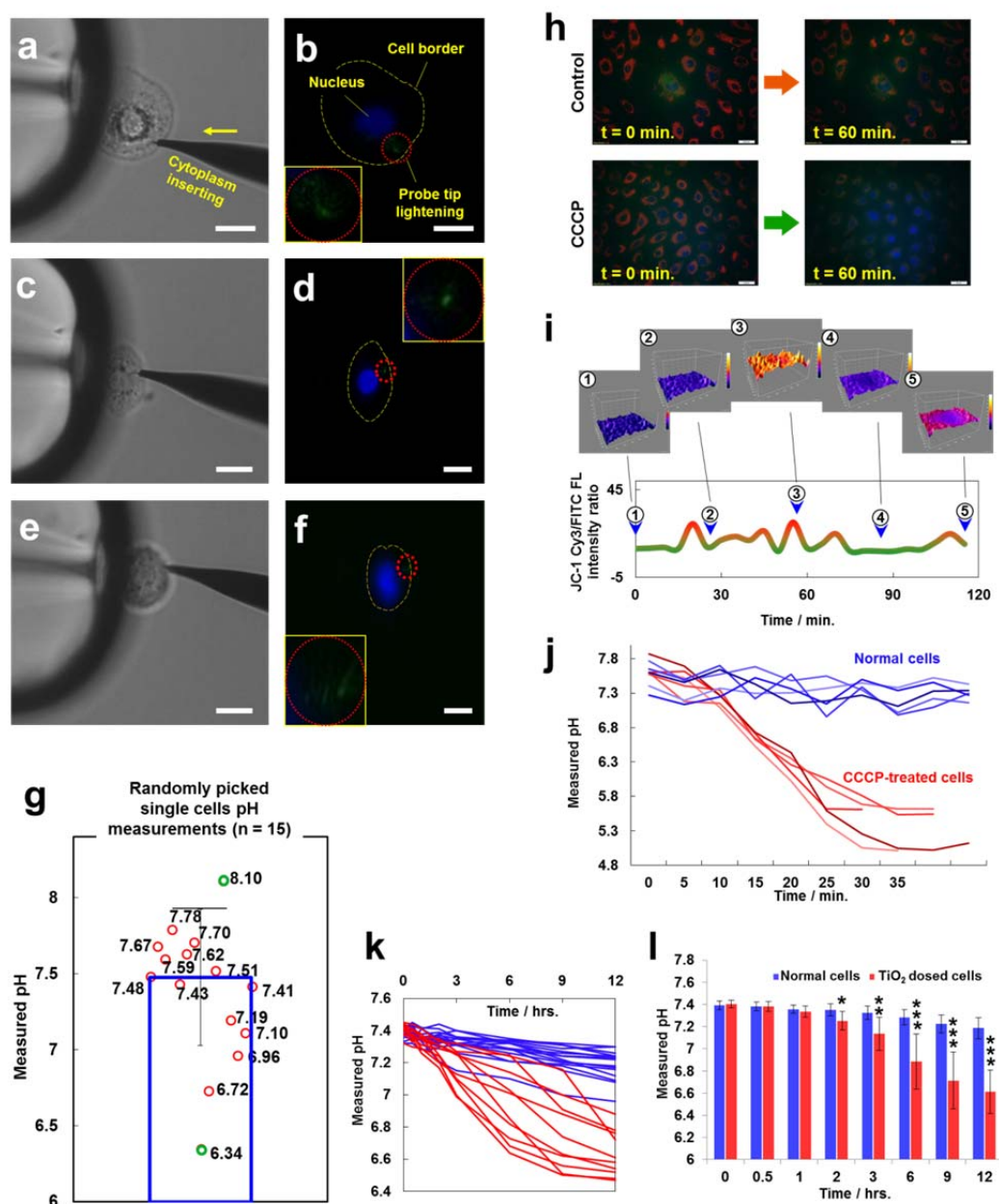


Figure 2 Early-stage cell deterioration illustrations by *in situ* single cell pH sensing. Three exemplary single A549 cell capturing and intracellular probing are shown under bright-field (**a**, **c**, **e**) and fluorescent channels (**b**, **d**, **f**). Merged fluorescent images were taken under DAPI (cell nucleus) and FITC (HPTS dye fluorescence) channels. The inset zoom-in views of the probe tip lightening area demonstrate a tiny sensing spot within the cytoplasmic region. (**g**) Quantification summary of intracellular pH measurements from 15 randomly chosen single cells. Each data points stand for signals from one cell and the bar graph shows the averaged median values \pm standard deviation. Green dots with measured pH of 6.34 and 8.10 are two suspected outliers. (**h**) Images of mitochondria membrane potential variation during CCCP toxicating, indicated by JC-1 dye staining.

90% confluent A549 cells were exposed to 50 μM CCCP for one hour, and epifluorescent images were taken under FITC/Cy3 channels and compared with control. **(i)** Images were calculated and 3-D plotted based on the fluorescent intensity ratio of Cy3/FITC, and were finally averaged and plotted vs. time. **(j)** Intracellular pH real-time measurement for five single A549 cells treated by the same CCCP-toxicating condition as was in **i**, and compared with non-treated cells. **(k)** Single cell real-time monitoring of intracellular pH during cell exposure to 100 $\mu\text{g}/\text{mL}$, 40 nm TiO_2 NPs for 12 hours. Red lines are tested cells while blue lines represent controls. **(l)** Bar graph shows the analyzed data from **k**. Statistical significance is indicated by the asterisk, where * means $p < 0.05$, ** means $p < 0.01$ and *** means $p < 0.001$. Scale bars: **a - f**, 10 μm ; **h**, 20 μm .

This novel probe can provide widespread biological applications. In addition to monitor pH changes in a single cell, it can also monitor pHs outside of a cell surface and other niche environment that other pH device may not be applicable. These unique features may unprecedentedly leverage biomedical and biological researches in single-cell heterogeneity-related areas, such as cell differentiation processes in stem cells and developmental biology studies, cell plasticity and cell fate determination, early-stage carcinogenesis studies, cytotoxicity studies, as well as development and evaluation of pH-responding drug delivery. For all these applications, ultimate multi-parametric probing of targeted micro-bio-sample through simultaneous, constant, optical monitoring, with minimum invasiveness, as would be promptly implemented by using our developed single cell sensing system, is of fundamental interest in the future precise medicine practices. Finally, a high-throughput single-cell-resolution analyzing workstation can be established based on this novel system, combining with automatic control of cell manipulation, microfluidic-devices, advanced imaging and multifunctional sensing probes.

Acknowledgements

The authors gratefully thank Qianyao Li and Jessica Terbush for their assistance in SEM/FIBs imaging, characterization and fabrication of the probe. This research was financially supported by National Institutes of Health grant (Award No.1R21GM104696-01).

References

- (1) Arriaga, E. A. *Single Cell Analysis: Technologies and Applications* **2009**, 223-234.
- (2) Fritz, J.; Raithel, E.; Thawait, G. K.; Gilson, W.; Papp, D. F. *Investigative radiology* **2015**.
- (3) Uğurbil, K.; Xu, J.; Auerbach, E. J.; Moeller, S.; Vu, A. T.; Duarte-Carvajalino, J. M.; Lenglet, C.; Wu, X.; Schmitter, S.; Van de Moortele, P. F. *Neuroimage* **2013**, *80*, 80-104.
- (4) Berker, Y.; Franke, J.; Salomon, A.; Palmowski, M.; Donker, H. C.; Temur, Y.; Mottaghy, F. M.; Kuhl, C.; Izquierdo-Garcia, D.; Fayad, Z. A. *Journal of Nuclear Medicine* **2012**, *53*, 796-804.
- (5) Rahbar, H.; DeMartini, W. B.; Lee, A. Y.; Partridge, S. C.; Peacock, S.; Lehman, C. D. *European journal of radiology* **2015**, *84*, 611-616.
- (6) Cevidane, L.; Bailey, L.; Tucker Jr, G.; Styner, M.; Mol, A.; Phillips, C.; Proffit, W.; Turvey, T. *Dentomaxillofacial Radiology* **2014**.
- (7) Pinker, K.; Bogner, W.; Baltzer, P.; Trattnig, S.; Gruber, S.; Abeyakoon, O.; Bernathova, M.; Zaric, O.; Dubsy, P.; Bago-Horvath, Z. *European radiology* **2014**, *24*, 913-920.
- (8) Bhattacharyya, S.; Khasnobish, A.; Ghosh, P.; Mazumder, A.; Tibarewala, D. *Biomedical Image Analysis and Mining Techniques for Improved Health Outcomes* **2015**, 39.
- (9) Idelson, C. R.; Vogt, W. C.; King-Casas, B.; LaConte, S. M.; Rylander, C. G. *Lasers in surgery and medicine* **2015**, *47*, 495-502.
- (10) Hassan, M.; Dufor, O.; Benquet, P.; Berrou, C.; Wendling, F. In *Neural Engineering (NER), 2015 7th International IEEE/EMBS Conference on*; IEEE, 2015, pp 1060-1063.

- (11) Burle, B.; Spieser, L.; Roger, C.; Casini, L.; Hasbroucq, T.; Vidal, F. *International Journal of Psychophysiology* **2015**.
- (12) Yuan, H.; Ding, L.; Zhu, M.; Zotev, V.; Phillips, R.; Bodurka, J. *Brain connectivity* **2015**.
- (13) Astolfi, L.; Cincotti, F.; Mattia, D.; Fallani, F. D. V.; Vecchiato, G.; Salinari, S.; Vecchiato, G.; Witte, H.; Babiloni, F. *Journal of Psychophysiology* **2015**.
- (14) Sánchez-Crespo, A.; Andreo, P.; Larsson, S. A. *European journal of nuclear medicine and molecular imaging* **2004**, *31*, 44-51.
- (15) Seifert, S.; Van der Lei, G.; Van Dam, H. T.; Schaart, D. R. *Physics in medicine and biology* **2013**, *58*, 3061.
- (16) Cheng, J.-C.; Boellaard, R.; Laforest, R. *Nuclear Science, IEEE Transactions on* **2015**, *62*, 101-110.
- (17) Heim, N.; Garaschuk, O.; Friedrich, M. W.; Mank, M.; Milos, R. I.; Kovalchuk, Y.; Konnerth, A.; Griesbeck, O. *Nature methods* **2007**, *4*, 127-129.
- (18) Cheng, A.; Gonçalves, J. T.; Golshani, P.; Arisaka, K.; Portera-Cailliau, C. *Nature methods* **2011**, *8*, 139-142.
- (19) Welsher, K.; Liu, Z.; Daranciang, D.; Dai, H. *Nano letters* **2008**, *8*, 586-590.
- (20) Wang, C.; Cheng, L.; Xu, H.; Liu, Z. *Biomaterials* **2012**, *33*, 4872-4881.
- (21) Hennig, S.; van de Linde, S.; Lummer, M.; Simonis, M.; Huser, T.; Sauer, M. *Nano letters* **2015**, *15*, 1374-1381.
- (22) Walker, C. L.; Lukyanov, K. A.; Yampolsky, I. V.; Mishin, A. S.; Bommarius, A. S.; Duraj-Thatte, A. M.; Azizi, B.; Tolbert, L. M.; Solntsev, K. M. *Current opinion in chemical biology* **2015**, *27*, 64-74.
- (23) Mickler, F. M.; Möckl, L.; Ruthardt, N.; Ogris, M.; Wagner, E.; Bräuchle, C. *Nano letters* **2012**, *12*, 3417-3423.
- (24) Kang, B.; Afifi, M. M.; Austin, L. A.; El-Sayed, M. A. *Acs Nano* **2013**, *7*, 7420-7427.
- (25) Zrazhevskiy, P.; Gao, X. *Nature communications* **2013**, *4*, 1619.
- (26) Alford, R.; Simpson, H. M.; Duberman, J.; Hill, G. C.; Ogawa, M.; Regino, C.; Kobayashi, H.; Choyke, P. L. *Molecular imaging* **2009**, *8*, 341.

- (27) Albanese, A.; Tang, P. S.; Chan, W. C. *Annual review of biomedical engineering* **2012**, *14*, 1-16.
- (28) Hoshino, A.; Hanada, S.; Yamamoto, K. *Archives of toxicology* **2011**, *85*, 707-720.
- (29) Kitamura, K.; Judkewitz, B.; Kano, M.; Denk, W.; Häusser, M. *Nature methods* **2008**, *5*, 61-67.
- (30) Yan, R.; Park, J.-H.; Choi, Y.; Heo, C.-J.; Yang, S.-M.; Lee, L. P.; Yang, P. *Nature Nanotechnology* **2012**, *7*, 191-196.
- (31) Zheng, X. T.; Li, C. M. *Chemical Society Reviews* **2012**, *41*, 2061-2071.
- (32) Actis, P.; Tokar, S.; Clausmeyer, J.; Babakinejad, B.; Mikhaleva, S.; Cornut, R.; Takahashi, Y.; López Córdoba, A.; Novak, P.; Shevchuck, A. I. *Acs Nano* **2014**, *8*, 875-884.
- (33) Tan, W.; Shi, Z.-Y.; Smith, S.; Birnbaum, D.; Kopelman, R. *Science* **1992**, *258*, 778-781.
- (34) Vitol, E. A.; Orynbayeva, Z.; Bouchard, M. J.; Azizkhan-Clifford, J.; Friedman, G.; Gogotsi, Y. *Acs Nano* **2009**, *3*, 3529-3536.
- (35) Patolsky, F.; Timko, B. P.; Yu, G.; Fang, Y.; Greytak, A. B.; Zheng, G.; Lieber, C. M. *Science* **2006**, *313*, 1100-1104.
- (36) Wu, W.-Z.; Huang, W.-H.; Wang, W.; Wang, Z.-L.; Cheng, J.-K.; Xu, T.; Zhang, R.-Y.; Chen, Y.; Liu, J. *Journal of the American Chemical Society* **2005**, *127*, 8914-8915.
- (37) Takahashi, Y.; Shevchuk, A. I.; Novak, P.; Murakami, Y.; Shiku, H.; Korchev, Y. E.; Matsue, T. *Journal of the American Chemical Society* **2010**, *132*, 10118-10126.
- (38) Singhal, R.; Orynbayeva, Z.; Sundaram, R. V. K.; Niu, J. J.; Bhattacharyya, S.; Vitol, E. A.; Schrlau, M. G.; Papazoglou, E. S.; Friedman, G.; Gogotsi, Y. *Nature Nanotechnology* **2011**, *6*, 57-64.
- (39) Zenobi, R. *Science* **2013**, *342*, 1243259.
- (40) Bendall, S. C.; Simonds, E. F.; Qiu, P.; El-ad, D. A.; Krutzik, P. O.; Finck, R.; Bruggner, R. V.; Melamed, R.; Trejo, A.; Ornatsky, O. I. *Science* **2011**, *332*, 687-696.
- (41) Elias, J. E.; Gygi, S. P. *Nature methods* **2007**, *4*, 207-214.
- (42) Stoeckli, M.; Chaurand, P.; Hallahan, D. E.; Caprioli, R. M. *Nature medicine* **2001**, *7*, 493-496.

- (43) Schober, Y.; Guenther, S.; Spengler, B.; Römpf, A. *Analytical chemistry* **2012**, *84*, 6293-6297.
- (44) Fujii, T.; Matsuda, S.; Tejedor, M. L.; Esaki, T.; Sakane, I.; Mizuno, H.; Tsuyama, N.; Masujima, T. *Nature protocols* **2015**, *10*, 1445-1456.
- (45) Lanni, E. J.; Rubakhin, S. S.; Sweedler, J. V. *Journal of proteomics* **2012**, *75*, 5036-5051.
- (46) Lan, X.; Cheng, B.; Yang, Q.; Huang, J.; Wang, H.; Ma, Y.; Shi, H.; Xiao, H. *Sensors and Actuators B: Chemical* **2014**, *193*, 95-99.
- (47) Yang, Q.; Wang, H.; Lan, X.; Cheng, B.; Chen, S.; Shi, H.; Xiao, H.; Ma, Y. *Sensors and Actuators B: Chemical* **2015**, *207*, 571-580.
- (48) Yang, Q.; Wang, H.; Chen, S.; Lan, X.; Xiao, H.; Shi, H.; Ma, Y. *Analytical chemistry* **2015**, *87*, 7171-7179.
- (49) Yang, Q.; Wang, H.; Lan, X.; Shi, H.; Xiao, H.; Ma, Y. In *ABSTRACTS OF PAPERS OF THE AMERICAN CHEMICAL SOCIETY*; AMER CHEMICAL SOC 1155 16TH ST, NW, WASHINGTON, DC 20036 USA, 2014.
- (50) Cheng, B.; Yuan, L.; Fang, X.; Lan, X.; Liu, J.; Ma, Y.; Shi, H.; Yang, Q.; Xiao, H. In *SPIE BiOS*; International Society for Optics and Photonics, 2014, pp 895011-895011-895016.
- (51) Schulman, S. G.; Chen, S.; Bai, F.; Leiner, M. J.; Weis, L.; Wolfbeis, O. S. *Analytica chimica acta* **1995**, *304*, 165-170.
- (52) Lee, S.-H.; Kumar, J.; Tripathy, S. *Langmuir* **2000**, *16*, 10482-10489.
- (53) Kermis, H. R.; Kostov, Y.; Rao, G. *Analyst* **2003**, *128*, 1181-1186.
- (54) Wencel, D.; MacCraith, B.; McDonagh, C. *Sensors and Actuators B: Chemical* **2009**, *139*, 208-213.
- (55) Chitarra, L.; Breeuwer, P.; Van Den Bulk, R.; Abee, T. *Journal of Applied Microbiology* **2000**, *88*, 809-816.
- (56) Jantas, D.; Greda, A.; Leskiewicz, M.; Grygier, B.; Pilc, A.; Lason, W. *Neurochemistry international* **2015**.
- (57) Mouat, M.; Manchester, K. *Comparative Haematology International* **1998**, *8*, 58-60.
- (58) Huss, J. M.; Kelly, D. P. *The Journal of clinical investigation* **2005**, *115*, 547-555.

- (59) Lin, M. T.; Beal, M. F. *Nature* **2006**, *443*, 787-795.
- (60) Wallace, D. C. *Nature Reviews Cancer* **2012**, *12*, 685-698.
- (61) Salminen, A.; Haapasalo, A.; Kauppinen, A.; Kaarniranta, K.; Soininen, H.; Hiltunen, M. *Progress in neurobiology* **2015**.
- (62) Melsner, S.; Lavie, J.; Bénard, G. *Biochimica et Biophysica Acta (BBA)-Molecular Cell Research* **2015**.
- (63) Park, J. S.; Kang, D. H.; Bae, S. H. *Biochemical and biophysical research communications* **2015**, *464*, 1139-1144.
- (64) Smiley, S. T.; Reers, M.; Mottola-Hartshorn, C.; Lin, M.; Chen, A.; Smith, T. W.; Steele, G.; Chen, L. B. *Proceedings of the National Academy of Sciences* **1991**, *88*, 3671-3675.
- (65) Reers, M.; Smiley, S. T.; Mottola-Hartshorn, C.; Chen, A.; Lin, M.; Chen, L. B. *Methods in enzymology* **1994**, *260*, 406-417.
- (66) Oriij, R.; Postmus, J.; Ter Beek, A.; Brul, S.; Smits, G. J. *Microbiology* **2009**, *155*, 268-278.
- (67) Khaled, A. R.; Kim, K.; Hofmeister, R.; Muegge, K.; Durum, S. K. *Proceedings of the National Academy of Sciences* **1999**, *96*, 14476-14481.
- (68) Lagadic-Gossmann, D.; Huc, L.; Lecureur, V. *Cell Death & Differentiation* **2004**, *11*, 953-961.
- (69) Liu, D.; Martino, G.; Thangaraju, M.; Sharma, M.; Halwani, F.; Shen, S.-H.; Patel, Y. C.; Srikant, C. B. *Journal of Biological Chemistry* **2000**, *275*, 9244-9250.

SECTION

2. CONCLUSIONS

In summary, three major aspects were covered in a series of internally-correlated studies that aimed not only to provide phenomenon to mechanism insights into MNMs related cytotoxicity as well as a special case on bioactive glass fibers, but also to develop a successive levels of optical fiber-based probes for quasi- to single cell level measurements, where the pH has been a constant emphasis. The ultimate expectations were to provide a feasible hint to pave the way of fabricating next generation single cell resolution sensors and thus, profoundly solve the cellular heterogeneity problem for the future precise biomedical practice.

We first quantitatively demonstrated that the cytotoxicity of 50-70 nm ZnO NPs to A549 cells was dose-, time-, hydrodynamic size, as well as irradiation wavelength-dependent. We found that the photo-catalytic properties of ZnO NPs can significantly enhance their cytotoxicity, and we discovered a unique nuclear decomposition process prior to membrane deformation during cell exposure to NPs. We thus hypothesize that the basic nuclear environment selectively attracts the positively charged electron-“holes” on ZnO NP surfaces generated by irradiation. Bearing this hypothesis, we looked deep into the physicochemical properties of ZnO NPs on ROS generation. ESR analysis clearly demonstrated that $\bullet\text{OH}$ generation is the function of irradiation time, hydrodynamic size, dosage, and local pH. Preferential $\bullet\text{OH}$ generation was actually correlated with irradiation, alkaline pH, high dissolved oxygen, and low ionic strength. We found the transiently generated $\bullet\text{OH}$ prefer to bound to the NP surface thus suggested high

concentration, localized ROS production region, which indicative of a novel, alternative mechanism for nanocytotoxicity.

Then, a special case of bioactive MNMs: borate- and silicon-based nano-/micro-glass fibers were comprehensively evaluated for their biocompatibility. Substantial glass-conversion was observed during fiber immersion, indicating an active ion-exchanging process between medium and fibers under dynamic flow conditions. These processes were lately proved good for cell growth and migration through appropriate adjustments. Moreover, the trace amount doping of metal species within the glass composition (such as copper and zinc) also demonstrate their potential importance in biocompatibility and bioactivity. These results for the first time provide quantitative basis for the biocompatible mechanism of such material, and widened our view of different MNMs that may interact with bio-systems.

Thirdly, we continuously developed a series of fiber-optic reflection-mode probes based on dye-doped ultra-thin aerogel dip-coating technique for pH sensing. Starting from a one-fiber spherical head probe, which can only measure maximally 50 – 70 μm range, then upgraded to a unique hexagonal 1-in-6 fiber configuration, and finally established a novel ratiometric-free, fiber-optic $\mu\text{-pH}$ probe with a featured “tip-cut” region, for single cell subcellular measurement. Many state-of-the-art techniques have been used during the progress that including sol-gel dip-coating, covalently bond OrMoSils, HMDS priming, aerogel formation, coaxial-twisting and gravitational-stretching, nano-/micro-fabrications use FIBs under SEM, as well as miscellaneous laser and fiber optic techniques. An ultimate linear pH sensing range of the probe is from ~ 6.0 – 8.0 and an optimized pH resolution up to ~ 0.02 pH unit can well be achieved with high-

spatiotemporal-resolution. These series of developed probes are especially useful for both extra-and intra-cellular macromolecular kinetics sensing, and their high-spatiotemporal resolution character of the probe provide unprecedentedly opportunities to study the cellular heterogeneity with single, live cells.

VITA

Qingbo Yang was born on September 17th, 1981 in Zhengzhou, Henan Province, China. In 2005, he received his Bachelor's degree in Bio-Engineering from Zhengzhou University in Zhengzhou, China. Then in 2010, he received his Master's degree in Molecular Biology and Biochemistry from Shanghai University in China. He joined Dr. Yinfu Ma's group in the Department of Chemistry at Missouri University of Science and Technology since September, 2010. In July 2016 he received his Ph.D. degree in Chemistry from Missouri University of Science and Technology.